ANALYSIS OF THE UNCERTAINTIES IN THE DETERMINATION OF THE STOKES PARAMETERS EMPLOYING THE PROOF OF CONCEPT PROTOTYPE OF THE SPECTROPOLARIMETER FOR THE GALILEO SOLAR SPACE TELESCOPE(GSST/INPE)

Adriany Rodrigues Barbosa

Master's Dissertation of the Graduate Course in Space Geophysics, guided by Drs. Luis Eduardo Antunes Vieira, and Franciele Carlesso, approved in March 29, 2021.

URL of the original document:
<http://urlib.net/8JMKD3MGP3W34R/44BFRP8>

INPE

São José dos Campos

2021

ANALYSIS OF THE UNCERTAINTIES IN THE DETERMINATION OF THE STOKES PARAMETERS EMPLOYING THE PROOF OF CONCEPT PROTOTYPE OF THE SPECTROPOLARIMETER FOR THE GALILEO SOLAR SPACE TELESCOPE(GSST/INPE)

Adriany Rodrigues Barbosa

Master's Dissertation of the Graduate Course in Space Geophysics, guided by Drs. Luis Eduardo Antunes Vieira, and Franciele Carlesso, approved in March 29, 2021.

URL of the original document:
<http://urlib.net/8JMKD3MGP3W34R/44BFRP8>

INPE

São José dos Campos

2021

INSTITUTO NACIONAL DE PESQUISAS ESPACIAIS

DEFESA FINAL DE DISSERTAÇÃO DE ADRIANY RODRIGUES BARBOSA
BANCA Nº 043/2021, REG 801828/2018

No dia 29 de março de 2021, as 14h, por teleconferência, o(a) aluno(a) mencionado(a) acima defendeu seu trabalho final (apresentação oral seguida de arguição) perante uma Banca Examinadora, cujos membros estão listados abaixo. O(A) aluno(a) foi APROVADO(A) pela Banca Examinadora, por unanimidade, em cumprimento ao requisito exigido para obtenção do Título de Mestre em Geofísica Espacial / Ciência do Ambiente Solar-Terrestre. O trabalho precisa da incorporação das correções sugeridas pela Banca Examinadora e revisão final pelo(s) orientador(es).

Título: "Analysis of the uncertainties in the determination of the stokes parameters employing the proof of concept prototype of the spectropolarimeter for the Galileo Solar Space Telescope (GSST/INPE)"

Eu, Alisson Dal Lago, como Presidente da Banca Examinadora, assino esta ATA em nome de todos os membros, com o consentimento dos mesmos.

Dr. Alisson Dal Lago - Presidente - INPE
Dr. Luis Eduardo Antunes Vieira - Orientador - INPE
Dr. Franciele Carlesso - Orientador - INPE
Dr. Delano Gobbi - Membro Interno - INPE
Dr. Ezequiel Echer - Membro Interno - INPE
Dr. Tardelli Ronan Coelho Stekell - Membro Externo - IFSP
Dr. Jenny Marcela Rodriguez - Membro Externo - Skoltech

To my parents Regina de Fatima and Silvio,

and my brother Silvio Junior

ACKNOWLEDGEMENTS

ABSTRACT

The study of the solar magnetic field is of great importance for our high-tech society. It is the key driver of many solar phenomena and has a huge impact on the terrestrial space environment. A better understanding of the Sun's magnetic field is fundamental to understand better how the Sun influences the Earth. Therefore, the development of technologies for studying the Sun is essential. In particular, the methods to measure the solar magnetic field are using ground-based or space-borne telescopes. The most reliable and accurate technique for solar magnetic field measurements is based on spectropolarimetry, i.e., the solar spectrum's in terms of intensity and polarization (Stokes vector). INPE's solar physics group is developing a spectropolarimeter Proof of Concept Prototype of the Spectropolarimeter (PCPS) through the Galileo Solar Space Telescope (GSST) Project. Within the master's project, the PCPS capabilities to determine the Stokes vector and the related uncertainties are investigated. The PCPS camera was characterized, and the Mueller Matrix for an Etalon state was estimated. During the exchange program (BEPE) at the MPS, SUSI / SUNRISE was analyzed. The SUSI cameras were studied, and also the theoretical Mueller matrix of the instrument. We used data from the Solar Optical Telescope (SOT) / Hinode to study image calibration. The SOT camera's readout defects were corrected, and the influence of radiation bands/cosmic ray spikes on the data was examined. We performed a simulation to validate the Mueller Matrix of the proof of concept. In the simulation, our Mueller matrix was multiplied by the estimated HMI Stokes parameters. The results show that in all polarization states, the intensity changes due to the polarization effect of sunspots. Therefore, we can obtain the Stokes parameter by PCPS by comparing the model's output with the observed value.

Key words: Spectropolarimetry; Stokes parameters; Mueller Matrix; GSST.

x

ANÁLISE DAS INCERTEZAS NA DETERMINAÇÃO DOS PARÂMETROS DE STOKES EMPREGANDO O DEMONSTRADOR DE CONCEITO DO ESPECTROPOLARÍMETRO PARA O GALILEO SOLAR SPACE TELESCOPE (GSST / INPE)

RESUMO

O estudo do campo magnético solar é de grande importância para nossa sociedade de alta tecnologia. Ele é o principal motor de muitos fenômenos solares e tem um grande impacto no ambiente espacial terrestre. Um melhor entendimento do campo magnético do Sol é fundamental para entender melhor como o Sol influencia a Terra. Portanto, o desenvolvimento de tecnologias para estudar o Sol é essencial. Em particular, os métodos para medir o campo magnético solar usando telescópios terrestres ou espaciais. A técnica mais confiável e precisa para medições do campo magnético solar é baseada na espectropolarimetria, ou seja, a caracterização do espectro solar em termos de intensidade e polarização (vetor de Stokes). O grupo de física solar do INPE está desenvolvendo um espectropolarímetro (PCPS) por meio do Projeto Galileo Solar Space Telescope (GSST). Dentro do projeto de mestrado, a capacidade do PCPS para determinar o vetor de Stokes e as incertezas relacionadas são investigados. A câmera PCPS foi caracterizada e a matriz de Mueller para um estado Etalon foi estimada. Durante o programa de intercâmbio (BEPE) no MPS, foram estudadas as câmeras SUSI e também a matriz de Mueller teórica do instrumento. Usamos dados do Solar Optical Telescope (SOT) / Hinode para estudar a calibração de imagens. Os defeitos de leitura da câmera SOT foram corrigidos e a influência das bandas de radiação / picos de raios cósmicos nos dados foi examinada. Realizamos uma simulação para validar a Matriz de Mueller do demonstrador de conceito. Na simulação, nossa matriz de Mueller foi multiplicada pelos parâmetros estimados de HMI Stokes. Os resultados mostram que em todos os estados de polarização, a intensidade muda devido ao efeito de polarização das manchas solares. Portanto, podemos obter o parâmetro de Stokes por PCPS comparando a saída do modelo com o valor observado.

Palavras-chave: Espectropolarimetria; Parâmetros de Stokes; Matrix de Mueller; GSST.

LIST OF FIGURES

LIST OF TABLES

LIST OF ABBREVIATIONS

AIA   Atmospheric Imaging Component

AOI   Angle Of Incidence

AOR   Angle Of Rotation

APS   Active Pixel Structure

BEPE   Bolsa Estágio De Pesquisa No Exterior

BFI   Broadband Filter Imager

CCD   Charge Coupled Devices

CEB   Camera Electronics Box

CMOS   Complementary Metal Oxide Semiconductor

CT   Correlation Tracker

EIS   Euv Imaging Spectrometer

EUV   Extreme Ultraviolet

EVE   Extreme Ultraviolet Variability Experiment

FG   Filtergraphs

FPP   Focal Plane Package

GSST   Galileo Solar Space Telescope

HMI   Helioseismic And Magnetic Imager

HR   Hertzsprung-Russell Diagram

INPE   Instituto Nacional De Pesquisas Espaciais

ISLiD   Image Stabilization And Light Distribution Unit

LC   Liquid Crystal

LCVR   Liquid Crystal Variable Retarder

LPS   Laboratório De Polarimetria Solar

MPS   Max Planck Institute For Solar System Research

NAOJ   National Astronomical Observatory Of Japan

NB   Without The Borders

NFI   Narrow Band Filter Imager

OTA   Optical Telescope Assembly

PA   Position A

PB   Position B

PC	Position C
PCPS	Proof Of Concept Prototype Of The Spectropolarimeter
PTC	Photon Transfer Curve
RTE	Radiative Transfer Equation
RWP	Rotating Wave Plates
SCIP	Sunrise Chromospheric Infrared Spectropolarimeter
SDO	Solar Dynamics Observatory
SG	Spectrographs
SNR	Signal-To-Noise Ratio
SoP	State Of Polarization
SOT	Solar Optical Telescope
SP	Spectropolarimeter
STD	Standard Deviation
SUSI	Sunrise UV Spectropolarimeter And Imager Instrument
TSI	Total Solar Irradiance
TuMag	Tunable Magnetograph
TV	Thermal Vacuum
XRT	X-Ray Telescope

LIST OF SYMBOLS

E_x	X component of the electric field vector
E_y	Y component of the electric field vector
$E_{0x}(t)$	amplitude of the X component electric field vector
$E_{0y}(t)$	amplitude of the Y component electric field vector
ω	angular frequency
δ	phase factors of the electric field vector
I	Stoke parameter
Q	Stoke parameter
U	Stoke parameter
V	Stoke parameter
S	Stoke vector
p	polarization vector
S₁	Stoke parameter
S₂	Stoke parameter
S₃	Stoke parameter
I_{meas}	Measured intensity
M	Mueller matrix
D	Diattenuation
T	Intensity of transmittances
L	angular momentum
S	spin angular momentum
m	magnetic quantum number
J	total angular momentum
°C	degrees Celsius

CONTENTS

1   INTRODUCTION

There are billions of stars in the Milky Way alone and an infinite number of them in the Universe (MCTIER; KIPPING; JOHNSTON, 2020). To better analyze these stars, the Hertzsprung-Russell diagram is employed. In the HR diagram, as shown in Figure 1.1, stars are classified according to their luminosity and surface temperature. The star's position on the HR diagram can provide more information about a star, such as its radius, its mass, and its current stage (STIX, 2004).

Although the Sun is the most influential star for humankind and has a wide range of responsibilities for life on Earth, we still recognized our Sun as an ordinary star compared to others. Its size and light emitted are average, and at the HR diagram, the Sun is located in the main sequence along with most of the other stars (STIX, 2004).

The Sun is not a rigid body, with a mass of approximately 1.9889×10^{30} kilograms, it is composed essentially of hydrogen (70.6%) that fuses to form helium (27.4%) during a thermonuclear reaction. The energy generated by this process is driven together by gravitational attraction, producing immense pressure and temperature at its core (SCHRIJVER; ZWAAN, 2000).

The Sun has a radius of 6.960×10^8 meters. Usually, it is divided into six regions, taking into account its properties. Figure 1.2 display the regions, the core, the radiative zone, and the convective zone. Followed by the photosphere (visible surface), the chromosphere and the corona (SHEKHTMAN; THOMPSON, 2018; STIX, 2004).

Its core creates all the electromagnetic radiation and heat emitted by the Sun. The thermonuclear reactions are the Source of energy and high temperatures. The energy moves in the form of electromagnetic radiation gradually towards the surface in the radiative zone taking up to 170,000 years to reach the convective zone. In the convection zone, through currents of plasma, energy remains to move outward.

The photosphere, the visible surface of the Sun, is the boundary between the Sun's interior and the solar atmosphere. It is a region of 500 kilometers thick where most of the Sun's radiation is emitted. Above the photosphere is the solar

atmosphere, consisted of the thin layers: the chromosphere and the corona. The chromosphere layer is formed by the lines of the magnetic field that narrow the charged solar plasma. Between the chromosphere and the corona, there is a transition region. In it, there is a sharp temperature gradient. The corona is the external Sun's atmosphere. However, because the surface of the Sun is too bright, it is not possible to see the corona in visible light. Nevertheless, the ionized elements inside the corona can be detected on the X-ray and at extreme ultraviolet wavelengths (NASA)[1](GÓMEZ, 2017; SHEKHTMAN; THOMPSON, 2018).

Figure 1.1 Hertzsprung – Russell diagram.
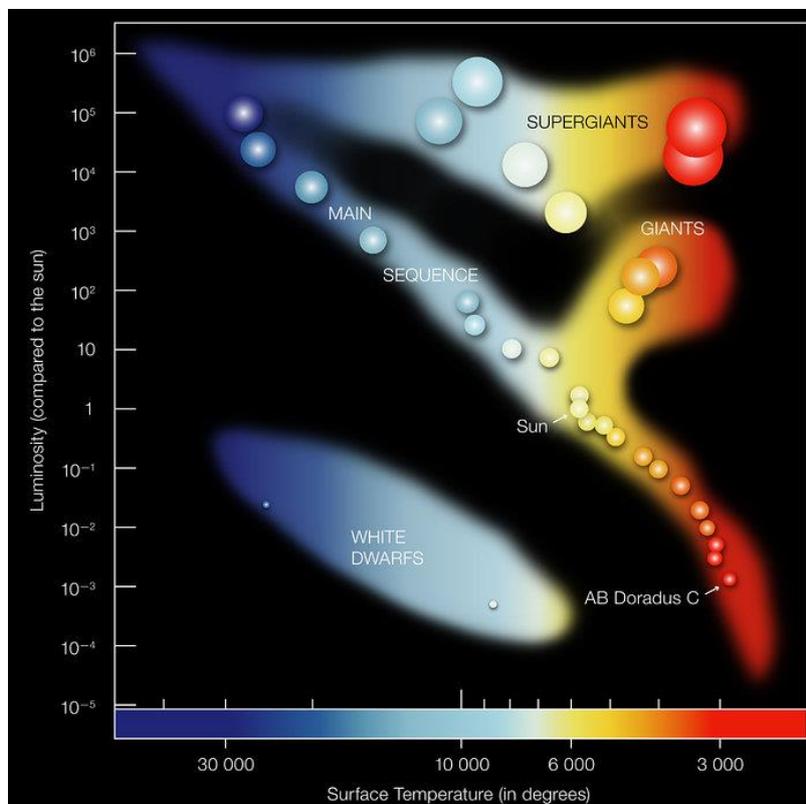
Source: ESO (2019)[2].

---

[1] https://www.nasa.gov/mission_pages/sunearth/science/solar-anatomy.html

[2] https://www.eso.org/public/brazil/images/eso0728c/

Due to its proximity to the Earth, it is possible to study and observe the fine structures of the Sun. This allowed us to gain a broad understanding of solar activity and solar phenomena and how they influence the Earth.

The evolution of the solar magnetic field is the primary driver of a series of phenomena that modulate the variability of the heliosphere on time scales from fractions of seconds to millennia (CHOUDHURI, 2007). In particular, the variability in the structure of the solar wind and its coupling with the Earth's magnetosphere affect the Earth's climate in ways that can be seen in decades and centuries (REINHOLD *et al.*, 2020).

Figure 1.2 Layers of the Sun.
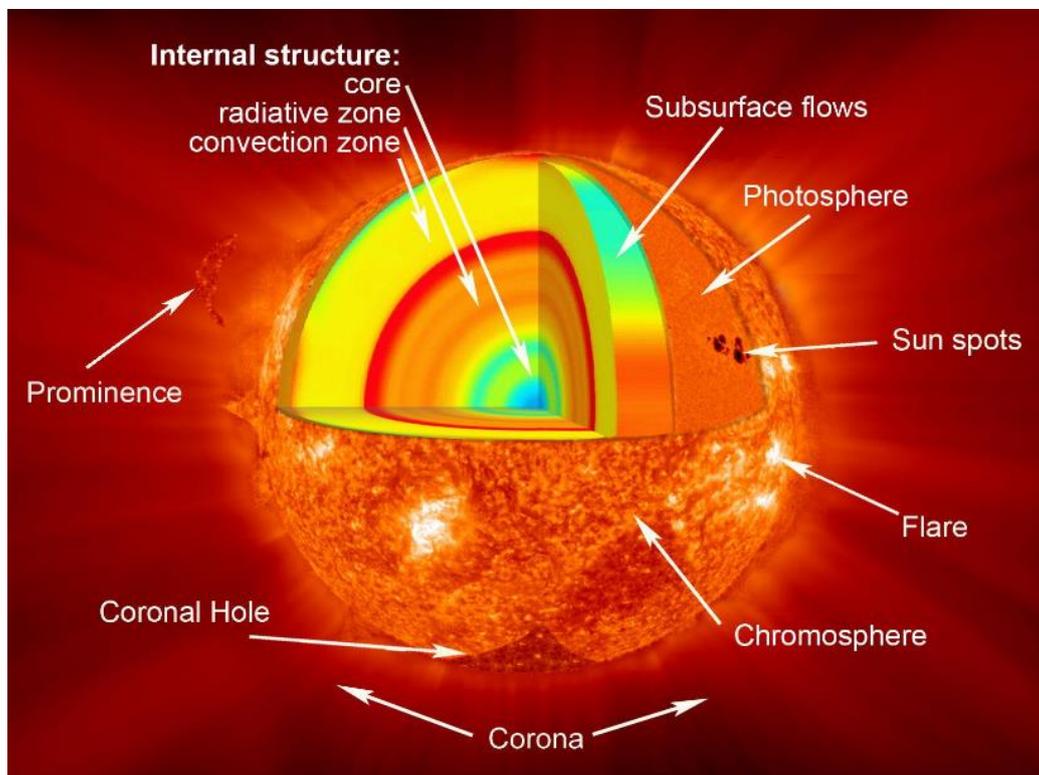
Source: NASA (2019)[3].

With the establishment of technological infrastructure developed after the industrial revolution and widely employed today, this influence becomes more expressive, as magnetic storms generate the injection of high-energy particles

---

[3] https://www.nasa.gov/images/content/462977main_sun_layers_full.jpg

into low orbits that can damage spacecraft, artificial satellites, or astronauts during spacewalks. Magnetic storms can also cause interference in satellite communication to disrupt or reduce the performance of global navigation systems. Even blackouts in electrical power grids may occur (BOTHMER; DAGLIS, 2007; ODENWALD, 2015).

Therefore, understanding and predicting solar events will be essential to ensure the safety of high technology. It also provides a better understanding of how the Sun influences the Earth. An example is a variation of Total Solar Irradiance (TSI) from the increase of sunspots during the solar maximum, and bright elements, and faculae on the solar surface (KRIVOVA; SOLANKI, 2008).

While in-situ measurements of the interplanetary magnetic field are available since the beginning of space exploration, in-situ observations near the solar surface and its atmosphere are not feasible yet. Alternatively, remote sensing techniques have been developed to estimate the solar magnetic field structure from the ground or near Earth's space (IGLESIAS, 2016).

The most prominent technique is the so-called spectropolarimetry, based on the analysis of changes of the electromagnetic spectrum in emission or absorption lines sensitive to the environmental magnetic field (e.g. COLLADOS *et al.*, 2012; DE PONTIEU *et al.*, 2014; DEL TORO INIESTA, 2003; FELLER *et al.*, 2014; GANDORFER *et al.*, 2010; KANO *et al.*, 2008; SCHMIDT *et al.*, 2012; SCHOU *et al.*, 2011; SOLANKI *et al.*, 2019). The final performance of the spectropolarimeter and also its cost depends on the location of the telescope, in space or at the surface. Not only the spatial, spectral and temporal resolution influences the quality of a solar spectropolarimetric measurement, the noise level in Stokes images also has a great contribution. Therefore, to guarantee a good calibration of the instrument and to be aware of its uncertainties is extremely important (IGLESIAS, 2016).

1.1 Objectives

The main topic of interest for this project is the estimation of the Stokes parameters of the Galileo Solar Space Telescope (GSST) Proof of Concept Prototype of the Spectropolarimeter (PCPS) and the estimation of the uncertainties of this instrument.

The specific objectives are:

- Review the mechanical design of the proof of concept to insert calibration components.
- Adequacy of the mechanical system to calibrate the polarizer package with uncertainty.
- Characterization of the proof of concept's camera.
- Data acquisition by the PCPS using a known light Source.
- Estimate the Mueller matrix with scanning in polarization in one state of Etalon (Fabry-Perot Interferometer).
- Study the Mueller Matrix for SUSI (Sunrise UV Spectropolarimeter and Imager instrument) from the SUNRISE 3 balloon project.
- Apply the Mueller matrix, estimated for the PCPS, in data to validate the experiment.

1.2 Project description

Figure 1.3 shows the activities carried out during the master's degree. In green, the activities developed at INPE stand out. In red, the activities developed during the exchange program, BEPE (*Bolsa Estágio de Pesquisa no Exterior*, text in Portuguese), at Max Planck Institute for Solar System Research (MPS) in Göttingen, Germany. The activities outlined in orange represent the analysis of cameras and images. In blue, the activities related to Mueller's Matrix are highlighted.

Figure 1.3 Project description Masters.
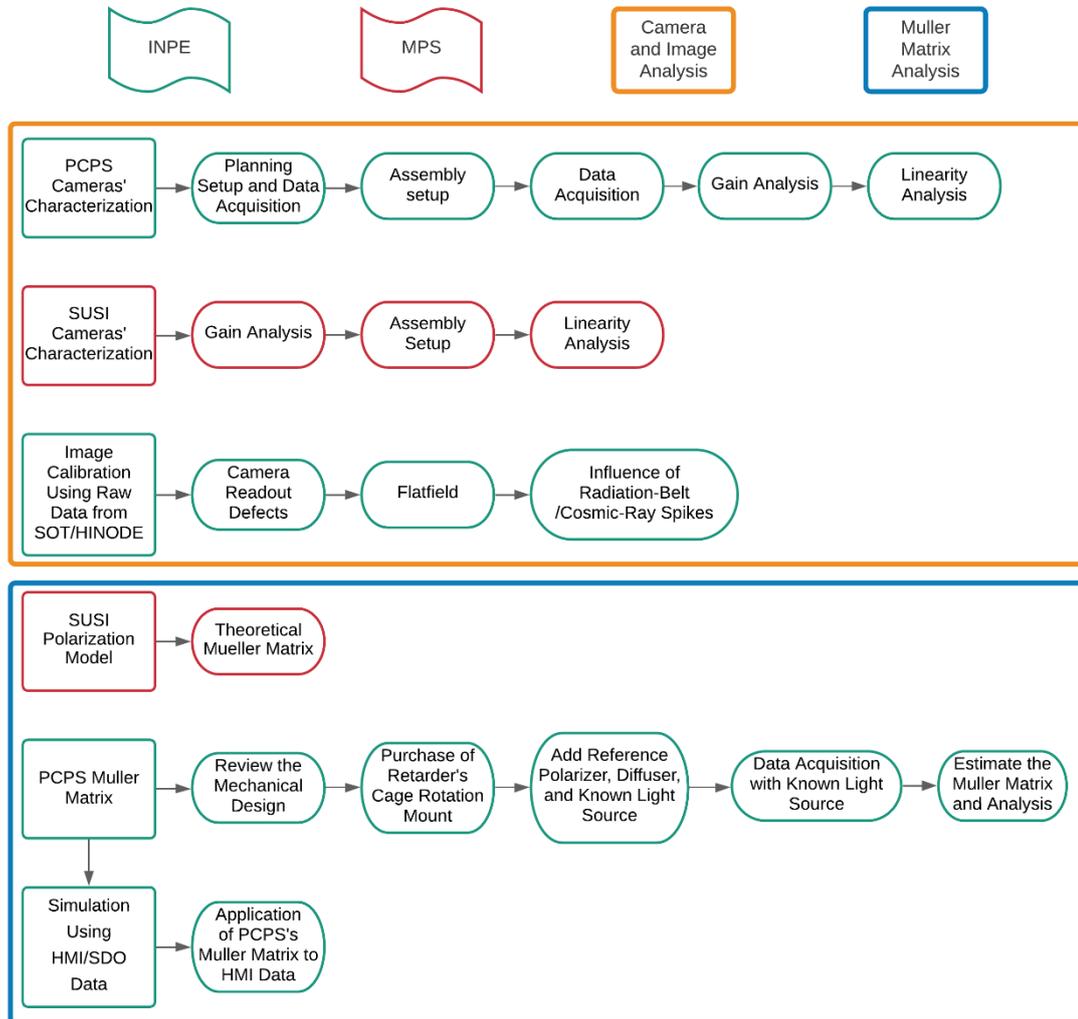
Source: Author.

1.3 Outline

The purpose of this work is to study the method of characterizing the components of spectropolarimeters. To better present the characterizations, the dissertation was divided into ten chapters, counting on this introduction.

Chapter 2 reviews the basic concepts related to this research. It describes the polarized light characterization and a brief overview of how the solar magnetic field is estimated.

Chapter 3 summarizes the instruments studied in this work and describes the main components of the solar polarimeter.

Chapter 4 details the optical and mechanical design of GSST's proof of concept. The description of the groups of components necessary for the calibration of the instrument's uncertainty is presented.

Chapter 5 describes the characterization of the proof of concept and SUSI cameras. The gain and the linearity of the cameras are analyzed. For GSST cameras, different operating modes have been studied. And a comparison between the characteristics of the cameras for the two instruments is presented.

Chapter 6 shows the calibration of the images acquired by Solar Optical Telescope (SOT) / Hinode. Here the camera readout defects were corrected, dark correction is applied, flatfield is employed, and the influence of radiation-belt/cosmic-ray spikes in the data is examined.

Chapter 7 details the characterization of the proof of concept' Mueller Matrix. The data acquisitions are detailed, and the chapter presents the matrices for each set described in chapter 4.

Chapter 8 presents a simulation made with Helioseismic and Magnetic Imager (HMI) / Solar Dynamics Observatory (SDO) data. The purpose of this chapter is to study the changes in the images that the proof of concept would take.

Chapter 9 summarizes the main results of this dissertation. The chapter also presents suggestions on the next step.

2   SPECTROPOLARIMETRY

One of the most widely used techniques in ground and satellite telescopes to estimate the magnetic field of the sun is spectropolarimetry. This technique is the measurement of light that has been evaluated spectroscopically and polarimetrically (DEL TORO INIESTA, 2003).

The objective of the spectro-polarimeters is to measure the four Stokes parameters with the highest possible polarimetric accuracy and resolution. However, it is not possible to optimize all of the spatial, spectral, and temporal characteristics simultaneously. Consequently, several trade-off combinations are necessary, depending on the scientific objective of the observations (STENFLO, 1994).

2.1   Stokes parameters

The study of the polarization of light is based on Stokes parameters. They are an ideal mathematical formalism to characterize the state of polarization (SoP) of any beam of light established by George Stokes in 1852. Here is a summary of this mathematical formalism following the approach of DEL TORO INIESTA, 2003; GOLDSTEIN, 2011; RODRIGUEZ, 2018.

Measuring the polarization of light requires defining the behavior of the electric field vector as the wave propagates.   Let us assume a quasi-monochromatic light beam, conveniently propagating along the Z-axis. Equations 2.1 represent the components of the electric field vector (E_x, E_y).

$$E_x(t) = E_{0x}(t)\cos\left[\omega t + \delta_x(t)\right]$$

$$E_y(t) = E_{0yx}(t)\cos\left[\omega t + \delta_y(t)\right] \tag{2.1}$$

Where $E_{0x}(t)$ and $E_{0y}(t)$ are the amplitudes of the electric field vector, ω is the angular frequency, and $\delta_x(t)$ and $\delta_y(t)$ are the phase factors of the electric field vector. Let us define $\delta = \delta x - \delta y$. If sin(δ) is negative, the rotation of the electric field is said to be counterclockwise. Therefore, rotation is clockwise if sin(δ) is positive.

The Stokes parameters can be defined in terms of the amplitudes and the phases as:

$$I = \langle E_x^2 \rangle + \langle E_y^2 \rangle$$

$$Q = \langle E_x^2 \rangle - \langle E_y^2 \rangle$$

$$U = 2\langle E_x E_y cos\delta \rangle$$

$$V = 2\langle E_x E_y sin\delta \rangle \qquad (2.2)$$

They are usually written in vector form, as $S = (I, Q, U, V)^T$, where the index T stands for transposition.

A condition for Stokes I is that the amount of polarized light cannot be greater than the total amount of light. Therefore:

$$I^2 \geq Q^2 + U^2 + V^2 \qquad (2.3)$$

By obtaining a set with the four Stokes parameters, a polarization vector or degree of polarization can be defined as Equation 2.4.

$$\boldsymbol{p} \equiv \left(\frac{Q}{I}, \frac{U}{I}, \frac{V}{I} \right)^T \qquad (2.4)$$

Consequently, through the intensity and the polarization vector, every beam of light can be characterized.

$$0 \leq p = \sqrt{\frac{Q^2 + U^2 + V^2}{I^2}} \leq 1 \qquad (2.5)$$

For non-polarized light or natural light $Q = U = V = 0$, so $p = 0$. If $p = 1$, the light beam is fully polarized then ($I2 = Q2 + U2 + V2$). If $0 < p < 1$ the light is partially polarized ($I2 > Q2 + U2 + V2$).

Except for the no light case ($I = 0$), one can write the equation 2.5 as:

$$\frac{Q^2}{I^2} + \frac{U^2}{I^2} + \frac{V^2}{I^2} = 1 \qquad (2.6)$$

Equation 2.6 is the surface equation of a sphere with radius 1, the so-called Poincaré sphere, represented at Figure 2.1.

Figure 2.1 The Poincaré sphere is formed by Stokes parameters, $S_1 = Q$, $S_2 = U$, and $S_3 = V$. The surface of the sphere corresponds to a fully polarized beam. The sphere's equator represents the linear state of polarization, while the sphere poles describe the circular polarization.
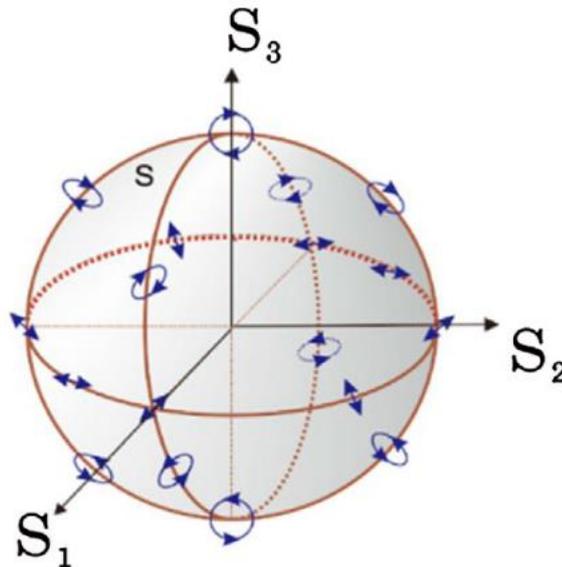
Source: Qian *et al.* (2017).

Each point on the sphere corresponds to a different polarization form. The equator represents various forms of linear polarization, the poles represent left and right circular polarization and other points on the sphere represent elliptically polarized light (BASS, 2010; DEL TORO INIESTA, 2003).

2.1.1 Measurement of Stokes parameters

Polarization measurement is based on monitoring the intensity of light that has passed through adequate optical components. For this purpose, it is

necessary to measure the motion of the electric field vector, taking into account the direction of movement ($\hat{x}\ and\ \hat{y}$) in addition to the phase differences between the electric field components. The most commonly used components are the linear polarizer and the linear retarder (DEL TORO INIESTA, 2003; SANTIAGO, 2004).

A linear polarizer is a device that reflects or absorbs any beam of light that is perpendicular to the optical axis of the linear analyzer (θ angle). That is, the light beam will only be transmitted if it is parallel to the θ angle direction. As shown in Figure 2.2(a), after the light beam passes through the linear polarizer, the new components x and y of the electric field will be:

$$E'_X = E_X cos\theta; \ E'_y = E_y sin\theta \tag{2.7}$$

A linear retarder is a device that induces, in the incoming light beam, a phase lag (retardance) δ to one of the Cartesian components. Considering x as the fastest axis, as displayed in Figure 2.2(b), the new components of the electric vector are:

$$E'_X = E_X; \ E'_y = E_y e^{i\delta} \tag{2.8}$$

The linear combination of the four Stokes parameters is the measured output intensity. Therefore, it is possible to determine the Stokes parameters by varying θ and δ (DEL TORO INIESTA, 2003; GOLDSTEIN, 2011; SANTIAGO, 2004).

Let us assume that a quasi-monochromatic light beam passes through a linear retarder and then through a linear polarizer. Equation 2.9 describes the beam characteristics after passing through these two optical devices.

$$E' = E_\theta \hat{e}_\theta = [E_x cos\theta + E_y sin\theta e^{i\delta}]\hat{e}_\theta \tag{2.9}$$

Figure 2.2 (a) Sketch of linear polarizer behavior inclined by an angle θ. (b) Sketch of linear retarder with retardance applied at Y-coordinate.
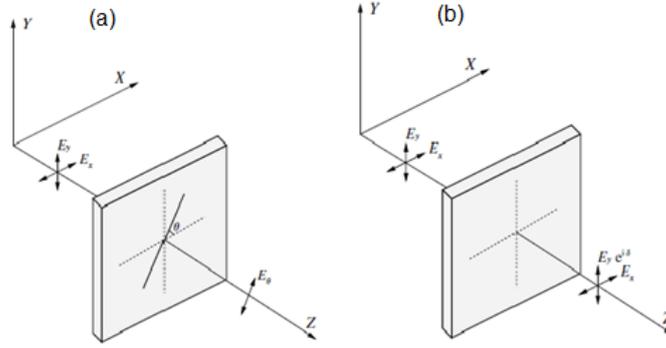
Source: Adapted from Del Toro Iniesta (2003).

The intensity measured in the output beam depends on both θ and δ as described above:

$$I_{meas}(\theta, \delta) = \langle E_\theta(\theta, \delta) E_\theta^*(\theta, \delta) \rangle = \langle E_x E_x^* cos^2\theta + E_y E_y^* sin^2\theta +$$

$$\frac{1}{2} E_x E_y^* sin2\theta e^{-i\delta} + \frac{1}{2} E_x^* E_y sin2\theta e^{i\delta} \rangle \tag{2.10}$$

Employing the definition of the Stokes parameters one can write Equation 2.2 as:

$$\langle E_x E_x^* \rangle = 1/2 \, (I + Q)$$

$$\langle E_y E_y^* \rangle = 1/2 \, (I - Q)$$

$$\langle E_x E_y^* \rangle = 1/2 \, (U + iV)$$

$$\langle E_x^* E_y \rangle = 1/2 \, (U - iV) \tag{2.11}$$

Therefore, Equation 2.10 can be rewritten as a linear combination of the four Stokes parameters:

$$I_{meas}(\theta, \delta) = \frac{1}{2}(I + Qcos2\theta + Ucos\delta \, sin2\theta + Vsin\delta \, sin2\theta) \tag{2.12}$$

Consequently, by varying δ and θ one can determine I, Q, U, and V.

$$I = I_{meas}(0,0) + I_{meas}(\pi/2,0)$$

$$Q = I_{meas}(0,0) - I_{meas}(\pi/2,0)$$

$$U = I_{meas}(\pi/4,0) - I_{meas}(3\pi/4,0)$$

$$V = I_{meas}(\pi/4,\pi/2) - I_{meas}(3\pi/4,\pi/2) \qquad (2.13)$$

The Stokes parameters fully characterize the SoP of light. Stokes I represents the total intensity. Stokes Q describes the difference between the vertical (90°) and horizontal polarization (0°). Stokes U expresses the difference between the polarization at 45° and -45°. Stokes V defines the difference between the clockwise and counterclockwise circularly polarized light. Table 2.1 shows the polarization states.

Table 2.1 Polarization states.

Polarization State	Stokes Vector	Description	Representation
I+Q	[1,1,0,0]	Horizontal Polarization	
I-Q	[1,-1,0,0]	Vertical Polarization	
I+U	[1,0,1,0]	+45° linearly polarized	
I-U	[1,0,-1,0]	-45° linearly polarized	
I+V	[1,0,0,1]	Right Hand Circular Polarization (RHCP)	
I-V	[1,0,0,-1]	Left Hand Circular Polarization (LHCP)	

Source: Adapted from Vieira et al. (2016).

2.2 Mueller matrix

When a light beam interacts with matter, a change in the polarization state occurs. So, the Stokes Vector entering (**S**) is different from the Stokes Vector that exits the instrument (**S**'). Fortunately, a linear transformation of the initial Stokes vector, defined by a 4x4 Mueller matrix (M), can express this modification of the SoP (DEL TORO INIESTA, 2003).

$$\mathbf{S' = MS}$$

Or

$$\begin{pmatrix} I' \\ Q' \\ U' \\ V' \end{pmatrix} = \begin{pmatrix} M_{11} & M_{12} & M_{13} & M_{14} \\ M_{21} & M_{22} & M_{23} & M_{24} \\ M_{31} & M_{32} & M_{33} & M_{34} \\ M_{41} & M_{42} & M_{43} & M_{44} \end{pmatrix} \begin{pmatrix} I \\ Q \\ U \\ V \end{pmatrix} \tag{2.14}$$

Let us suppose that the beam of light has undergone more than one change in its polarized state. Considering N as the number of interactions, each being defined as $\mathbf{M}_n$ with $n \in \{0, 1, ..., N - 1\}$. Acknowledging $n = 0$ being the first interaction, the measured Stokes vector is given by:

$$S' = \left(\prod_{n=N-1}^{0} M_n \right) S \tag{2.15}$$

The main elements that change the polarization state of a beam of light are the Earth's atmosphere; detector and data processing system; and optics components as image-forming optics, polarization analysis optics, and optical wavelength selection. In the literature, as BASS, 2010; DEL TORO INIESTA, 2003; STENFLO, 1994, it is possible to find the Mueller Matrix of several optical components.

For an ideal component, elements on the main diagonal would have a unit value, while elements off-diagonal would be zero. However, real polarization elements have some common defects and it alter the intensity of the Mueller matrix. Among the effects that cause aberrations are: retardance, depolarization,

diattenuation, and a typical factor that shows the quantity of all three elements (BASS, 2010; GOLDSTEIN, 2011).

Diattenuation, *D*, occurs when the intensity transmittance of the element is a function of the incident polarization state. The maximum and minimum intensity of transmittances defines *D*.

$$D = \frac{T_{max} - T_{min}}{T_{max} + T_{min}} \tag{2.16}$$

For an ideal polarizer, the Diattenuation is equal to one. When *D* is equal to zero, all incident polarization states are transmitted with the same attenuation. For an ideal retarder, the Diattenuation is equal to zero even when the SoP changes during transmission. As the maximum and the minimum intensity of transmittances are equal ($T_{max} = T_{min}$).

Retardance is the phase change introduced by the device between its polarization states. The retardance of a birefringent retardant, with refractive indices n_1 and n_2 and thickness t, can be expressed in radians such as:

$$\delta = \frac{2\pi(n_1 - n_2)t}{\lambda} \tag{2.17}$$

Depolarization is related to scattering and loss of coherence in the polarization state. A small amount of depolarization is correlated to scattered light from all optical components.

2.3 Zeeman effect

Many interaction processes between radiation and matter can produce polarized light or change its polarization state. In the solar polarimetry context, the effects that affect the light's polarization due to the magnetic field are the Zeeman Effect, the Hanle effect, Faraday rotation, and Faraday depolarization (TRIPPE, 2014). In this work, the focus is on the Zeeman Effect, which allows instruments to detect weak magnetic fields (~ 1 Gauss) (LANDSTREET, 2014).

When electrons transition between two energy levels, a spectral line is produced. The Zeeman Effect consists of the splitting or widening of the spectral lines into several polarized components by the action of a magnetic field (DEL TORO INIESTA, 2003; ZEEMAN, 1897).

The change in the spectral lines occurs due to the coupling of the electron orbital angular moment to the external magnetic field. To successfully explain the magnetic field effect in atoms, let us apply the LS or Russell-Saunders coupling scheme. To summarize, an atom has four quantum numbers that describe the quantum-mechanical state of the energy. An orbital angular momentum (L), a spin angular momentum (S), a magnetic quantum number (m), and a total angular momentum (J), where J = L + S.

The applied magnetic field interacts with the energy level J to split the energy state with equidistantly distributed (2L +1) sub-levels, whose shifts in energy are proportional to M that can range from -L to +L. Hence, according to the number of allowed energy transitions, the original spectral line is divided into the Zeeman components. One can divide the Zeeman components into three groups: π, σ_b, and σ_r. The π components correspond to ΔM equals to zero, and are linearly polarized. The σ_b match to $\Delta m = +1$ and are elliptically polarized. The σ_r are also elliptically polarized and correspond to $\Delta m = -1$ (GONZALEZ, 2006).

There are two types of Zeeman Effect. The normal Zeeman Effect occurs when atoms do not have total spin angular momentum (S = 0). Thus, the total angular momentum is equal to the orbital angular momentum (J = L). This effect is simpler than the anomalous Zeeman Effect due to the formation of the Lorentz triplets. Figure 2.3 presents the anomalous Zeeman effect, the most common since the atoms have total spin angular momentum. It makes the behavior of atomic states in an external magnetic field more complicated. Generally, we can not distinguish between them. The difference is how to describe each effect. One can explain the normal Zeeman effect based on the classical theory, as Lorentz's model. However, one can only use the quantum mechanics that consider the spin of electrons to explain the anomalous effect (DEL TORO INIESTA, 2003).

Figure 2.3 Anomalous Zeeman effect.
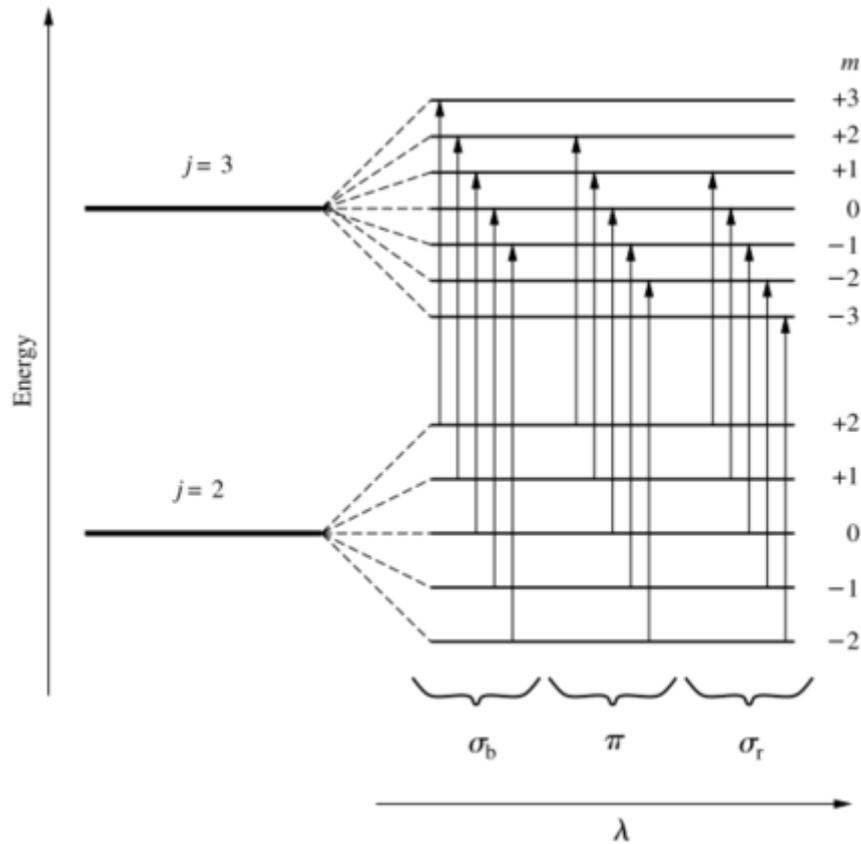
Source: Del Toro Iniesta (2003).

2.4   Radiative transfer equation and inversion codes

The radiative transfer equation (RTE) is used to describe how a polarized light beam is transferred considering the changes that a magnetic field produces in its polarization state.

While in the RTE the properties of the atmosphere are assumed to be known, the unknown data are the four Stokes profiles. However, the problem is just the opposite, the data are composed of the observed Stokes profiles and the unknown are the solar physical quantities. Therefore, to solve this problem inverting the RTE is essential to obtain the magnetic, dynamic and thermodynamic properties of the solar photosphere (DEL TORO INIESTA; RUIZ COBO, 2016).

There are many different models and techniques of inversion. However, basically the radiative transfer equations are solved in order to calculate the synthetic Stokes parameters. In an iterative way, the input parameters are modified until the difference between the synthetic and observed Stokes parameters is less than a predetermined error (DEL TORO INIESTA; RUIZ COBO, 2016; DEL TORO INIESTA, 2003).

3   INSTRUMENTS FOR SOLAR SPECTROPOLARIMETRY

Several groups have been developing ground and space-based instruments for solar spectropolarimetry e.g., DE PONTIEU et al., 2014; GANDORFER et al., 2010; KANO et al., 2008; SCHMIDT et al., 2012; SCHOU et l., 2010. However, achieving the necessary spatial, temporal, and spectral resolutions is still a challenge. Figure 3.1 shows a comparison between different instruments with their information, such as the location of the observatory, year of introduction, spectral range, and aperture. Data from different instruments were used in this work, including SOT / Hinode, HMI / SDO and SUSI / SUNRISE III.

In this chapter, a description of these instruments and the main components of solar polarimeters are presented.

Figure 3.1 Instruments used for solar polarimetry. The vertical axis represents the year of introduction; the horizontal axis displays the spectral range. The bubble radio shows the size of its aperture and its color the location of the observatory.
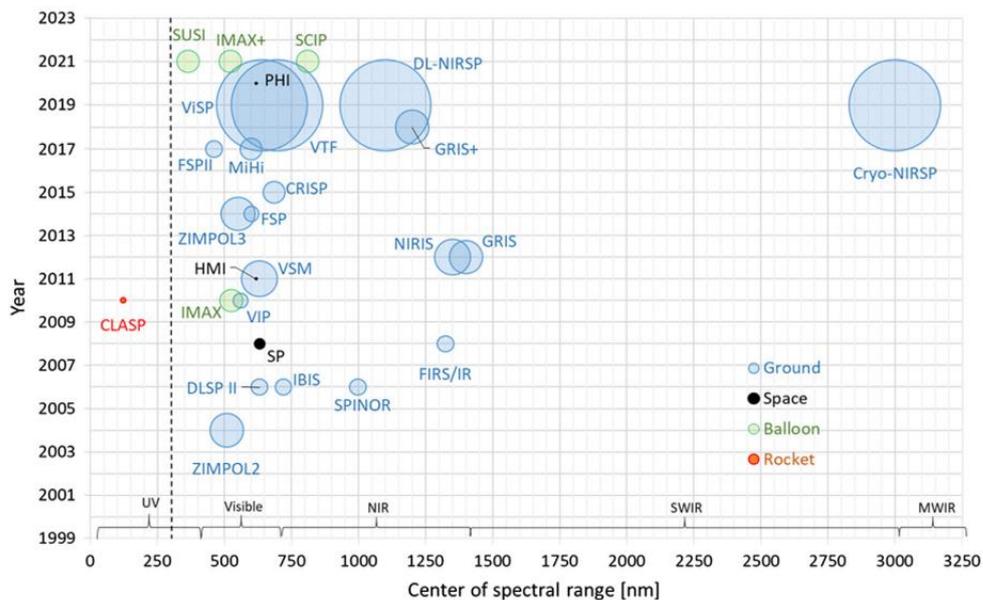
Source: Iglesias and Feller (2019).

3.1   Solar polarimeters components

The necessary components for solar polarimeters are the detector, the wavelength discriminators, and the polarization modulator.

3.1.1 Cameras

Cameras achieve a fundamental part of the solar spectropolarimetry measurements, simultaneously with polarization modulators and wavelength discriminators. The camera is a vital part, since it quantifying the number of photons detected by the sensor in a given time of exposure. By requiring excellent performance, scientific imagers are different from commercial cameras. The first have more demanding specifications, promoting design and characterization processes with latest technologies. These cameras are strongly correlated to high resolution and accuracy of spectropolarimeters, since rapid sensor are fundamental(IGLESIAS; FELLER, 2019)

Basically, the camera is composed of two main elements: the image sensor and the camera's electronics (front-end electronics). The image sensor converts the input light to analog output voltage. The front-end electronics coordinate the signals of the image sensor operation, digitize and process its analog data outputs (IGLESIAS, 2016).

The current technological developments of image sensors from scientific cameras such as CMOS (complementary metal oxide semiconductor) and CCDs (charge coupled devices) have enabled the use of fast and low noise detectors. Both sensors follow the same line of work, the difference is where and how each step occurs in the detector. First, charge generation occurs through the transformation of photons into electrons (through the photoelectric effect). Then the charge collection takes place where the electrons are accumulated in each pixel during the time of exposure (using a capacitor). Subsequently, there is the conversion of charge to voltage where the accumulated electrons are converted into a signal. Then the pixel values are read out; optionally, the signal is digitalized (IGLESIAS, 2016; MESEGUER, 2013).

Figure 3.2 shows the architecture for CMOS sensors, on a single pixel occur the charge generation, collection and conversion to voltage. That is, each pixel contains a photodiode with a capacitor, along with an element for voltage conversion. The reading of the voltages occurs through the multiplexing of the pixel values to a common bus, and then the voltage is directed to an amplifier.

20

The number of bus and amplifiers depends on the design of the sensor, as well as the number of steps in which multiplexing is performed and the number of common buffers. In cases of active pixel structure (APS), a buffer and amplifier are added for signal processing, such as multisampling or amplification (BIGAS *et al.*, 2006; IGLESIAS, 2016; MESEGUER, 2013).

Figure 3.3 displays the architecture for CCDs. The pixel complexity is lower when compared to CMOS, since the pixels only have a photodiode plus a capacitor operating only the generation and collection of charge. The conversion to voltage occurs after the charge be carried vertically from line to line to a register and then transported horizontally to the amplification and read out stage. That means that the read out starts only when the exposure is finished. The analog to digital transformation occurs outside the CCD's chip (IGLESIAS, 2016; JANESICK, 2001; MESEGUER, 2013).

Figure 3.2 Schematic for CMOS pixels architecture.
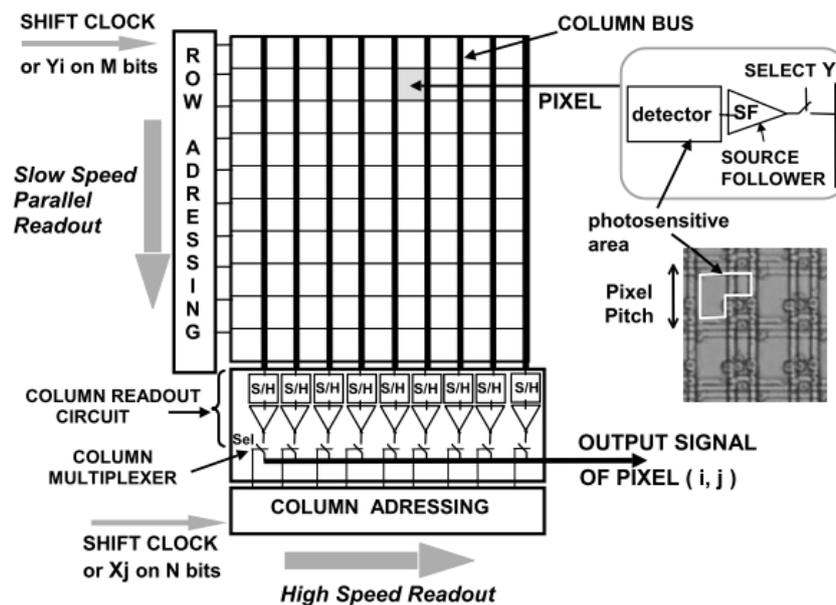
Source: Magnan (2003).

Figure 3.3 Schematic for CCD pixels architecture.
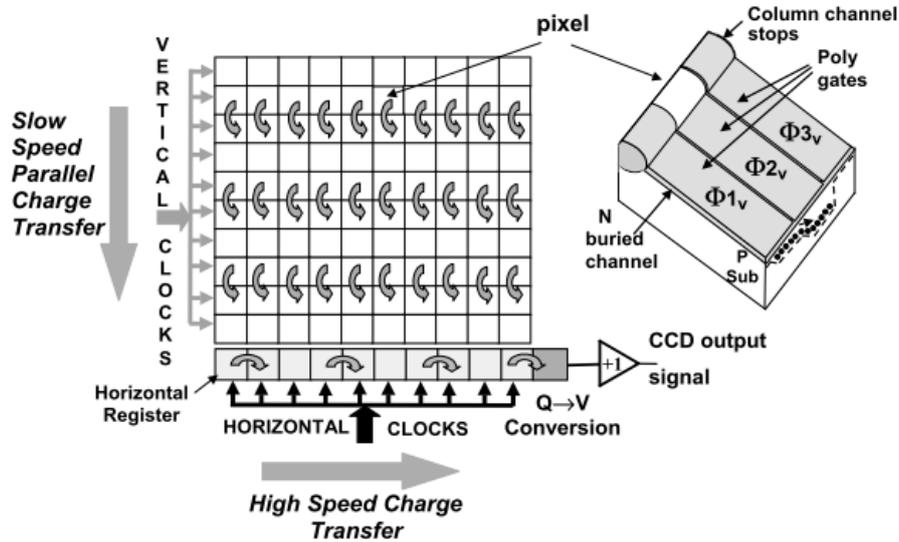
The main advantages of CMOS sensors are the possibility and flexibility to acquire images in a short period of time. The high speed of image capture. Lower cost when compared to CCD. Lower power consumption. High level of integration and possibility of miniaturization. However, they are still very noisy and less sensitive than CCDs (BIGAS *et al.*, 2006; HOFFMAN *et al.*, 2005).

In the literature, it is possible to find diversified implementations of these imagers, depending on the needs of operation, as well as several revisions. JANESICK et al. (2007, 2009, 2010); JANESICK; ANDREWS; ELLIOTT, (2006), as well as MAGNAN (2003) provides a precise comparison between the sensors. For a complete explanation of the CMOS sensors, see BIGAS et al. (2006) and HOFFMAN *et al.* (2005) for CCDs see JANESICK (2001) or HOWELL (2006).

CCDs have long been the majority for solar observation instruments, as HMI/SDO (WACHTER *et al.*, 2012) and SOT/HINODE (LITES *et al.*, 2013). However, major performance improvements and cost savings have motivated the use of CMOS (IGLESIAS; FELLER, 2019), as SUSI/SUNRISE III.

Even though the distinctions are quite subtle, it is interesting to analyze light as a flux of photons instead of classical waves to study the detectors'

uncertainty. In this case, three different types of photon statistics may occur, Poisson, super-Poisson, and sub-Poisson. The Poisson and Super Poisson statistics in the light detection are consistent with the classic light theory, although the sub-Poisson statistics are not consistent. Figure 3.4 shows the difference between the three different types of statistics. One can see that the super-Poisson distribution is broader than Poisson distribution, while sub-Poisson light is narrower (FOX, 2006).

Figure 3.4 Comparison of the photon statistics of light with Poisson, sub-Poisson, and super-Poisson distribution.
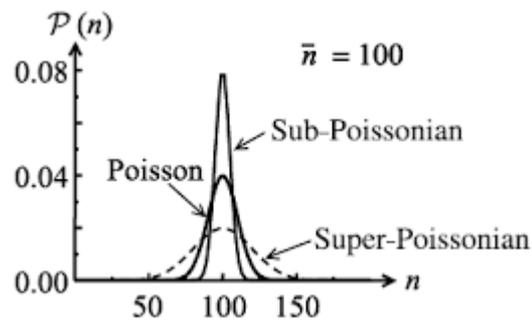
Source: Fox (2006).

The photon statistics are significant because of the shot noise in photodiodes. A photodiode is a semiconductor device that produces electrons in an external circuit when photons excite electrons from the valence band to the conduction band.

The photocurrent generated by the beam will fluctuate because of the underlying fluctuations in the impinging photon number. The fluctuations manifest themselves as noise in the photocurrent. Shot noise is a quantum noise effect, which is related to the discreteness of photons and electrons (FOX, 2006).

3.1.2 Wavelength discriminators

The wavelength is closely related to the change in the polarization of light caused by physical phenomena. Therefore, the equipment used for wavelength identification together with the polarization package is essential. The three most successful ways to do spectral scanning are spectrographs (SGs), filtergraphs

(FGs), and integral field solutions. These have the function of imagining two spatial dimensions and a spectral dimension in a two-dimensional intensity detector. The difference between them is which dimensions are observed simultaneously and which are multiplexed in time (IGLESIAS, 2016).

For spectrographs, the spectral dimension and one of the spatial dimensions are simultaneously imaged. Therefore, the surface of the sun must be scanned to obtain the remaining spatial information to generate a 2D map. Consequently, SGs are applied where SNR and spatial resolution requirements are less strict. For FGs, the spectral dimension is multiplexed in time, while the two spatial information are simultaneously imaged. This can be achieved using a narrow-band filter, as Michelson and Fabry – Perot interferometers (IGLESIAS; FELLER, 2019; IGLESIAS, 2016).

Figure 3.5 shows the scheme for the Michelson interferometer. In it, the light beam from the Source is divided at the beam splitter. The light is recombined at the same beam splitter after being reflected from the two mirrors (BASS, 2010).

Figure 3.5 Scheme for the Michelson interferometer.
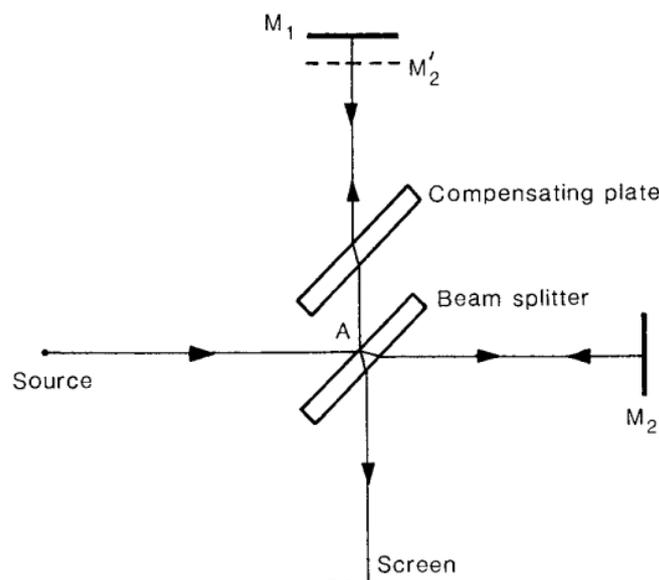
Source: Hariharan (2007).

Integral Field is a method where the spectral dimension and the two spatial dimensions are simultaneously imaged on an individual detector. The trade-off is a shortened spatial/spectral field of view and a complicated optical setup. The solar community started applying these techniques more recently, and they are still under development (IGLESIAS; FELLER, 2019).

HMI/SDO selected the Michelson interferometer (SCHOU *et al.*, 2012; WACHTER *et al.*, 2012). However, SUSI and SOT use spectrographs (ICHIMOTO *et al.*, 2008; LITES *et al.*, 2013).

3.1.3 Polarization modulators

The polarization package encodes the polarization information in intensity since the camera is only sensitive to light intensity. One has to change the diattenuation vector of the analyzer to modify the polarization signal. One can acquire this variation by changing the θ and or δ angle. The number of measurements required depends on the type of the polarimeter. However, at least four steps are needed to determine all four Stokes parameters (DEL TORO INIESTA, 2003).

Multiple components and technologies can modulate in space, spectrum, and time the output intensity based on the input Stokes parameter (IGLESIAS; FELLER, 2019). One can acquire spatial modulation by employing devices that divided the incoming intensity into spatially separated detectors, as a Birefringent plate or Polarizing beam splitter. By linearly combining the intensity signals recorded in different polarimetric channels, one can measure multiple Stokes parameters simultaneously (BASS, 2010; DEL TORO INIESTA, 2003; IGLESIAS; FELLER, 2019).

In the temporal modulation, the modulator switching its optical properties over time. Consequently, one can modify the polarization of the input light at different instants of time. Regardless of the type of modulator, the intensity value of each modulation state is imaged by a scientific camera. By linearly combining the measured intensity values, one can acquire the Stokes parameters (BASS, 2010; IGLESIAS; FELLER, 2019; STENFLO, 1994).

There are many technologies to perform temporal modulation in solar polarimeters. The most commonly used are Rotating Wave Plates (RWP) and Liquid Crystal Variable Retarders (LCVR) (IGLESIAS; FELLER, 2019).

RWP is the modulator used in HMI / SDO (COUVIDAT *et al.*, 2012; WACHTER *et al.*, 2012), SP/HINODE (ICHIMOTO *et al.*, 2008; LITES *et al.*, 2013), and SUSI/SUNRISE 3. This solution generates a fixed retardance with a variable axis. An electric motor rotates the waveplate producing retardance by varying the fast optical axis orientation (BASS, 2010). Besides working in most wavelengths, the RWPs have high surface quality with uniform characteristics and are stable in time. The increase of vibration, moving parts, power consumption, and weight are the disadvantages of this method due to the optical and mechanical design of the polarimeter is more complicated (IGLESIAS; FELLER, 2019; STENFLO, 1994; WACHTER *et al.*, 2012).

With the LCVR, also known as Nematic liquid crystal, one can obtain a variable retardance with a fixed axis after applying a voltage. IMAX/ SUNRISE 1 and 2 (MARTÍNEZ PILLET *et al.*, 2010) and GSST use this modulator. When an external electric field is applied, the liquid crystal molecules are aligned with the electric field. It reduces the birefringence of the cell. In the absence of an external voltage, LC acts as a retarder, and its retardation is proportional to the birefringence of the liquid crystal material (BASS, 2010; DROUILLARD II *et al.*, 2004). Figure 3.6 shows the Nematic liquid crystal and the influence of the application of voltage on behavior.

Unlike RWL, LCVR does not introduce moving parts. However, its optical characteristics can vary with temperature and do not show uniformity throughout the aperture (IGLESIAS; FELLER, 2019).

Figure 3.6 Liquid Crystal Variable Retarder (LCVR) structure showing molecular alignment without voltage (a) and with voltage (b).
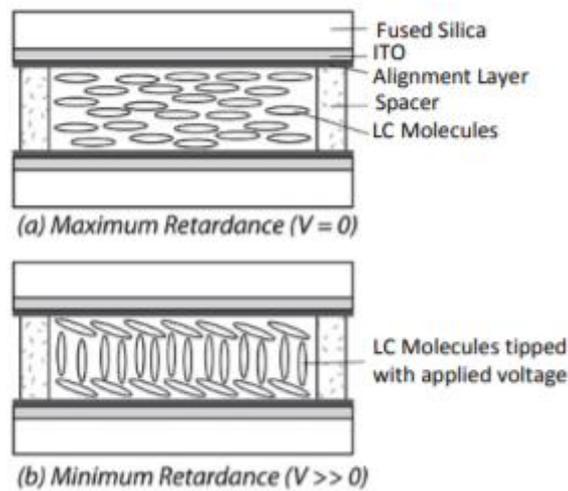
Source: Meadowlark Optics (2021).

3.2   Solar optical telescope (SOT) /HINODE

Hinode is a joint mission between Japanese, American, European, and British space agencies. The mission was launched in September 2006 to investigate the solar magnetic activity, including its production, energy transfer, and the dissipation of magnetic energy. Onboard the spacecraft are three instruments: the Solar Optical Telescope (SOT), the EUV Imaging Spectrometer (EIS), and the X-Ray Telescope (XRT) (KOSUGI *et al.*, 2007).

XRT and EIS are used to observe the energy release and dissipation of the magnetic field, while SOT conducts high-resolution photometric and magnetic observations of the magnetic flux emergence and its evolution in the photosphere and chromosphere (TSUNETA *et al.*, 2008).

The difference between the Hinode mission and other solar observation missions lies in the realization of coordinated and synchronized observation of the photosphere, chromosphere, and corona. The synchronization of observations is essential to understand how changes in the magnetic fields of the photosphere and chromosphere cause the coronal plasma dynamic response.

Figure 3.7 describes the STO. It consists of the Optical Telescope Assembly (OTA) and the Focal Plane Package (FPP). The OTA is a diffraction-limited

Gregorian telescope with an aperture of 0.5 meters. It can obtain continuous, atmosphere-seeing free diffraction-limited images with 0.2-0.3 arcsec. The images also have broad spectral resolution, approximately 0.8 nm, and high sensitivity of fully calibrated polarization. At the highest resolution, the observed bands are between 380 nm and 670 nm (SUEMATSU *et al.*, 2008).

FPP contains four different subsystems: • Broadband Filter Imager (BFI) •Narrow Band Filter Imager (NFI) • Spectropolarimeter (SP) • Correlation Tracker (CT) (SUEMATSU *et al.*, 2008; TSUNETA *et al.*, 2008).

The broadband filter imager (BFI) records diffraction-limited images, over a range of wavelengths from 388.3 nm to 668.4 nm. Irradiance data will be obtained over this time period from observations in the blue (450.4 nm), green (555.0 nm) and red (668.4 nm) continuum. The FPP narrowband filter imager (NFI) records magnetograms with a large spatial resolution, suitable for a large field of view, and has a medium polarization accuracy (4×10^{-3}). Combined, the BFI and NFI constitute the Filtergraph (FG). The filtered image is recorded on a dedicated camera using a 4096 x 2048 pixel frame transmission CCD camera. The observations cover the area from the photosphere to the chromosphere under quiet and active solar conditions (TSUNETA *et al.*, 2008).

The spectropolarimeter (SP) performs the highest precision polarimetry with a photometric measurement accuracy of approximately 10^{-3}. With a high spectral resolution, 2.15 pm, it provides complete Stokes parameters of the Fe I 630.15 / 630.25 nm line, with a spatial sampling of 0.16 arcsec (LITES *et al.*, 2013).

Figure 3.7 System overview of Solar Optical Telescope (SOT).
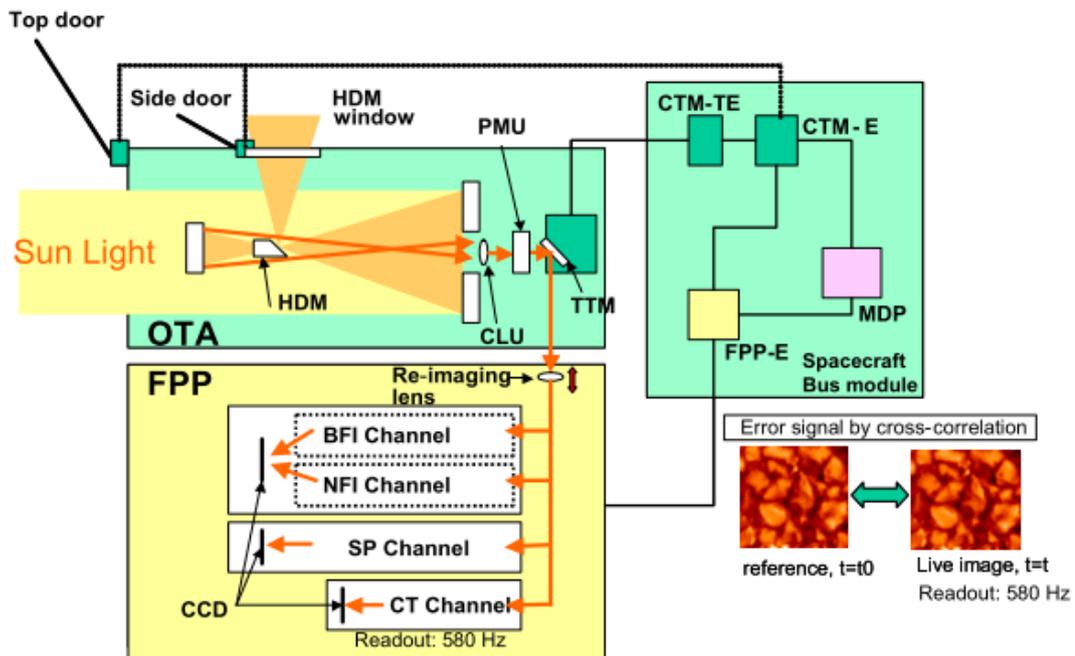
Source: Tsuneta *et al.* (2008).

3.3 Sunrise ultra-violet spectropolarimeter and imager (SUSI) /SUNRISE

SUNRISE is a balloon-borne observatory designed for high-resolution solar observations. Its operation in the stratosphere gives access to the UV range and prevents image deterioration caused by atmospheric seeing. After the flight, the instrument can be recovered and it can be upgraded and improved for a subsequent flight. The project aims to investigate the structure and dynamics of the magnetic field from the deepest observable photospheric layers to the chromosphere. Currently, Sunrise's third flight is being prepared for launch in 2022[4].

The Sunrise III will consist of three new instruments.

- SCIP (Sunrise Chromospheric Infrared Spectropolarimeter) is an infrared slit spectropolarimeter. The National Astronomical Observatory of Japan

---

[4] https://www.mps.mpg.de/solar-physics/sunrise

(NAOJ) is developing it. It aims to study the chromosphere using the Ca infrared line at two spectral regions, around 768.5 and 851.5 nm[5].

- TuMag (Tunable Magnetograph) is a magnetograph and tachograph being developed by the Spanish Space Solar Physics Consortium. It will produce 2D maps of two different layers in the Sun at a high temporal cadence. It will explore spectral lines at the visible region at 525.02 or 525.06 nm (FeI) and 517.3 nm (Mg Ib2)[6].

- SUSI (Sunrise Ultra-violet Spectropolarimeter and Imager) is a UV slit spectropolarimeter. The Max Planck Institute for Solar System Research (MPS/Germany) is currently developing it. It will study the near-ultraviolet range between 300 nm and 410 nm, which is difficult to approach from the ground[7].

Figure 3.8 displays the optical layout from SUSI and the ISLiD (Image Stabilization and Light Distribution unit). SUSI has three CMOS cameras, two cameras for the spectrograph for dual-beam polarimetric setup (SP), and one camera for the synchronous slit-jaw imager (SJ).

---

[5] https://hinode.nao.ac.jp/meeting/hinode-13/s62.html
[6] https://www.iaa.csic.es/seminars/tumag-magnetografo-para-sunrise-iii
[7] https://www.mps.mpg.de/solar-physics/sunrise-instrumentation

Figure 3.8 SUSI (Sunrise Ultra-violet Spectropolarimeter and Imager) and ISLiD (Image Stabilization and Light Distribution unit) optical design.
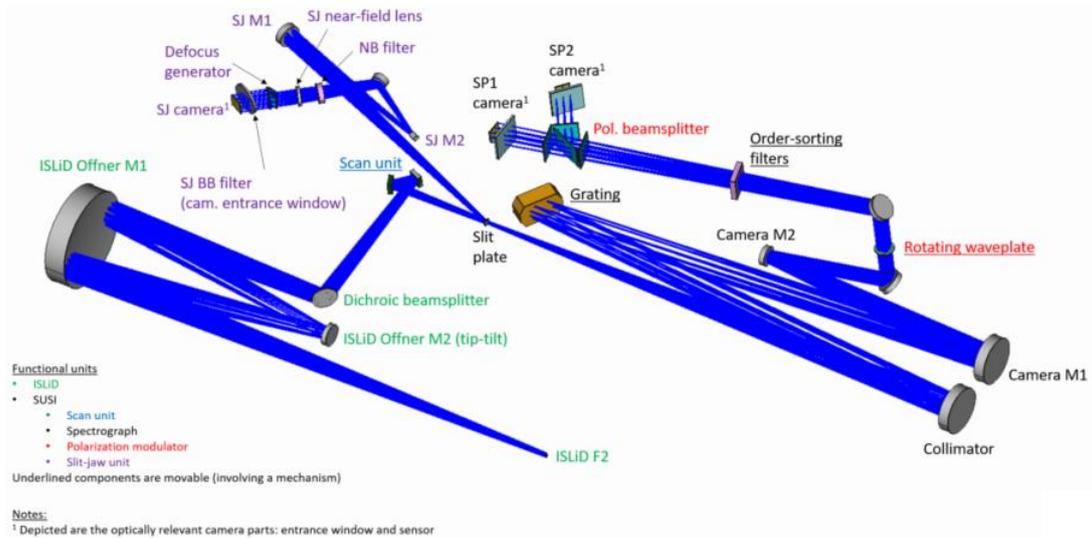
Source: SUSI group (2020).

3.4 Helioseismic and magnetic imager (HMI) / solar dynamics observatory (SDO)

The SDO (Solar Dynamics Observatory) is a mission designed to understand the causes of changes in the sun and its impact on the Earth. It has three instruments that observe the solar atmosphere in many wavelengths simultaneously (SCHOU *et al.*, 2012).

The Atmospheric Imaging Component (AIA) can simultaneously display multiple high-resolution full-disk images of the Sun's atmosphere and transition regions. It consists of four telescopes. These telescopes use normal-incidence multilayer coating optics and can achieve narrow-band imaging of seven extreme ultraviolet (EUV) lines (LEMEN *et al.*, 2012).

The Extreme Ultraviolet Variability Experiment (EVE) consists of several irradiance instruments that measure the solar extreme-ultraviolet (EUV) irradiance from 0.1 to 105 nm (WOODS *et al.*, 2012).

Helioseismic and Magnetic Imager (HMI) studies the oscillation and magnetic field of the photosphere. Figure 3.9 shows the layout of the optical path of HMI. It consists of the front window, a blocking filter, a tunable five-element Lyot filter,

two Michelson interferometers, and two 40096x4096 pixels CCD cameras. The operation is essentially in monochromatic light at 6173 Å (SCHOU *et al.*, 2012; WACHTER *et al.*, 2012).

Figure 3.9 Schematic diagram of the HMI optical layout.
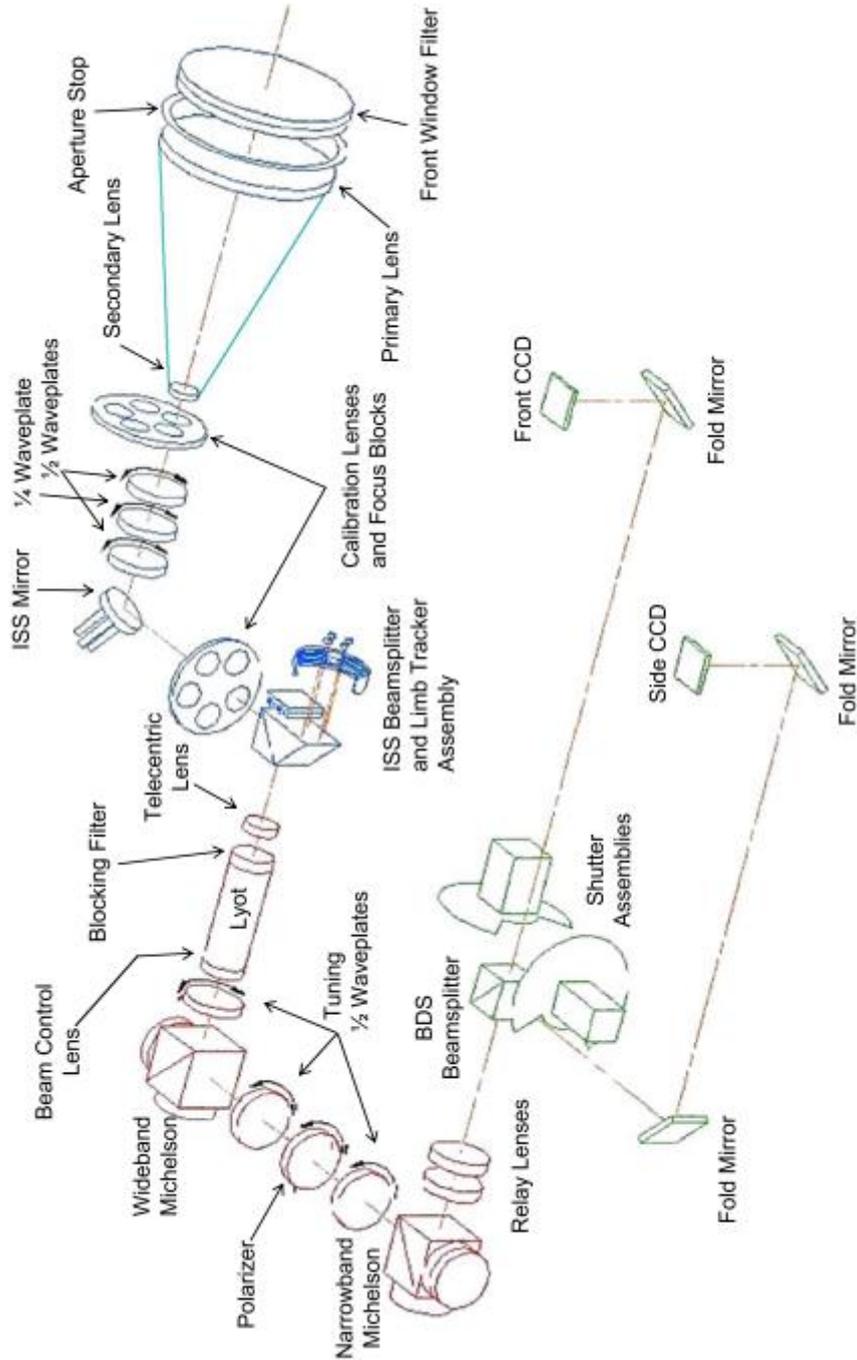
Source: Schou *et al.* (2012).

4 GALILEO SOLAR SPACE TELESCOPE (GSST)

This research is linked to Galileo Solar Space Telescope (GSST), under development at INPE. The purpose of the mission is to obtain magnetic field measurements of the solar photosphere by spectropolarimetry technique. The main scientific objectives for this mission are: (1) understand the evolution of the magnetic structures of the solar corona (2) understand the Sun's influence on Earth's climate, and (3) understand the Sun's influence**Erro! Fonte de referência não encontrada.** on the geospace. The first phase, as can be seen in **Erro! Fonte de referência não encontrada.**4.1**Erro! Fonte de referência não encontrada.**, is the development of a magnetograph and visible-light imager instrument, a proof-of-concept prototype of the spectropolarimeter (PCPS), and an advanced prototype. The second phase is the installation of the advanced prototype in a ground-based observatory. The third and fourth phases are related to the development of instruments for space-based platforms.

Figure 4.1 Long-term planning of the project Galileo Solar Space Telescope.
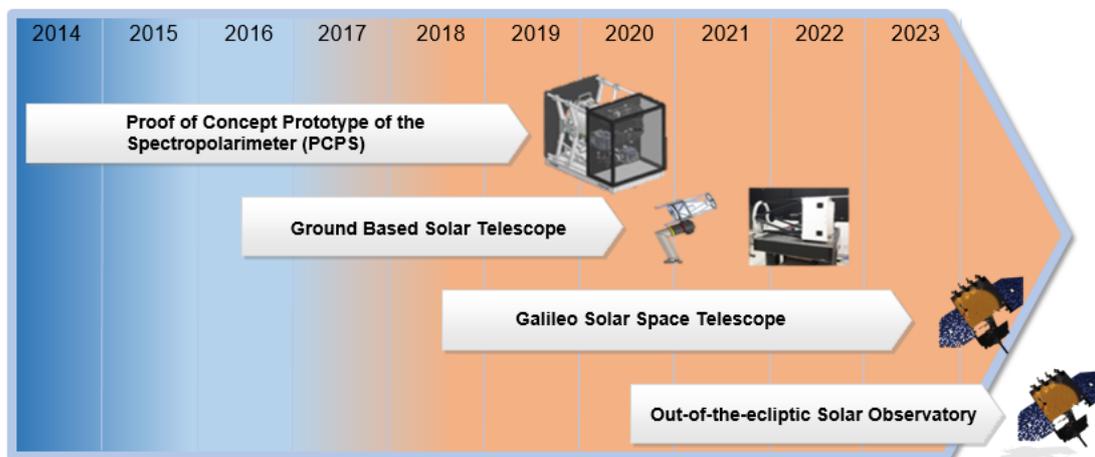
Source: Adapted from Vieira et al. (2016).

The master's main topic of interest is the estimation of the Stokes parameters from the PCPS and its uncertainties. Figure 4.2 shows the necessary steps to obtain the vector magnetic field for the Sun. In red are highlighted the steps to achieve the master's aim project.

Figure 4.2 Diagram to estimate the solar magnetic field. The red highlight is the master's project scope.
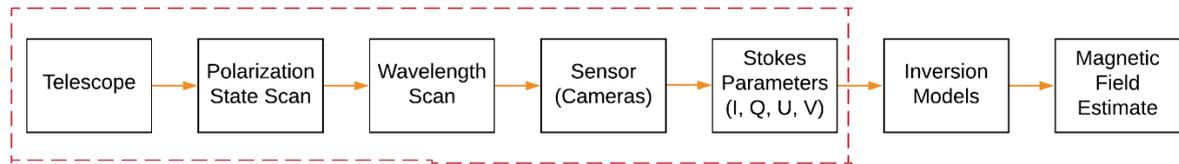
4.1 Proof of concept prototype of the spectropolarimeter (PCPS) for the Galileo solar space telescope (GSST/INPE)

The proof-of-concept prototype of the spectropolarimeter is a functional version of the instrument. Its purpose is to test the control system, synchronization, data acquisition and image concept, and optical design restrictions. Since it is a proof of concept, the PCPS is inside the LPS (*Laboratório de Polarimetria* Solar, text in Portuguese). It needs the help of a heliostat, displayed in Figure 4.3 (a), to direct sunlight to the telescope.

The proof of concept consists of a Ritchey-Chrétien telescope, a polarization modulation package, a Fabry-Pérot Etalon interferometer, sCMOS cameras, and narrowband filters. Figure 4.4 represents the simplified block diagram of the PCPS.

The GSST group chose the Ritchey-Chrétien system because it has better optical performance than Schmidt-Cassegrain and Gregorian designs. The compact size compared to an achromatic lens was also considered. The aperture of the optical telescope for the proof of concept is 150 mm. The intermediate optics were adapted to a system with a focal length of 1370 m (f / 9 system) with two-inch lenses.

The pre-filter is one of the most critical components of the entire system, as it eliminates unwanted wavelengths by reflecting them. The proof of concept has two pre-filters; the light passes through them right after passing through the telescope. They have a 7.5 Å spectral window, centered on the selected line, 6302.5 Å.

34

Figure 4.3 (a) shows the exterior of the LPS building with highlight the closed heliostat and the aperture of the window. (b) represents a drawing of the internal layout of the LPS. One can see the opening through which the light enters, the optical table, and the PCPS.
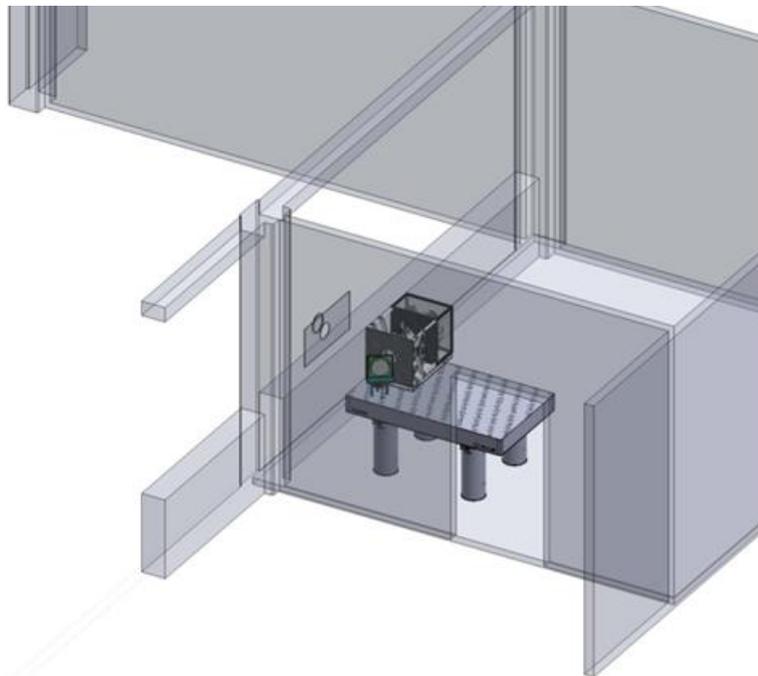
Source: (a) Dal Lago (2021) and (b) Author.

Figure 4.4 Simplified block diagram of the Galileo Solar Space Telescope's proof of concept.
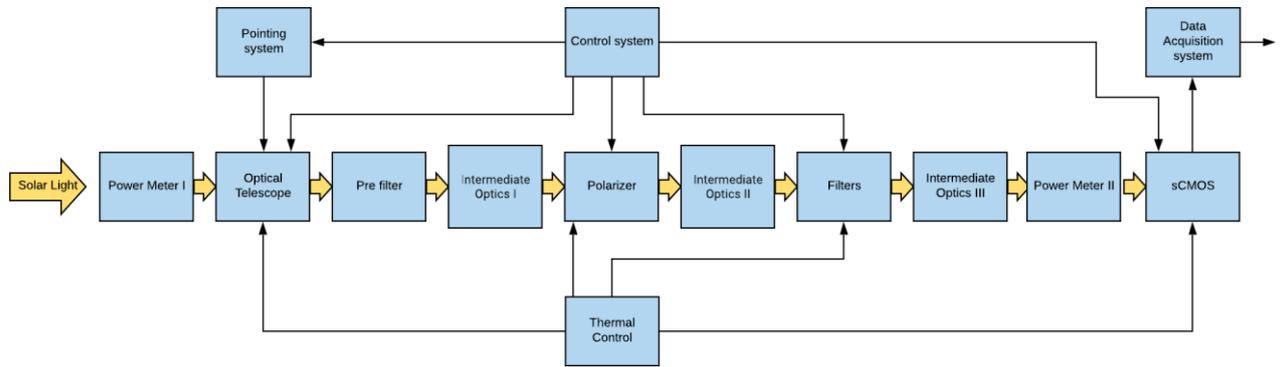
The polarization system consists of two variable liquid crystal retarders (LCVR) followed by a linear polarizer. It can select sixteen states of polarization (SoP) by changing the combination of LCVRs voltages. It is important to note that the position of LCVR1 is different from that of LCVR2 while the linear polarizer is fixed.

The Fabry-Pérot interferometer (Etalon) is a tunable filter composed of parallel mirrors of great reflection (95%). It can select operating wavelengths, 6301.5 Å to 6302.5 Å, with bandwidth on each channel. It is the component responsible for spectral scanning, achieving 64 spectral positions. One can acquire these positions by changing the voltage that feeds the etalon.

The sensor for the output of the data acquisition system is a Zyla5.5 sCMOS camera. In the CMOS sensor (Complementary Metal-Oxide Semiconductor), every pixel in the array contains a photodiode, a capacitor, and a charge to voltage conversion stage plus an amplifier (MESEGUER, 2013). Figure **4.5**4.5 shows the linear optical path modeled by OpticStudio (Zemax) software. Here, one can see the components required for the operation and the behavior of the beam inside the spectropolarimeter. As mentioned in the introduction, optical parts introduce errors in the polarization of light. In our instrument, the component that has the main influence is the polarization component. We assumed that the polarization states remain constant during the scanning of the etalon. Thus, the number of variables and the processing time

decrease. Consequently, the error inserted by the elements after the polarization package is considered negligible.

To simplify the estimates of uncertainties, one can divide the spectropolarimeter into four blocks. The first block represents the first Mueller Matrix (M0). Highlighted by the red rectangle in Figure **4.5**.5, all elements before the polarization package belong to this block. The blue rectangle marks where the other Mueller Matrices (M1, M2, and M3) are located, in this case, the polarization package. Each component of the polarization package has its matrix, Figure **4.6**4.6 shows its detailed representation.

Figure 4.5 PCPS' linear optical path.
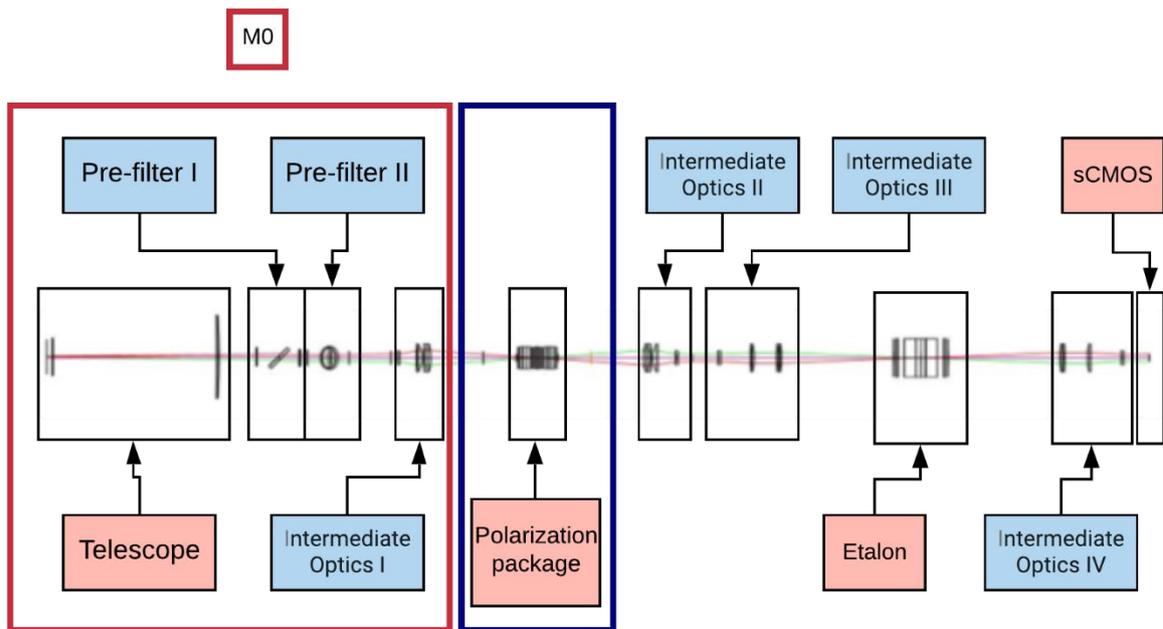
Source: Author.

Figure 4.6 Detailed polarization package with its Mueller Matrices.
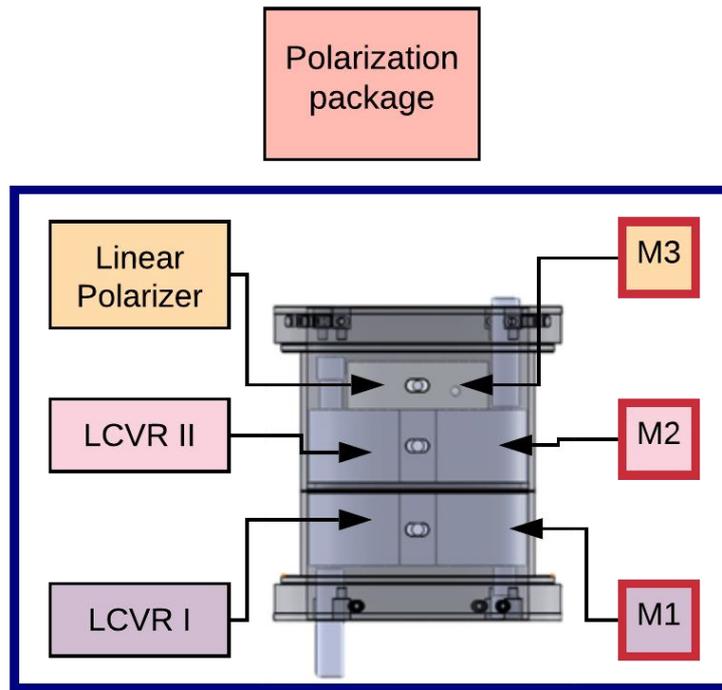
Source: Author.

Linearly mounting the spectropolarimeter is not feasible. Therefore, one can insert mirrors in the optical path to bend the light beam and thus decrease the size of the instrument. Figure **4.7**.7 shows the side view of the mechanical model of the spectropolarimeter. In this view, one can see the telescope and the pre-filters in detail, red rectangles. Figure **4.8**.8 presents the front view. Here the other components can be seen in detail, including the mirrors.

Figure 4.9 presents proof of concept showing a comparison between the mechanical layout and the instrument's assembly.

Figure 4.7 Side view of the mechanical model of the proof of concept.
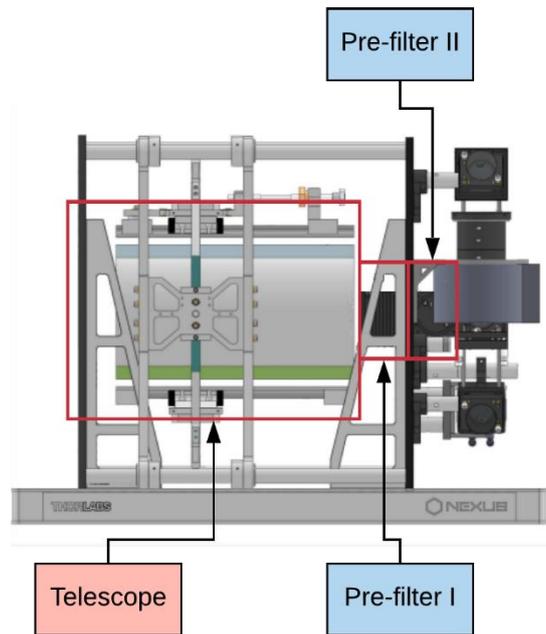
Source: Author.

Figure 4.8 Front view of the mechanical model of the PCPS.
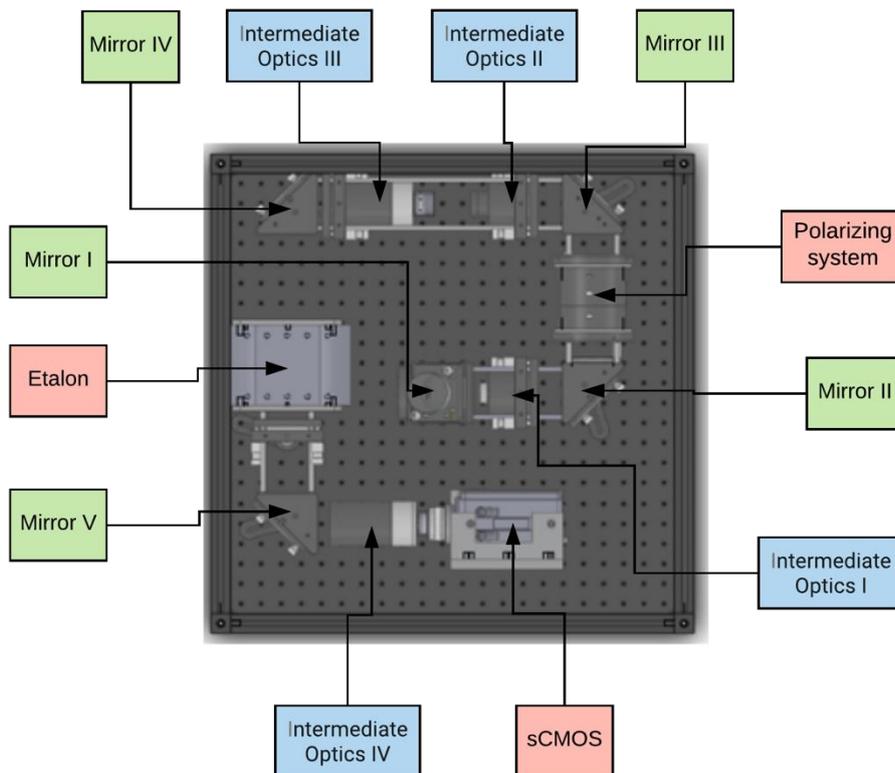
Source: Author.

Figure 4.9 (a) Proof of concept's 3-D view of the mechanical design. (b) Proof of concept assembly. (c) Spectropolarimeter mechanical design. (d) Spectropolarimeter assembly.
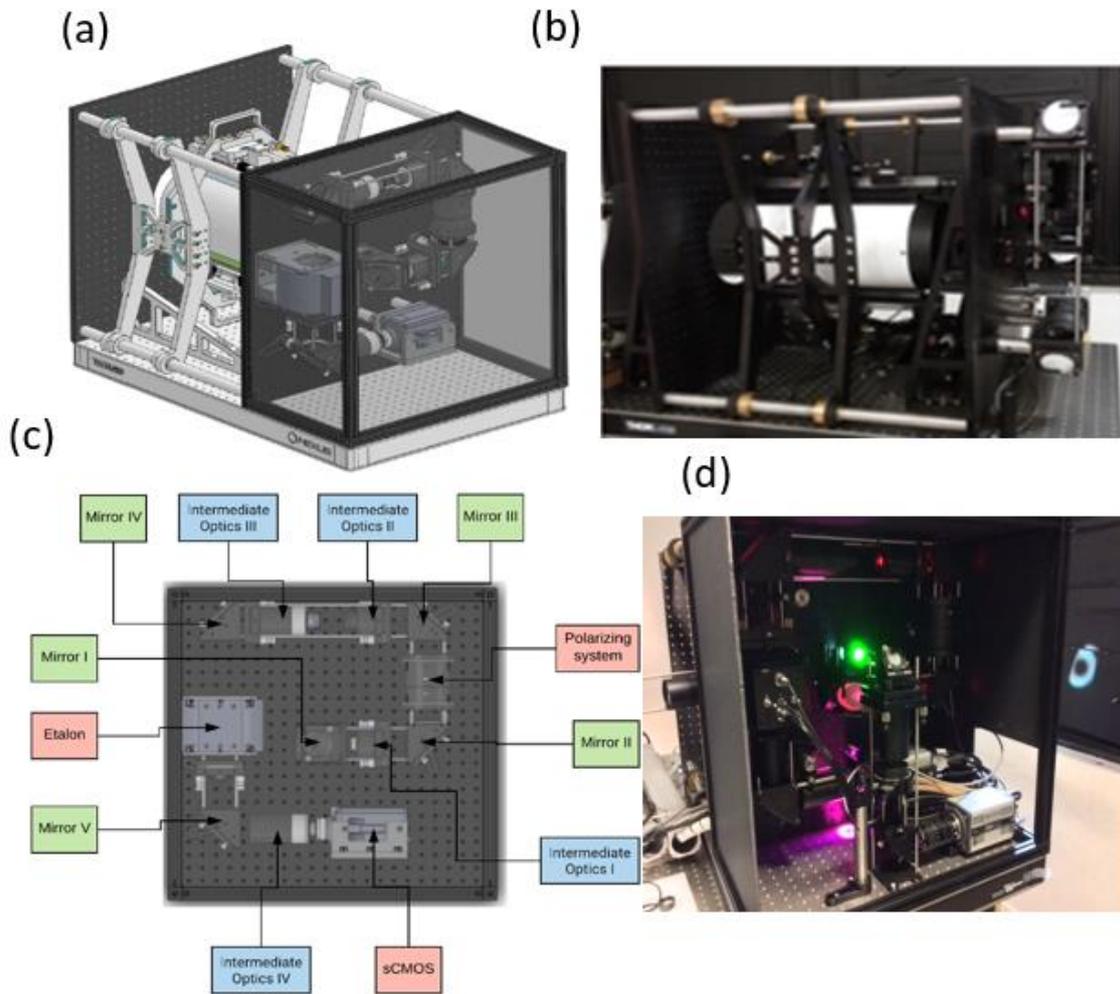
Source: Author.

5   CAMERA CALIBRATION

Detectors have a fundamental part in the sensitivity of the polarimetric measurements. These can induce significant polarimetric problems if all four Stokes parameters are not measured on the same resolution element (DEL TORO INIESTA, 2003).

Due to pixel structure and readout electronics, all cameras have nonlinearities. For an ideal detector, the signal would increase proportionally with the increase of the light intensity. In other words, there would be no change in the camera's gain. For small polarization signals, 1% of nonlinearity is considered significant (KELLER, 1996).

5.1   SUSI camera

There are three cameras on the SUSI instrument, two for high gain (SP) and one for low gain (SJ). At BEPE, the engineering models (EM) of the cameras were tested. MPS bought the sensors and developed the detector within the institute, including electronics, mechanics, operating codes, including flight care. Figure 5.1 shows a section of the drawing of the SUSI camera.

Figure 5.1 SUSI camera.
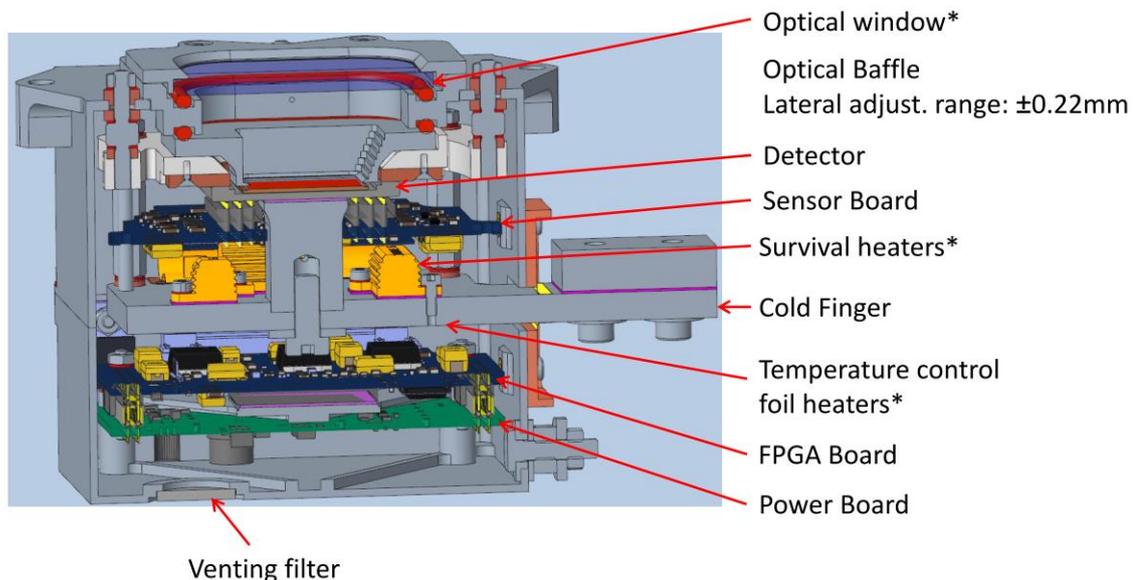
Source: SUSI group (2020).

5.1.1 Analysis from thermal vacuum test

In November 2019, Dr. Klaus Heerlein performed thermal vacuum tests. In this section, the author analyzed the data from this test. The aim is to evaluate the camera performance under thermal vacuum (TV). In this test, the camera was installed to the TV chamber "Voetsch-2" with a LED (OSRAM 365 nm) in front of it. No optics were utilized in this test. The sensor has 2048x2048 pixels and the data was acquired to 100 exposition times with 50 frames each.

5.1.1.1 SP data

Analysis of data from high gain (SP = 1.54936 DN/e$^-$). The temperature on the sensor coldfinger was 15 °C. The study started with the analysis of only one exposure time, then expanded to all one hundred times of exposure, with the subtraction of the dark.

Figure 5.2 gives the average intensity of each pixel from the 50 frames and 100 exposure times. It can be noted that the edges do not follow the same behavior as the rest of the sensor. The right, left and bottom edges have values close to zero. However, the top edge shows equivalent values with the rest of the sensor, except for a band around the 2000 line where the pixels have values greater than the average. Therefore, 100 pixels from each border were excluded in later analyzes. A structure from the top left section is also noted, with a mean intensity lower than the rest of the sensor.

Figure 5.3 shows the gain map for the SP camera. The gain represents the slope of the linear regression line of the mean intensity and the variance. This gain map plots the average intensity vs. the variance for each pixel and each exposition time. In this case, a threshold had to be placed because of the camera saturation, which influences the linear fit. After approximately 3600 counts, the pixels start to saturate, so the variance starts to decrease. The threshold of 3300 counts was chosen because, after it, the sensor has a stronger nonlinear behavior.

Figure 5.2 2D map of the average intensity, for all frames and time expositions, for each pixel. The X and Y-axis display the pixels' numbers, and the color bar represents the mean intensity for the SP camera.
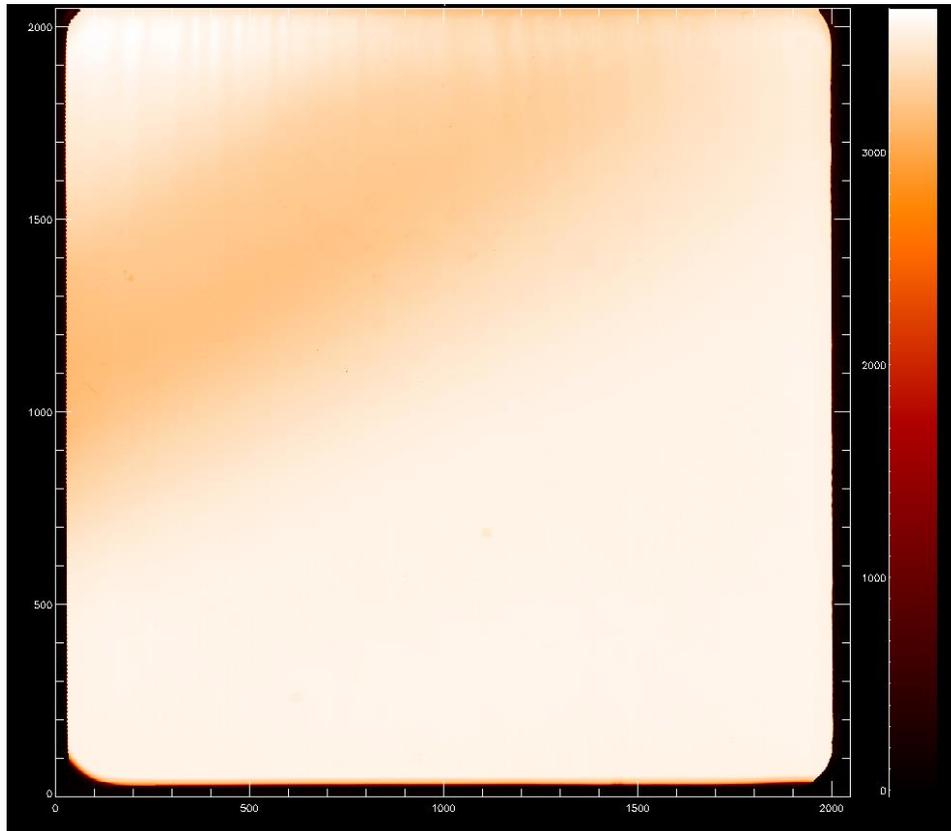
Source: Author.

Figure 5.3 Gain Map for SP camera. The X-axis displays the mean intensity in DN for each pixel and each exposition time. The Y-axis represents the variance for each pixel and each exposition time. The red line represents the fit between mean and variance calculated until the threshold of 33000 DN for all the 100 levels of exposition time. Pixels at the borders of the sensor were disregarded.

Source: Author.

43
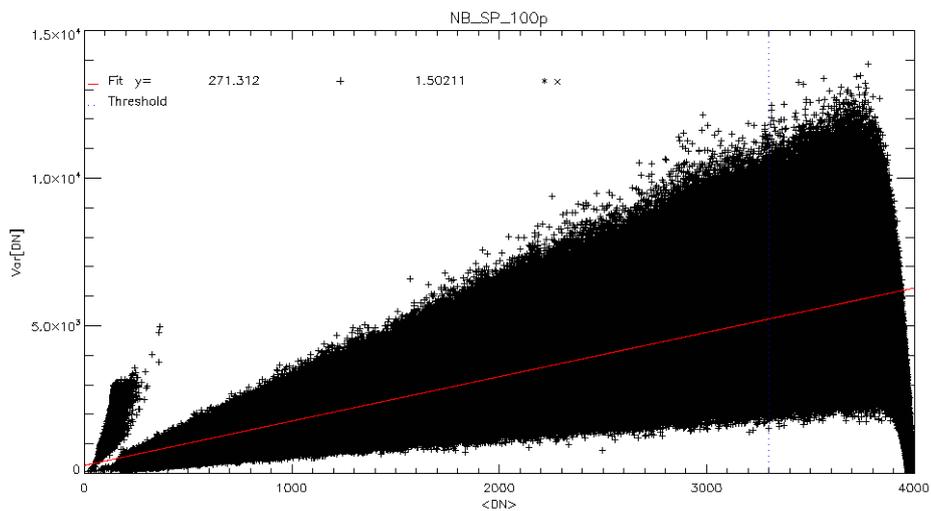
One interesting thing about Figure 5.3 is the small branch of pixels with much steeper gain values. One can see that the Photon Transfer Curve (PTC) is strongly nonlinear in this region. After some analysis, it was noticed that they are not in a specific location on the sensor.

Figure 5.4 also shows a gain map for the SP camera. However, in this case, data from the first exposure time were not included. Contrary to Figure 5.3, the segments with pixels with a steeper gain value do not appear, revealing that the level 0 image is dominated by a fixed pattern noise that distorts the PTC.

Figure 5.4 Gain Map for SP camera. The X-axis displays the mean intensity in DN for each pixel and each exposition time. The Y-axis represents the variance for each pixel and each exposition time. The red line represents the fit between mean and variance calculated until the threshold of 33000 DN for the last 99 levels of exposition time. Pixels at the borders of the sensor were disregarded.
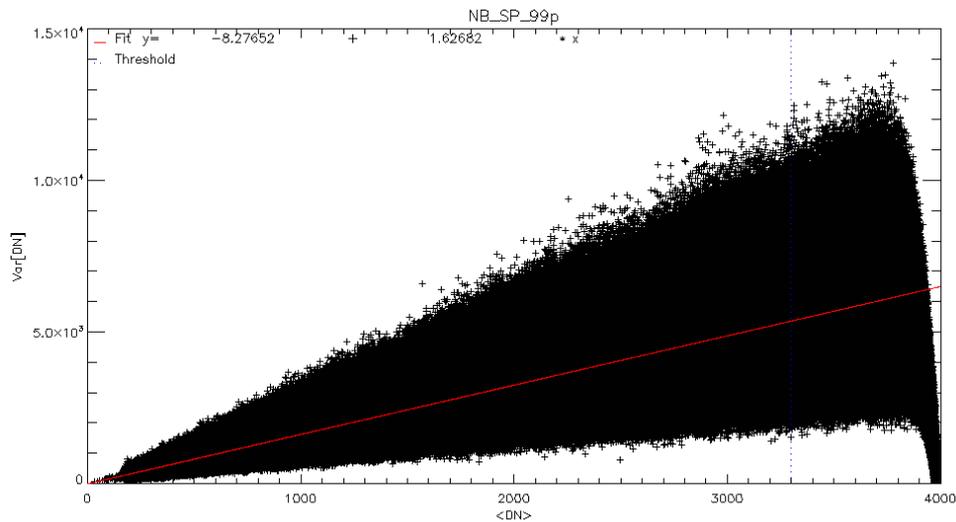
Source: Author.

The histogram of the slope from the SP without the borders (NB) is shown in Figure 5.5 by the black line. The gain was calculated for each pixel individually until the intensity levels reached a specified limit, 1800 DN. This threshold was chosen to ensure that all values are within the linear regime. The blue line represents the expected Gaussian, considering the measurement uncertainty due to noise. In this way, it is possible to see to what extent the histogram is consistent with the measurement uncertainty due to noise. From this, we can see the actual gain fluctuations in the sensor, compared to the noise.

The gain value of the pixels presents a Gaussian behavior, despite having a deviation in the left side. The gain values were expected to all be positive, but after a check, it was noted that less than 0.001% of the pixels have negative slope values.

Figure 5.5 Histogram from the Slope for the SP camera. The X-axis displays the gain value for each pixel. The Y-axis represents the relative number of the pixels. Pixels at the borders of the sensor were disregarded.
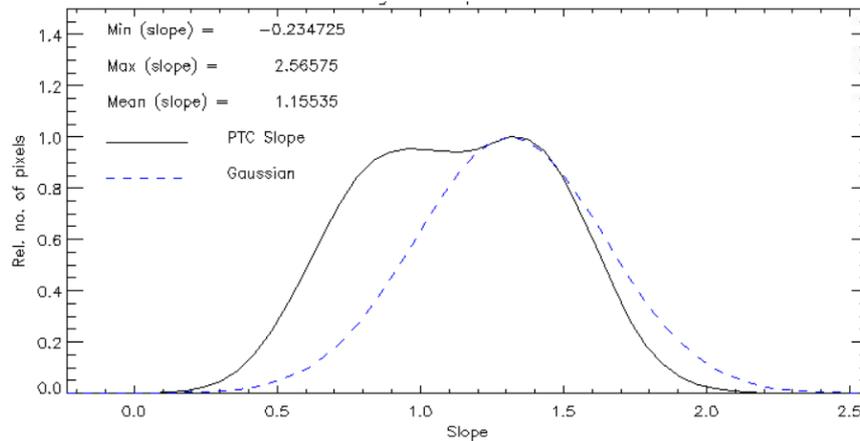
Source: Author.

Figures 5.6 displays a 2D gain map that represents the slope calculated for each pixel independently. One can notice the upper left structure, this structure has a higher gain than the other parts of the sensor. However, it is the opposite of the average intensity, as shown in Figure 5.2.

A quadratic function of the incoming intensity (S), given in equation 5.1, is the simplest method to describe the non-linear behavior (KELLER, 1996).

$$S = A + BX + CX^2 \tag{5.1}$$

Figure 5.7 shows the linearity from SP NB with a threshold (1800 DN). The red line represents the least-square polynomial fit. In this, the non-linearity is around 1-2%, which is significant. Due to the structure present in the upper left top of the sensor, there is a need for additional measures to have greater reliability in the results. Therefore, measurements of linearity with the triangular target were performed, the results are presented in section 5.1.2.

45

Figure 5.6 2D map of the Gain value for each pixel. The X and Y-axis display the pixels' numbers, and the color bar represents the slope value for the SP camera. Pixels at the borders of the sensor were disregarded.
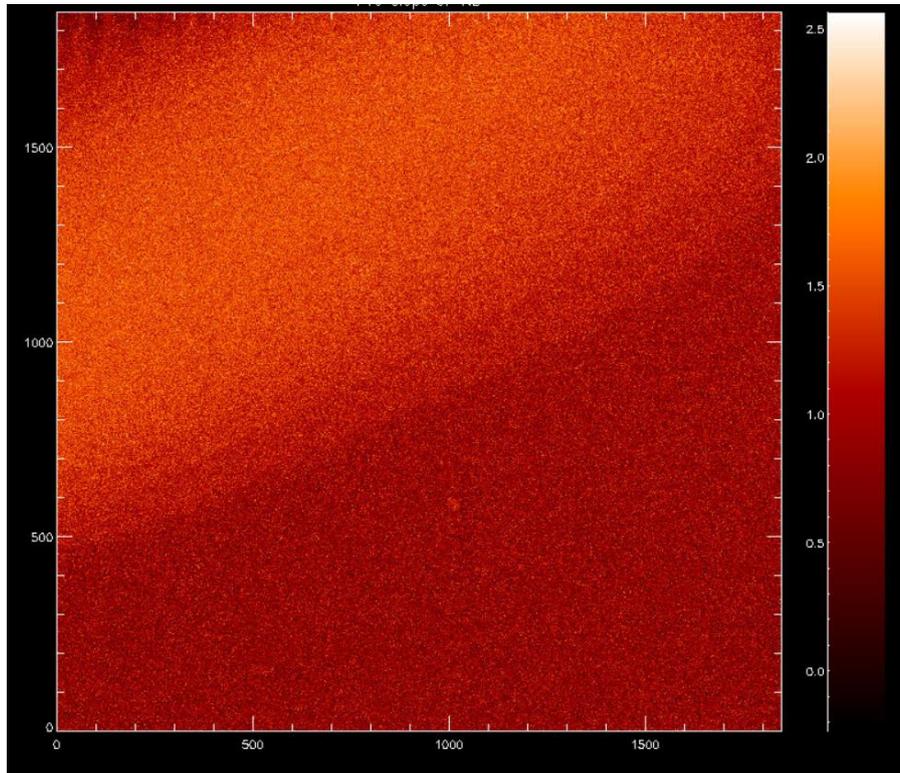
Source: Author.

Figure 5.7 Linearity graph for SP camera. The X-axis displays the exposition time in seconds, and the Y-axis represents the mean intensity for each pixel in DN. Each black dot presents a pixel, while the red line represents the least-square polynomial fit. Pixels at the borders of the sensor were disregarded.

Source: Author.

46
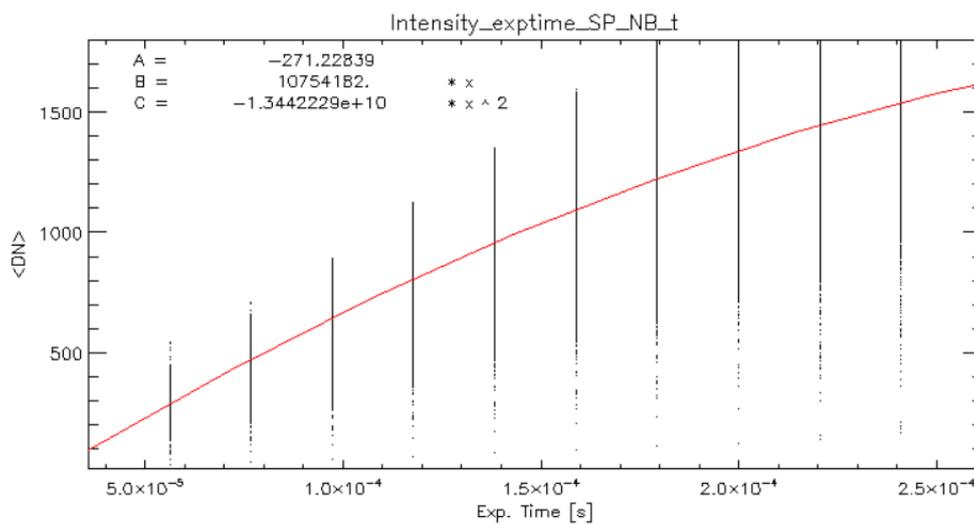
5.1.1.2 SJ data

Analysis of data from low gain (SJ = 0.01906 DN/e$^-$). The temperature on the sensor coldfinger was 15 °C. Figure 5.12 gives the average intensity of each pixel from the 50 frames and 100 exposure times. As Figure 5.2, Figure 5.8 shows that the edges do not follow the same behavior as the rest of the sensor. Therefore, 100 pixels from each border were also excluded in later analyzes in this data set. The structure from the top left section is also noted, with a mean intensity lower than the rest of the sensor.

Figure 5.8 map of the average intensity, for all frames and time expositions, for each pixel. The X and Y-axis display the pixels' numbers, and the color bar represents the mean intensity for the SJ camera.
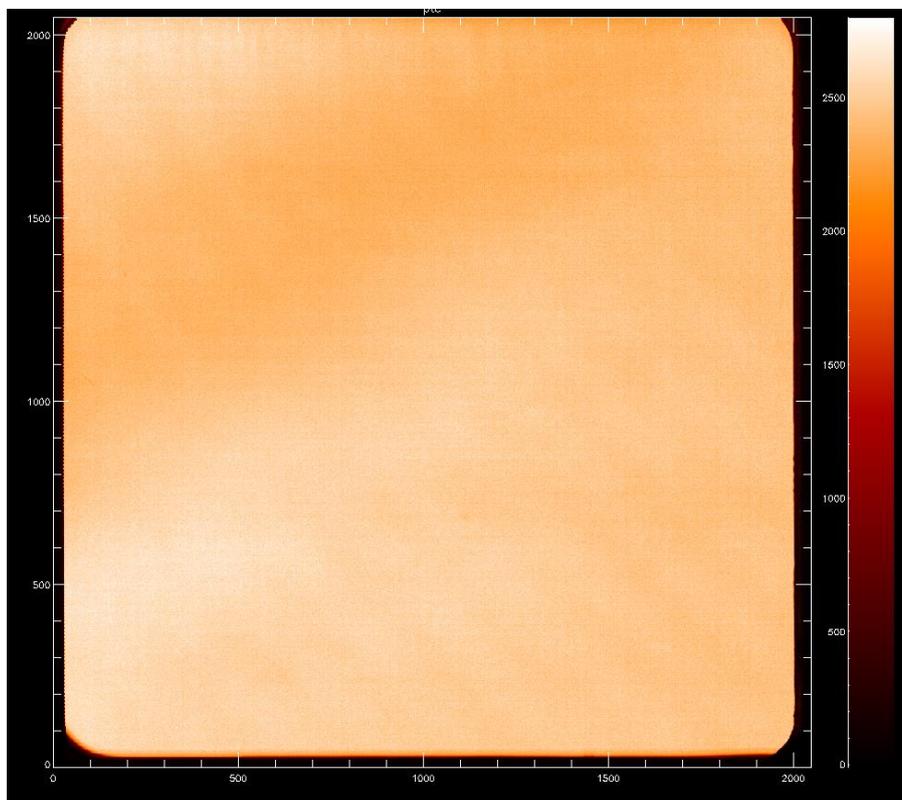
Source: Author.

The same analyzes were done for the SP camera were performed for the SJ camera, and similar results were found. However, an interesting result was the extent to which the gain histogram is consistent with the uncertainty (blue line), as shown in Figure 5.9.

47

Again, to avoid problems with saturation, the gain was calculated until the intensity reaches a specific limit where the values are within the linear regime, in the case of 1000 DN. The gain value of the pixels presents a Gaussian behavior, with a smaller deviation than the SP camera.

Figure 5.9 Histogram from the Slope for the SJ camera. The X-axis displays the gain value for each pixel. The Y-axis represents the relative number of the pixels. Pixels at the borders of the sensor were disregarded.
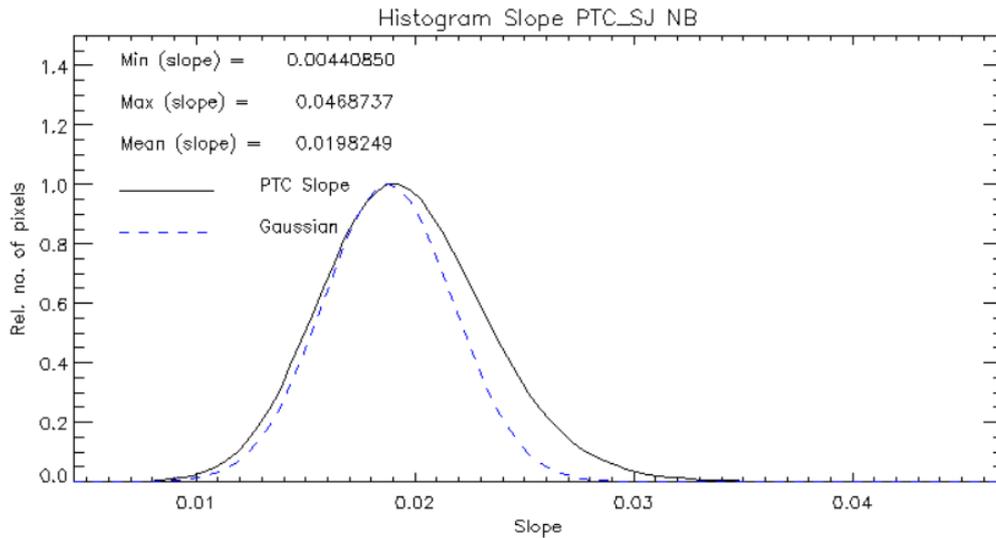
Source: Author.

5.1.2 Linearity with triangular target (LT data) for SP camera

The linearity test was done on a mechanical structure made on purpose to test the sensors, shown in Figure 5.10. This structure allows one to place a light Source at one end and the sensor at the other. In addition to isolating all external light, the box makes it possible to position optical elements in an aligned manner. For these tests, the sensor was illuminated with the triangular target before the led.

Figure 5.11 presents the average intensity of each pixel for one of the LT test. One can notice that, also in this test, the edge on the left does not have the same behavior as expected for an illuminated area of the sensor. Besides, a few columns around 100 and some rows around 1950 where the average intensity is higher. However, unlike Figure 5.2, no other structure is observed.

48

Figure 5.10 Mechanical structure for detailed camera characterization.
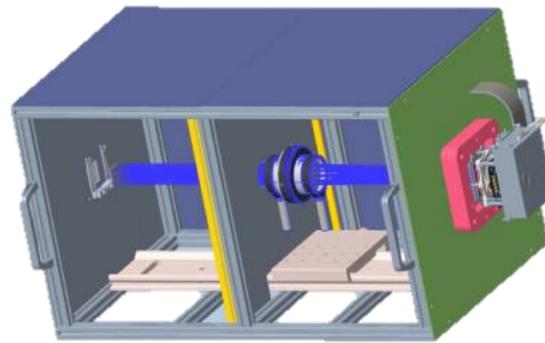
Source: SUSI group (2020).

Figure 5.12 shows the ratio of Target and Dark, with a focus on the unlighted area of the sensor. For tests with the triangular target (LT), Target represents the images acquired with the LED on. Dark represents the images obtained with the LED off. The interesting point, in this case, is that these stripes have an alternating pattern. However, it is expected a continuous pattern. Probably a shift in the readout time, a common mode error, caused it.

Figure 5.11 2D map of the average intensity, for all frames and time expositions, for each pixel. The X and Y-axis display the pixels' numbers, and the color bar represents the mean intensity for the SP camera for the test with the triangular target.
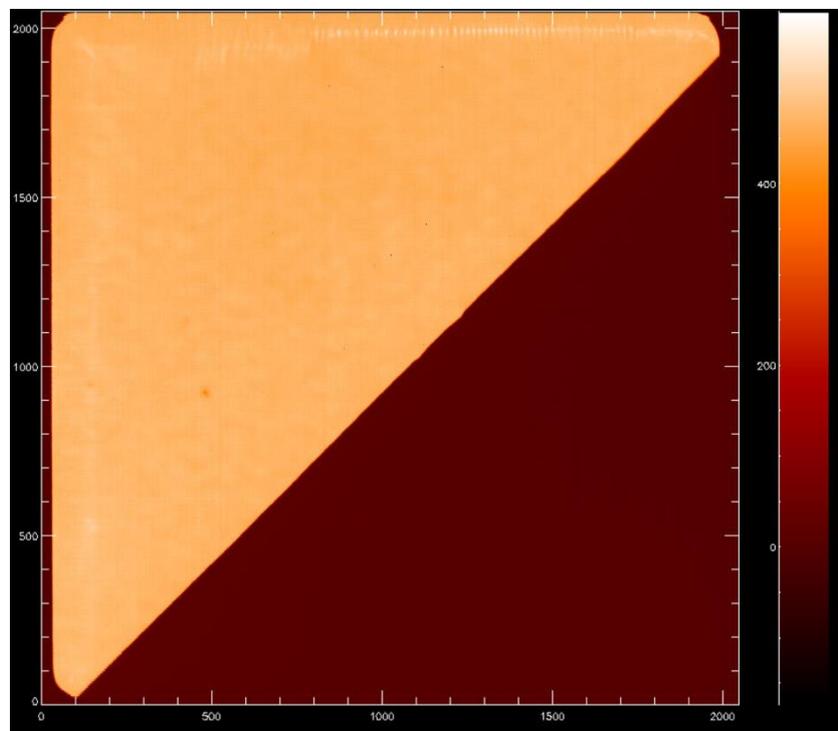
Source: Author.

Figure 5.12 2D map of the ratio of the average intensity over the dark value. The X and Y-axis display the pixels' numbers, and the color bar represents the ratio for the SP camera for the test with the triangular target. The range of the color bar was designed to focus on the dark area of the sensor.
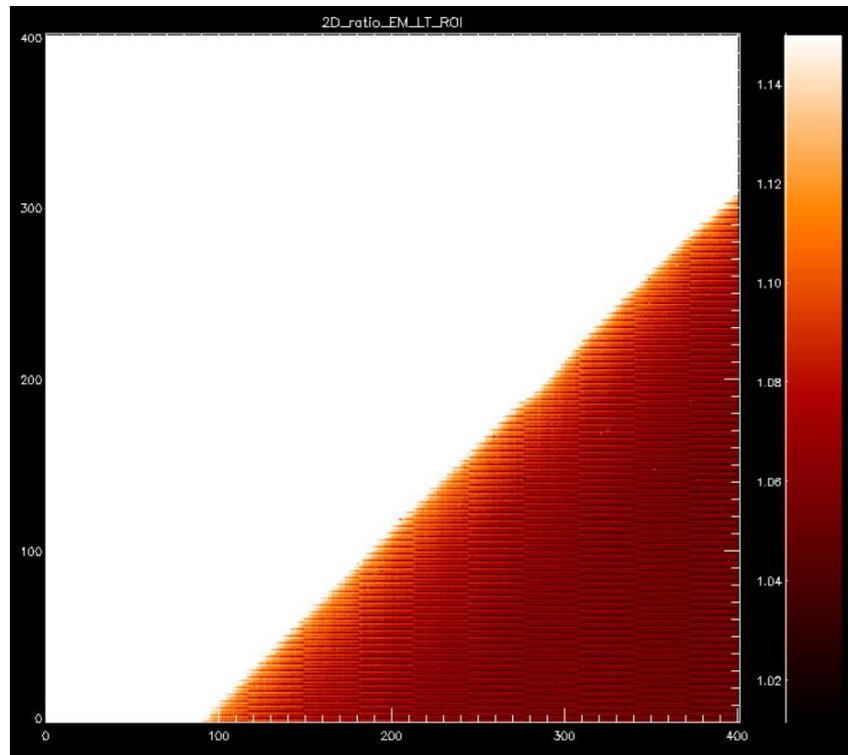
Source: Author.

Figure 5.13 shows the linearity of the LT test. For this analysis, a region of interest of 30x30 pixels was chosen in the illuminated area of the sensor. The non-linearity is around 1%, which is still significant.

To better understand the sensor's behavior, the terms of the quadratic function were determined from the exposition time and intensity for each pixel individually. Parameter B represents the slope, and parameter C represents the quadratic term. Figure 5.14 shows the histogram of parameter C. The first peak (in black) displays the pixels from the unlighted region of the sensor. It was expected a Gaussian curve would describe C from the bright area; however, a two peaks curve described it.

50

Figure 5.13 Linearity graph for SP camera with the triangular target. The X-axis displays the exposition time in seconds, and the Y-axis represents the mean intensity for each pixel in DN. Each black dot presents a pixel, while the red line represents the least-square polynomial fit.
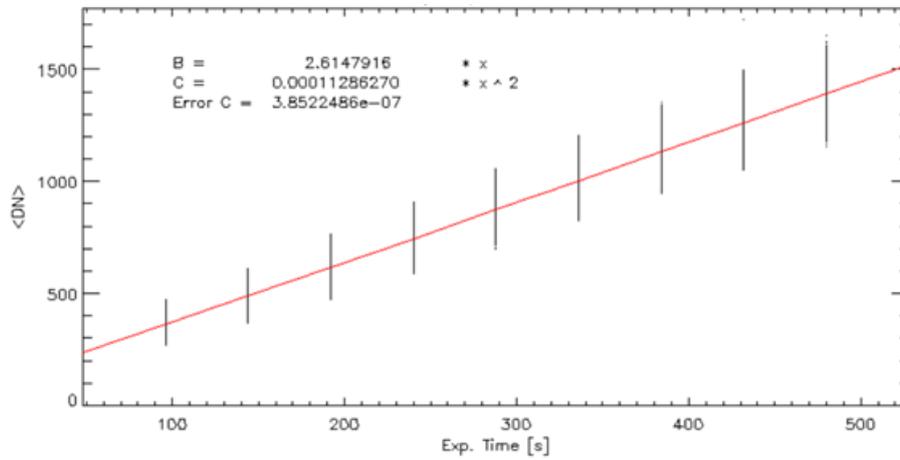
2D maps of each C parameter were plotted to identify pixels with different values. Figure 5.15 (a) shows a 2D map with only even rows for C. Figure 5.15 (b) represents the odd rows from parameter C. One can see in the first 250 columns the pixels of the even rows have a lower value for C than the rest of the illuminated area. However, the opposite is true for odd rows. A shift in readout probably caused this, considering that the behavior can also be observed for parameters A and B. Figure 5.16 (a) and (b) also shows the different behavior for parameter A.

Figure 5.14 Histogram Parameter C. The X-axis displays the parameter C value. The Y-axis
        represents the relative number of the pixels. The black line represents the histogram
        of parameter C, while the red line represents the histogram for the error of calculation
        of parameter C.
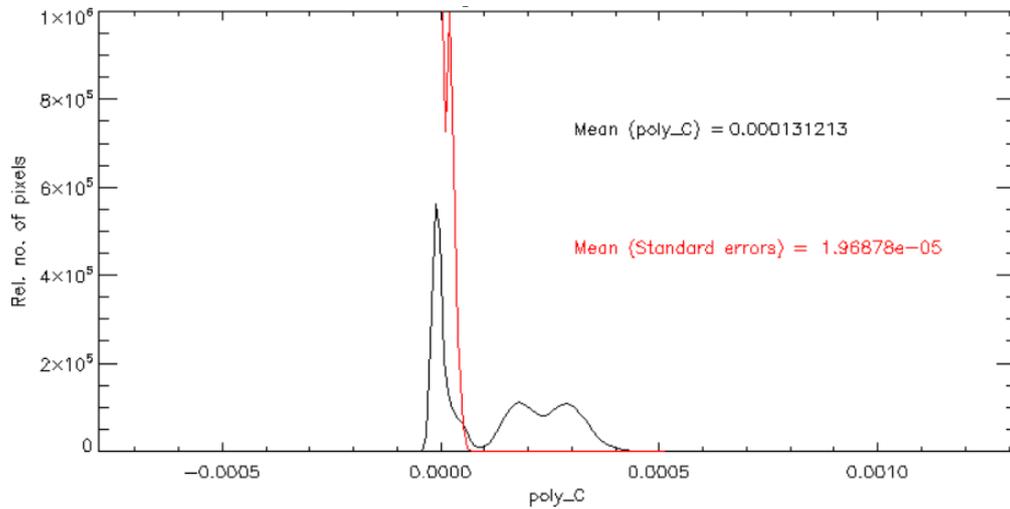
Source: Author.

Figure 5.15 (a) 2D map of the parameter C for each pixel. The X-axis displays all the pixels, and
        the Y-axis represents only the even pixels. The color bar represents the parameter C
        value for the SP camera. (b) 2D map of the parameter C for each pixel. The X-axis
        displays all the pixels, and the Y-axis represents only the odd pixels. The color bar
        represents the parameter C value for the SP camera.
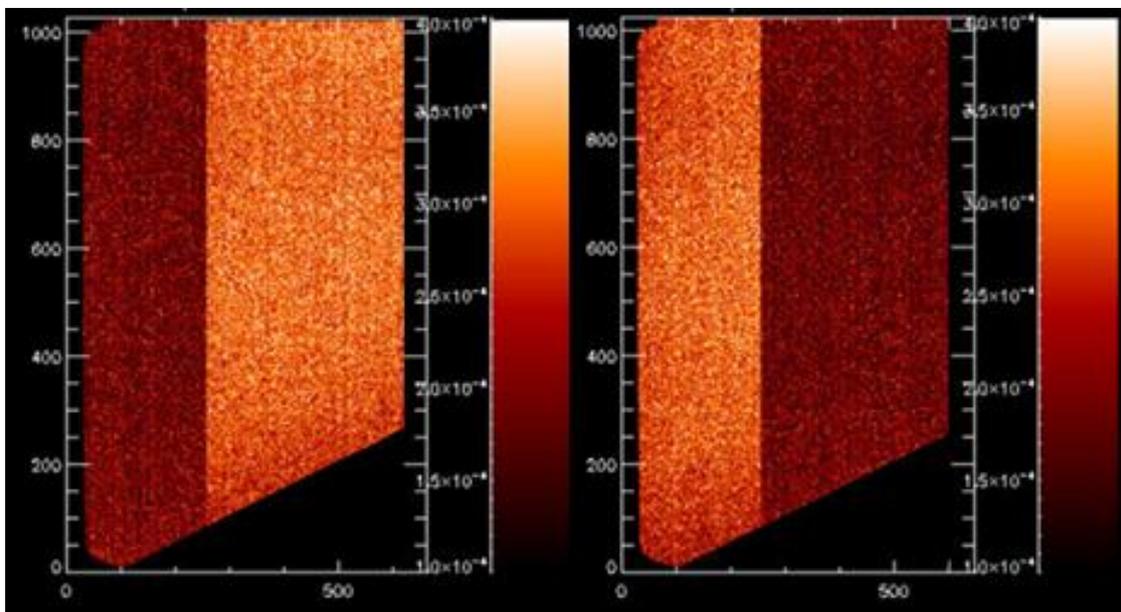
Source: Author.

Figure 5.16 (a) 2D map of the parameter A for each pixel. The X-axis displays all the pixels, and the Y-axis represents only the even pixels. The color bar represents the parameter A value for the SP camera. (b) 2D map of the parameter A for each pixel. The X-axis displays all the pixels, and the Y-axis represents only the odd pixels. The color bar represents the parameter A value for the SP camera.
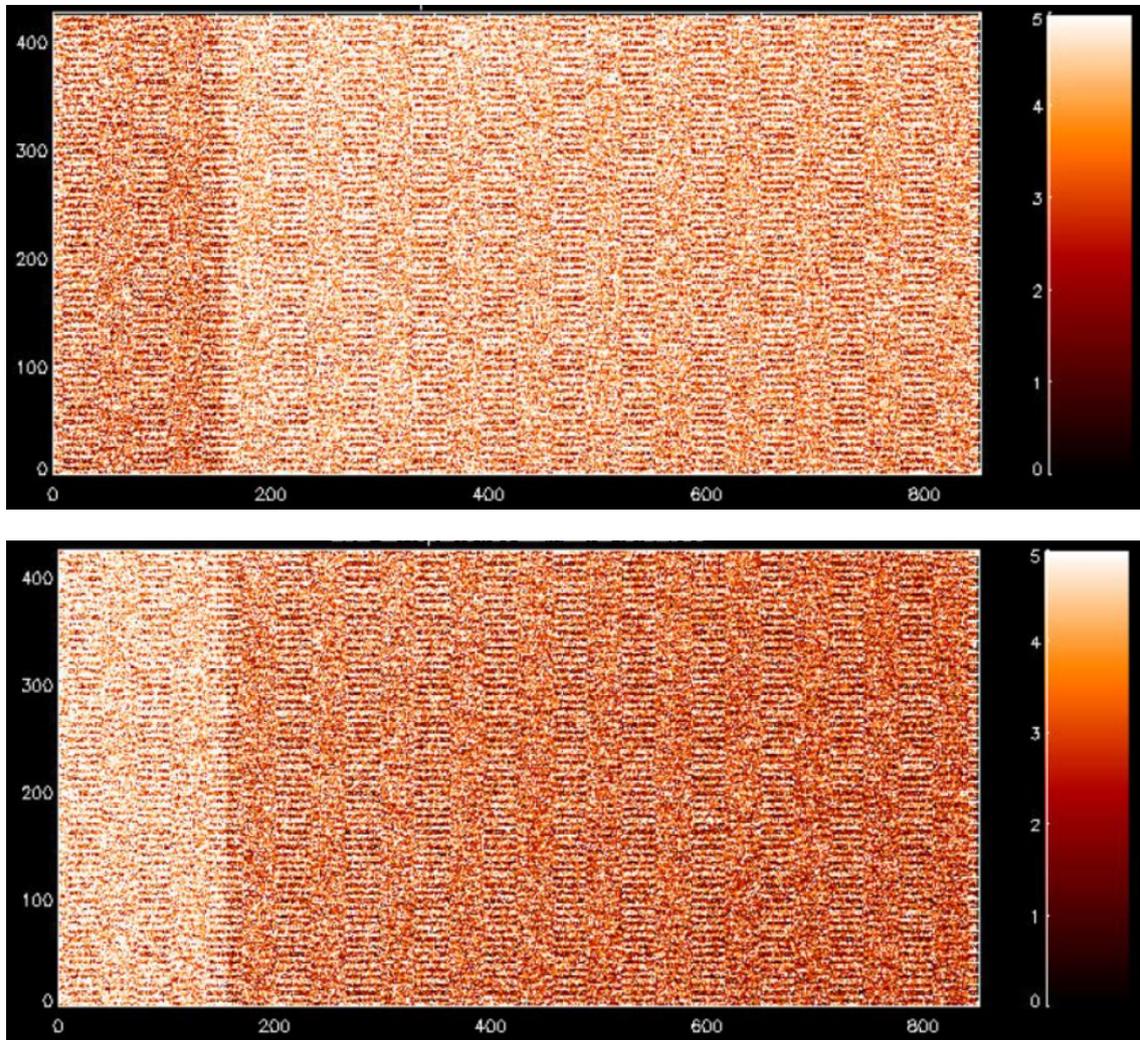
Source: Author.

5.2 PCPS camera

Two cameras were characterized, the Andor's Zyla 5.5 sCMOS air-cooled and water-cooled. Table 5.1 shows the specifications of the Andor Zyla 5.5 cameras. For this particular camera, two shutter operation modes are available: rolling shutter and global shutter. For Global mode, each pixel in the sensor initiates and ends an exposure together. For Rolling mode, at each pixel row exposure starts and ends slightly offset in time from its neighbor, beginning from the center and moving towards extremities. Besides the two shutter modes, for

53

Zyla 5.5, there is a possibility of having different exposure times, with a minimum of 9×10^{-6} seconds.

Table 5.1 Specific specifications for Andor Zyla 5.5 camera.

Model	Zyla 5.5		
Sensor type	Front Illuminated Scientific CMOS		
Active pixels (W x H)	2048 x 2048		
Pixel readout rate (MHz)	200 (100 MHz x 2 sensor halves) 560 (280 MHz x 2 sensor halves)		
Read noise (e⁻) Median [rms]		Rolling Shutter	Global Shutter
	@200 MHz	0.9 [1.2]	2.3 [2.5]
	@560 MHz	1.2 [1.6]	2.4 [2.6]
Maximum Quantum Efficiency	60%		
Sensor Operating Temperature			
Air cooled	0ºC (up to 30ºC ambient)		
Water cooled	-10ºC		
Dark current, e⁻ /pixel/sec @ min temp	0.10		
Air cooled	0.019		
Water cooled			
Readout modes	Rolling Shutter and Global Shutter		

Continue

54

Table 5.1 Conclusion.

Maximum dynamic range	33,000:1
Photon Response Non-Uniformity (PRNU)	
Half-light range	< 0.01%
Low light range	<0.1%
Pixel size (W x H)	6.5 µm
Pixel well depth (e⁻)	30,000
Linearity (%, maximum)	
Full light range	Better than 99.8%
Low light range (< 1000 e⁻ signal)	Better than 99.9%

Source: Andor (2020).

5.2.1 Data acquisition

The objective of the camera characterization is to understand the behavior of each pixel separately. Moreover, to determine the best mode of operation of the camera. In this characterization, the integrating sphere was used to characterize the cameras operating at a controlled temperature in a class 10,000 cleanroom.

During the planning of the tests, the instruments necessary for the alignment of the camera with the sphere and the calibration of the cameras were chosen. Figure 5.17 shows the setup design for the calibration.

Figure 5.17 Setup design for the calibration. Figure (a) shows the front view of the setup, highlighting the sphere and the camera. Figure (b) shows the 3D view, focusing on the polarizer present in some tests and the Spectrometer Flame S-XR1.
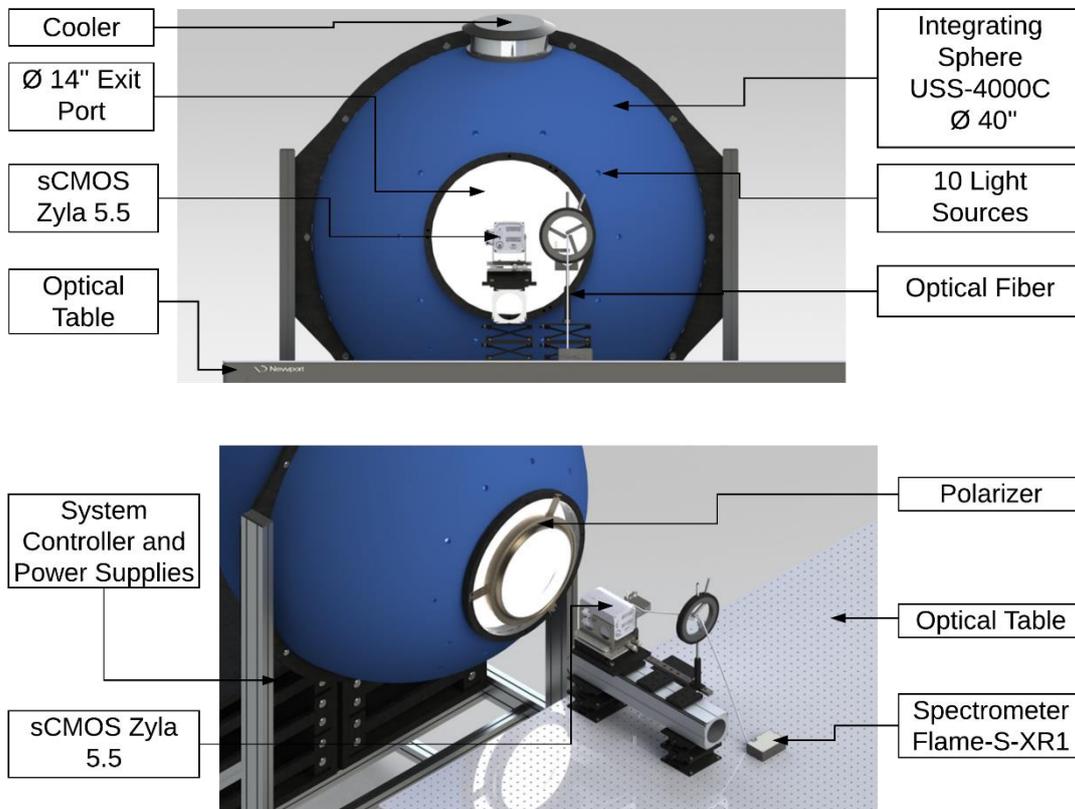
Since it is essential that the number of photons reaching each pixel be equal, the USS-4000C integrating sphere was used. It is 40 inches in diameter, with ten tungsten filament internal halogen lamps, evenly distributed around the exit door, and has a 14-inch aperture. The sphere provides a Lambertian Source, that is, a light Source of the same radiance whatever the direction of observation (LABSPHERE, 2008).

The first step was to align the camera with the sphere. Figure 5.18 shows the mechanical set used to ensure that the camera was concentric with the light Source. Then, the fine adjustment was performed with auxiliary 3-axis positioners for use in micropositioning applications.

The author analyzed the theoretical uniformity of the irradiance of the ideal Lambertian light Source to choose the position of the camera related to the sphere. As shown in Figure 5.19, uniformity starts high when near the Source.

However, it drops, and some distance is required for uniformity to be up again. Recognizing that uniformity is determined as the ratio of the irradiance at the edge of the object (E_e) to the axial irradiance (E_o), E_e / E_o.

Figure 5.18 Align the integrating sphere with the camera.

Source: Author.

Figure 5.19 Theoretical uniformity values for a perfectly Lambertian font.
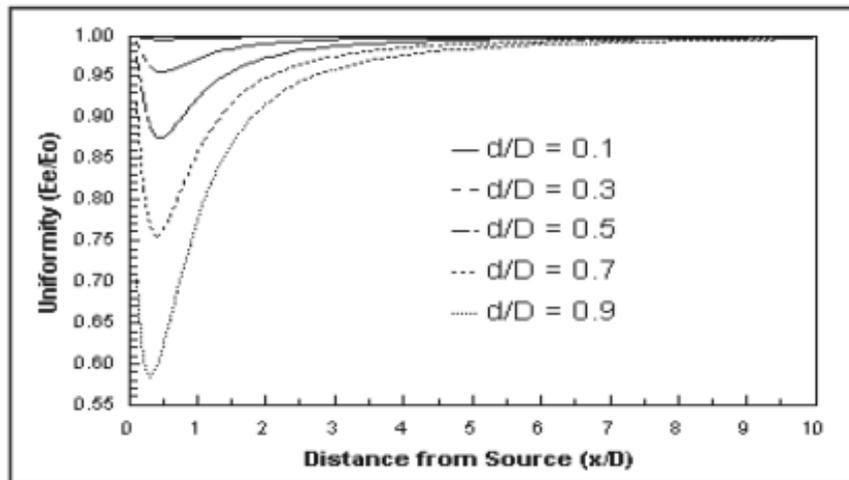
Source: Labsphere (2008).

In this case, the sphere aperture diameter is $D = 355.6mm$ (14 inches), the diameter at which the sensor is allocated is $d = 60mm$. So d/D is approximately 0.2. Therefore, three x/D positions were tested: 0.2 (PA), 0.75 (PB), and 2.0 (PC). Besides, the intensity varies with the exposure time, the value of the attenuator, and the temperature control. By changing the attenuator plate, one can change the flow of light entering the sphere.

Among the different positions, position C (furthest from the light Source) exhibited the most desirable uniformity in the sensor. In this position, more tests were performed with a reference polarizer in front of the sphere (see Figure 5.1b). Therefore, it is possible to check if there is any change in the pixels' value concerning polarization.

Figure 5.20 represents the mean intensity from the fifty frames for position PA, PB, and PC, respectively. The images are from the air-cooled camera in global mode. They have the same exposure time (minimum) and attenuator (maximum).

Figure 5.20 Mean intensity for position PA, PB, and PC.
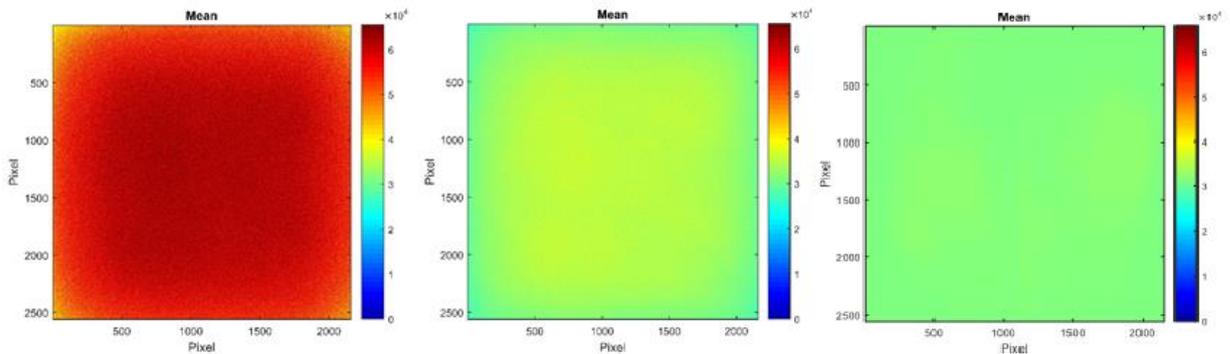
Source: Author.

As foreseen, PC showed the best uniformity, while PB showed a greater variation. However, PA did not show the expected good uniformity. It is probably due to the effect of the sphere edges or the Vignette effect caused by the fact that the sensor is not coincident with camera mechanics, being located a little behind.

Unfortunately, the water-cooled camera showed problems in the Peltier. Consequently, water droplets were formed on the sensor, which impaired the images analysis. For this reason, the author only analyzed the data from the air-cooled camera (AIR). Only one region of interest at the center of the sensor (500x500 pixels) was analyzed to save space for data storage and processing time. The data for the plate 10 (PL10) of the attenuator was analyzed, this plate did not block the entrance of the lamp light in the sphere.

5.2.2 Data analysis

The purpose of this analysis is to understand the behavior of the camera with the different operation modes. Therefore, data were acquired with two types of shutter operation, the temperature control on and off, the camera's filters on and off, and different exposure times. The acquired data was divided into different blocks to facilitate analysis, as shown in Table 5.2. For each configuration, there is an image with fifty frames. Each image has a dark acquired without the light Source. In all analyzes of the images, the dark was subtracted.

Table 5.2 Summary in the division of the data of the camera for the analysis.

Block	Cooling	Shutter	Varying into
B1	On	Global	Corrections
B2	On	Global	Exposition time
B3	On	Rolling	Corrections
B4	On	Rolling	Exposition time
B5	Off	Global	Corrections
B6	Off	Global	Exposition time
B7	Off	Rolling	Corrections
B8	Off	Rolling	Exposition time

Source: Author.

Each of the even blocks (B1, B3, B5, B7) has four tests with different combinations of filters, as shown in table 5.3. Each test has same exposure time (minimum). Odd blocks (B2, B4, B6, B8) have ten tests with different expositions time. For each test, 50 frames were acquired, increasing the exposure time and with both filters off. Data acquisition was done with the cooling on and off. In both cases, the temperature was constant before starting the test. For cooling ON, the temperature was -0.44°C. While for cooling OFF, the temperature was 25.83°C.

The tests were repeated with the reference polarizer in front of the sphere to study the behavior of the pixels concerning polarization. Hence there are three sets of data. POL90, as the 90-degree reference polarizer. POL0 is the 0-degree reference polarizer, and POLN is the data set acquired without the polarizer.

5.2.2.1 Analyze the impact of Shutter and cooling types on image acquisition

Figure 5.21 shows the average intensities for the fifty frames for test number 9. Among the acquired images, test number 9 is the one with the highest number of exposure (3×10^{-2} s). In this test, several pixels reach saturation. An interesting point is how the images are divided by a horizontal line in the middle of the sensor. It shows the division of different behaviors in the pixel reading out. This effect is more prominent for the Global Shutter (B2 and B6). One can also see the influence of cooling. When cooling was off (B6, B8), the pixel intensity is higher for both Shutters. It shows that the pixels are more uniform when the cooling is ON.

One can see the influence of the reference polarizer on image acquisition. The images acquired without the polarizer have a greater intensity than the data taken with the reference polarizer, as expected. As the light Source is not polarized, the transmittance of the polarizer should be the same, regardless of the angle of the reference polarizer. However, in all blocks, one can note that the intensity for POL0 is greater than that of POL90. A possible reason for this is that pixels may have a predisposition for polarization or the transmittance of the reference polarizer is not uniform for different angles. However, further analysis is needed to conclude.

Figure 5.21 Influence of the reference polarizer on image acquisition. Tests with the highest exposure time value were analyzed (_9). Blocks 2 and 6 are from Global Shutter, while Blocks 4 and 8 are from Rolling Shutter. B2 and B4 have the cooling on, while in B6 and B8, the cooling is off.
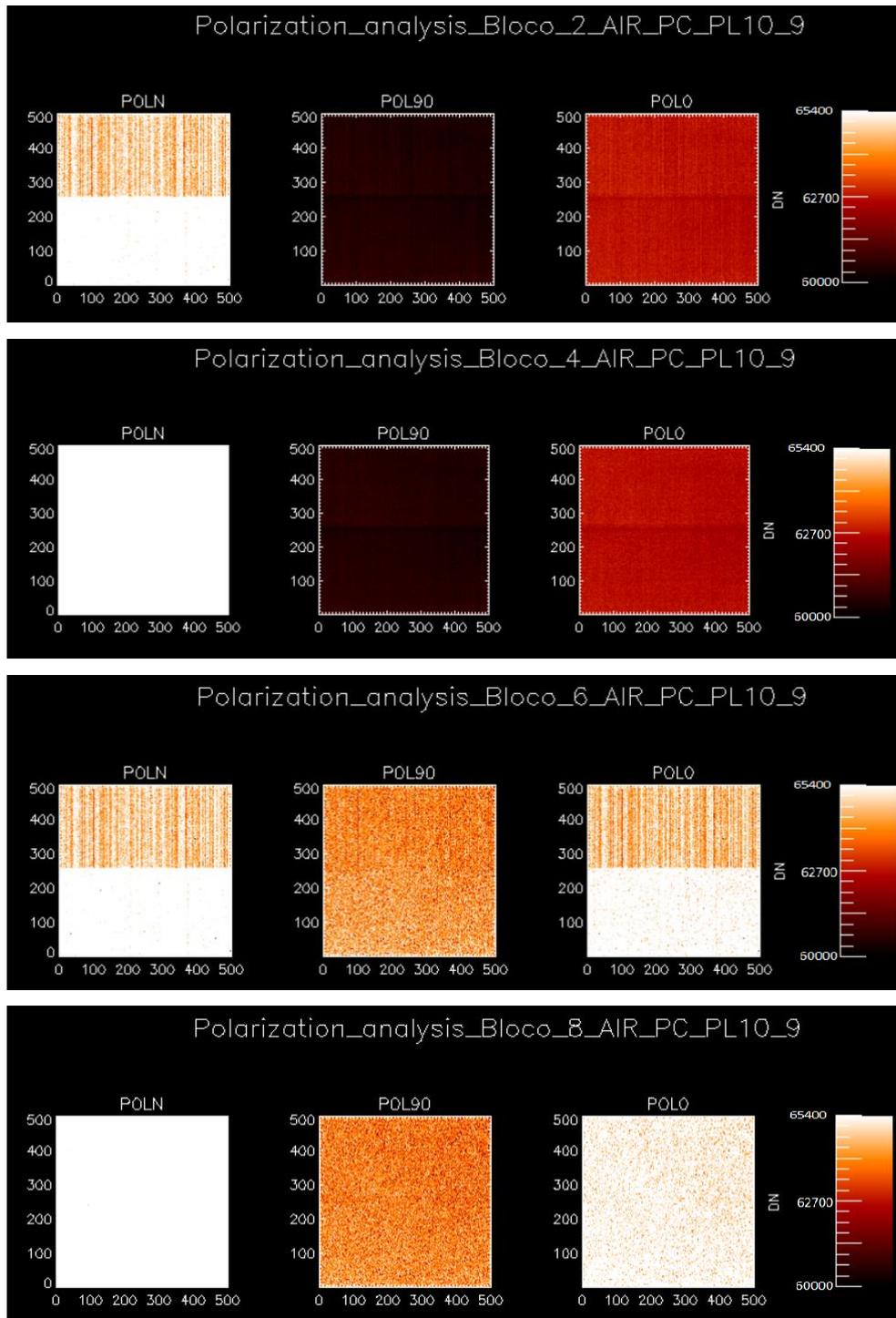
Source: Author.

Figure 5.22 displays the histogram of the data in Figure 5.21. When the cooling is on (B2 and B4), the POL90 and POL0 curves show a uniform Gaussian

behavior for both Shutters. One can see that all the pixels in POLN reach saturation for the Rolling Shutter (B4 e B8). Meanwhile, for B2 and B6 (Global) the bottom area of the sensor does not reach saturation. For B6 and B8 (cooling off), the Gaussian behavior changes due to the greater variance between the pixel values, resulting in a larger Gaussian base for POL 90 and POL0. POLN's behavior does not change since the values are close to saturation.

Figure 5.22 Histograms from tests with the highest exposure time value were analyzed (_9). Blocks 2 and 6 are from Global Shutter, while Blocks 4 and 8 are from Rolling Shutter. B2 and B4 have the cooling on, while in B6 and B8, the cooling is off.

Continue

62
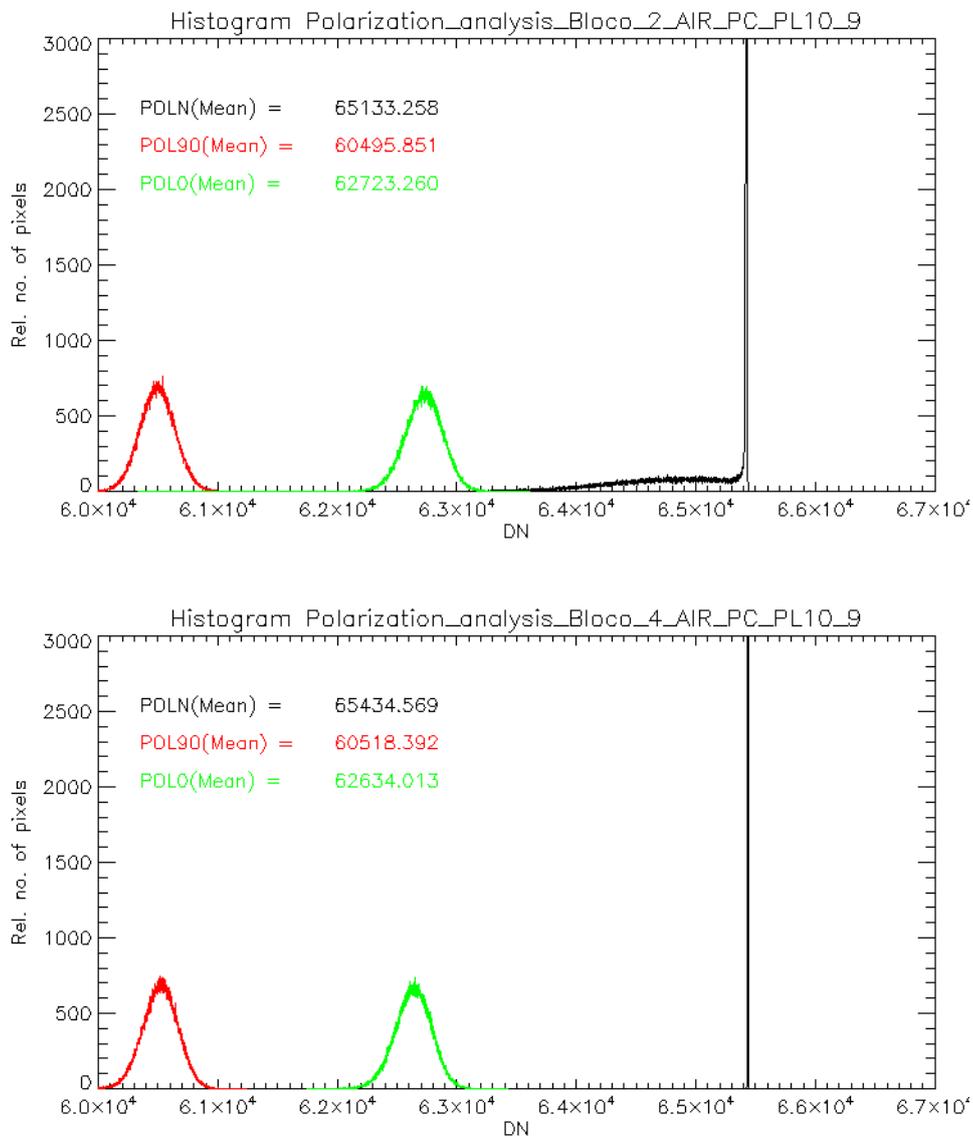
Figure 5.22 Conclusion.
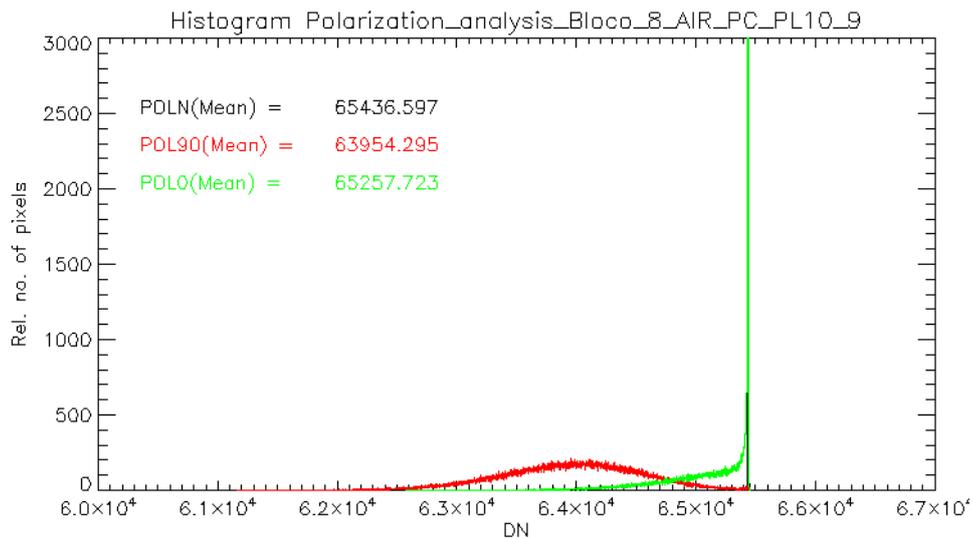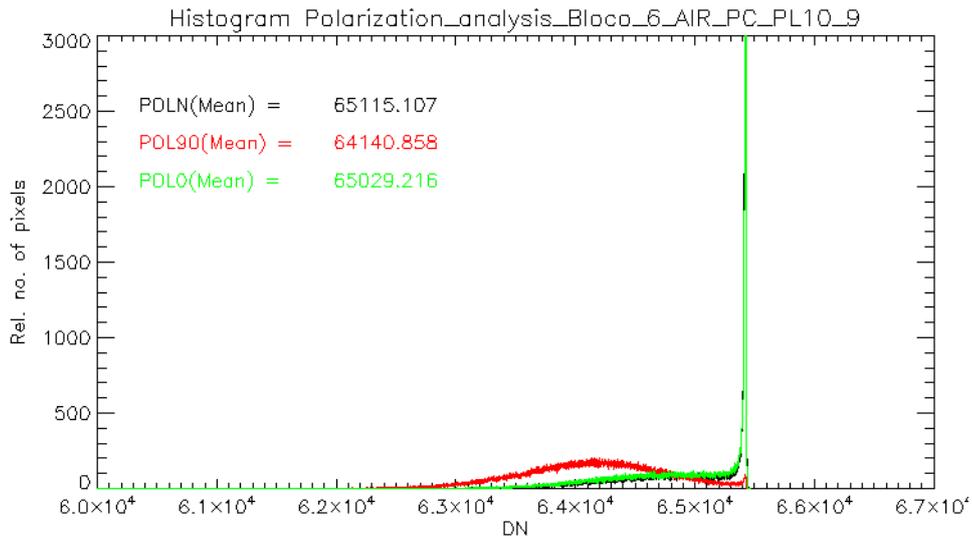
Source: Author.

5.2.2.2 Analyze the impact of the shutter and cooling types on the average of a series of images

Figure 5.23 shows the average intensities for ten testes with different exposure times for the even blocks with POLN. Figure 5.24 shows the histogram of this blocks. The same behavior for a single test is present for the average of 10 tests concerning cooling and the type of Shutter. In Figure 5.23, when the cooling was off (B6, B8), the pixel intensity is greater.

The division of different behaviors in the pixel reading out is clearer with the Global Shutter (B2 and B4). For POLN, this effect is not significantly apparent for the Rolling Shutter. This mode of operation has a more uniform intensity in the sensor, with a lower intensity average than in the Global Shutter.

One can see in Figure 5.24 that, for Rolling (B4 and B8), the histogram curves have Gaussian behavior, while for Global (B2 and B6), there is a deviation on the left side. This deviation was not present in the analysis of only one exposure time. This deviation was not present in the analysis of only one exposure time. And it is caused by a larger than expected number of pixels with low intensity. Accumulation of readout errors can be responsible for this.

Figure 5.23 Comparison between the type of shutter and cooling for even blocks, which represent the average of the different exposure times. Data acquired without the reference polarizer (POLN). Blocks 2 and 6 are from Global Shutter, while Blocks 4 and 8 are from Rolling Shutter. B2 and B4 have the cooling on, while B6 and B8 don't.
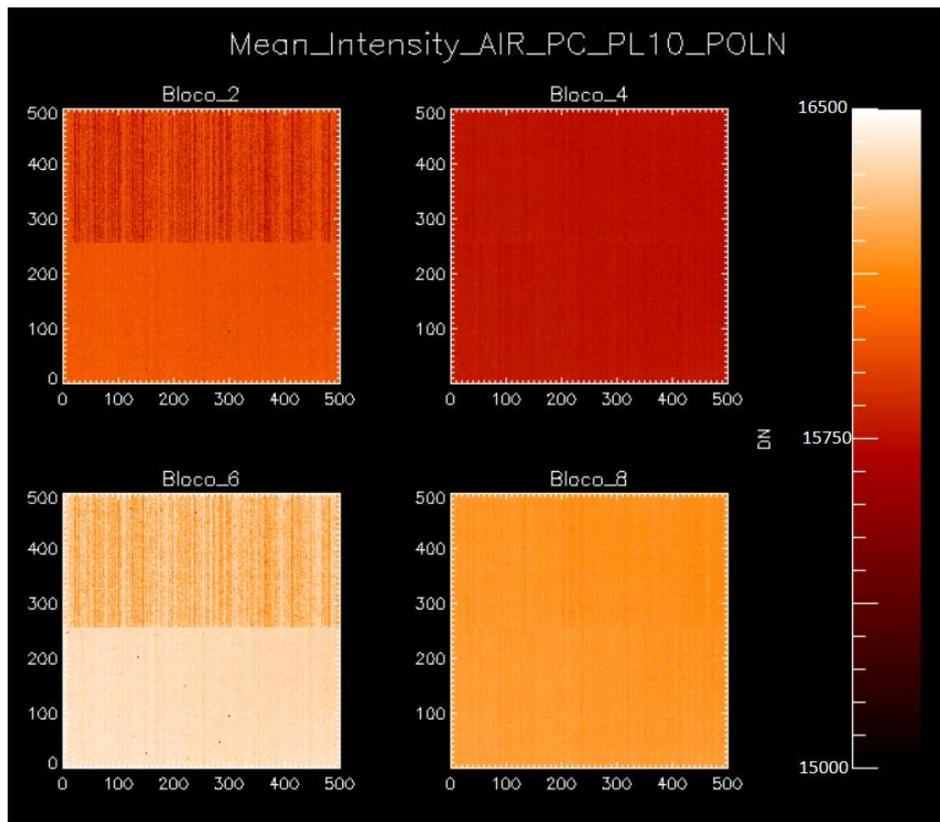
Source: Author.

Figure 5.24 Histogram mean intensity of exposure time from POLN even blocks. Blocks 2 and 6 are from Global Shutter, while Blocks 4 and 8 are from Rolling Shutter. B2 and B4 have the cooling on, while B6 and B8 don't.
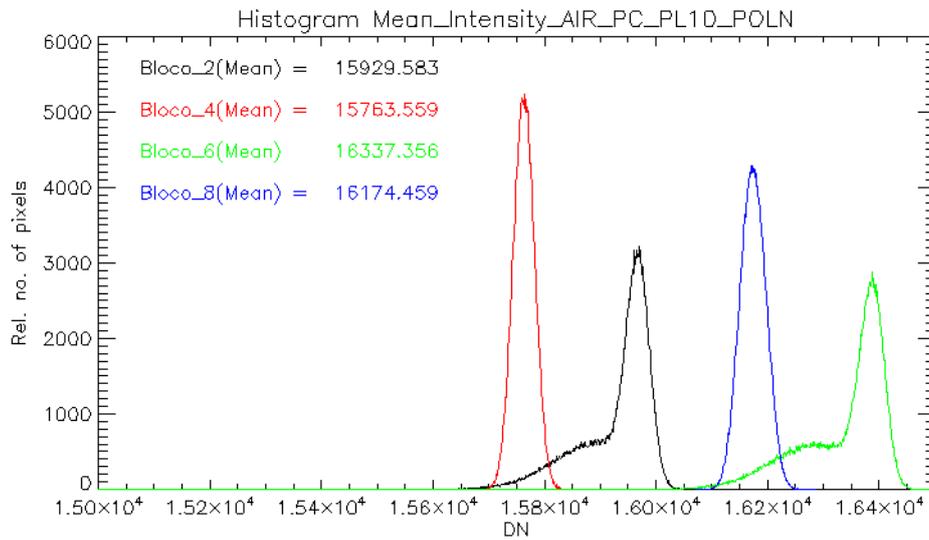
Source: Author.

Figure 5.25 presents the same analysis as Figure 5.23. Although, the data set was acquired with the reference polarizer at 0°. As in Figure 5.23, Blocks 2 and 6 (Global) present the division in the sensor due to the readout. However, B2 and B4 show the division more discreetly.

The histogram in Figure 5.26 confirms that for POL0 data, blocks 2 and 4 show much more similar results than POLN (Figure 5.22). One can see that has a deviation on the left side. Further analysis is needed to conclude the reason for the deviation.

Figure 5.25 Comparison between the type of shutter and cooling for even blocks, which represent the average of the different exposure times. Data acquired with the reference polarizer at 0° (POL0). Blocks 2 and 6 are from Global Shutter, while Blocks 4 and 8 are from Rolling Shutter. B2 and B4 have the cooling on, while B6 and B8 don't.
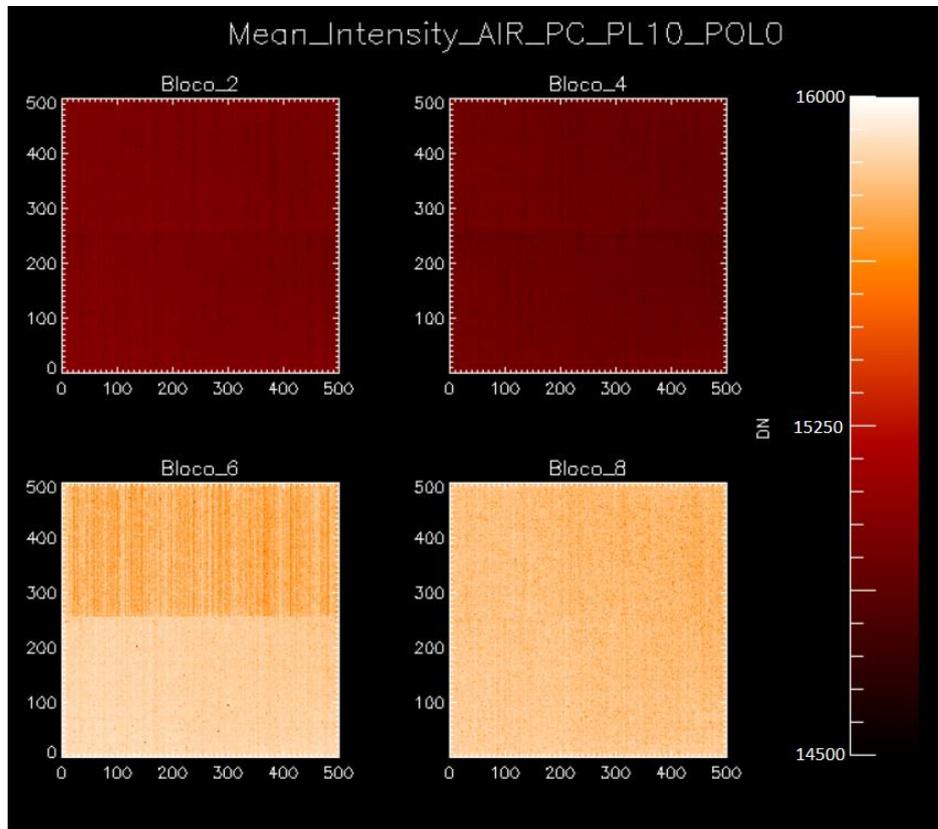
Source: Author.

Figure 5.26 Histogram mean intensity of exposure time from POL0 even blocks. Blocks 2 and 6 are from Global Shutter, while Blocks 4 and 8 are from Rolling Shutter. B2 and B4 have the cooling on, while B6 and B8 don't.
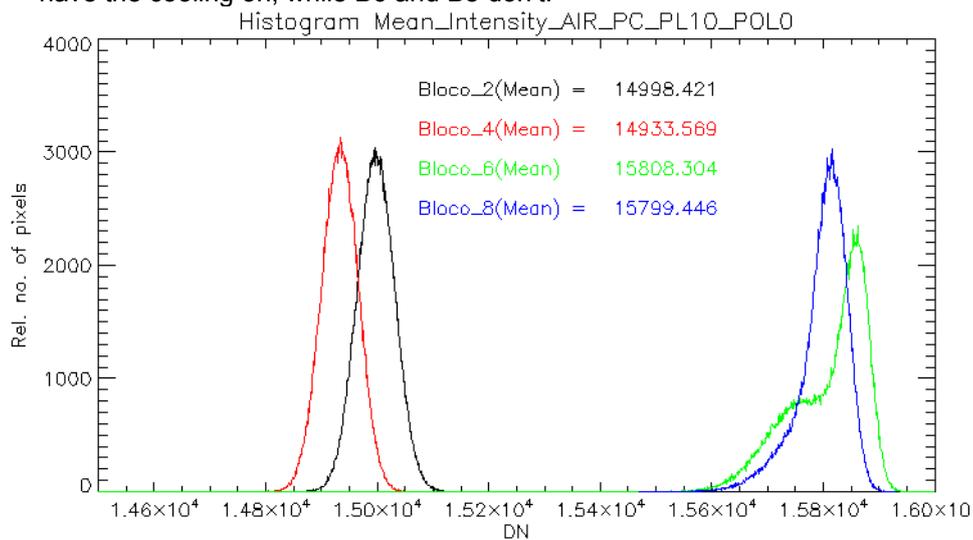
Source: Author.

Figure 5.27 presents the analysis of the even blocks for the POL90. Herein none of the blocks, there is a sharp division, as seen in Figure 5.23. Figure 5.28, which shows the histogram for POL90 data, shows the four curves as Gaussian without deviations. The division due to the readout can still be seen, even if in a less clear way. However, a behavior such as Figure 5.24 was expected.

Figure 5.27 Comparison between the type of shutter and cooling for even blocks, which represent the average of the different exposure times. Data acquired with the reference polarizer at 90° (POL90). Blocks 2 and 6 are from Global Shutter, while Blocks 4 and 8 are from Rolling Shutter. B2 and B4 have the cooling on, while B6 and B8 don't.

Source: Author.

Figure 5.28 Histogram mean intensity of exposure time from POL90 even blocks. Blocks 2 and 6 are from Global Shutter, while Blocks 4 and 8 are from Rolling Shutter. B2 and B4 have the cooling on, while B6 and B8 cooling is off.

Source: Author.

Figure 5.29 shows the histogram of the standard deviation (STD) for the even blocks of POLN. The Global blocks (B2 and B6) have a slightly higher stander deviation than Rolling Shutter (B4 and B8). One can note that the standard deviation does not change much depending on the cooling. It occurs because the minimum temperature reached with the cooling on is -0.44 °C. If the cooling temperature reaches -25°C, one may see a significant difference in the standard deviation.

Figure 5.29 Histogram mean standard deviation of exposure time from POLN even blocks. Blocks 2 and 6 are from Global Shutter, while Blocks 4 and 8 are from Rolling Shutter. B2 and B4 have the cooling on, while B6 and B8 don't.

5.2.2.3 Analyze the impact of filters on image acquisition

Spurious Noise Filter (filter) and Blemish correction (correction) are the two types of filters that Zyla offers. The first one identifies and compensates for spurious high noise pixels. The last one minimizes the spots of hot pixels, which means more useful pixels. To know the influence of these filters, the odd blocks in Table 3 are analyzed.

Each of these blocks has four tests with different combinations of filters, as shown in Table 5.3. For each test, 50 frames were acquired, all with the same exposure time (minimum).

Table 5.3 Summary on dividing camera data for filter analysis.

Test	Filter	Correction
1	Off	Off
2	Off	On
3	On	On
4	On	Off

Figure 5.30 presents an analysis of the filters for Block 5, where the Shutter is Global and Cooling is OFF for the data acquired without the reference polarizer (POLN). One cannot see a significant variation between the panels. In all cases, the region of interest has pixels with a lower intensity on the main diagonal. Figure 5.31 presents the histogram for Block 5. One can see that the behavior of the curves is very similar. However, Tests_1 and Test_2 (Filter OFF) slightly present a larger number of pixels with the average intensity.

Figure 5.30 Analysis of Filters for B5 (Global Shutter, Cooling OFF) for POLN. Teste_1 stands for filter OFF, correction OFF. Test_2 represents filter OFF, correction ON. Teste_3 expresses filter ON, correction ON. Teste_4 means filter ON, correction OFF.
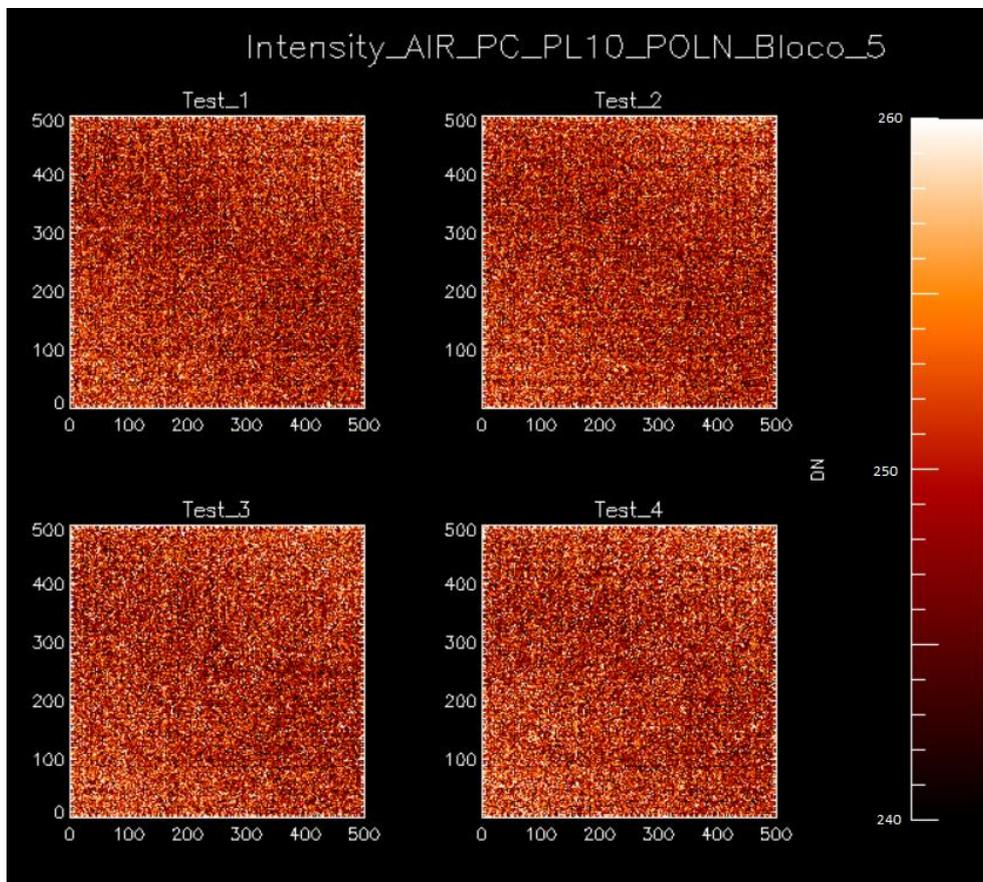
Source: Author.

Figure 5.31 Histogram of Filters for B5 (Global Shutter, Cooling OFF) for POLN. Teste_1 stands for filter OFF, correction OFF. Test_2 represents filter OFF, correction ON. Teste_3 expresses filter ON, correction ON. Teste_4 means filter ON, correction OFF.

Histogram Intensity_AIR_PC_PL10_POLN_Bloco_5

Test_1(Intensity) = 249.79204
Test_2(Intensity) = 249.79908
Test_3(Intensity) = 251.52343
Test_4(Intensity) = 253.29112
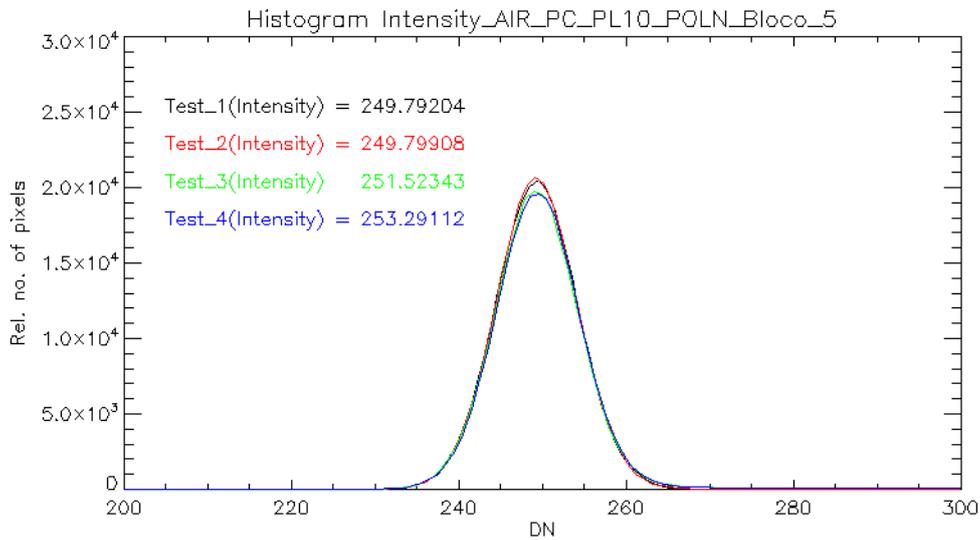
Source: Author.

In Figure 5.32, there is also no visible difference between the panels. The analysis of block 7 (Rolling) has an average intensity lower than that of set 5 (Global), and it is possible to distinguish the readout behavior of the sensor. In contrast to Figure 5.31, the histogram shown in Figure 5.33 does not display any variation in intensity between the different types of filter combinations available.

Figure 5.32 Analysis of Filters for B7 (Rolling Shutter, Cooling OFF) for POLN. Teste_1 stands for filter OFF, correction OFF. Test_2 represents filter OFF, correction ON. Teste_3 expresses filter ON, correction ON. Teste_4 means filter ON, correction OFF.
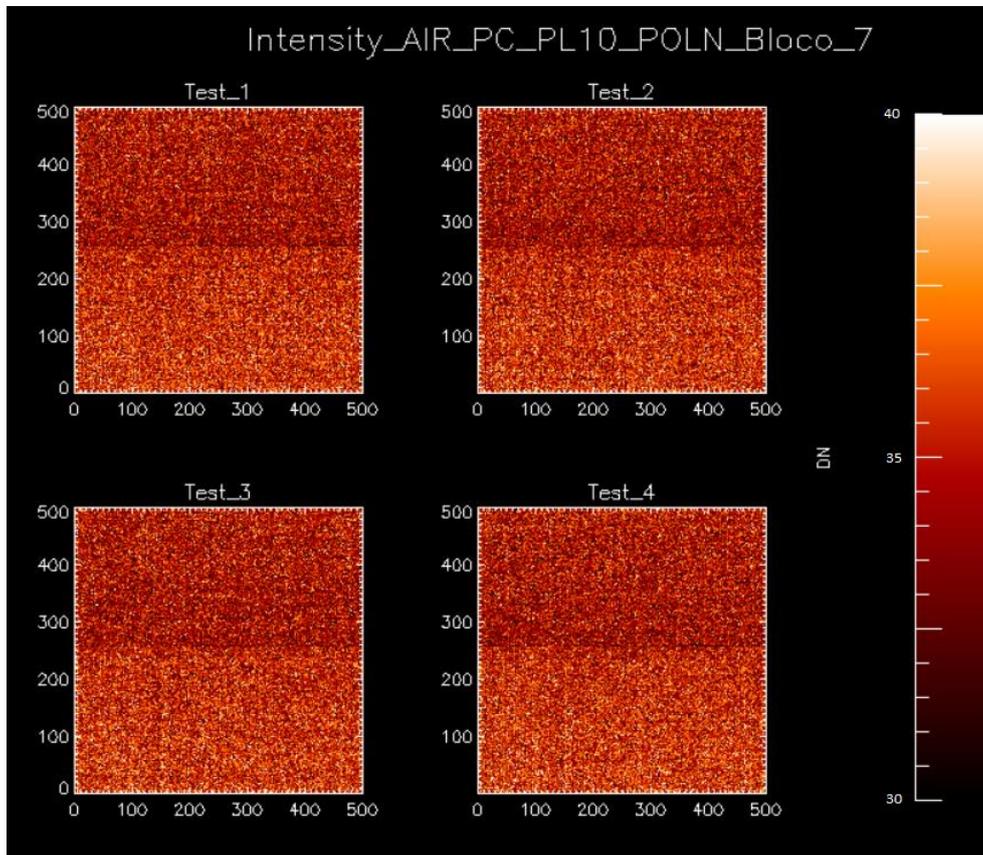
Source: Author.

Figure 5.33 Histogram of Filters for B7 (Rolling Shutter, Cooling OFF) for POLN. Teste_1 stands for filter OFF, correction OFF. Test_2 represents filter OFF, correction ON. Teste_3 expresses filter ON, correction ON. Teste_4 means filter ON, correction OFF.
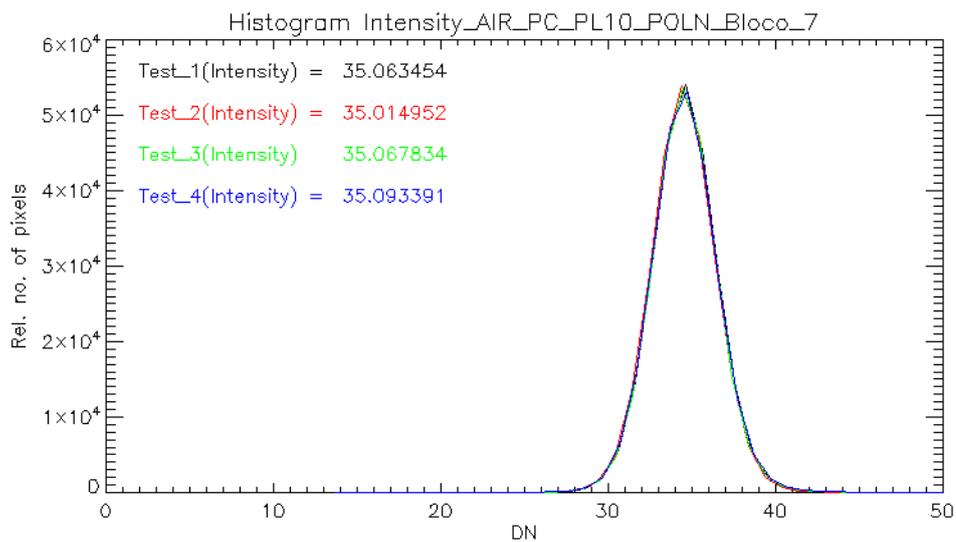
Source: Author.

The analysis were made for data with Cooling OFF (B5 and B7), as it is expected that they will have higher noise and, consequently, that the influence of the filter and the correction will be greater. Figure 5.34 and Figure 5.35 show the histograms for the standard deviation of data from Block 5 B5 (Global Shutter, Cooling OFF) and Block 7 B5 (Rolling Shutter, Cooling OFF), respectively.

One can see that the standard deviation is greater for the Global Shutter. However, for both Shutters, significant differences in standard deviation between tests are not shown. Hence, it is necessary to acquire the data again, with a longer exposure time and more tests, for the analysis to be reliable.

Figure 5.34 Histogram of the standard deviation (STD) of Filters for B5 (Global Shutter, Cooling OFF) for POLN. Teste_1 stands for filter OFF, correction OFF. Test_2 represents filter OFF, correction ON. Teste_3 expresses filter ON, correction ON. Teste_4 means filter ON, correction OFF.
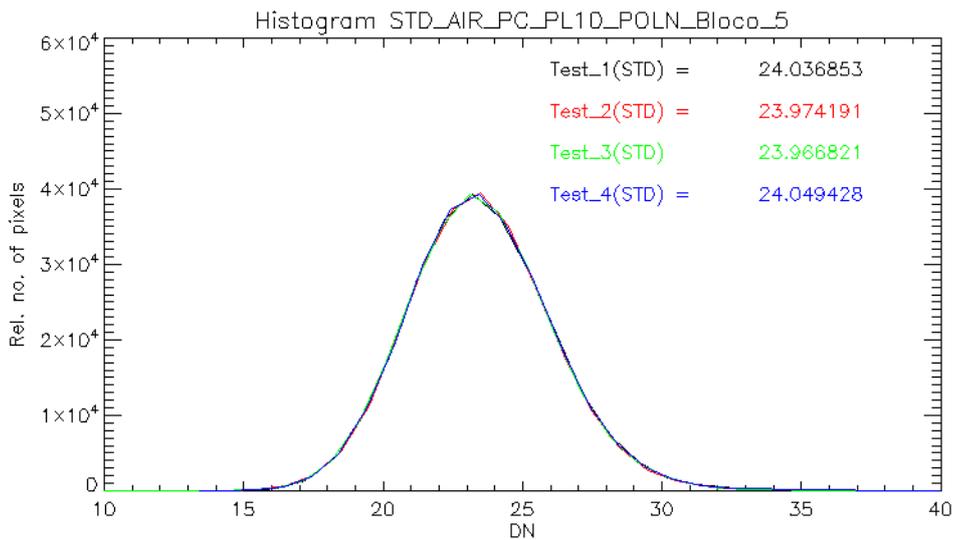
Source: Author.

Figure 5.35 Histogram of the standard deviation (STD) of Filters for B7 (Rolling Shutter, Cooling OFF) for POLN. Teste_1 stands for filter OFF, correction OFF. Test_2 represents filter OFF, correction ON. Teste_3 expresses filter ON, correction ON. Teste_4 means filter ON, correction OFF.

Histogram STD_AIR_PC_PL10_POLN_Bloco_7

Test_1(STD) = 9.5470109
Test_2(STD) = 9.5293016
Test_3(STD) = 9.5273145
Test_4(STD) = 9.5403979
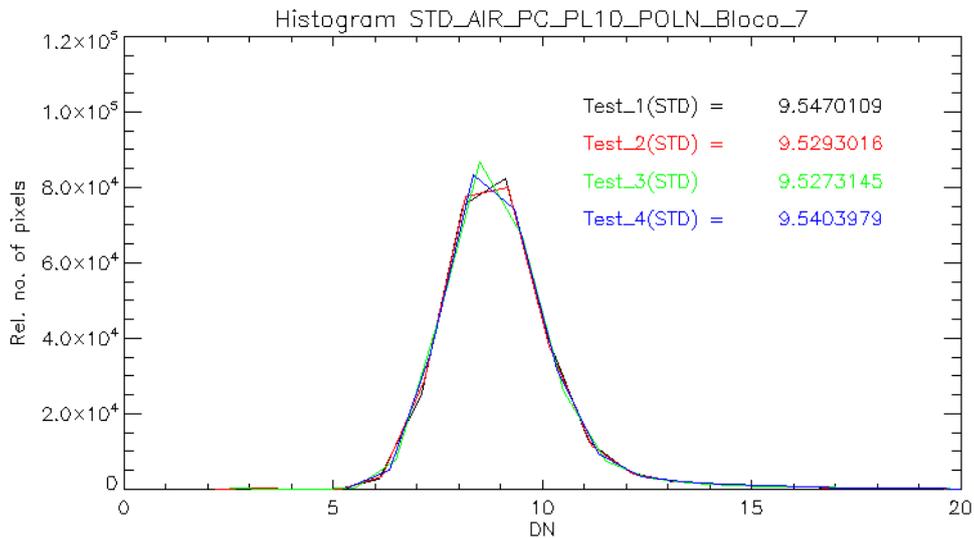
Source: Author.

5.2.2.4 Gain analysis

The purpose of the gain analysis is to see if there are any regions of the sensor with unusual behavior. The gain expresses the slope of the linear regression line of the mean intensity and the variance. For this analysis, pixels with an intensity greater than 5000 were disregarded.

Figure 5.36 shows the 2D gain map for data acquired without the reference polarizer (POLN). The data with Global Shutter is Block 2 and Block 6, while Block 4 and Block 8 are from Rolling Shutter. B2 and B4 have the cooling on, while B6 and B8 cooling is off. One can notice that images with Global Shutter (B2 and B6) have a higher gain than images with Rolling Shutter. It is interesting to see that when the cooling is off, the gain is also higher. The division of the sensor caused by the readout can also be observed.

Figure 5.36 2D map representing the gain for each pixel for each block for POLN (without the reference polarizer). Blocks 2 and 6 are from Global Shutter, while Blocks 4 and 8 are from Rolling Shutter. B2 and B4 have the cooling on, while B6 and B8 cooling is off.
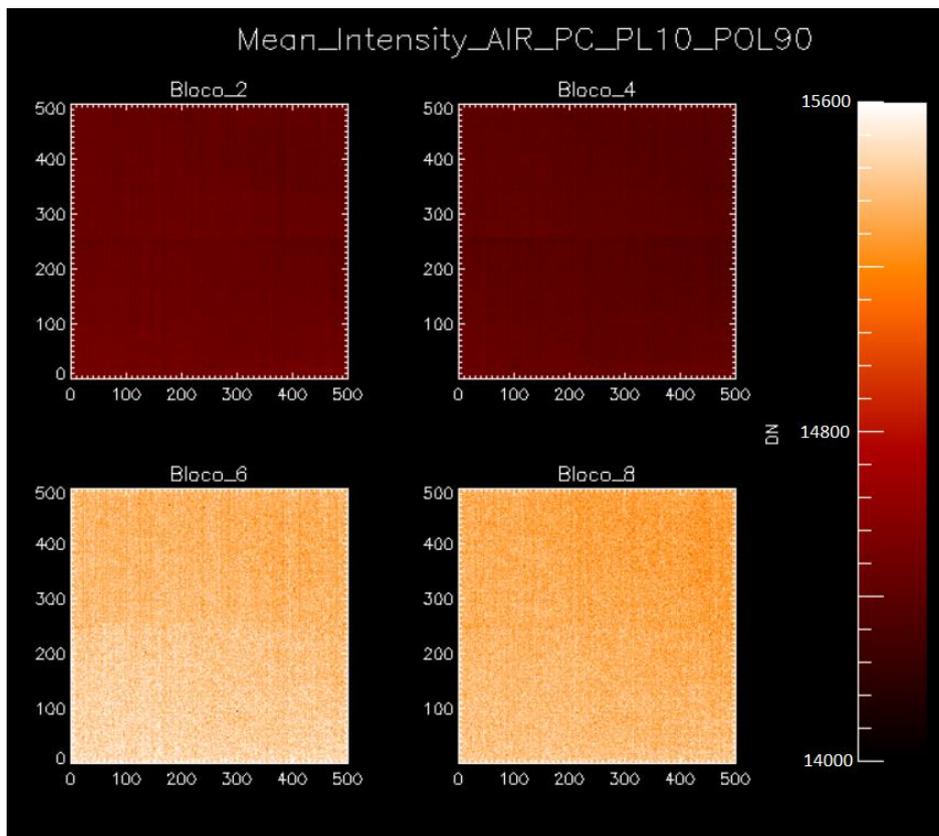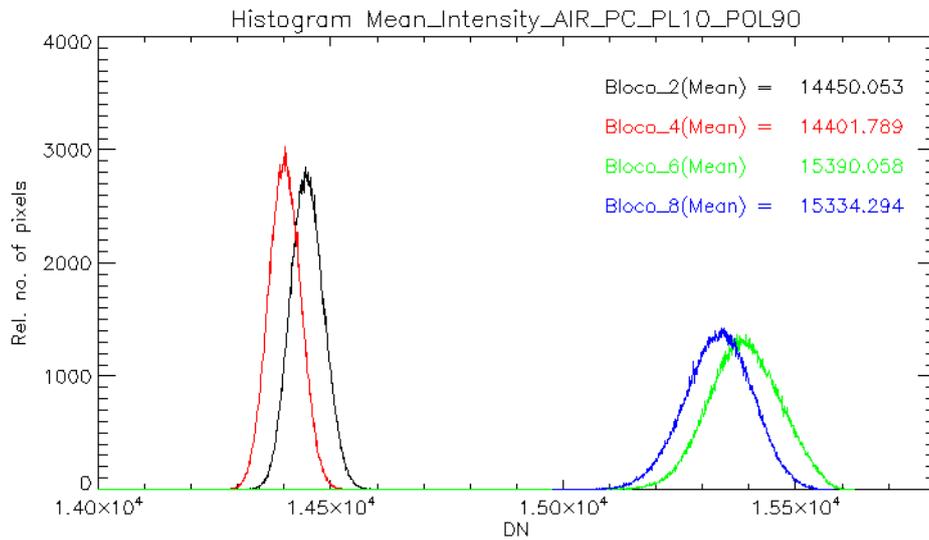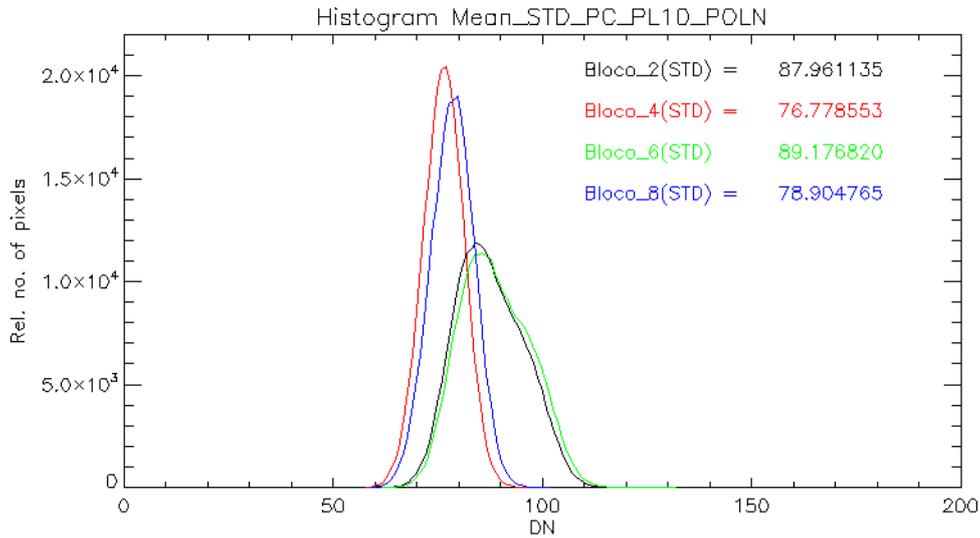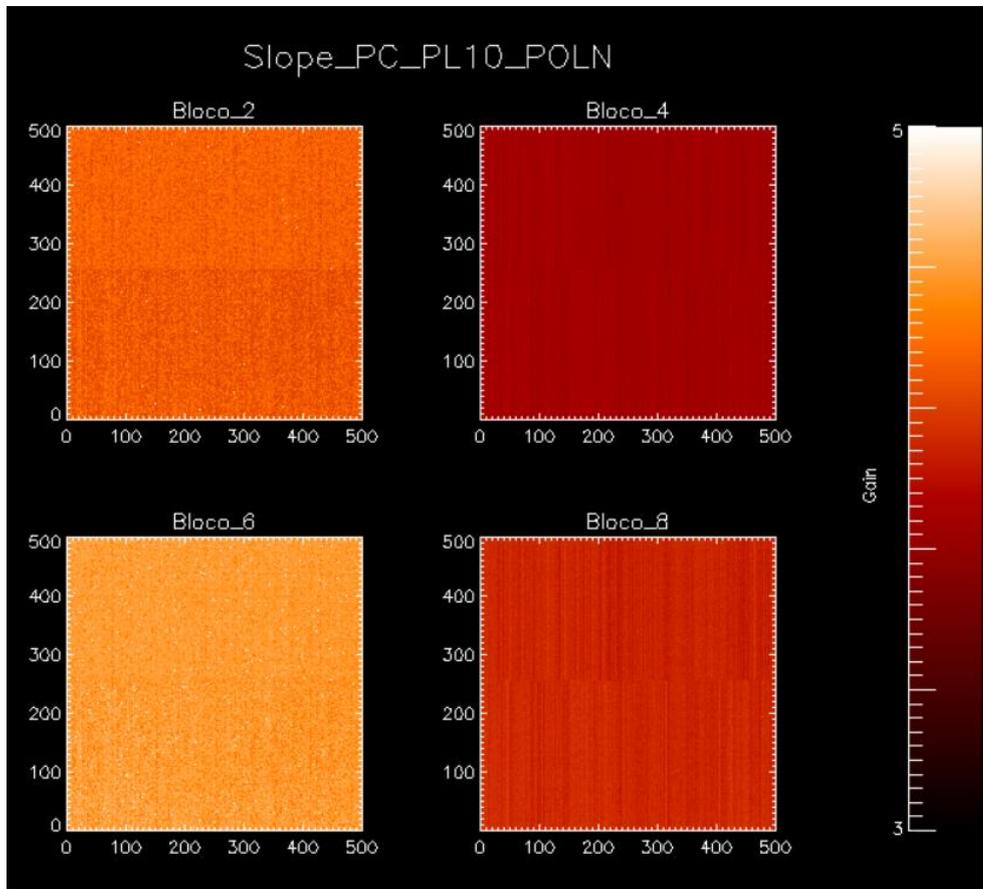

Source: Author.

Figure 5.37 displays the histograms of the data in Figure 5.36. The curves for even blocks for POLN are shown. One can see that the curve of B4 and B6 (Rolling) has a Gaussian-like behavior, while curves B2 and B6 (Global) have deviations to the left. The deviation from B2 (Global, cooling ON) is large enough to be considered a new peak. It means that in the sensor, there are two regions with pixel concentrations with different gains, or there is a shift in gain as one changes the pixel row or column.

Figure 5.37 Histograms from the gain calculated for each pixel for POLN. Blocks 2 and 6 are from Global Shutter, while Blocks 4 and 8 are from Rolling Shutter. B2 and B4 have the cooling on, while in B6 and B8, the cooling is off.
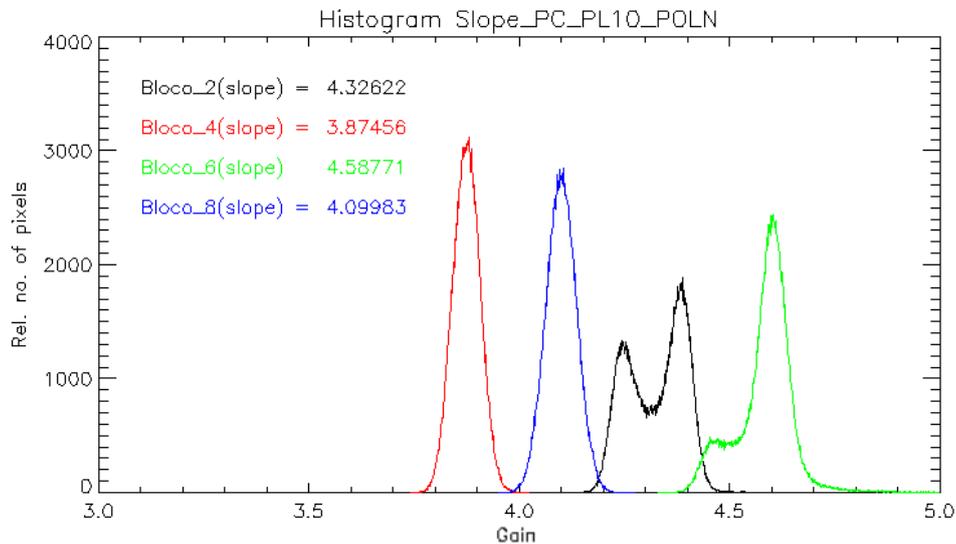
Source: Author.

To find out if there is a shift due to a column or row, one can plot a 2D map representing only the even or odd pixels of a row or column. Figure 5.38 shows, separately, the gain for the odd and even lines of the sensor for B2 and B6 (Global). While figure 5.39 shows the slope for the even and odd columns. In both figures, one cannot see the difference between the even and the odd images. However, in both figures, one can notice that the upper part of the sensor has a higher gain than the lower section.

Figure 5.40 shows the histogram for the even and odd lines, while Figure 5.41 shows the histogram for the columns. Again, one can see that the curves behavior is equivalent regardless of whether they are even or odd. Consequently, the two peaks for B2 (Shutter: Global, cooling: ON) present in Figure 5.37, Figure 5.40, and Figure 5.41 are due to the readout difference that divides the sensor.

Figure 5.38 2D map representing the gain for each pixel for Global Shutter and POLN (without the reference polarizer). B2 has the cooling ON, while B6 has the cooling OFF. The left panels represent only the pixels in the even lines. The right panels display only the odd lines of the sensor.
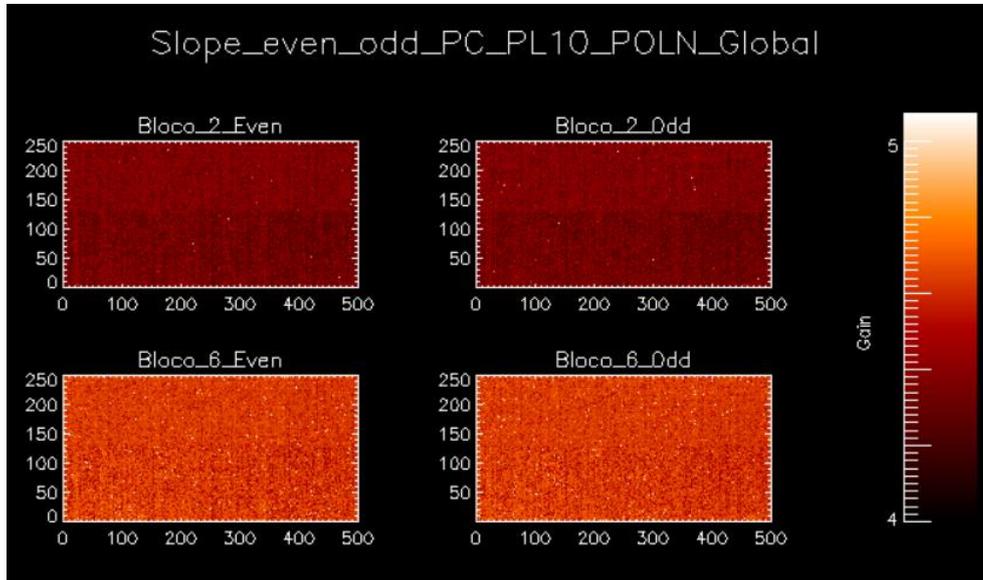
Source: Author.

Figure 5.39 2D map representing the gain for each pixel for Global Shutter and POLN (without the reference polarizer). B2 has the cooling ON, while B6 has the cooling OFF. The left panels represent only the pixels in the even column. The right panels display only the pixels in the odd column of the sensor.
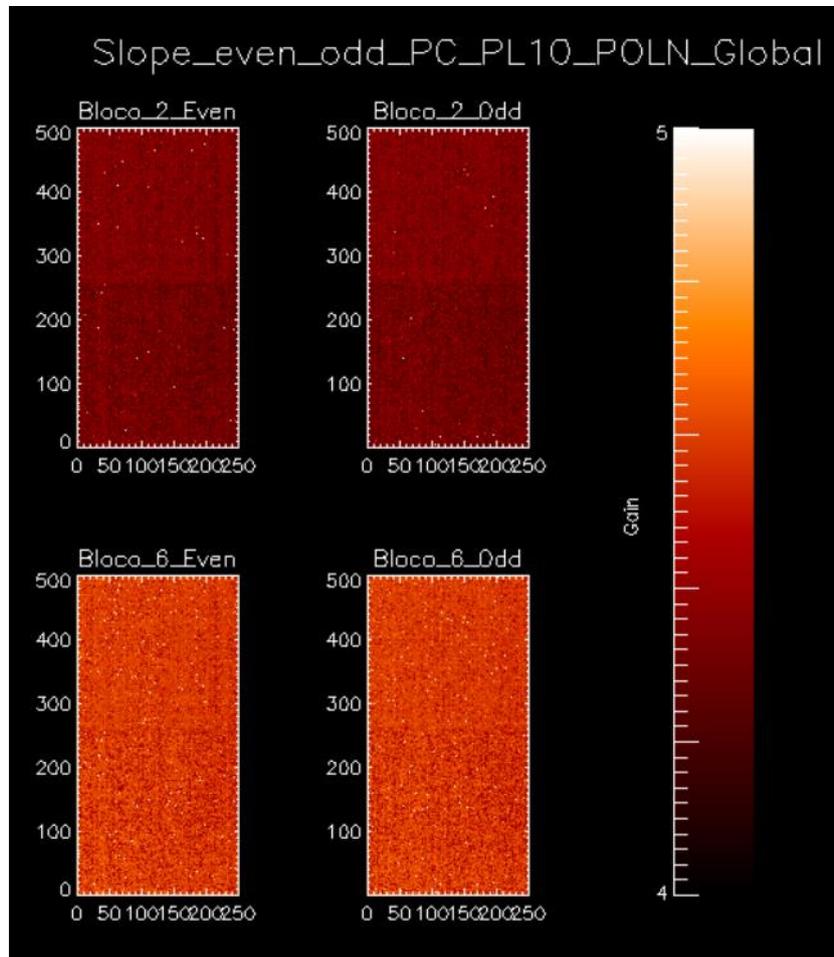
Source: Author.

Figure 5.40 Histograms from the gain calculated for each pixel for POLN. B2 has the cooling ON, while B6 has the cooling OFF. The even and odd pixels represent the sensor's rows.
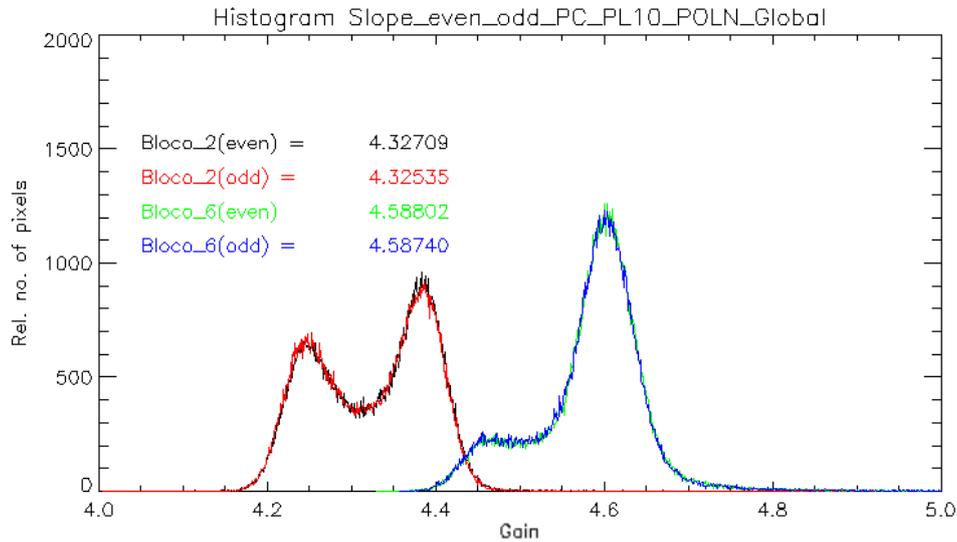
Source: Author.

Figure 5.41 Histograms from the gain calculated for each pixel for POLN. B2 has the cooling ON, while B6 has the cooling OFF. The even and odd pixels represent the sensor's columns.
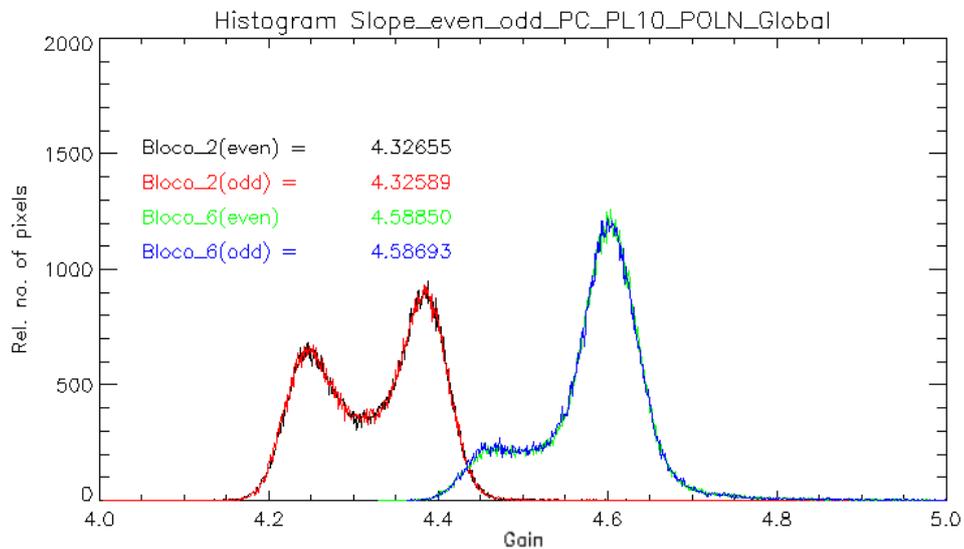
Source: Author.

One reason for this phenomenon to happen more intensely at Shutter Global and with cooling ON may be related to linearity. It is possible that even with the 5000DN threshold, many pixels are outside the linearity of the camera, aggravating the division caused by the readout.

Figure 5.42 shows the 2D slope for each pixel for POL90 (with the reference polarizer at 90°), while Figure 5.43 presents the gain map for POL0 (with the reference polarizer at 0°), respectively. One can observe that the gain behavior appears to be more uniform in POL0 and POL90 than in POLN, with the readout effect being more discreet for the data acquired with the polarizer. Observing the histogram of each data set (Figure 5.44 of POL90 and Figure 5.45 of POL0), one can perceive that the Gaussian distribution of all blocks shows no deviation.

Figure 5.42 2D map representing the gain for each pixel for each block for POL90 (with the reference polarizer at 90°). Blocks 2 and 6 are from Global Shutter, while Blocks 4 and 8 are from Rolling Shutter. B2 and B4 have the cooling on, while B6 and B8 cooling is off.
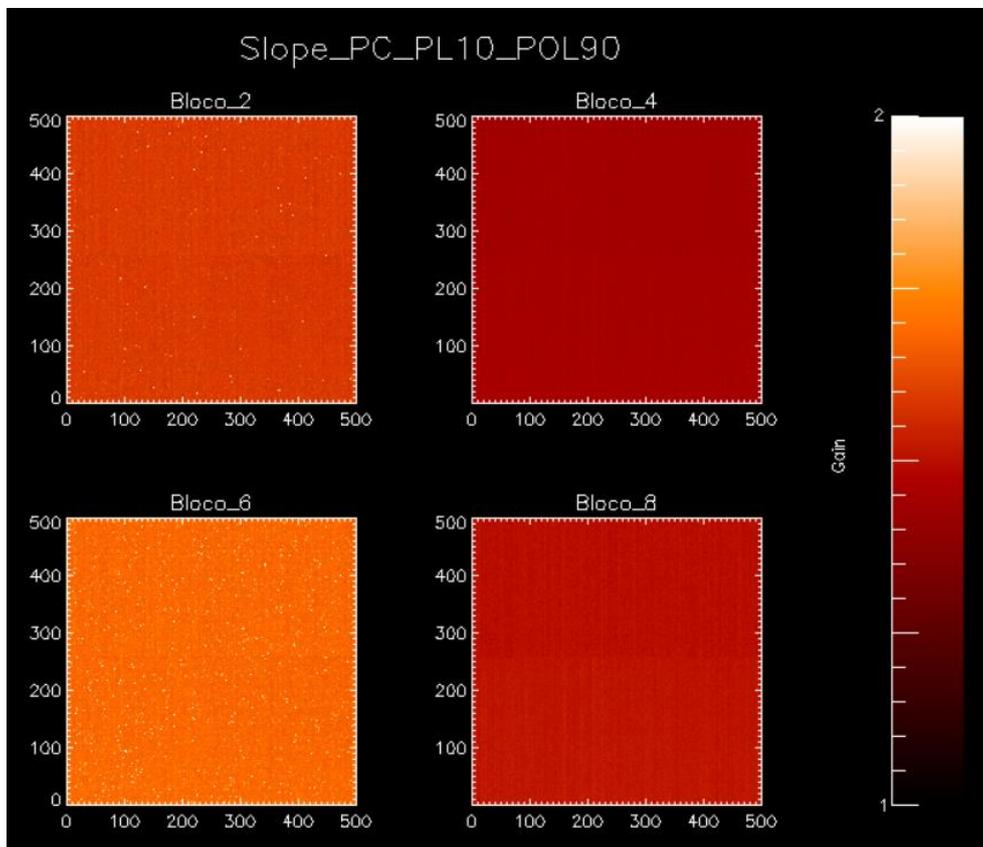
Source: Author.

Figure 5.43 2D map representing the gain for each pixel for each block for POL0 (with the reference polarizer at 0°). Blocks 2 and 6 are from Global Shutter, while Blocks 4 and 8 are from Rolling Shutter. B2 and B4 have the cooling on, while B6 and B8 cooling is off.
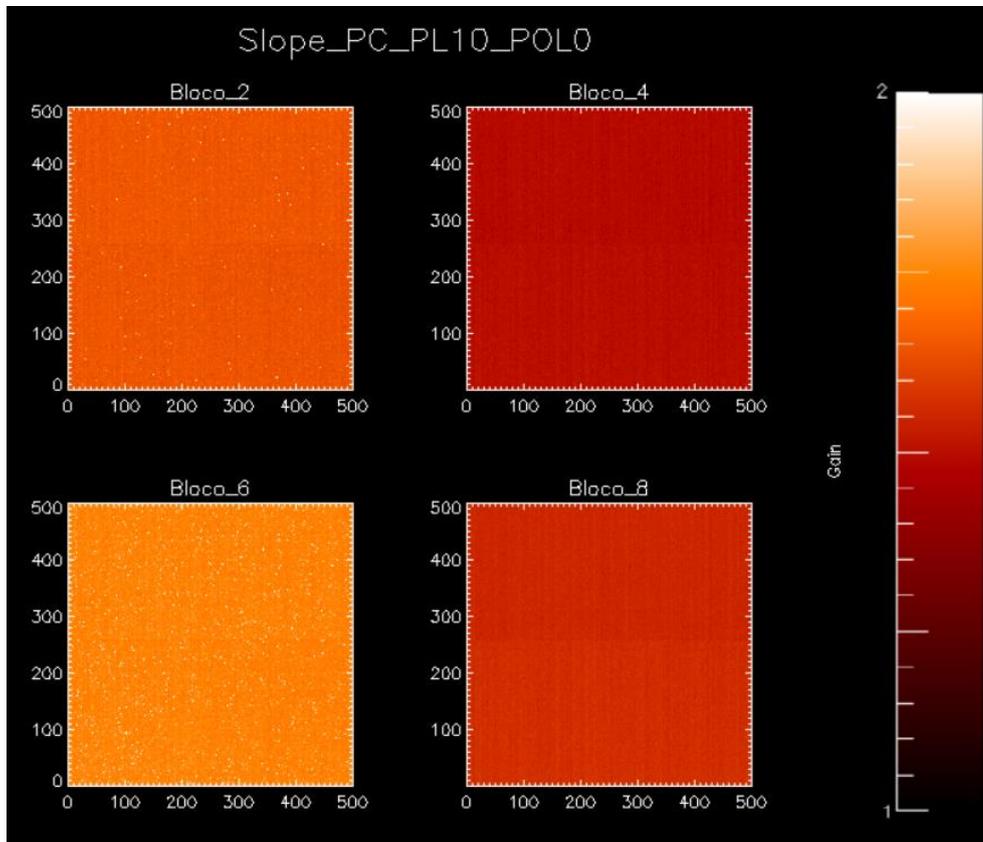
Source: Author.

Figure 5.44 Histograms from the gain calculated for each pixel for POL90. Blocks 2 and 6 are from Global Shutter, while Blocks 4 and 8 are from Rolling Shutter. B2 and B4 have the cooling on, while in B6 and B8, the cooling is off.

Source: Author.

81
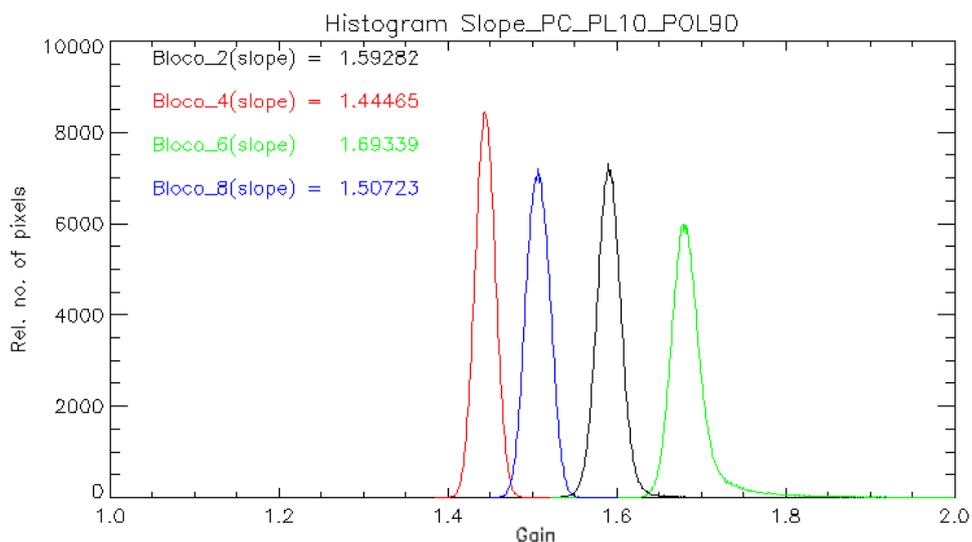
Figure 5.45 Histograms from the gain calculated for each pixel for POL0. Blocks 2 and 6 are from Global Shutter, while Blocks 4 and 8 are from Rolling Shutter. B2 and B4 have the cooling on, while in B6 and B8, the cooling is off.
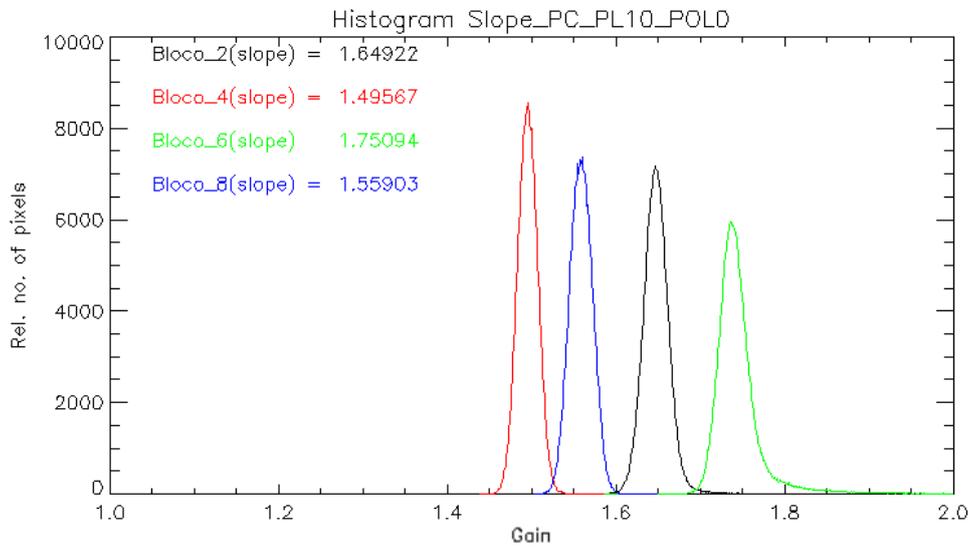
Source: Author.

5.2.2.5 Linearity analysis

Graphs of the sensor linearity were plotted for the even blocks of POLN. The x-axis represents the exposure time in second while the y-axis portrays the intensity in DN. Table 5.4 reveals the exposure times used to acquire the data.

Table 5.4 Exposure time for data acquisition.

| Test	Time [s]
1	9×10^{-6}
2	5×10^{-5}
3	1×10^{-4}
4	5×10^{-4}
5	1×10^{-3}
6	5×10^{-3}
7	1×10^{-2}
8	2×10^{-2}
9	3×10^{-2}

Source: Author.

Figures 5.46 and Figure 5.47 show the linearity's graph for the Global Shutter with cooling on and off, respectively. Conversely, Figures 5.48 and 5.49, respectively, show the linearity's graph with cooling on and off for the Rolling Shutter For this analysis, the least-square polynomial fit was calculated for all pixels with an intensity below the 5000 DN. Above the threshold, the pixels had values close to saturation. Thus, they were disregarded. The red line represents the least-square polynomial fit, and the green line represents the intensity threshold.

Each asterisk represents one pixel. As the exposure time increases, the pixel intensity variance also increases. As expected, this effect is most effective on the Global Shutter (B2 and B6) and for cooling off (B6 and B8).

The non-linearity of the camera was estimated for the POLN data as a comparison between the intensity obtained by the equation with the measured value. For all blocks, non-linearity was around 2-3%. This result is meaningful. However, as the analysis was carried out with few exposure times that are considerably sparse between themselves, the non-linearity has a significant

error. New analyzes with a larger number of exposure times must be performed to define the sensor's non-linearity.

Figure 5.46 Linearity for POLN Block 2 (Shutter: Global, Cooling: ON). The red line represents the polynomial adjustment of least squares between the exposure time and the intensity. The green line represents the intensity threshold.
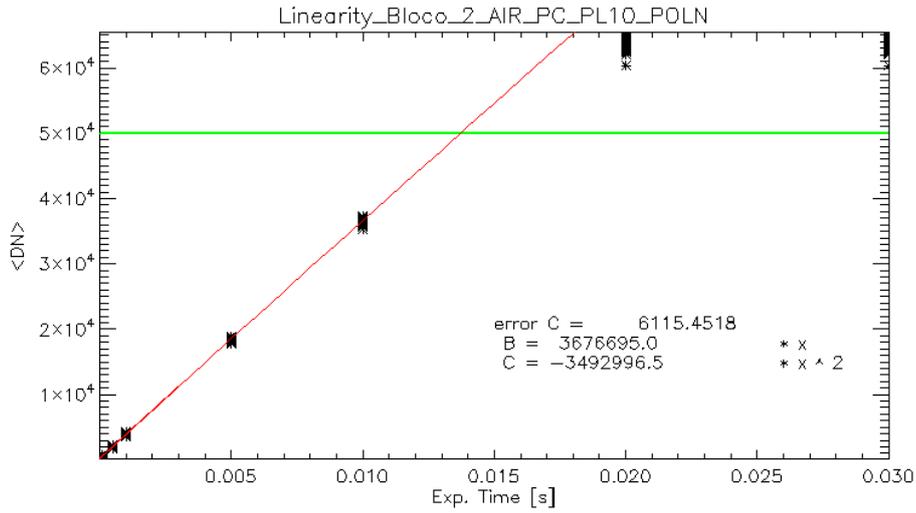
Source: Author.

Figure 5.47 Linearity for POLN Block 6 (Shutter: Global, Cooling: OFF). The red line represents the polynomial adjustment of least squares between the exposure time and the intensity. The green line represents the intensity threshold.
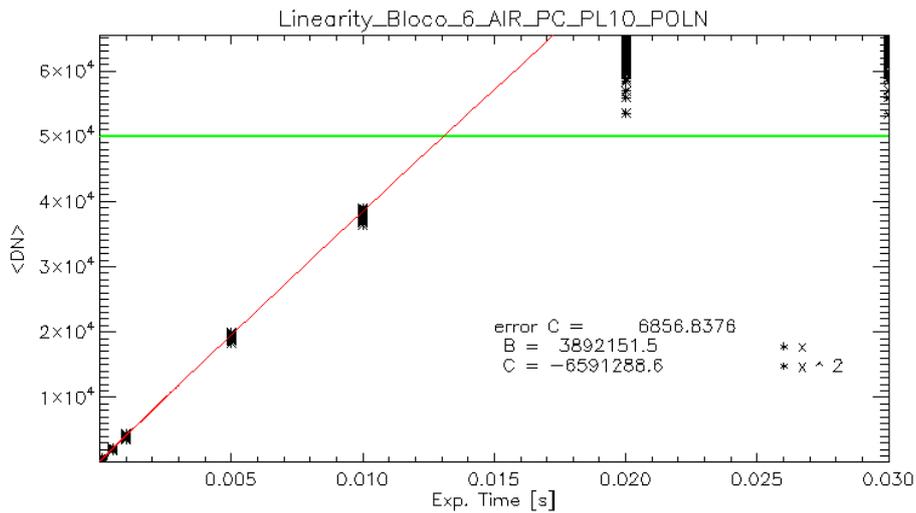
Source: Author.

Figure 5.48 Linearity for POLN Block 4 (Shutter: Rolling, Cooling: ON). The red line represents the polynomial adjustment of least squares between the exposure time and the intensity. The green line represents the intensity threshold.
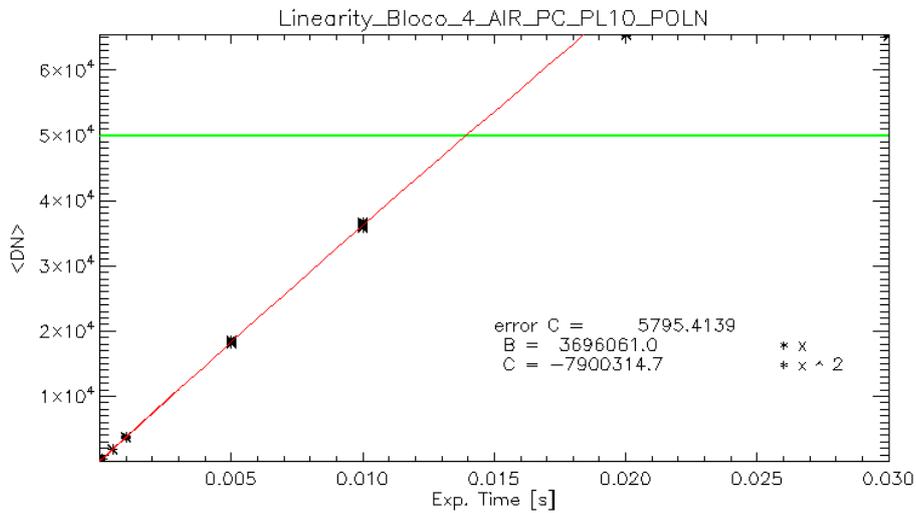
Source: Author.

Figure 5.49 Linearity for POLN Block 8 (Shutter: Rolling, Cooling: OFF). The red line represents the polynomial adjustment of least squares between the exposure time and the intensity. The green line represents the intensity threshold.
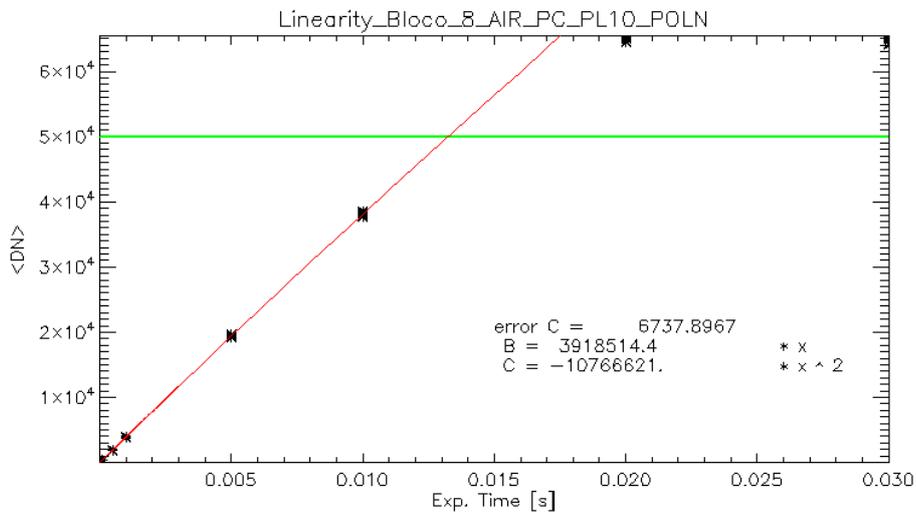
Source: Author.

5.2.3 Summary of results

In general, when cooling is off (B6 and B8), the pixel intensity is higher than when it is on (B2 and B4). The same is true for the global Shutter (B2 and B6) than Rolling Shutter (B4 e B8). In both shutters and cooling modes, the sensor divides the upper and lower part. This division is due to readout and it is more intense for Shutter Global (B2 and B6). By analyzing the gain, in Figure 5.36 and

Figure 5.37, one can notice that for B2 (Global, cooling ON), this effect is even more intense. It is because the cooling of the camera is also divided into two parts.

The Spurious Noise Filter (filter) and Blemish correction (correction) showed no significant differences in the images. However, since the image used for this analysis was obtained under a shorter exposure time, the intensity is lower. Therefore, it would be interesting to retake the test with a longer exposure time.

Regarding the polarizer effect, the difference between the tests acquired with (POL90 and POL0) or without (POLN) is clear. As expected, images captured without a polarizer have greater intensity than data captured with a reference polarizer. However, the difference in intensity between POL90 and POL0 was not foreseen. Since the light Source is not polarized, the transmittance of the polarizer should be the same despite the angle of the reference polarizer. The possible reason is that the pixel may have a polarization tendency, or the transmittance of the reference polarizer is not uniform for different angles. However, further analysis is needed to conclude.

6 IMAGE CALIBRATION

This chapter describes the study of a method to calibrate spectropolarimeter images. The data of SOT / Hinode was used because of their open data policy, and once processed, it is available to the scientific community.

Level 0 data contains whole images and a complete list of the files. This data-level is not calibrated, so it is called "raw data". Therefore, for quantitative analysis, it is necessary to calibrate the data. Level 1 data has been calibrated, and has the unit of the instrument data number. Level 2 data has been further processed (inversion models) into physical units.

The objective of this study is to calibrate the images from level 0 to level 1. For this, the codes provided by the SOT group were used through SolarSoftWare (SSW) system. The SolarSoft system is mainly an IDL-based system. This environment provides a consistent appearance for widely distributed joint investigation agencies to facilitate data exchange and facilitate coordinated analysis.

6.1 Hinode filtergraph (FG) analysis

For the calibration of FG images, the *fg_prep* routine was used. Figure 6.1 shows each step for the calibration process. Each raw image (L0) from the FITS file list is processed one at a time. The routine follows the following steps:

I. Read files.

  a) Identify the type of data: BFI or NFI image;

  b) Read the data;

II. Calibration for each data file:

  a) Correct camera readout defects;

  b) Subtract dark image from the frame;

  c) Multiply the Image by the gain image;

  d) Optional: Remove radiation-belt/cosmic-ray spikes and streaks.

Figure 6.1 Flowchart with Calibration Steps for FG Images.

| L0 | → | Missing Pixels | → | Dark Subtraction | → | Flatfield | → | Radiation spike removal | → | L1 |
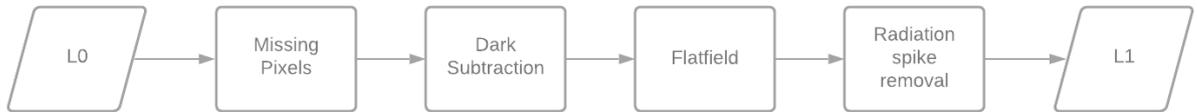
Source: Author.

A sunspot in December 2006 was selected to study the working principle of the FG image calibration process. The following results are for the BFI images and the Ca II H line (396.85 nm). The analysis were performed for a single file (.00000 file) instead of an average of all the files from the entire event. The L0 data of this event was calibrated to achieve L1 data. Figure 6.2 presents the L0, the image without calibration (original) for the first file. Figure 6.3 displays the L1, the resulted image after all the calibration steps for the same file.

Figure 6.2 L0: Image without calibration (original) for .00000 file.
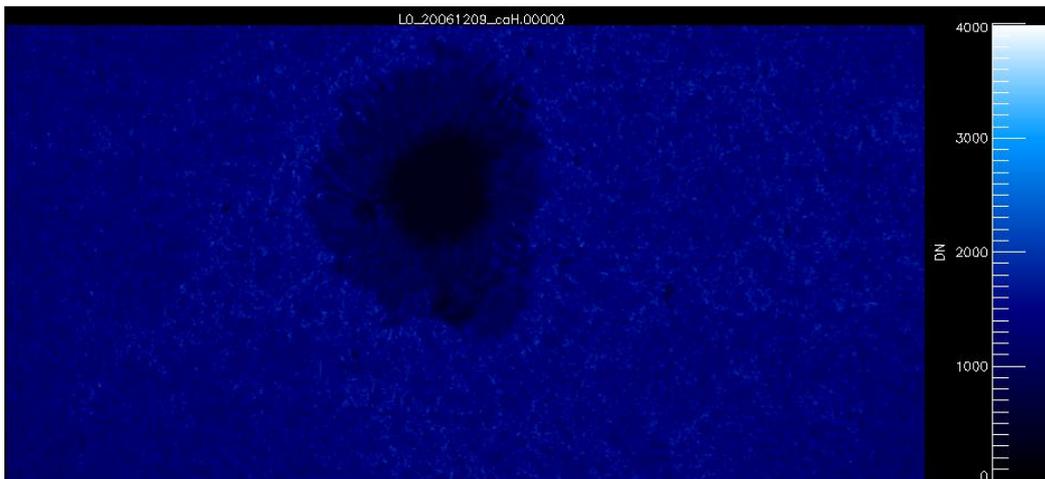
Source: Author.

Figure 6.3 L1: Image with calibration (after FG_PREP) disregard spike for .00000 file.
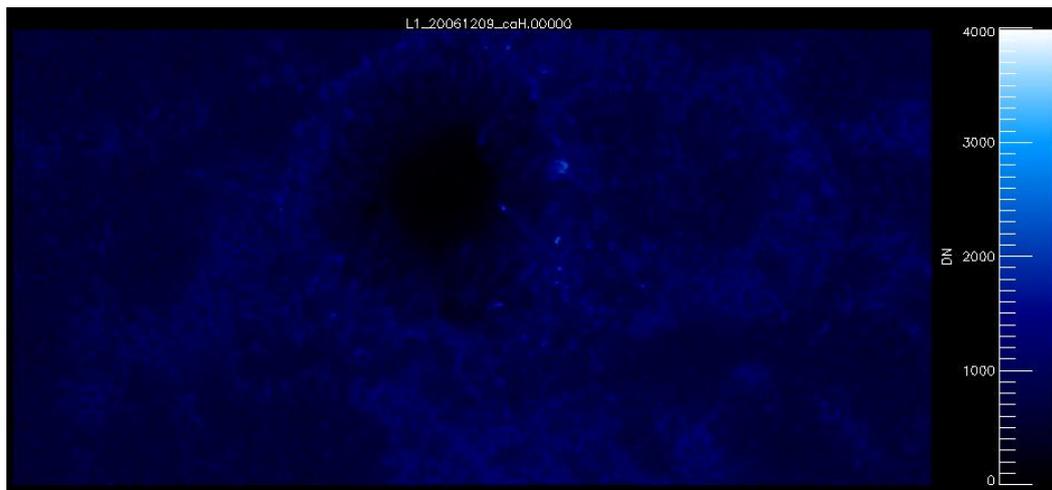
Comparing the calibrated image (L1), Figure 6.2, with the original image (L0), Figure 6.3, one can notice that the average intensity of L1 has decreased compared to L0. Each calibration step was performed individually, for only one FITS file, to better understand the process.

6.2 Missing pixels

The first calibration process is Missing Pixels. The routine FG_SHIFT_PIX is responsible for it. The purpose of this process is to correct FG's CCD readout defects. For this, the input image is analyzed and checked for missing pixels. For missing pixels, the value is defined from an interpolation with the values of neighboring pixels. This routine can also manage the anomalies that exist in the camera, such as the anomalies in the bottom edge and the first column. Figure 6.4 shows the image resulted after L0 is processed by FG_SHIFT_PIX.

Figure 6.4 Image_out_SHIFT_PIX.00000: The resulting image after L0 was processed by FG_SHIFT_PIX for .00000 file.
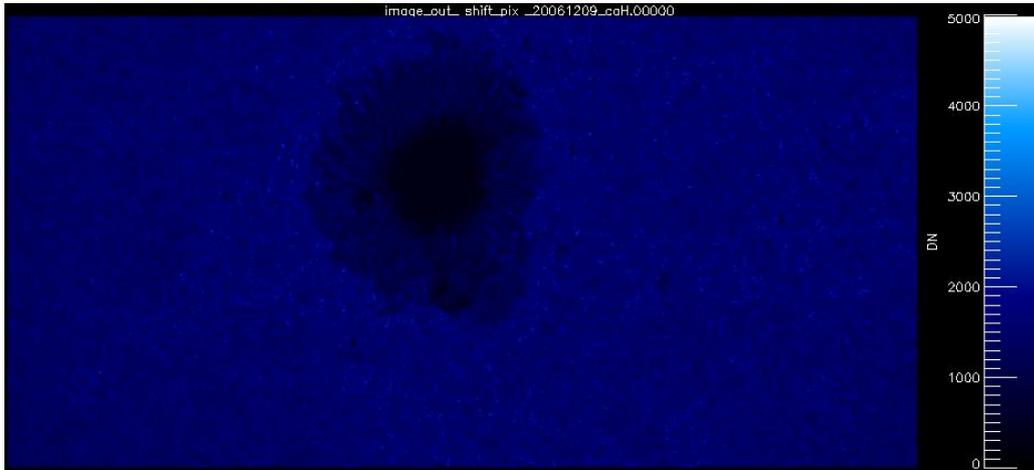
To better observe the changes made by this process, the image resulting from the calibration was subtracted from the original image (L0), as displayed in Figure 6.5. Figure 6.6 shows the histogram for these data.

Figure 6.5 L0-Image_out_shift_pix: Image resulted from the subtraction of Image_out_shift_pix from L0.
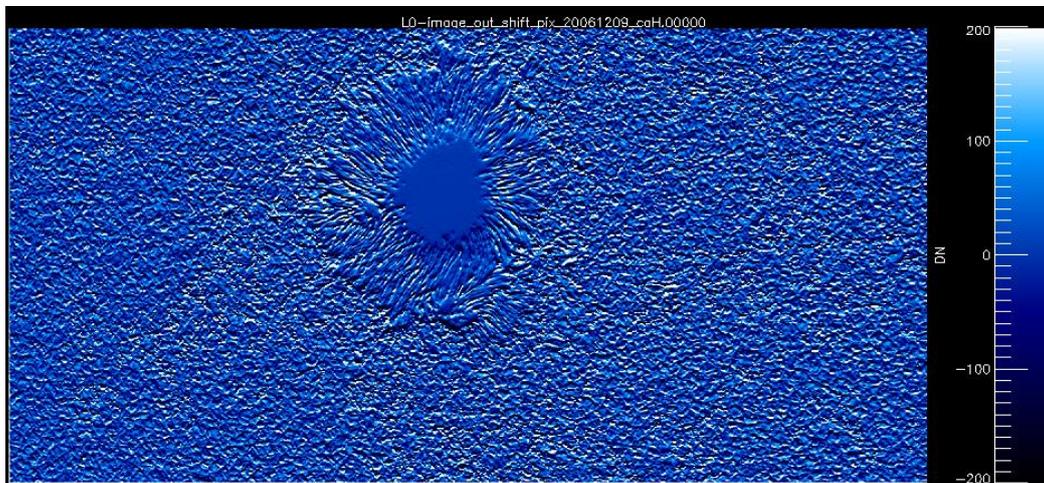
Figure 6.6 Histogram of Image resulted from the subtraction of Image_out_shift_pix from L0.

Histogram L0-image_out_shift_pix_20061209_caH.00000

Min = -1627
Max = 3775
Mean = 1.76207
Stddev = 139.180
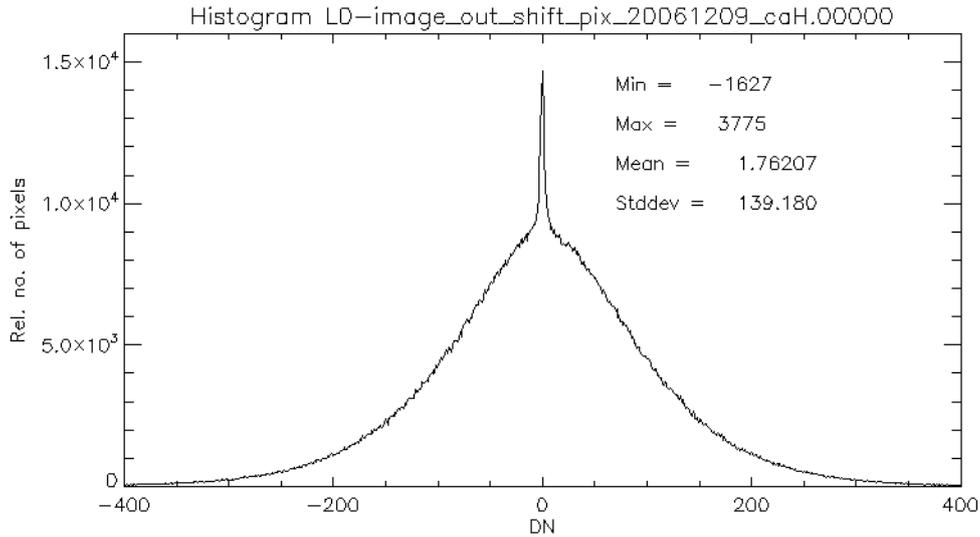
Source: Author.

In Figure 6.5, one can notice the abnormal behavior of the left and bottom edges, the pixels have a greater intensity than any of the rest of the sensors presenting a white/light blue border that should not exist. As seen in Figure 6.6, after this stage of the calibration process, for most pixels, there is no significant change as the average is close to zero.

6.3 Dark image

The next calibration process is the dark level correction done by the FG_DARK_SUB routine. The ADC offset and dark currents are subtracted from raw SOT/FG images on each half of CCD. ADC offset is temperature-dependent and different for the left and right halves of CCD.

The CCD temperature and the CEB (camera electronics box) temperature are defined first. Then, an artificial dark is created using a regression of the ADC offset on CEB and CCD temperature as well as dark currents. This dark image is subtracted from the L0 and negative values are set to zero. Figure 6.7 and Figure 6.8 show the L0 image processed by FG_DARK_SUB and created dark image, respectively.

Figure 6.7 Image_out_dark_sub.00000: The resulting image after L0 was processed by FG_ dark_sub for .00000 file.

Figure 6.8 and Figure 6.9 shows that the sensor has a uniform behavior regarding the dark image for each half of the CCD. It is also possible to notice the strange behavior of the pixels in the first column. This anomaly is usually corrected by the FG_SHIFT_PIX calibration step. But, since it was not used to calibrate Figure 6.7, the oddity border appears in Figure 6.6.

Figure 6.8 L0-Image_out_dark_20061209_caH.00000: Image resulted from the subtraction of Image_out_dark from L0.

92
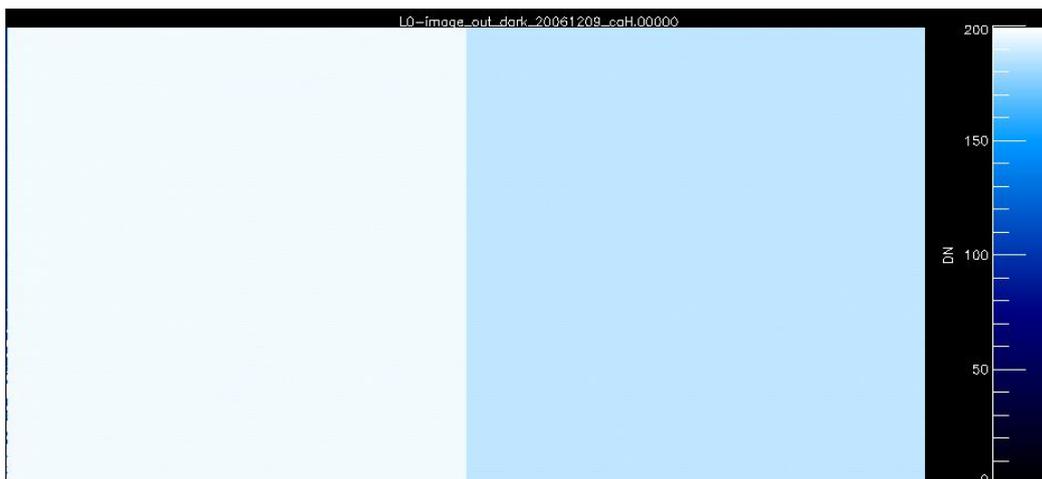
Figure 6.9 Histogram of Image resulted from the subtraction of Image_out_dark from L0.
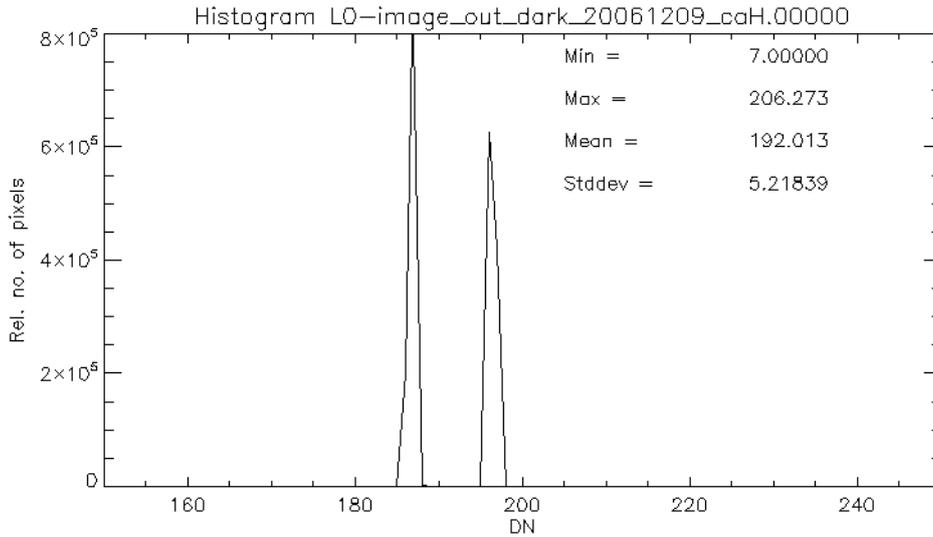
Source: Author.

6.4 Flatfield

Flatfield correction is a technique to eliminate the effects of image artifacts caused by changes in sensitivity between pixels of the detector and distortion of the optical path. The routine responsible for it is FG_FLATFIELD. The first step is to find an appropriate flatfield reference image in the database considering image wavelength, exposure time, the temperature of the FG CCD and CEB, and summing/binning.

Then the gain image is created by dividing one by the reference flatfield image.

$$Gain = 1/flatfield \qquad (6.1)$$

The output image is equal to the input image multiplied by the gain and a scale factor. The scale factor is the number of effective exposures for Stokes IV or Stokes IQUV.

$$Image\ out\ Flatfield = L0 * Gain * scale\ factor \qquad (6.2)$$

Figure 6.10 shows the result after the raw image goes through the Flatfield calibration process. The subtraction of the flatfield result from the L0 image is displayed in Figure 6.11 One can see the sunspot, where the correction is more uniform than in the rest of the sensor. Negative values are noted in the bottom corners of the image, while in the upper left side of the image there is a structure with an intensity above the average.

Figure 6.10 Image_out_flatfield.00000: The resulting image after L0 was processed by FG_ flatfield for .00000 fits.

Source: Author.

Figure 6.11 L0-Image_out_ flatfield.00000: Image resulted from the subtraction of Image_out_ flatfield from L0.
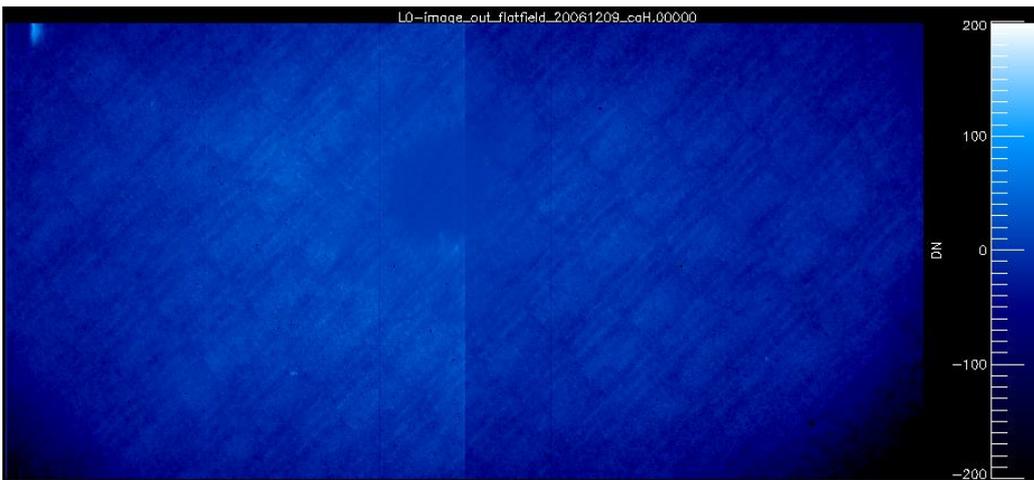
Source: Author.

The reference Flatfield image for the observations 20061209_caH .00000 is shown in Figure 6.12. These flatfield reference images are pre-normalized to average 1. As expected, the structures found in Figure 6.11 can also be seen in Figure 6.12, except for the sunspot.

Figure 6.12 Flatfield_refimage_20061209_caH .00000 Flatfield Reference image used for flatfield for .00000 file.
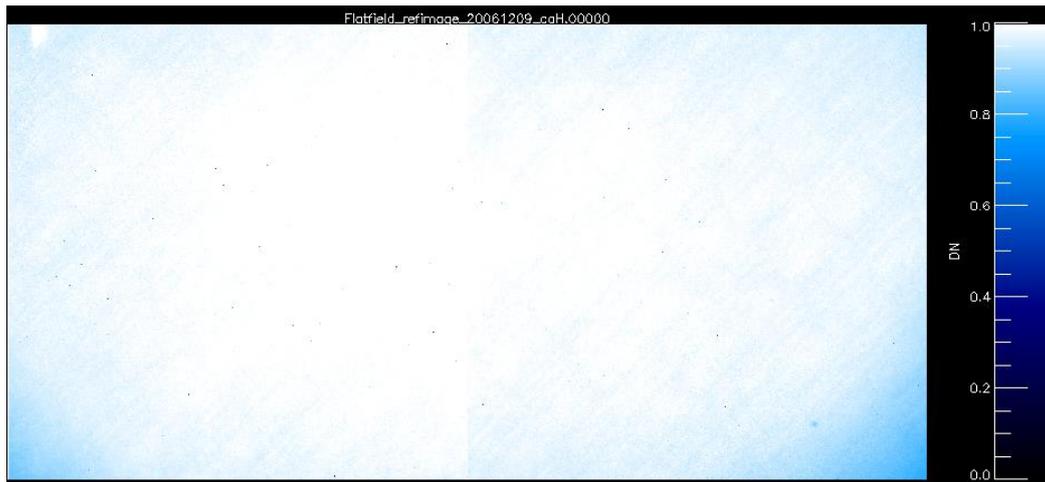
Source: Author.

The gain image is presented in Figure 13. In this image, it is possible to see the division line of the CCD into two halves again in a more subtle way. One can notice that the sensor has a uniform behavior, with few pixels with high gain values.

Figure 6.13 Gain_image_20061209_caH .00000 Gain image calculated from the reference flatfield image.
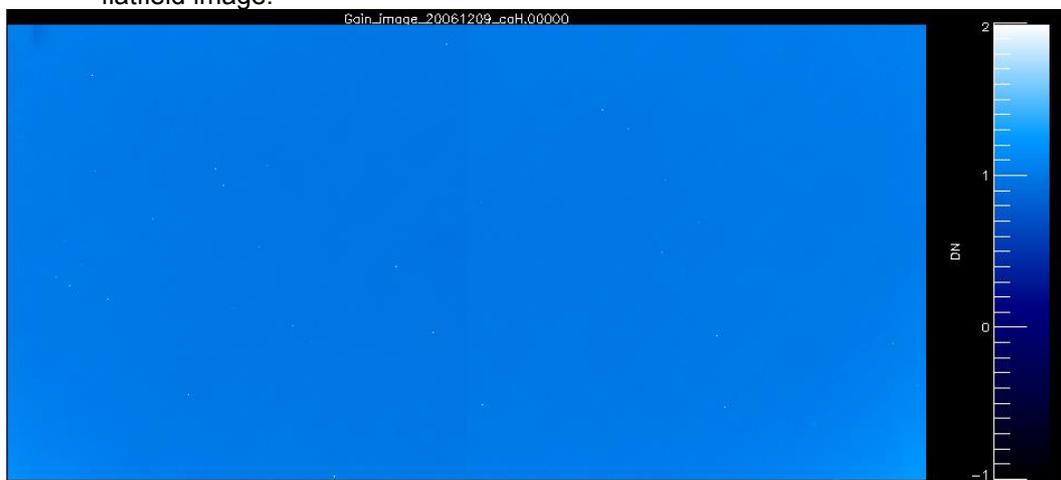
Source: Author.

6.5   Bad pixels

The last non-optional calibration process for FG_PREP is the process that handles bad pixels. This process is done by the FG_BAD_PIX routine to correct the FG CCD camera fix pattern defects as Dead pixels, Hot pixels, and fixed flaws on the sensor (as dust).

When calibrating FG data using FG_PREP, all calibration steps are performed automatically. After each step, the routine marks the pixels with very different values from their neighbors. FG_BAD_PIX reads bad pixels marked by other calibration steps and corrects the pixel values through triangulation and interpolation.

Therefore, when this process is done independently, the bad pixels have not been marked and are not corrected. Thus, as shown in Figure 6.14 and Figure 6.15, the image resulting from step BAD_PIX is the same as the original image.

Figure 6.14 L0-Image_out_ BAD_PIX.00000: Image resulted from the subtraction of Image_out_bad_pix from L0.
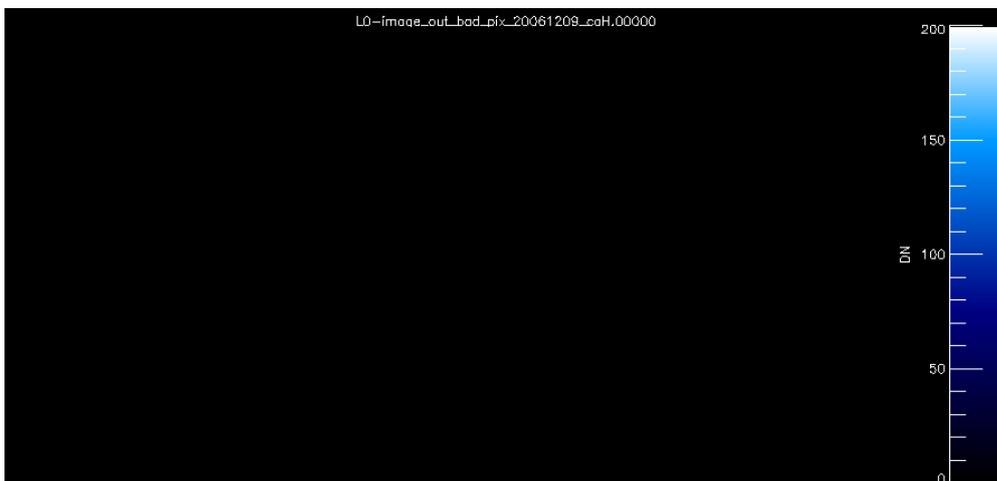
Source: Author.

Figure 6.15 Histogram of Image resulted from the subtraction of Image_out_bad_pix from L0.
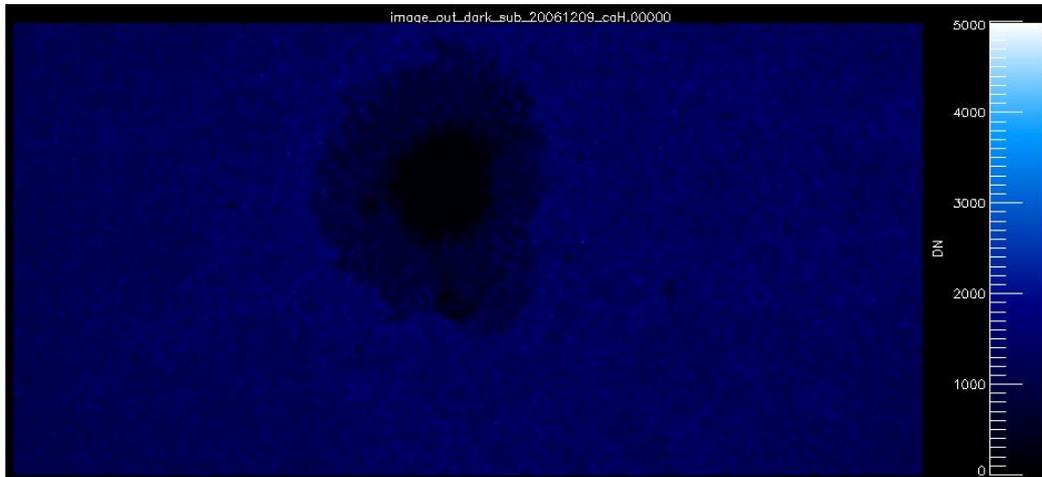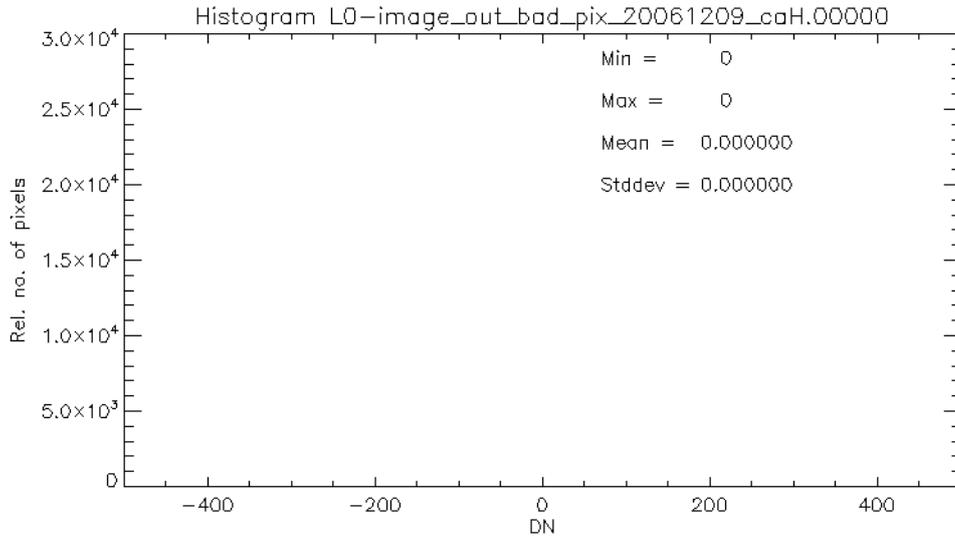

Source: Author.

6.6 Comparison between steps

Figure 6.16 represents the histogram of the data of each step of the calibration process. The behavior of each step is very close. The curve of SHIFT_PIX is superposed on the curve of BAD_PIX. The stage with the biggest difference is the DARK_SUB curve.

Figure 6.16 Histogram Image_out comparation: Histogram comparing the resulting image from each calibration step to a 0.00000 file.

Source: Author.

97
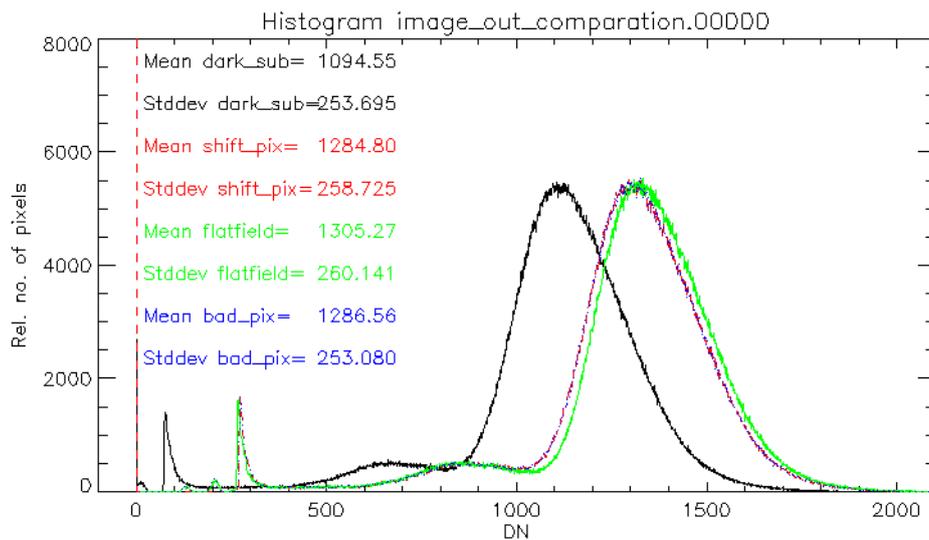
6.7 Influence of peaks and streaks of cosmic radiation / ray belt in the image

Removing peaks and streaks from the cosmic radiation/ray belt by the DESPIKE function is an optional image calibration process. For L1 images, this option has been activated. Hence, these values are disregarded.

To better understand how much this step interferes with the whole process, the calibration of the original image was made again with the DESPIKE option disabled. The result was the image calibrated without discounting the cosmic radiation/ray belt (L1D) shown in Figure 6.17.

Figure 6.18 shows the histogram data from L0, L1 and L1D for only 1 FITS data, .00000. One can see that the behavior curve from the data not calibrated (L0) has the same behavior to the data calibrated without disregard to the radiation (L1D). After both calibration processes, the average intensity decreases. In the process in which radiation is disregarded (L1) this decrease is more pronounced.

Figure 6.17 L1D_20061209_caH.00000 Image with calibration (after FG_PREP) with spike for .00000 files.
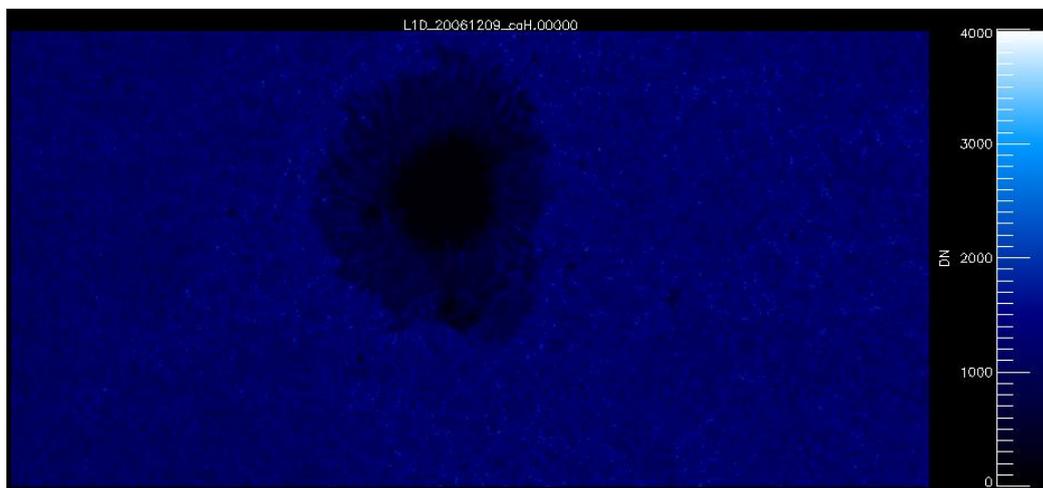
Source: Author.

Figure 6.18 Histogram comparing the data from the original image (L0), with the data from the calibrated image that disregards radiation peaks (L1), with the data from the calibrated image that does not exclude radiation peaks (L1D) to an FTIS file .00000 file.
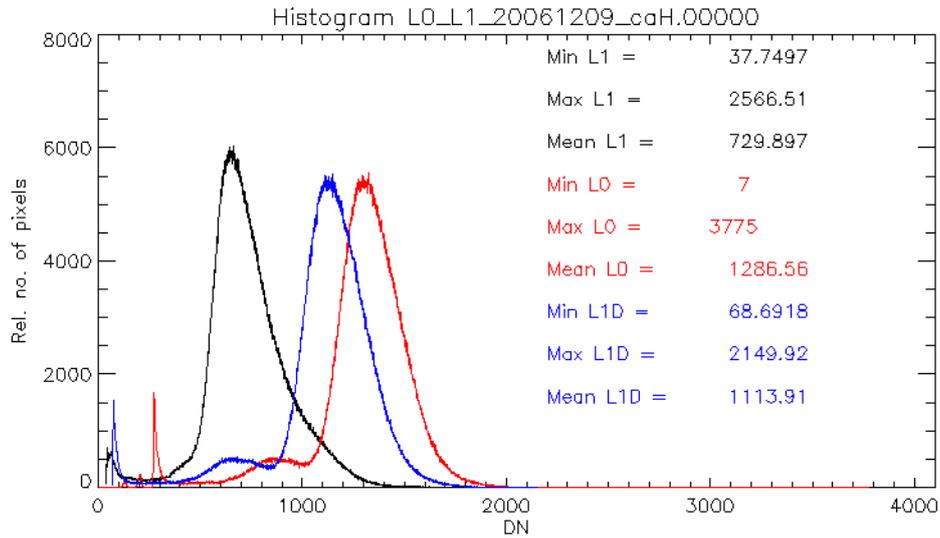
Source: Author.

Figure 6.19 shows the same Histogram, but for all FITS files of the event.

Figure 6.19 Histogram comparing the data from the original image (L0), with the data from the calibrated image that disregards radiation peaks (L1), with the data from the calibrated image that does not exclude radiation peaks (L1D) for all FTIS file of the solar.
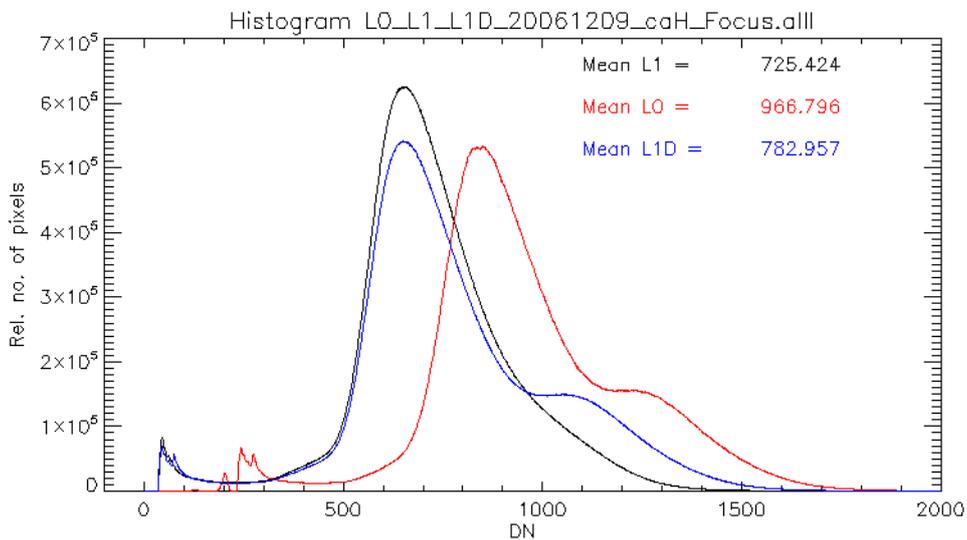
Source: Author.

For all files, it is possible to see that the behavior of the calibrated data, L1 and L1D, is much more similar than for just one file. The first peak of the histogram represents the sunspot, with lower intensity than the rest of the sensor. The

calibrated data curves (L1 and L1D) show, in Figure 6.18 and Figure 6.19, the first peak before the original data (L0). The results confirm the importance of the calibration process to understand the factors that influence the value of the intensity of the structures of solar events. At the end of the Gaussian curve, both L1D and L0 show a slight rise. This is the representation of the radiation-belt/cosmic-ray that are disregarded in L1 (black curve).

7 MUELLER MATRIX

The study of the polarization uncertainties is essential for the calibration of the polarimeters. It is necessary to understand all the polarization characteristics of telescopes and instruments to distinguish them from solar polarization signals. The quantity should be determined with the highest possible accuracy.

7.1 SUSI

During BEPE, the author had the opportunity to do preliminary study of SUSI's Mueller Matrix. This study was done in a theoretical way since the instrument was not assembled by the end of the internship. SUSI group wrote codes to check the polarimetric efficiency of the instrument's mirrors with different coatings. In the first code, all elements were considered ideal mirrors, as proposed by STENFLO, (1994). Hence, the instrument's Mueller matrix was the same as the Mueller's matrix for an ideal mirror, represented in Equation 7.1.

$$\begin{pmatrix} 1 & 0 & 0 & 0 \\ 0 & 1 & 0 & 0 \\ 0 & 0 & -1 & 0 \\ 0 & 0 & 0 & -1 \end{pmatrix} \tag{7.1}$$

In the codes, reflectivity values for different mirror coatings were incorporated. Therefore, it would no longer be assumed to be ideal. The variation of the uncertainty as a function of the component angle was also added.

Figure 7.1 presents an example of the simulation for mirrors with Al coating plus oxide layer. Ellips equals one means that the matrix is being calculated in ellipsometric mode. p1 and p2 represent the ellipsometric parameters psi (amplitude ratio) and delta (phase difference) in degree. AOI means the angle of incidence [deg], and AOR means the angle of rotation [deg]. For mirrors, this indicates the angle between Stokes + Q and the plane of incidence. Consequently, when AOR equals zero, the Stokes + Q is perpendicular to the plane of incidence.

Figure 7.1 Theoretical Mueller Matrix Simulation with Al coating plus oxide layer.

```
Component      p1      p2    Ellips.  AOI     AOR      Mueller matrix                      Cumulative Mueller matrix
=================================================================================================================================
M1            45.00  180.00 1        0.0     0.0      0.8985  0.0000  0.0000  0.0000       0.8985  0.0000  0.0000  0.0000
                                                      0.0000  0.8985  0.0000  0.0000       0.0000  0.8985  0.0000  0.0000
                                                      0.0000  0.0000 -0.8985  0.0000       0.0000  0.0000 -0.8985  0.0000
                                                      0.0000  0.0000 -0.0000 -0.8985       0.0000  0.0000 -0.0000 -0.8985
---------------------------------------------------------------------------------------------------------------------------------
M2            45.00  180.00 1        0.0     0.0      0.8985  0.0000  0.0000  0.0000       0.8073  0.0000  0.0000  0.0000
                                                      0.0000  0.8985  0.0000  0.0000       0.0000  0.8073  0.0000  0.0000
                                                      0.0000  0.0000 -0.8985  0.0000       0.0000  0.0000  0.8073 -0.0000
                                                      0.0000  0.0000 -0.0000 -0.8985       0.0000  0.0000  0.0000  0.8073
---------------------------------------------------------------------------------------------------------------------------------
M3            44.19  146.86 1       45.0    90.0      0.9020 -0.0254 -0.0000  0.0000       0.7282 -0.0205 -0.0000  0.0000
                                                     -0.0254  0.9020  0.0000 -0.0000      -0.0205  0.7282  0.0000 -0.0000
                                                     -0.0000  0.0000 -0.7550  0.4929      -0.0000  0.0000 -0.6095  0.3979
                                                      0.0000  0.0000 -0.4929 -0.7550       0.0000  0.0000 -0.3979 -0.6095
---------------------------------------------------------------------------------------------------------------------------------
M4            44.19  146.86 1       45.0    90.0      0.9020 -0.0254 -0.0000  0.0000       0.6573 -0.0370 -0.0000  0.0000
                                                     -0.0254  0.9020  0.0000 -0.0000      -0.0370  0.6573  0.0000  0.0000
                                                     -0.0000  0.0000 -0.7550  0.4929      -0.0000  0.0000  0.2640 -0.6009
                                                      0.0000  0.0000 -0.4929 -0.7550      -0.0000 -0.0000  0.6009  0.2640
---------------------------------------------------------------------------------------------------------------------------------
Offner1 M1    45.00  180.00 1        4.0     0.0      0.8985  0.0000  0.0000  0.0000       0.5906 -0.0332 -0.0000  0.0000
                                                      0.0000  0.8985  0.0000  0.0000      -0.0332  0.5906  0.0000  0.0000
                                                      0.0000  0.0000 -0.8985  0.0000       0.0000 -0.0000 -0.2372  0.5399
                                                      0.0000  0.0000 -0.0000 -0.8985       0.0000  0.0000 -0.5399 -0.2372
---------------------------------------------------------------------------------------------------------------------------------
Offner1 M2    45.00  180.00 1        8.1     0.0      0.8985  0.0000  0.0000  0.0000       0.5307 -0.0299 -0.0000  0.0000
                                                      0.0000  0.8985  0.0000  0.0000      -0.0299  0.5307  0.0000  0.0000
                                                      0.0000  0.0000 -0.8985  0.0000      -0.0000  0.0000  0.2131 -0.4851
                                                      0.0000  0.0000 -0.0000 -0.8985      -0.0000 -0.0000  0.4851  0.2131
---------------------------------------------------------------------------------------------------------------------------------
Offner1 M3    45.00  180.00 1        4.0     0.0      0.8985  0.0000  0.0000  0.0000       0.4768 -0.0268 -0.0000  0.0000
                                                      0.0000  0.8985  0.0000  0.0000      -0.0268  0.4768  0.0000  0.0000
                                                      0.0000  0.0000 -0.8985  0.0000       0.0000 -0.0000 -0.1915  0.4358
                                                      0.0000  0.0000 -0.0000 -0.8985       0.0000  0.0000 -0.4358 -0.1915
---------------------------------------------------------------------------------------------------------------------------------
```

Source: SUSI group (2020).

In Figure 7.1, only some elements of SUSI are presented. However, one can notice the behavior of the matrix of each component and how the instrument was planned. Since polarization modulator and wavelength discriminator are not present, the best for these components is to have the Mueller Matrix elements, except for the diagonal elements, closer to zero.

7.2 PCPS

The study of the Mueller Matrix for the proof of concept was done experimentally. Data with a known light Source has been acquired and has been modeled. However, the Mueller matrix was not calculated for each element individually. Sets of elements were assumed for the M0 matrix, as described in section 4.1.

7.2.1 PCPS data acquisition

The ideal way to calculate polarization uncertainty is to add a new retarder and polarizer to the optical path, preferably before the telescope. However, due to the required diameter of the components, only the polarizer was available and was

added (reference polarizer), as shown in **Erro! Fonte de referência não encontrada.**7.2.

Figure 7.2 Reference polarizer, positioned before the telescope.
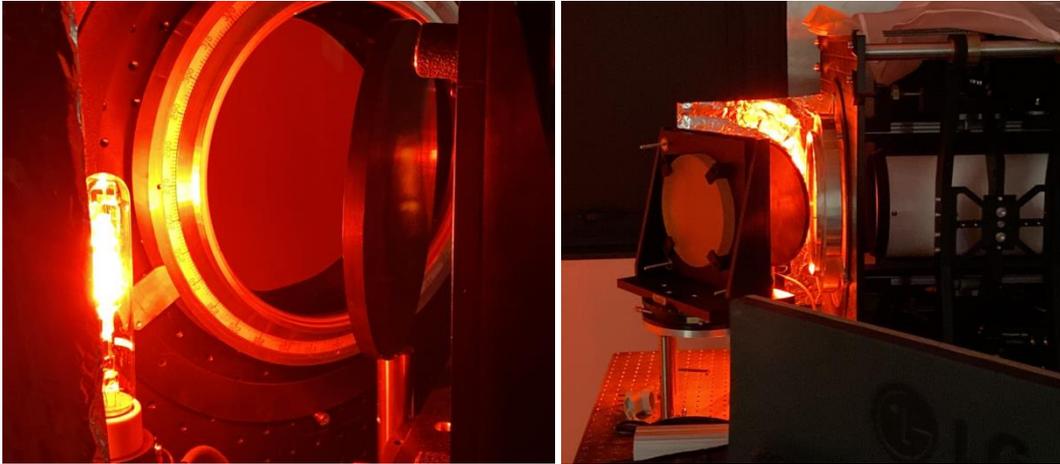
Source: Author.

It is necessary to use a known light Source to calculate the Mueller Matrix. The ideal would be to use a uniform light Source, such as an integrated sphere. However, in this case, an integrated sphere with a large diameter would be necessary, and due to the laboratory configurations and the position of the prototype, it was not possible. Therefore, to obtain greater beam uniformity, a barium sulfate screen was placed between the polarizer and the lamp.

With this new configuration, seven data sets were acquired using the Phillips Neon Spectral Lamp (see ANNEX A). In each set, the reference polarizer has a different angle (10°, 20°, 30°, 45°, 90°, 135°). The ideal would be to obtain 36 sets of images varying the polarizer angle from 10 to 10 degrees. However, with these seven angles, it is already possible to estimate the characteristics of the instrument and verify if any modulation occurs.

Each of these data sets has 1,024 images. One can obtain 16 positions of the polarization package by varying the voltage in LCVR I and II. Each polarization position has 64 spectral positions. Changing the voltage that feeds the etalon, the distance between your mirrors also changes, performing the spectral scan.

Only the central area of the sensor is analyzed to save data storage space and processing time. In other words, only the center 500x500 pixels. It is important to note that each pixel must be analyzed separately.

Figure **7.37**.3 display a time series for one central pixel with 7,168 values. Here the intensity values of a single-pixel (256;256) for the 7 data sets, 16 states of polarization, and 64 spectral positions are presented. In the first panel, the uncalibrated intensity data is displayed. The second panel shows the background intensity, which is subtracted after data calibration. The last panel shows the calibrated data after dark deduction and normalization. Since the maximum intensity that can be measured is the value of direction 0 plus direction 90, the value was normalized to twice the maximum value.

Each image has a polarization ring, which is a region where the interference generated by etalon is positive. Figure 7.4 summarizes information for a data cube, where the reference polarizer was at 0°, and a SoP (state 1) before data calibration. In the upper left panel, the data cube with 64 images is shown. The x and y-axis represent the number of pixels, and the z-axis represents the image number where the spectral position is changed. In the upper right panel, a single image from the data cube is presented. The lower-left chart displays a vertical slice of the data cube, both in the x and y-axis. The lower-right chart reveals a single image from the vertical slice of the data cube in the y-axis. Here one can see how the diameter of the ring changes as the distance between the mirrors change.

Figure 7.3 Intensity for 1 pixel (256;256) for 7x1024 images.
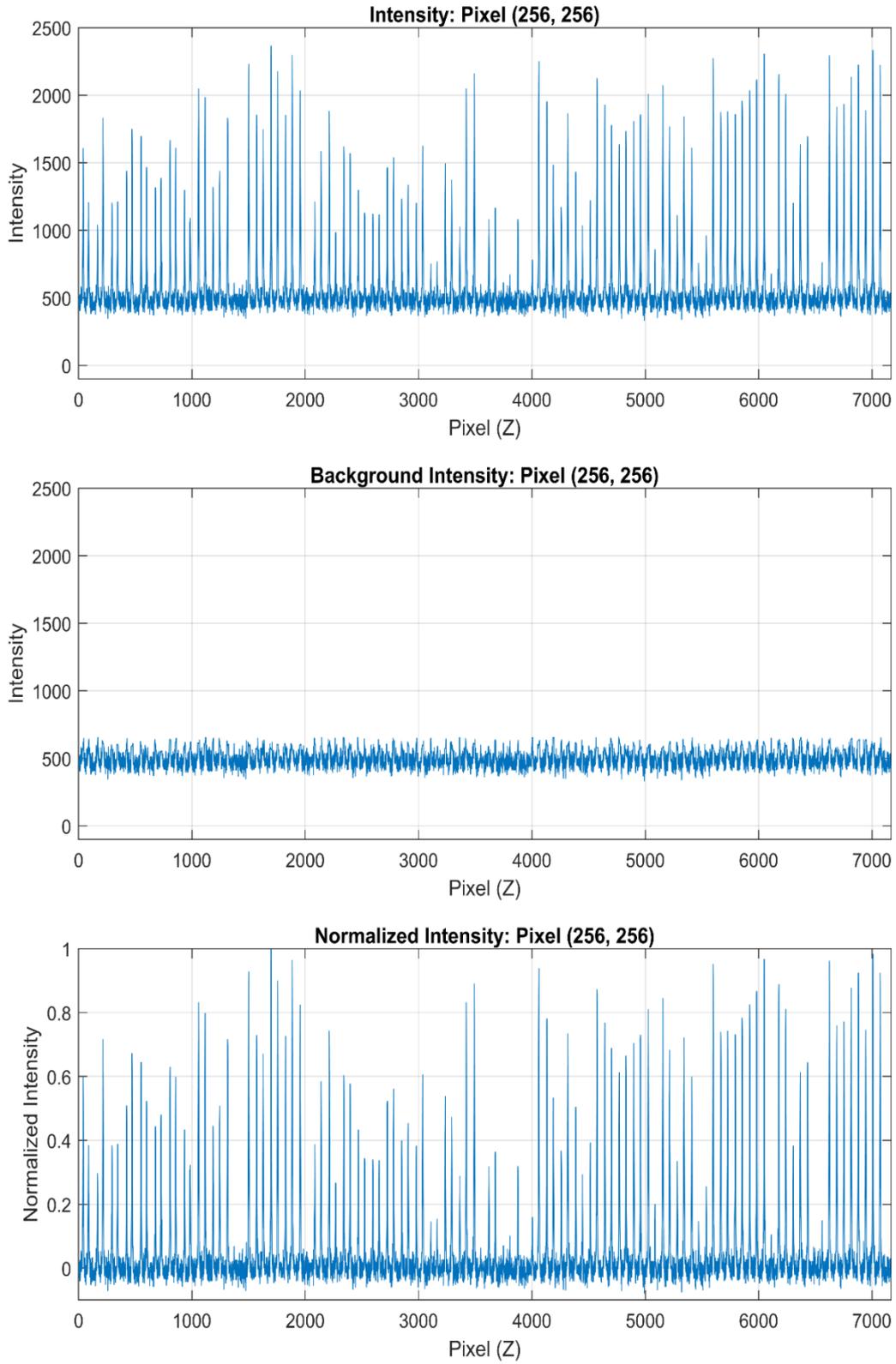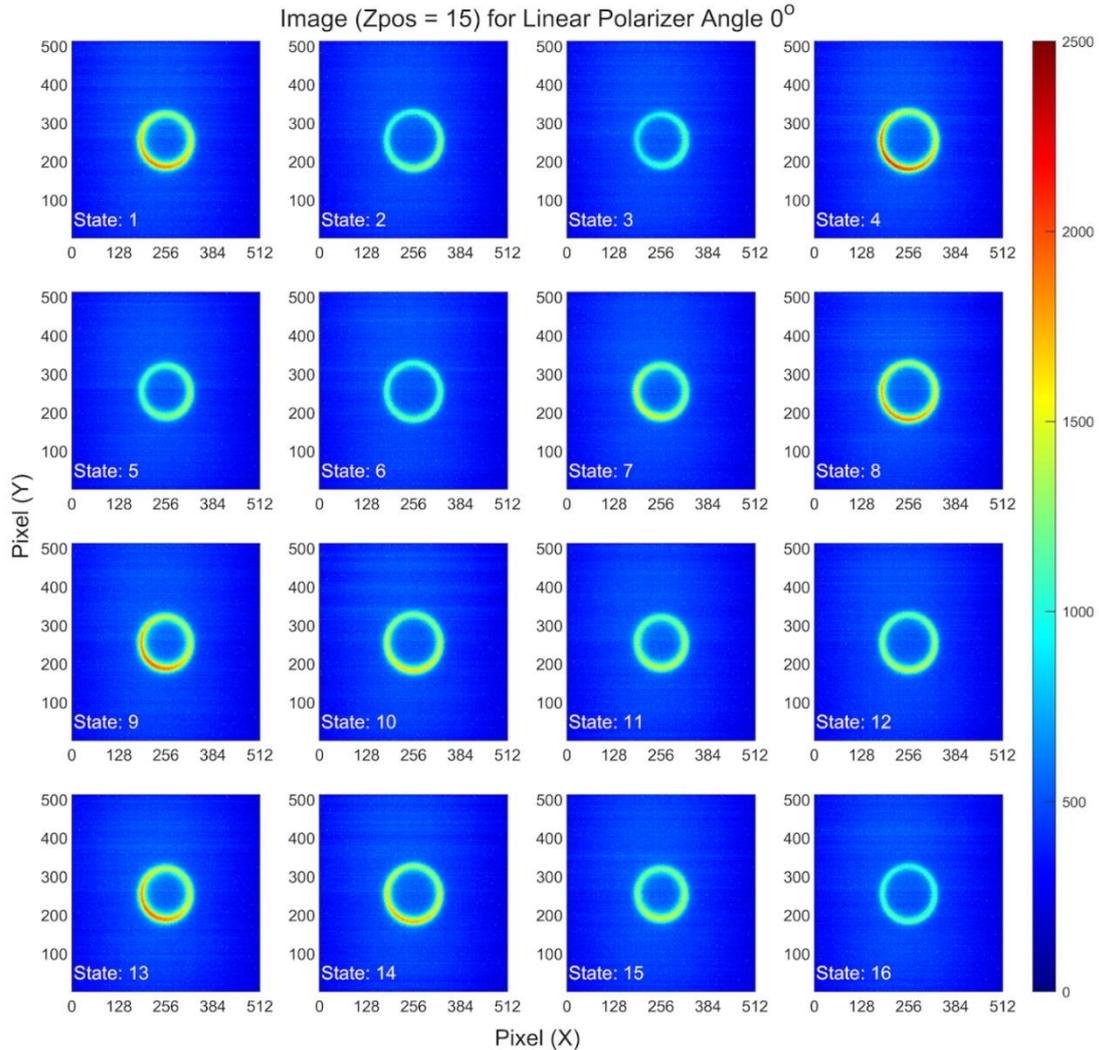

Source: Author.

Figure 7.4 Data cube for one data set (0°) and one polarization state (State 1). The color bar shows the intensity of the pixels before the background reduction and normalization.
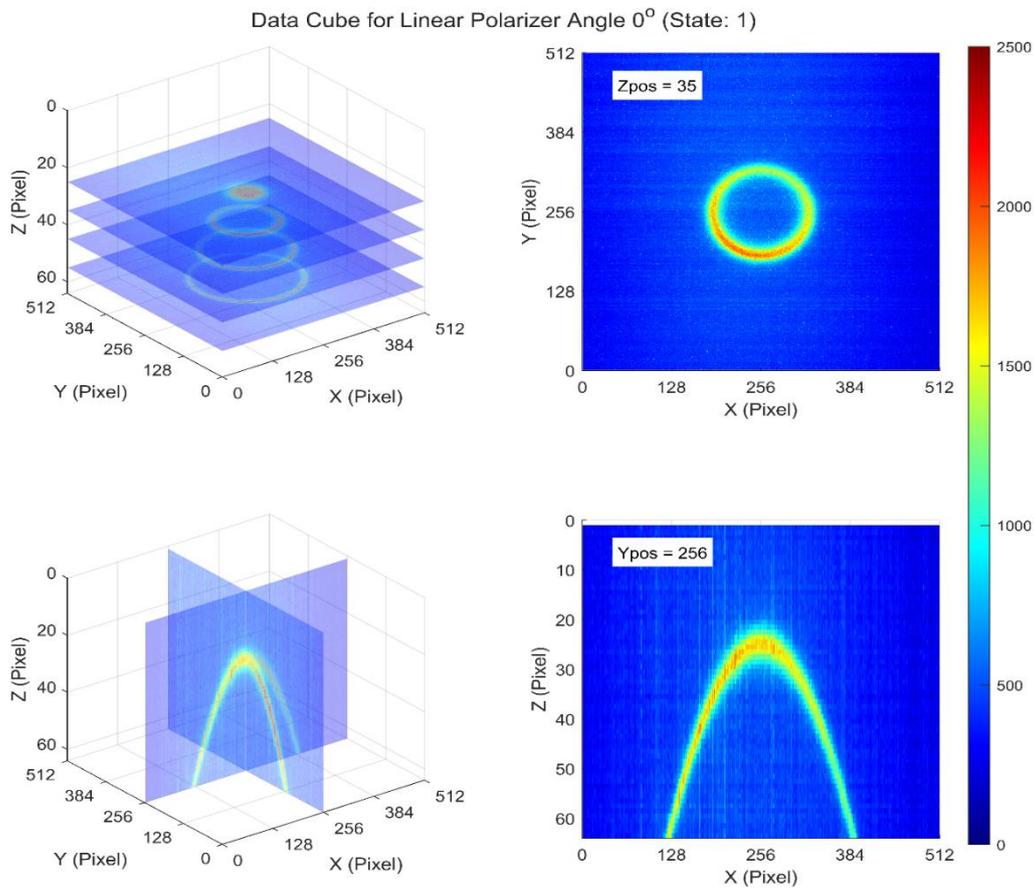
Source: Author.

Figure **7.57**.5 shows a comparison between the polarization states for a data set (0 degrees) with a spectral position equal to 15, before the data calibration. By changing the polarization states, the intensity of the ring changes. In some polarization states, the intensity of the ring is not uniform. One can see that one side of the ring is brighter than the other. It happens possibly because the barium sulfate screen was not perfectly parallel to the polarizer.

Figure 7.5 Polarization states for a data set (0 °) with spectral position equal to 15.
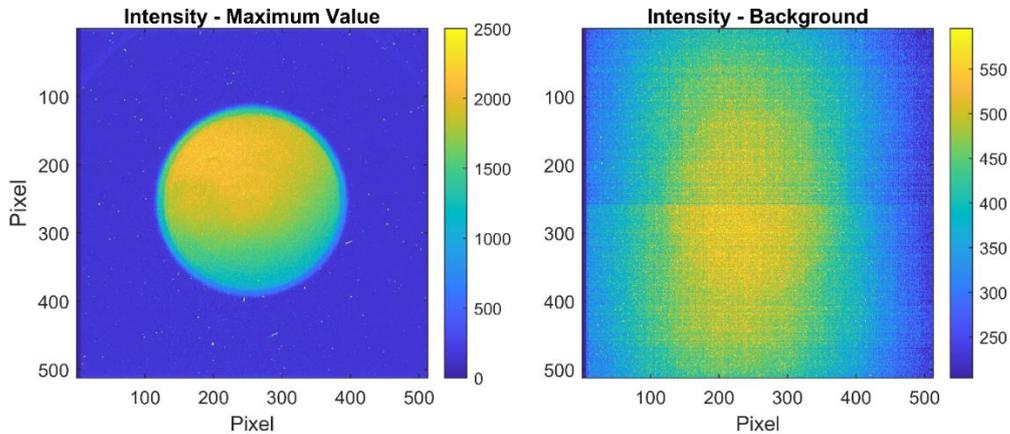

Source: Author.

Figure **7.6**7.6 shows the maximum value of the intensity of each pixel and its background. That means, regardless of the data set or the spectral position, or the polarization state, the maximum pixel value is displayed. Figure 7.3 shows all the values that a single pixel has considering all data sets. In Figure 7.6, only one of them (the maximum) is represented.

When the distance between the Fabry-Pérot mirrors changes, its Muller matrix will also change. However, as only the maximum intensity value is considered, the Mueller matrix for etalon was admitted constant in this work.

By showing the maximum value, we have a circle instead of a ring. The image on the right panel shows the background of the maximum intensity image. The horizontal distribution of this image is due to the camera's reading mode.
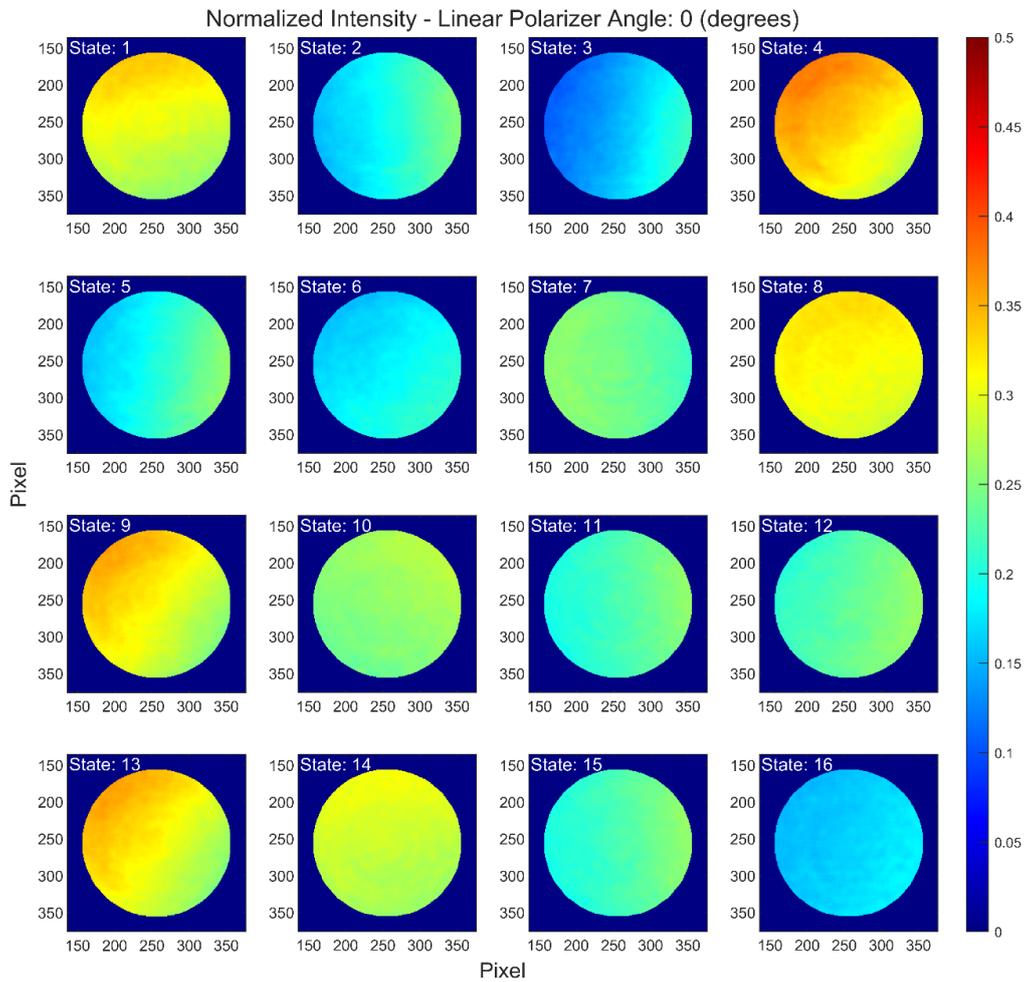
Figure 7.6 Maximum intensity for each pixel.

Source: Author.

Figures 7.7 and 7.8 show the intensity variation for each polarization state. Figure 7.7 shows the maximum intensity value for each pixel for the data set with the reference polarizer at 0°. Here, depending on the SoP, there are variations in which part of the circle the intensity value is higher (i.e. State 1, 4, 9, 13). This change is related to polarization aberration.
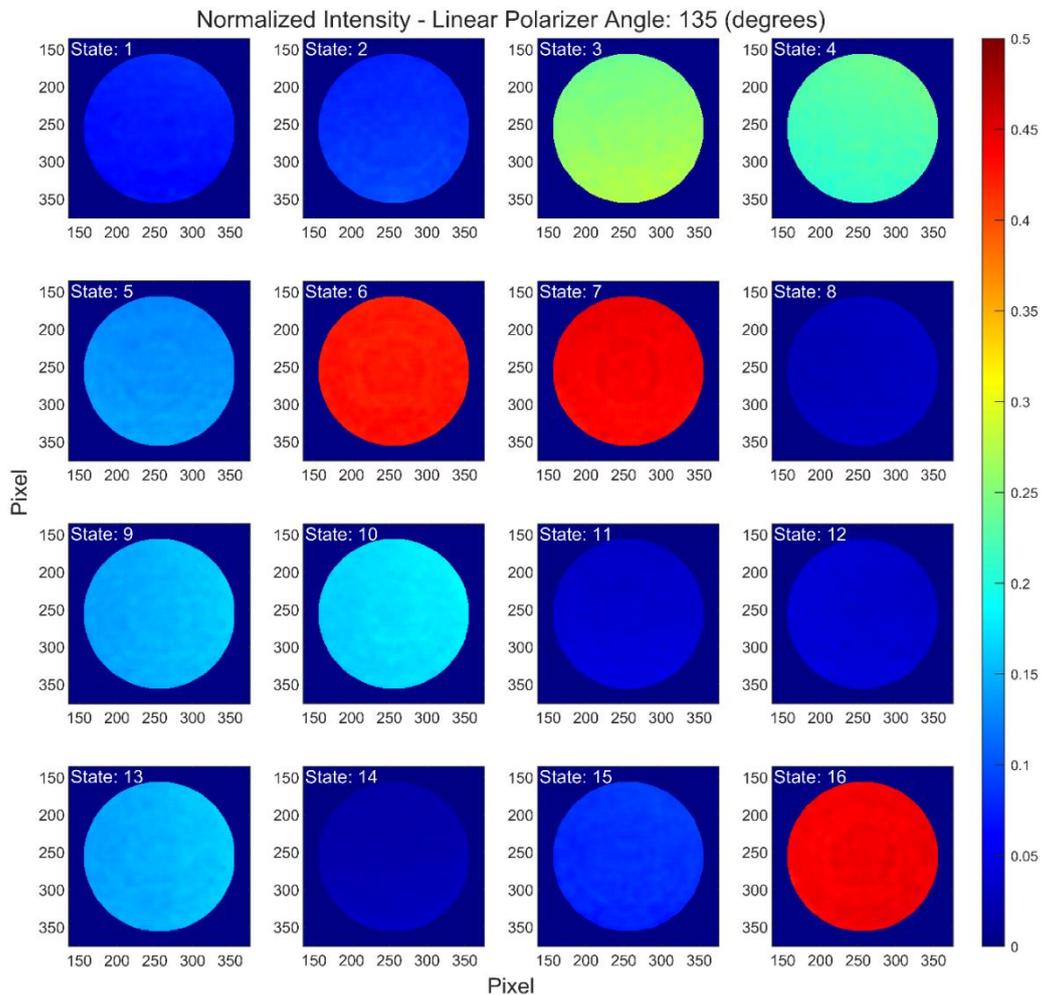
Figure 7.7 Maximum normalized intensity for each state of polarization. Reference polarizer at 0°.

Figure 7.8 exposes the maximum intensity value for each pixel for the data set with the reference polarizer at 135°. In contrast to the previous Figure, Figure 7.8 does not present huge variations in intensity in the same state of polarization. This shows that the variations are just effects of aberrations in the polarization, and it will appear in the Mueller matrix. Therefore, it is necessary to calculate a Mueller Matrix for each SoP and not just one for the instrument as a whole.

Figure 7.8 Maximum normalized intensity for each state of polarization. Reference polarizer at
135°.

ANNEX B contains the other Figures with the values with the maximum normalized intensity for each SoP with the reference polarizer at 10 °, 20 °, 30 °, 45 °, and 90 °.

Figure 7.9 shows how the intensity varies for a row of pixels among different data cubes, that is, data acquired with different values in the reference polarizer. This variation occurs because of diattenuation, which depends on the angle of incidence. Since each beam passes through the optical component at a different angle, the intensity varies for each data set and polarization state. Each chart shows a polarization state. Most states show that the curves maintain a uniform

and virtually linear pattern. Nevertheless, in State 1, one can see that the intensity curves have a different slope when changing the reference polarizer angle, especially 0, 90, and 135 degrees.

Similar to Figure 7.9, Figure 7.10 also shows the intensity changes between different data cubes. However, it is alongside a column of pixels. One can see at Figure 7.10 that most of the polarization states have slopes. It shows that the Diattenuation effect is greater when comparing the pixels of the same column.

Figure 7.9 Image profile for normalized intensity for row 257.
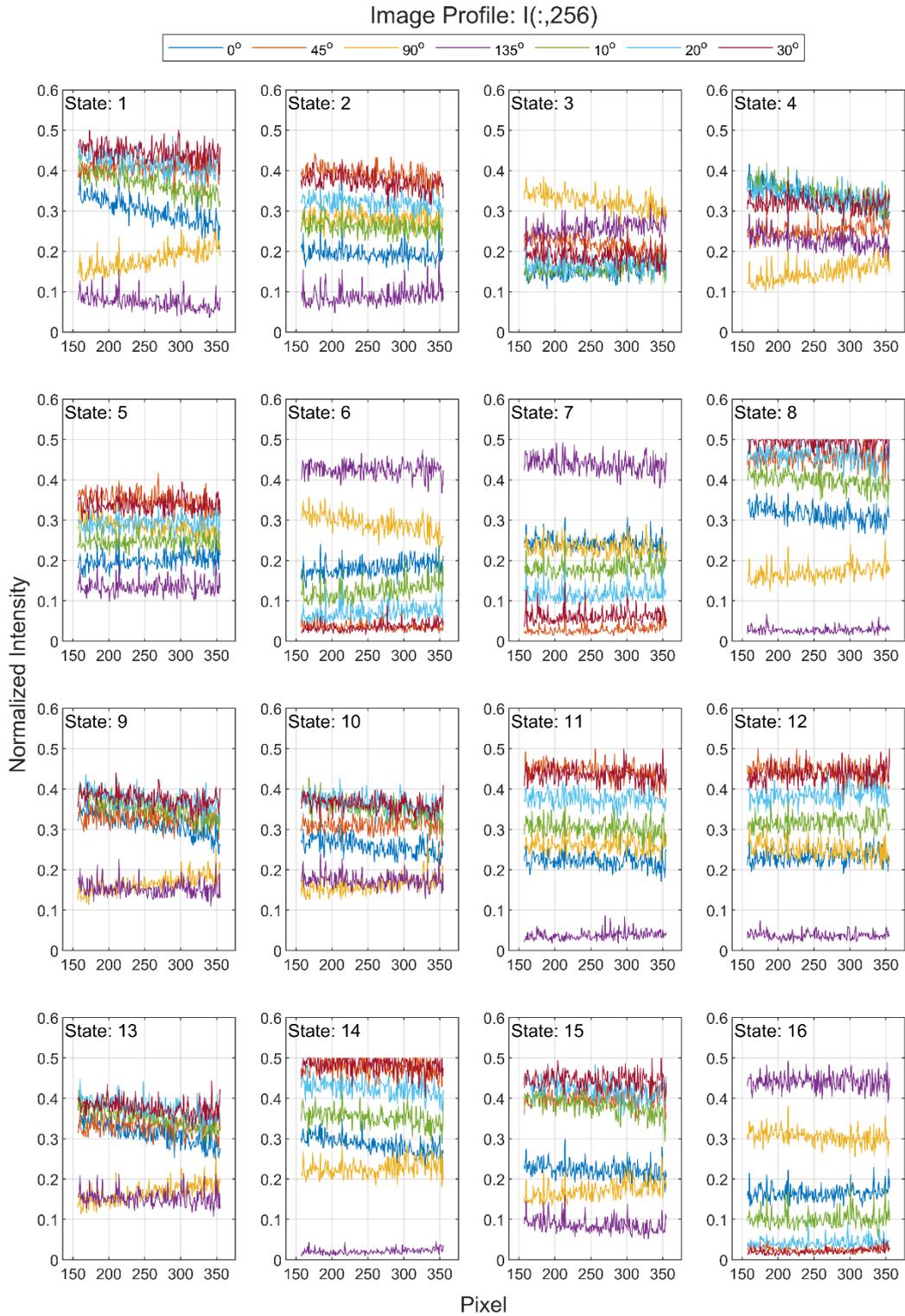
Source: Author.

Figure 7.10 Image profile for normalized intensity for column 257.

Image Profile: I(256,:)
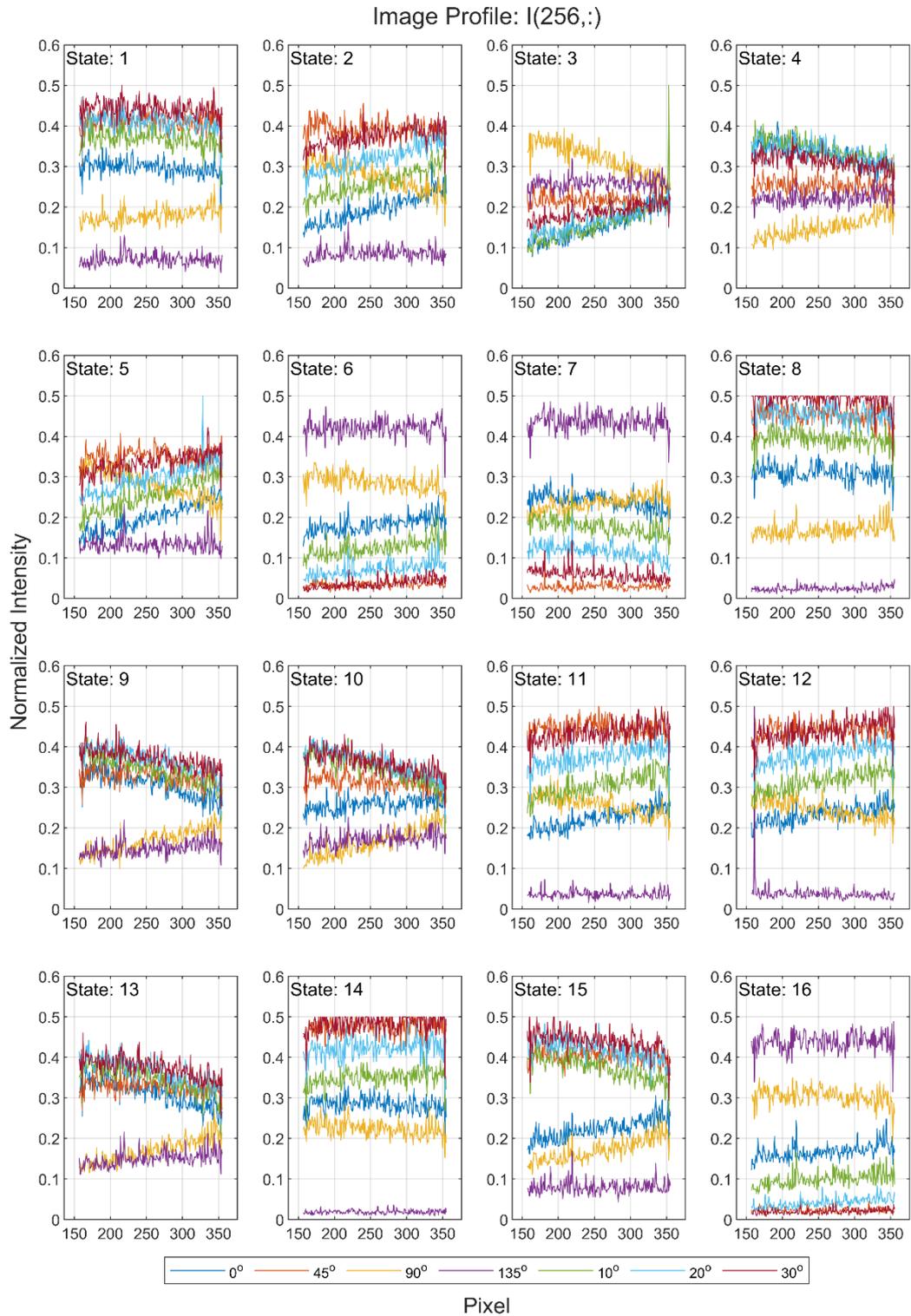
Source: Author.

7.2.2 Determination of PCPS' Mueller matrix

After the subtraction of the dark and normalization, the data is input in a code that was written to calculate the Mueller matrix. The code presents a model where the Mueller matrix is determined. The model was developed by the GSST group, especially for the proof of concept. The purpose of the model is to compare the Stokes input parameters with the Stokes output parameter acquired in section 7.2.1.

Each optical element has an associated Muller matrix (M0, M1, M2, M3) that is combined in a Muller matrix (M) for the entire instrument according to equation 2.14. Table 7.1 summarizes the components and the respective Mueller matrices calculated by the model.

Table 7.1 Summary of the components that introduce uncertainty in the polarization of light and their respective Mueller matrices.

Matrix	Mueller Matrices	Components
M0	General linear retarder	Telescope; pre-filter I; pre-filter II; Mirror I, Intermediate Optics I; Mirror II
M1	General linear retarder	Liquid Crystal Variable Retarder I (LCVR I)
M2	General linear retarder	Liquid Crystal Variable Retarder II (LCVR II)
M3	Linear polarizer	Polarizer

Source: Author.

Figure 7.11 summarizes a comparison between the observed data and the data obtained by the model for a single pixel. In the first panel on the left, one can notice that the model data is highly linear relative to the observed data. The right panel displays the Gaussian error of the model. The second panel shows the comparison between the data of a single pixel for each data set (different angles

for the reference polarizer). The comparison for three different pixels is shown in the third panel. As one can see, the model showed a good correlation with the observed data.

Figure 7.11 Comparison between observed data and the model.
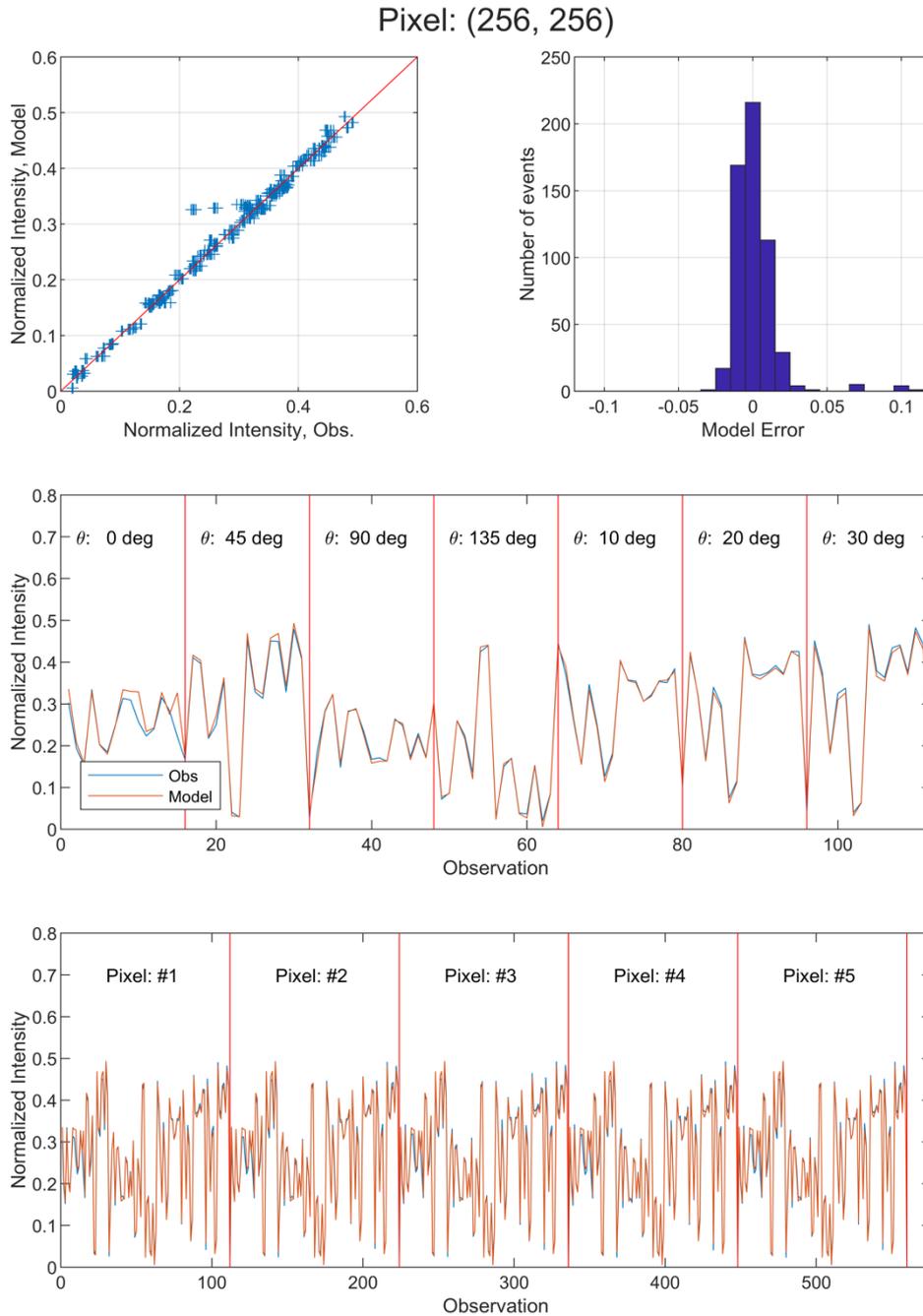
Source: Author.

Figure 7.12 shows the comparison between the observed data and the model concerning the polarization states. Each red dot represents a measured value for each data set (0, 10, 20, 30, 45, 90, 135 degrees). It is possible to notice that the red dots follow the blue sinusoidal line.

Figure 7.12 Comparison between the observed data and the model in relation to the polarization states.
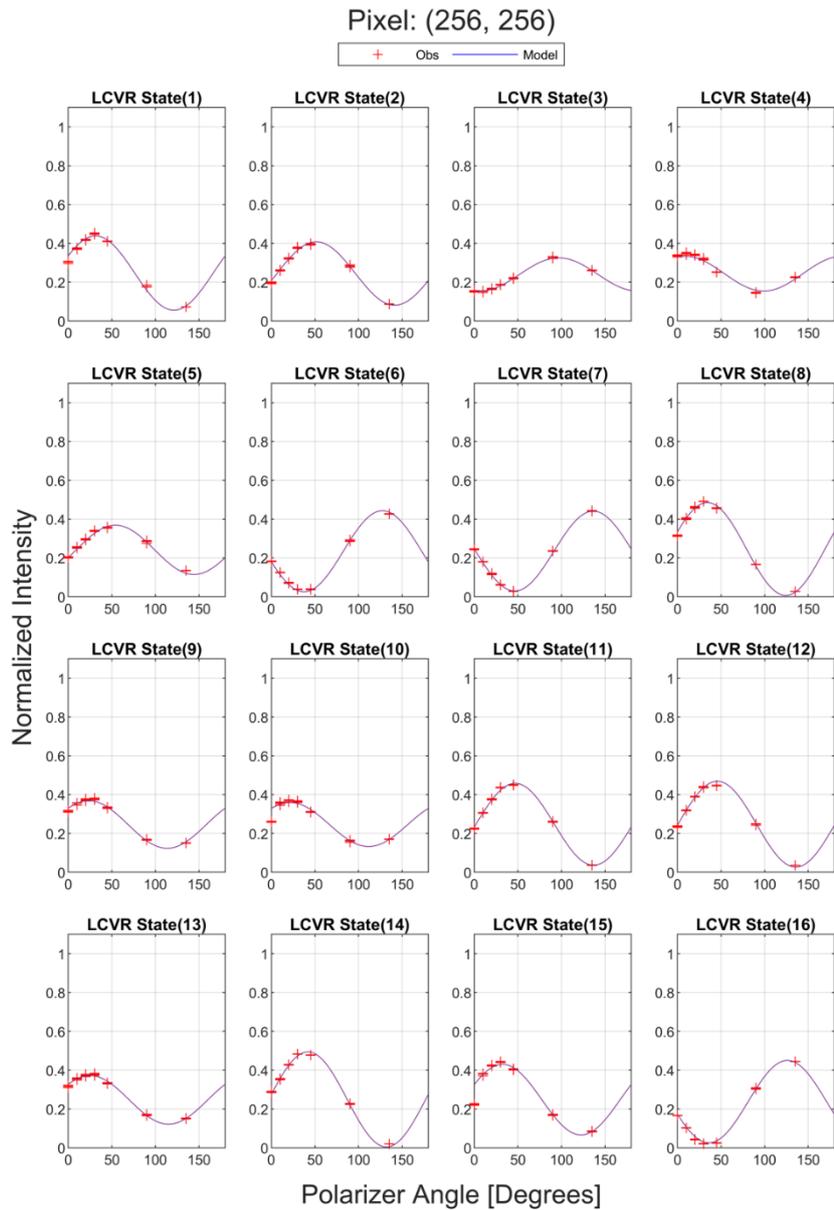
Source: Author.

Below are listed, according to BASS (2010), the Mueller matrices for the optical elements used:

- General linear retarder:

$$\begin{pmatrix} 1 & M12 & M13 & M14 \\ M21 & cos^2(2\theta) + sin^2(2\theta)\cos(\delta) & \cos(2\theta)\sin(2\theta)(1-\cos(\delta)) & \sin(2\theta)\sin(\delta) \\ M31 & \cos(2\theta)\sin(2\theta)(1-\cos(\delta)) & cos^2(2\theta)\cos(\delta) + sin^2(2\theta) & -\cos(2\theta)\sin(\delta) \\ M41 & -\sin(2\theta)\sin(\delta) & \cos(2\theta)\sin(\delta) & \cos(\delta) \end{pmatrix} \quad (7.2)$$

Where θ is the angle of the fast axis and δ is the phase difference between the fast and slow axis.

The elements, M12, M13, M14, M21, M31, and M41, were calculated using the calibration of a measurement sequence where **S** and **S'** were known, as described by DROUILLARD II et al. (2004).

- Linear Polarizer (horizontal transmission):

$$\frac{1}{2}\begin{pmatrix} 1 & 1 & 0 & 0 \\ 1 & 1 & 0 & 0 \\ 0 & 0 & 0 & 0 \\ 0 & 0 & 0 & 0 \end{pmatrix} \quad (7.3)$$

As seen in Equation 7.2 and Equation 7.3, each Mueller matrix has parameters that need to be calculated. For M0, it is necessary to calculate the delay and inclination with the main axis. For M1 and M2, the same calculation as M0 must be performed, although the calculation must be performed for each polarization state. For M3, it is necessary to calculate the orientation of the polarizer with the original beam. Since only the reference polarizer was added for testing, circular polarization is not considered. Even with the delay caused by the telescope.

Rewriting the Equation 2.15, one has the following equation.

$$\begin{pmatrix} I_{output} \\ Q_{output} \\ U_{output} \\ V_{output} \end{pmatrix} = \begin{pmatrix} M11 & M12 & M13 & M14 \\ M21 & M22 & M23 & M24 \\ M31 & M32 & M33 & M34 \\ M41 & M42 & M43 & M44 \end{pmatrix} \begin{pmatrix} I_{input} \\ Q_{input} \\ U_{input} \\ V_{input} \end{pmatrix} \quad (7.4)$$

Recalling that Stokes I consists of measures for the intensity of light. The intensity of polarized light at 0 ° / 90 ° is Q. Stokes U is the intensity of polarized light at 45 ° / 135 °. In addition, the intensity of the circularly left / right polarized light is V.

According to PATTY et al. (2018), the elements of the Mueller matrix are related to the Stokes vector in the following way:

$$\boldsymbol{M} = \begin{pmatrix} I \rightarrow I & Q \rightarrow I & U \rightarrow I & V \rightarrow I \\ I \rightarrow Q & Q \rightarrow Q & U \rightarrow Q & V \rightarrow Q \\ I \rightarrow U & Q \rightarrow U & U \rightarrow U & V \rightarrow U \\ I \rightarrow V & Q \rightarrow V & U \rightarrow V & V \rightarrow V \end{pmatrix} \quad (7.5)$$

For example, the M11 element compares the input intensity to output intensity. Therefore, this element can be interpreted as a simple transmittance. Moreover, the M12 element relates the linear polarization at 0°/90° to the output intensity. Hence, one can interpret M12 as the linear ratio of input to output light intensity at 0°/90°.

Figure 7.13 shows the polarization circle resulting from Mueller's matrix. There is only one Mueller Matrix for M0. Each pixel shows the maximum intensity, and each panel represents a coefficient of M0. Here some elements are symmetrical, and others are asymmetric. Diagonally, M22 is approximate -M33. Besides, M23 $\cong$ M32, M24 $\cong$ -M42, and M34 $\cong$ -M43.

Figure 7.13 Mueller Matrix image for M0.
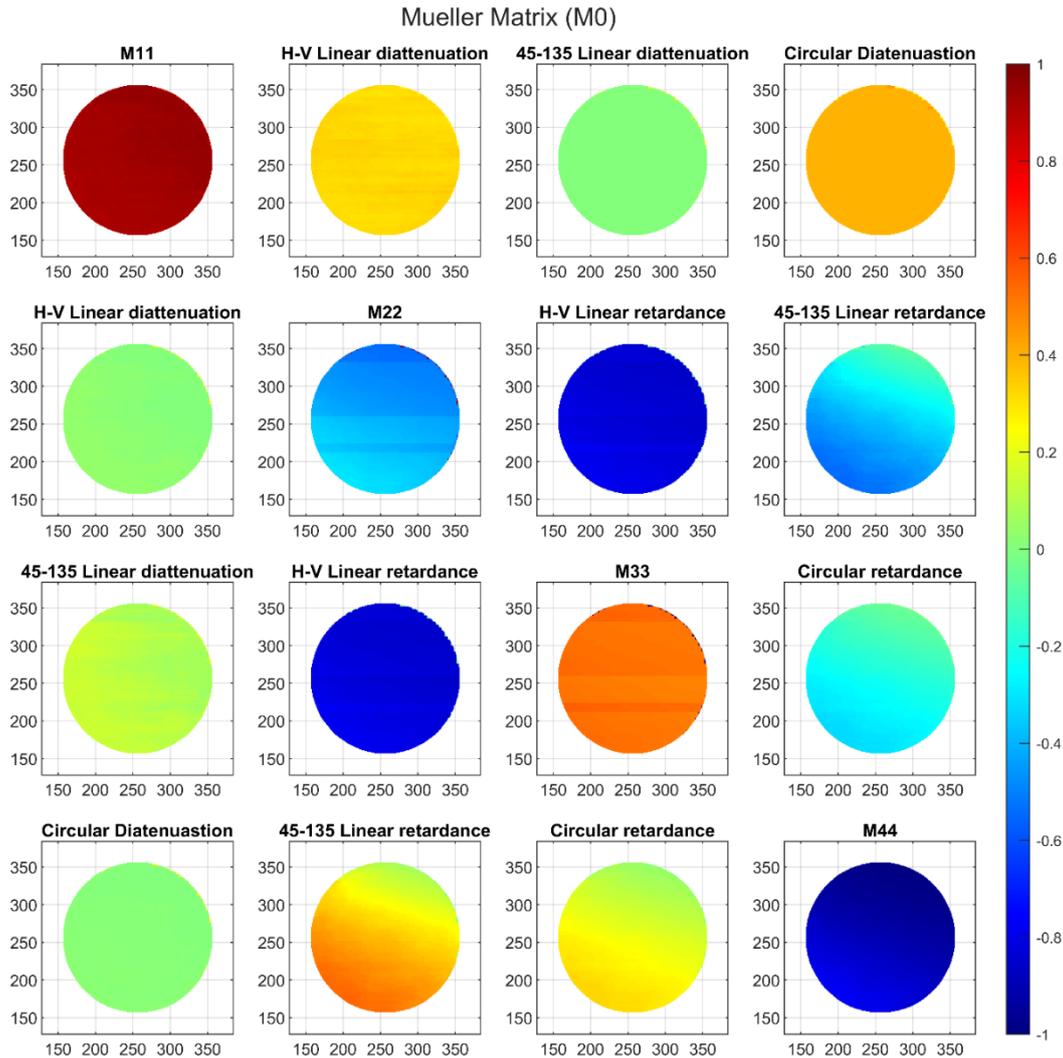
Source: Author.

It is important to remember that M0 represents a set of several optical elements. Ideally, it should not present diattenuation, retardance, or depolarization. The elements that represent the diattenuation do not have their intensity varying significantly from zero, except for M14. However, some values differ significantly from zero for linear retardance and considerable for circular retardance. The telescope introduced this retardance.

Another interesting point that Figure 7.13 shows are the gradients present in some elements, e.g. M22, M33, M24, and M42. This is because the light beams are passing through the optical components at very different angles. The diffuser

(barium sulfate plate present in the data acquisition) was not correctly aligned. The gradients are not desirable, so one has to work to make each matrix's element uniform.

M1 is the Mueller Matrix that represents the first LCVR. There are sixteen matrices for M1, one for each SoP. The images of M1 for different SoP are in ANNEX C. Two matrices (M1 [State1] and M1 [State8]) were chosen for analysis. Figure 7.14 displays M1 for polarization state 01. As expected from a retarder, M1 introduces a retardance, and the same symmetries observed in M0 are found in M1 [State1]. As desirable, the diattenuation elements are uniformly zeroed. However, some elements have gradients, such as M24, M42, M34, and M43

Figure 7.14 Mueller Matrix image for M1 State 01.
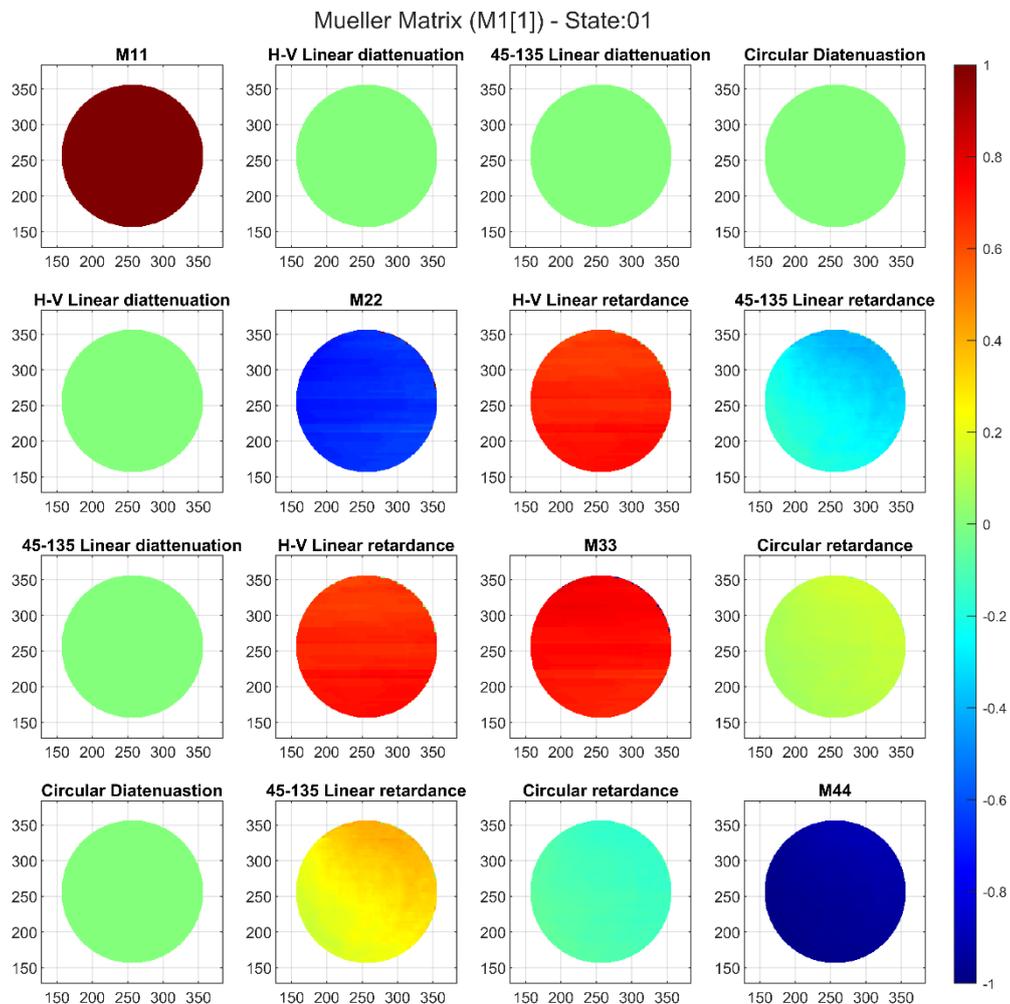
Source: Author.

Figure 7.15 shows M1 for SoP 8. Except for some elements having a gradient, M1[State8] behaves like a Mueller Matrix of an ideal component, which is not desirable. As a retarder, the first LCVR should introduce retardance in the polarization of light.

Figure 7.15 Mueller Matrix image for M1 State 08.

Mueller Matrix (M1[8]) - State:08
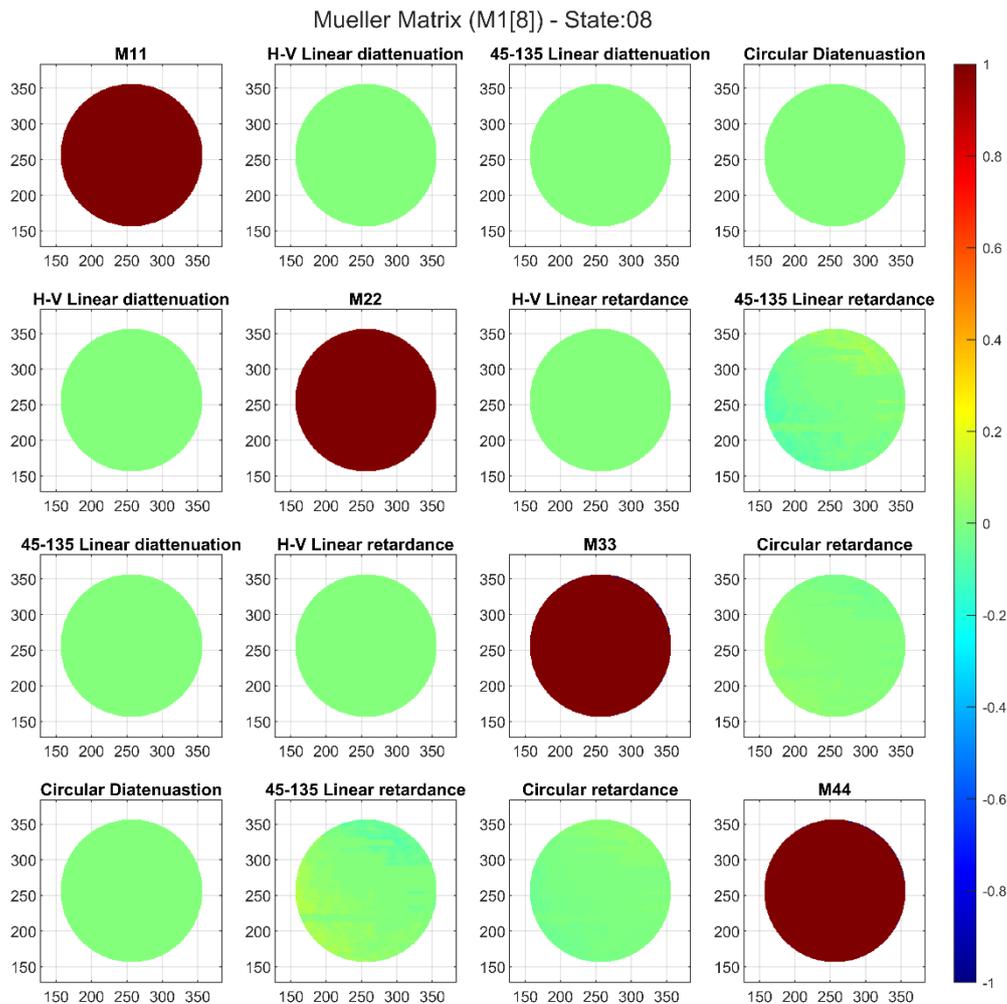
Source: Author.

Similar to M1, there are sixteen matrices for M2, one for each SoP. Figures 7.16 and 7.17 show the images of Mueller's Matrix for the second LCVR with SoP 01 and 08, respectively. As desired, for both SoPs, one can notice the presence of retardation and gradient, and the absence of diattenuation. One can also remark the different values of intensities for the same element where you can even change the polarization signal, e.g. M22. An interesting point is that M2 [8]

121

has the same symmetry as M0 (M22 ≅ -M33, M23 ≅ M32, M24 ≅ -M42, and M34 ≅ -M43), while M2 [1] does not. The images of M2 for the other SoP are in ANNEX D.

Figure 7.16 Mueller Matrix image for M2 State 01.
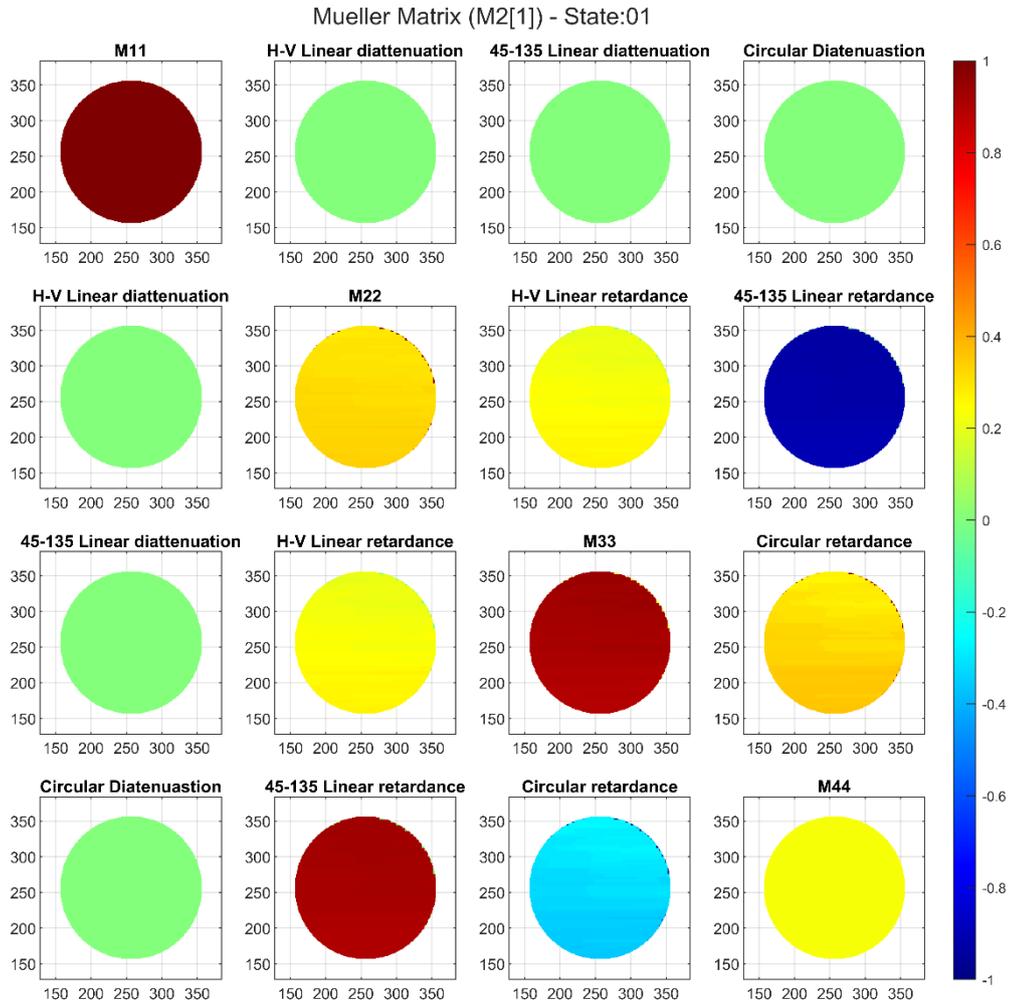
Source: Author.

Figure 7.17 Mueller Matrix image for M2 State 08.

Mueller Matrix (M2[8]) - State:08
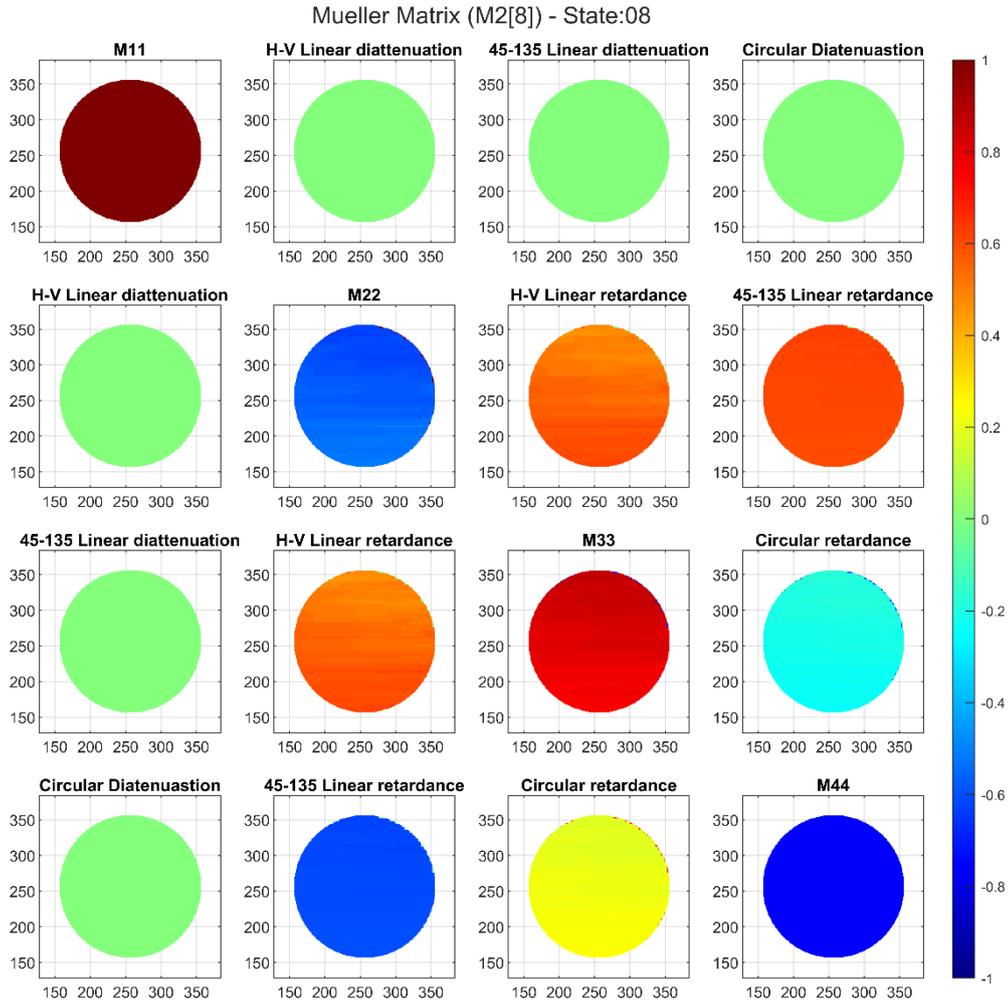
Source: Author.

Figure 7.18 display the resulting Mueller Matrix of M2[1] . M1[1] . M0. Here, in addition to M0, there are effects caused by the liquid crystals. As expected, there is a retardance, and some elements do not have uniform intensities. One can also see that in the first line, the elements have a high diatenuation as M0.

Figure 7.18 Mueller Matrix image for M2 [1] X M1 [1] X M0.
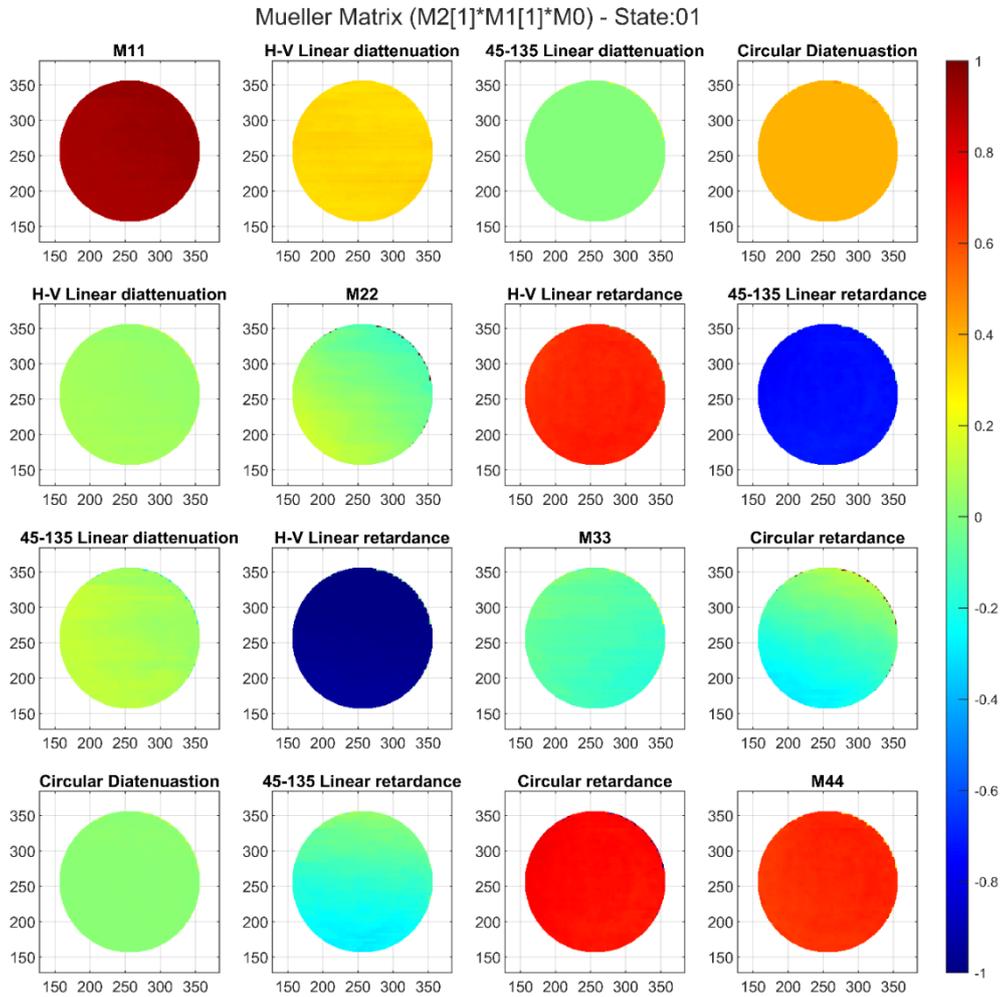
Source: Author.

The complete Mueller matrix of the instrument is the multiplication of each matrix, M3.M2.M1.M0. Figure 7.19 shows the Mueller matrix of the instrument for the first state of polarization, M3.M2[State1].M1[State1].M0. As expected, when the polarizer matrix (M3) is included, the intensities value is halved, including M11. And the last two lines have their elements with values close to zero. The images of M3.M2.M1.M0 for the other SoP are in ANNEX E.

Figure 7.19 Mueller Matrix image for the instrument (M3 X M2[1] X M1[1] X M0).

Mueller Matrix (M3*M2[1]*M1[1]*M0) - State:01
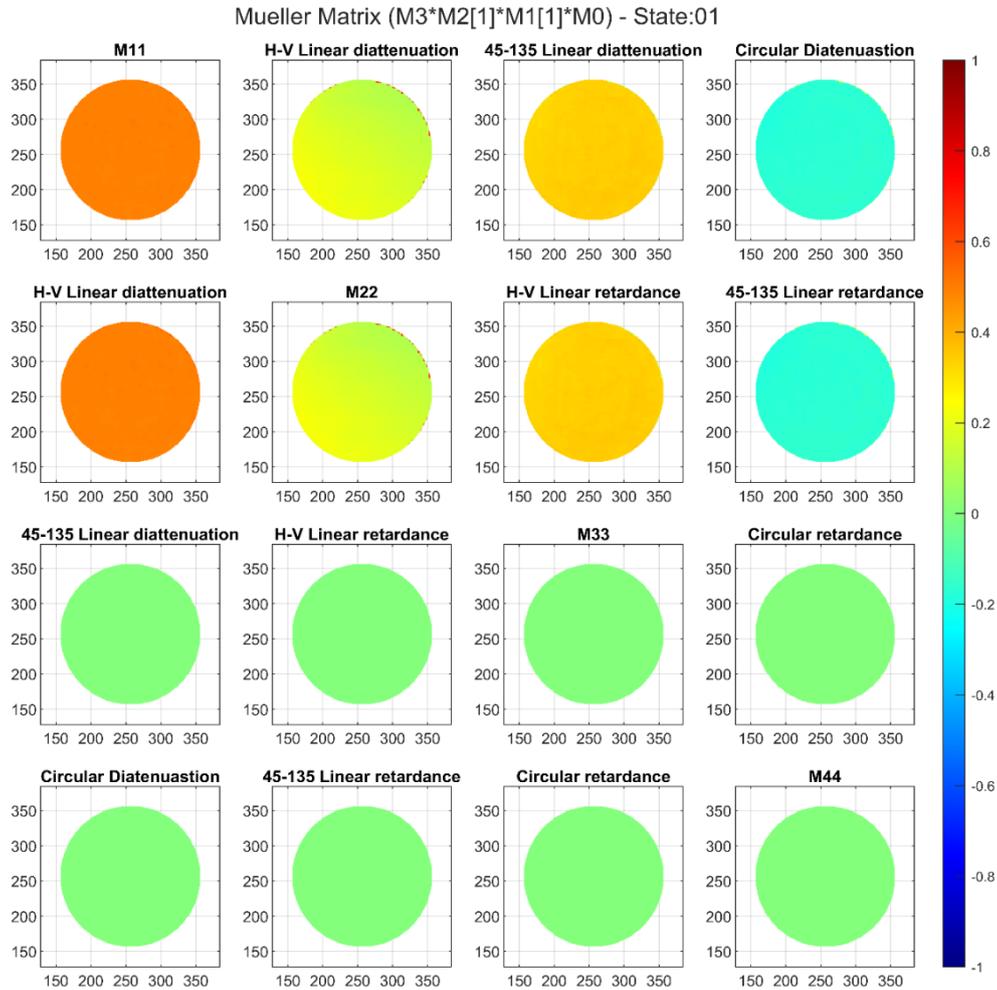
Source: Author.

Figure 7.20 shows in each panel the Poincaré sphere for a single-pixel (256x256) for a given Mueller Matrix. The red line describes the change in the polarization of a beam of light as it passes through the component. The axes S1, S2, and S3 represent Stokes parameters Q, U, and V, respectively. S1 expresses the horizontal and vertical linear polarization. S2 is linear polarization at + or - 45 degrees, and S3 represents circular polarization.

The first panel shows the Poincaré sphere of M0. The second displays the sphere of the matrix obtained by multiplying M1 [State12] and M0. The third panel expresses the Poincaré sphere for the matrix resulting from the multiplication of M2 [State12], M1 [State12], and M0. The red circle around the sphere shows on

the three panels that the polarization is elliptical. The red ring underneath is just a projection. In all the panels, one can notice the presence of circular polarization. Without the effect of this, the red line would be on the plane of S1 and S2. Stokes S3 = V is presented by the slope of the red circle. For the matrix obtained by multiplying M3, M2, M1, and M0, the 3D representation of the polarization would be a vector in the direction of S1, owning only the linear horizontal e vertical component of the polarization.

Figure 7.20 Poincaré sphere for a single-pixel (256x256) for different matrices. The first panel shows the sphere for M0. The second panel displays the Poincaré sphere for the matrix resulting from the multiplication of M1 [State12] with M0. The third panel represents the sphere of the matrix obtained by multiplying M2 [State12], M1 [State12], and M0. The axes represent Stokes parameters, S1 = Q, S2 = U, and S3 = V.
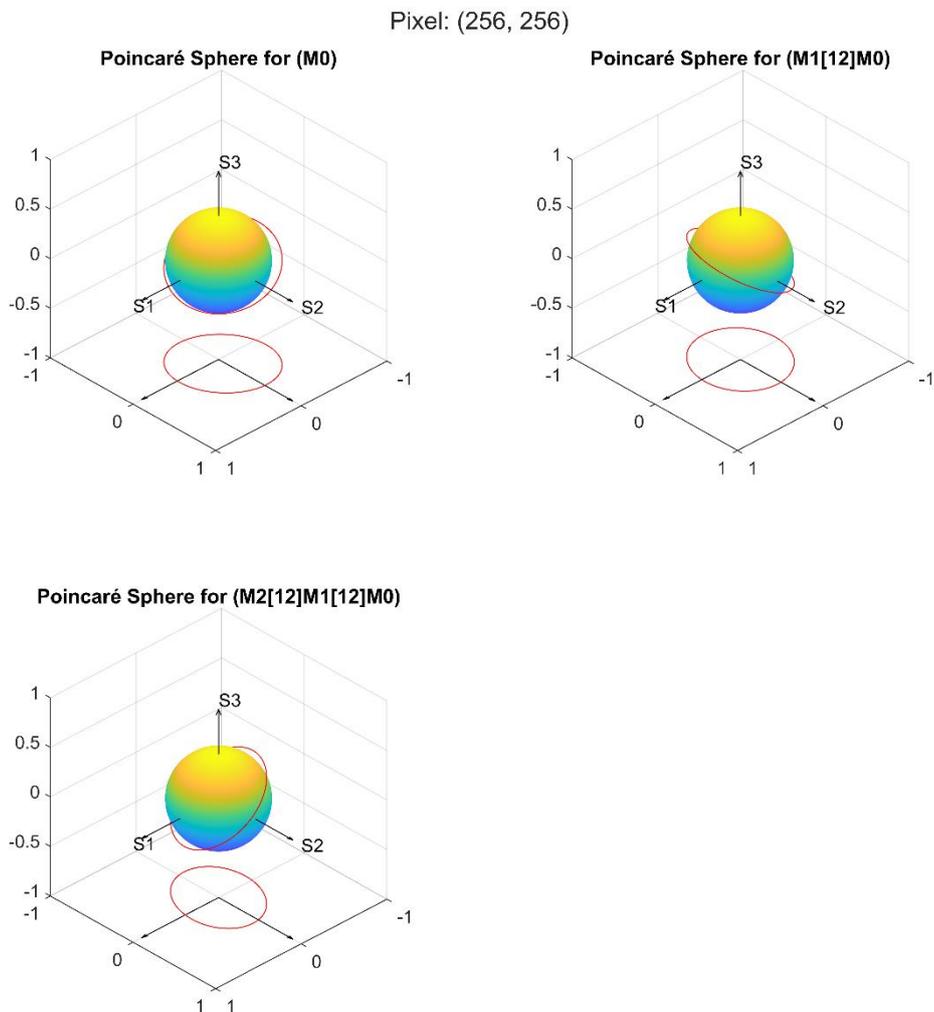
Source: Author.

7.2.3 LCVR's response to voltage variation

In the data presented in Section 7.2.1 and Section 7.2.2, the voltage selection of the liquid crystal was carried out randomly. Therefore, the voltage behavior of LCVR was studied to find the best combination for the polarization states.

Figure 7.21 displays the LCVR's retardance response to the voltage provided by the manufacturer. Both LCVRs are from the same manufacturer and model but have a slightly different voltage response.

Figure 7.21 LCVR retardance response to voltage variation.
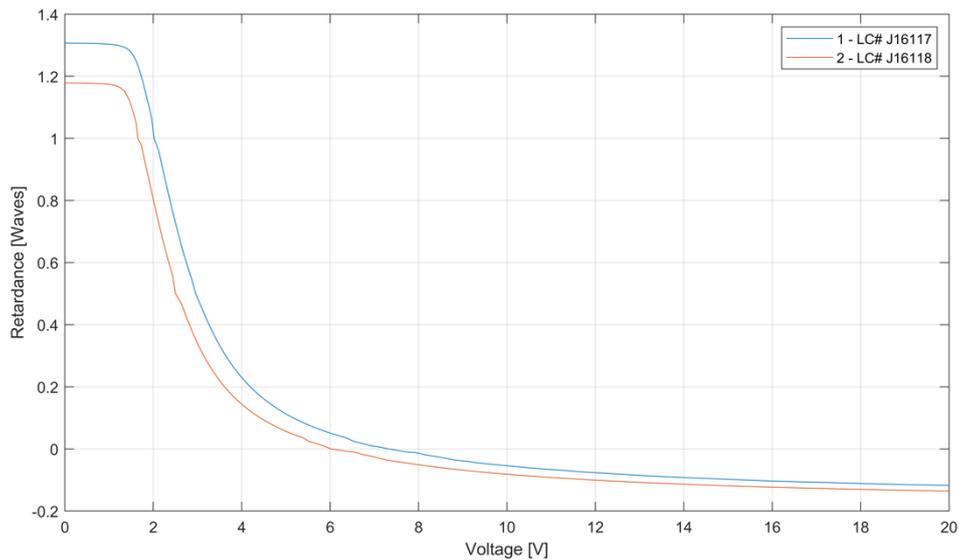
Source: Meadowlark Optics (2021).

Figure 7.22 shows the behavior of a light beam when it passes through the polarization package. The first LCVR has a constant retardance, while the voltage varies to the second LCVR. The angle of the linear polarizer also varies. For the first panel, the voltage of the first liquid crystal is kept constant at 3.35V. As the voltage of the second liquid crystal and the angle of the linear polarizer change, one can see a small shift at the normalized intensity. On the second panel, the voltage of the LCVR1 remains constant at 6.03V. This image serves as a reference to observe the intensity variation for different parameters of the polarization package. When the image is uniform, it means that there is no variation in the intensity, even with changes in the polarization package. In this

127

case, the light is circular polarized and it is possible to measure the circular polarization.

Figure 7.22 Change in the polarization for a light beam when it passes through a constant LCVR, a second LCVR, and a linear polarizer. The color bar shows the polarization intensity.
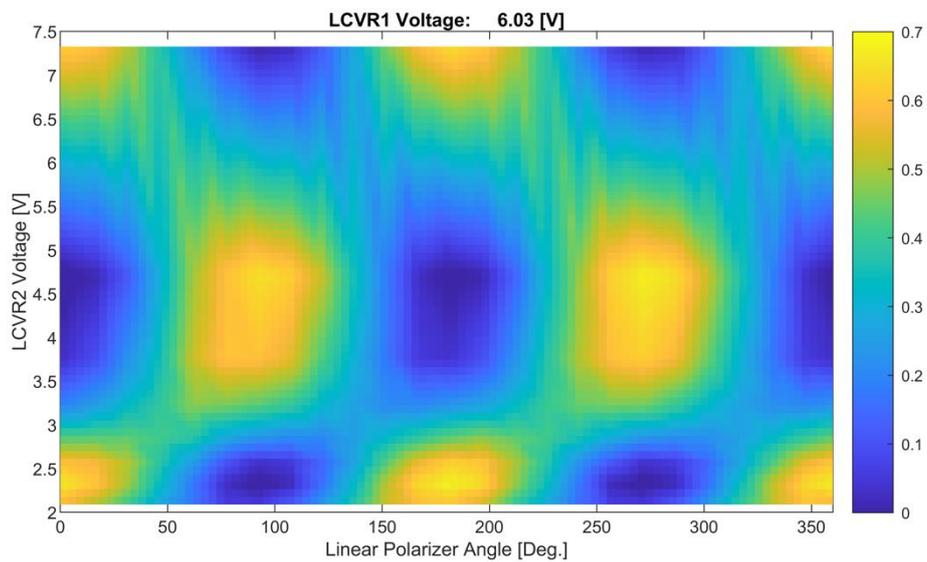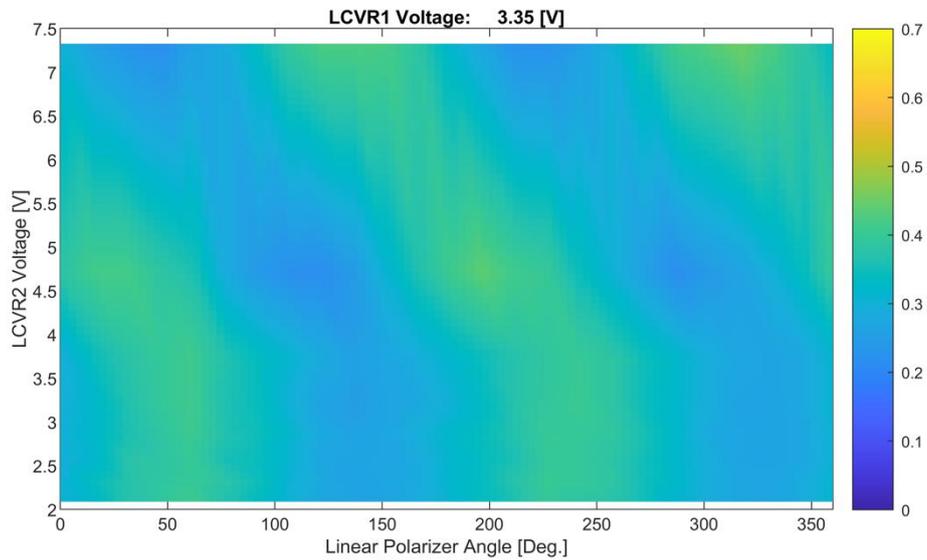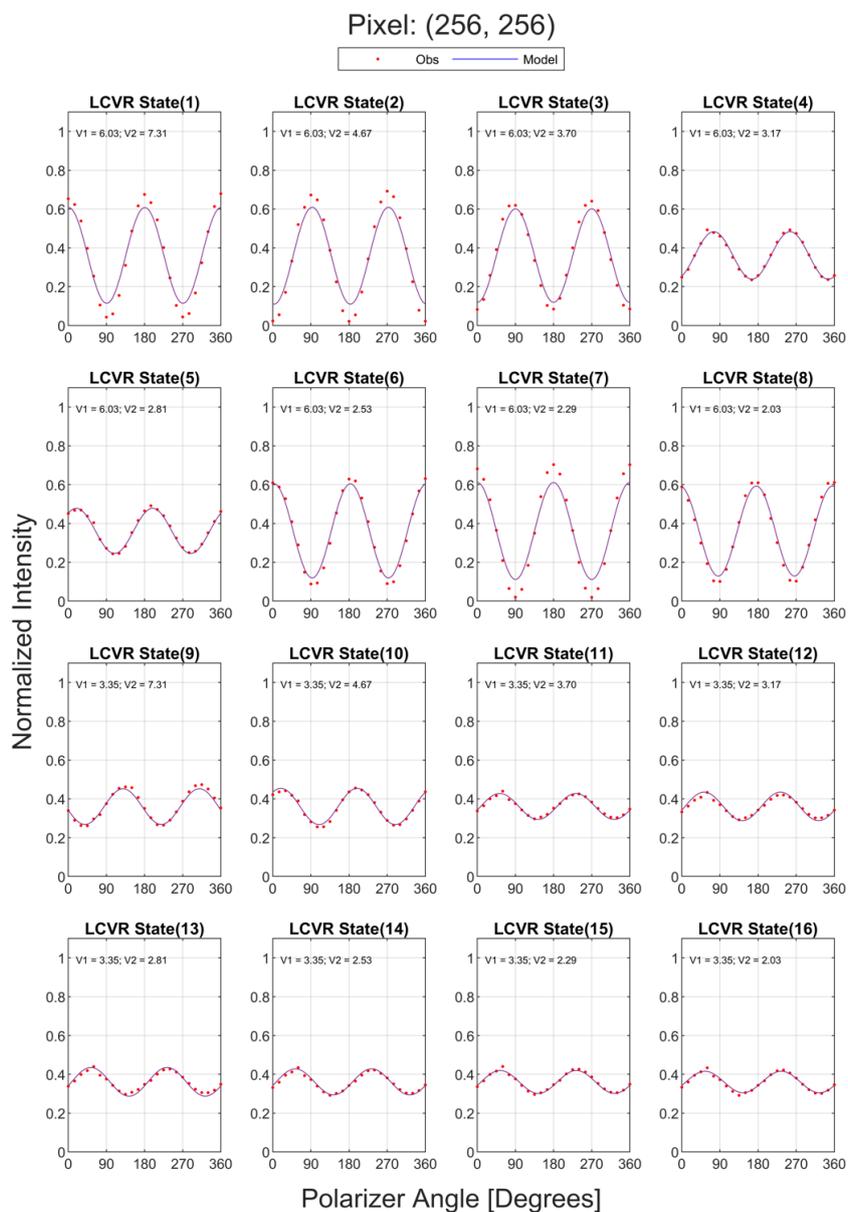

Source: Author.

Figure 7.23 displays the response for the observed data and for the model of the polarization states to the new voltages. A new scan was done every 15

degrees of the reference polarizer. The first eight panels (State 1-8) show the model's behavior with the LCVR1's voltage constant at 6.03V and the retardance is close to zero for LCVR1. The last eight panels (State 9-16) show the model's behavior with the first LCVR's voltage constant at 3.35V and the retardance is close to 1/4 for LCVR1. A new scan was done for every 15 degrees of the reference polarizer. As the retardance is not precisely 1/4, one can see that the polarization is elliptical. The polarization will be circular when the retardance is 1/4 in the LCVR1. Consequently, states 9 to 16 in would be uniform.

Figure 7.23 Model behavior for new voltages applied to LCVRs.

Source: Author.

8   RECONSTRUCTION OF IMAGES BY STATE OF POLARIZATION

Due to the situation caused by the COVID 19 pandemic, it was not feasible to acquire data with sunlight using PCPS. To overcome this limitation, we simulated the system's response as input the observation provided by HMI/SDO instrument.

While PCPS employs a tunable filter, HMI/SDO images of the solar disk using five filters across the 6173 Angstroms spectral line (Fe I absorption line). Figure 8.1 shows the spectral response of the HMI filters. For each filtergram, the Stokes parameters are estimated by the HMI Science team.

Here, we employed observations of a sunspot in the active region AR 12790 observed on 2020/12/06. Figure 8.2 shows the solar full-disk estimates of the Stokes parameter for the filtergram at the central wavelength. On the panel referring to the Stokes I, one can see a sunspot. In the panel referring to the Stokes V, one can notice the active regions.

Figure 8.3 shows the relationship of Stokes parameters with the positions of the HMI filters. In the vertical, there are five different wavelengths for the HMI filters. In the horizontal, one can see the Stokes I, Q, U, and V. One can notice that for a given Stokes parameter, there is a change in polarization within the active region when the state of the filter changes. For example, Stokes V for Filter 01 and Filter 03. This variation is welcome as it shows that the HMI instrument can process the polarization variation caused by the Zeeman Effect.

The simulation of the system's response consists of multiplying the estimated HMI Stokes parameters for the intensity of each pixel by the corresponding Mueller matrices of the PCPS. Thus, the observation results that the proof of concept would observe if it had the same configuration as the HMI when observing the solar event are simulated.

Figure 8.4 presents the synthetic images for four polarization states based on the Stokes Parameters estimated for the five HMI/SDO filtergrams. Each panel shows the data that the proof of concept would measure. The image intensity depends on the wavelength, magnetic field strength, and direction. Consequently, the magnetic field in the sunspot leads the large variations across the images. Positive and negative variations about the average indicate that the

PCPS encodes the polarization effects due to the Zeeman splitting. The second line panels illustrate the wavelength change in the intensity corresponding to the right and left circular polarization. Furthermore, structures nearby the sunspot in the same active region exhibit the same behavior.

Complementary, Figure 8.5 displays the simulation of all PCPS' polarization states with a single HMI's wavelength (Filter 01). One can notice that in all polarization states of the PCPS, there are changes in the polarization intensity in the sunspot and other structures in the active region. The Figures for the other HMI wavelength are presented in ANNEX F. Changes in the intensity due to the sunspot's polarization effects and nearby structures are present in all LCVRs states.

From this analysis, we can conclude that the PCPS consistently encodes the Zeeman splitting's polarization effects. Consequently, the Stokes parameters can be obtained by comparing the model's output and the observations.

Figure 8.1 One possible configuration of the HMI filters at five positions across the spectral line. The black dashed lines give the HMI filter transmission profiles at 8.6 pm tuning spacing. The solid black line shows the outline of the solar spectrum.
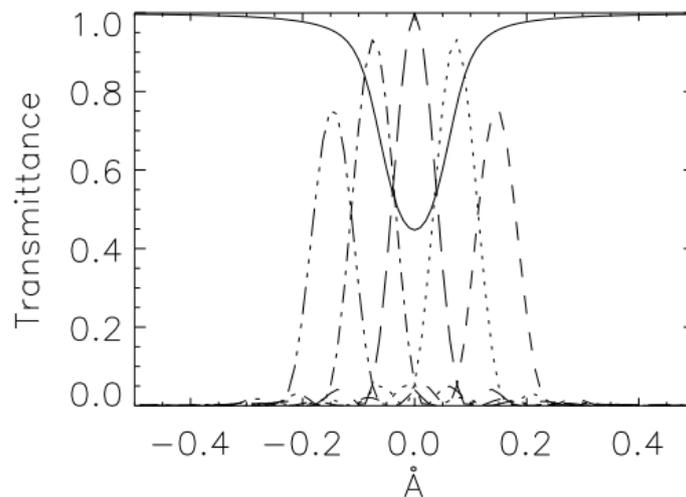
Source: Norton *et al.* (2006).

Figure 8.2 Fill-disk Estimates of the Stokes parameters for the central wavelength for 2020/12/06.
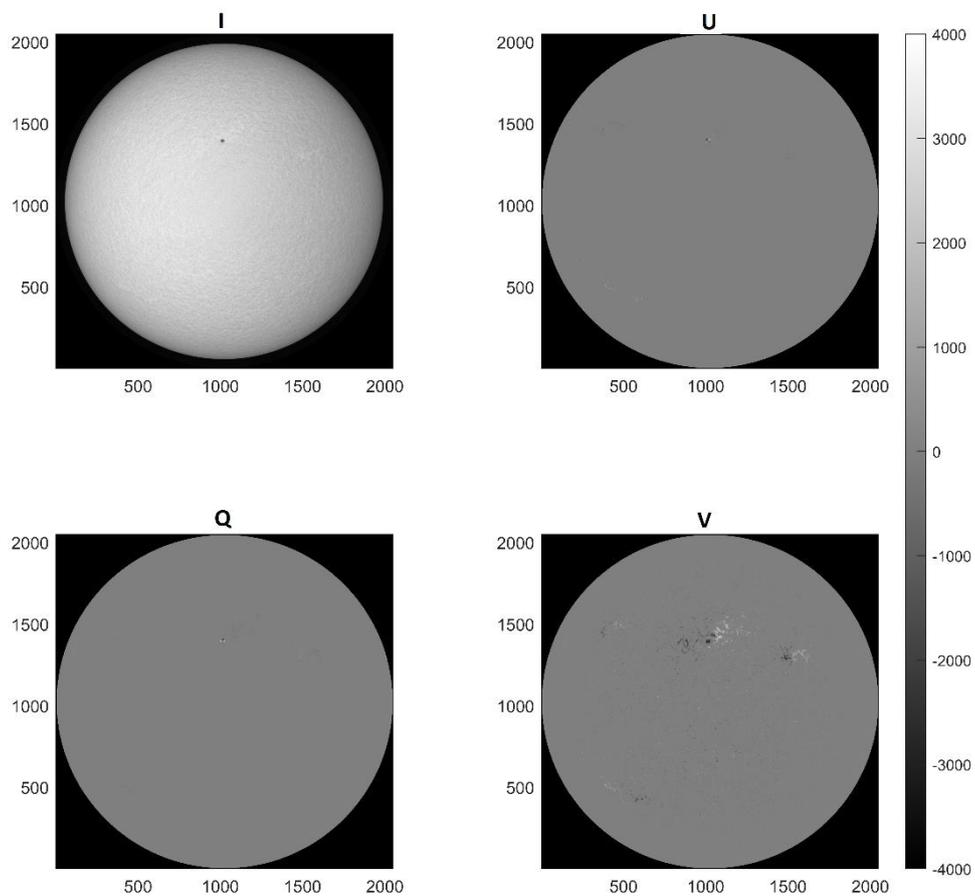
Source: Author.

Figure 8.3 Changes in Stokes parameters for different wavelengths in a region of interest. For consistency with our previous analysis, the y-axis is reversed in relation to the original HMI data.
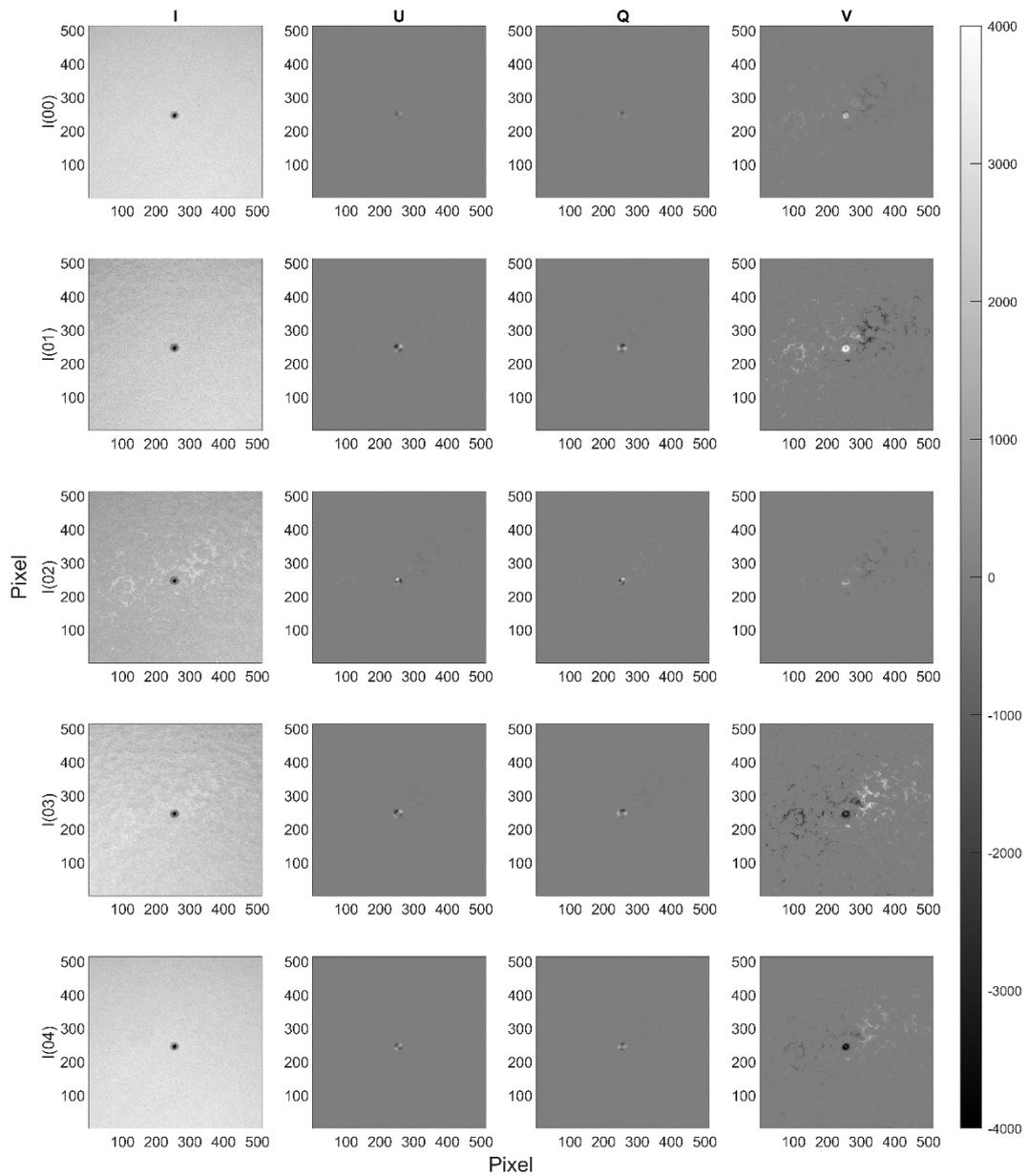
Source: Author.

Figure 8.4 Comparisons of solar event simulations. Horizontally, there are the five wavelengths of the HMI. In the vertical, there are four of the 16 polarization states of the PCPS.
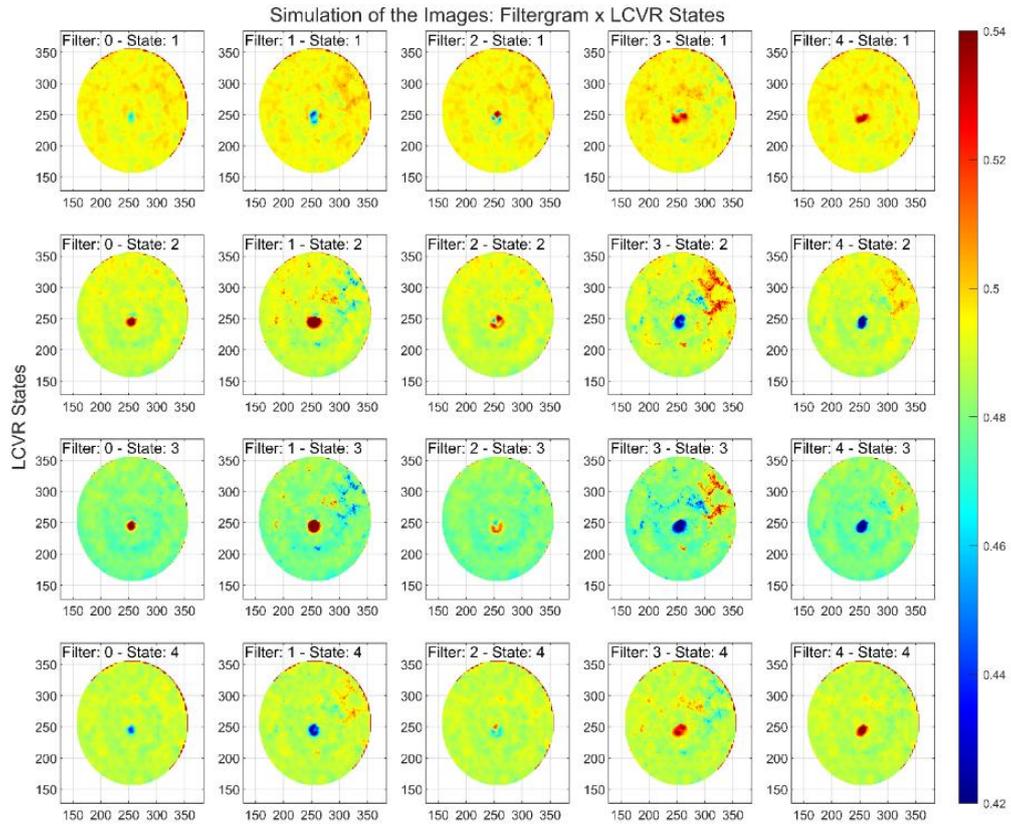
Source: Author.

Figure 8.5 Simulation for each PCPS's polarization state for HMI Filter 01.
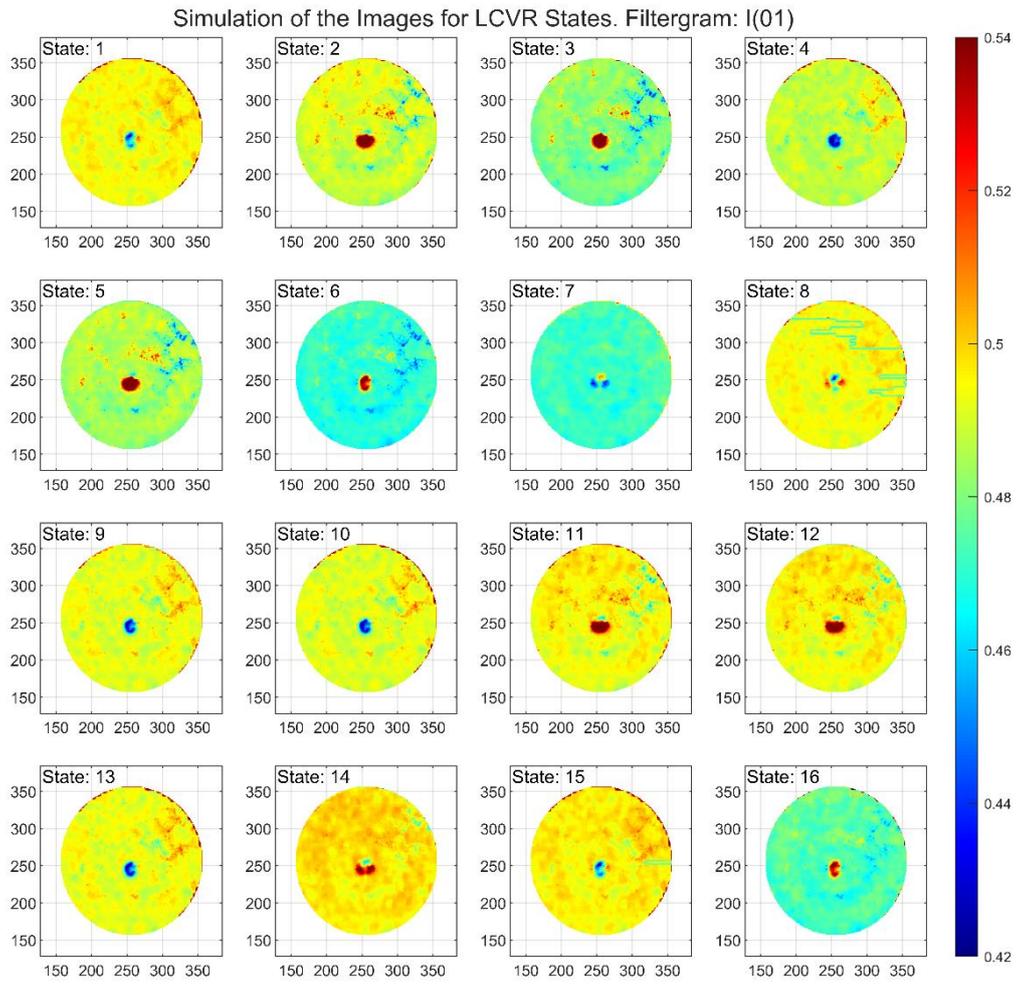
Source: Author.

9   CONCLUSION

In this work, estimation of the Stokes parameters and the uncertainties of polarimeters were studied and developed. The work analyzed the data of different polarimeters, focusing on the instrument developed at INPE, the Proof of Concept Prototype of the Spectropolarimeter (PCPS).

Many studies on the SUSI engineering model cameras and PCPS cameras were developed. Software tools based on IDL were used and developed to analyze the results of the camera characterization. The analysis includes statistical methods and visualization tools. For SUSI cameras, the edges of the sensor showed to behave quite differently from the rest of the camera. Therefore, the edges were excluded from the analyzes. Although 1% is considered significant for non-linearity, the analysis proved to be efficient. However, it is expected that the flight models have lower values of non-linearity.

For the PCPS camera, two types of Shutters (Global and Rolling) and cooling (ON and OFF) were studied, as well as two filters available in the camera itself. In all operation modes, the sensor separates the upper and lower parts due to camera readout. However, shutter Rolling (B4 and B8) obtained better results than Global (B2 and B6), with less standard deviation and lesser readout effect. There is no significant difference between the results obtained for the data acquired with Cooling ON or OFF. The 2-3% non-linearity for POLN is high. However, due to the small amount of data, the analysis error is significant. In general, more data within the linearity region has to be acquired to improve the camera characterization.

The SOT / Hinode image calibration showed the importance of each step on the sensor performance, including analysis of the radiation belt and cosmic-rays that have a critical role in space instruments.

SUSI Mueller matrix was studied in a theoretical way. The focus is on how the position of the optical components interferes with the uncertainty of the instrument. We estimated the PCPS Mueller matrix for each pixel, and the model presented an excellent response to the observed data. Since the angles of

incident light beams differ from pixel to pixel, the study showed the importance of calculating the Mueller matrix for each pixel.

To validate the PCPS Mueller matrix, we applied it to data. The ideal would be the application in data obtained by itself with sunlight. However, due to the pandemic, it was not feasible to use PCPS to acquire data with sunlight. Thus, a simulation using data from the HMI / SDO was carried out. The results show that in all polarization states, the intensity changes due to the polarization effect of sunspots and other magnetic field features in the photosphere. It means that the PCPS can encode the Zeeman splitting's polarization effects.

9.1   Suggestions for future work

- Collect more data to characterize the PCPS camera, with more exposure time, and within the linear range.

- Perform the characterization of the entire sensor area.
- Acquire data using sunlight with PCPS.
- Add a reference retarder to the proof-of-concept optical path using the newly purchased rotational 60mm cage mounting.
- Acquire data with PCPS using a known source of light with the reference polarizer and retarder.
- Calculate the Mueller Matrix for the new data.
- Apply new Mueller Matrix to data.

REFERENCES

ANDOR. **Zyla sCMOS**: speed and sensitivity for physical science imaging and spectroscopy. Belfast: Andor, [S.d.].

BASS, M. **Handbook of optics**: geometrical and physical optics, polarized light, components and instruments. 3.ed. [S.l.]: McGraw-Hill, 2010.

BIGAS, M. et al. Review of CMOS image sensors. **Microelectronics Journal**, v. 37, n. 5, p. 433–451, 2006.

BOTHMER, V.; DAGLIS, I. A. **Space weather**: physics and effects. Berlin: Springer, 2007.

Carlesso, F. **Relative spectral power as a function of the wavelength of the Philips Neon lamp**. [mensagem pessoal]. Mensagem recebida por <adriany.rbarbosa@gmail.com> em 02 fev. 2021.

CHOUDHURI, A. R. An elementary introduction to solar dynamo theory. **AIP Conference Proceedings**, v. 919, n. 1, p. 49–73, 2007.

COLLADOS, M. *et al.* GRIS: the GREGOR infrared spectrograph. **Astronomische Nachrichten**, v. 333, n. 9, p. 872–879, 2012.

COUVIDAT, S. *et al.* Wavelength dependence of the Helioseismic and Magnetic Imager (HMI) instrument onboard the Solar Dynamics Observatory (SDO). **Solar Physics**, v. 275, n. 1/2, p. 285–325, 2012.

Dal Lago, A. **Imagem Heliostato**. [mensagem pessoal]. Mensagem recebida por <adriany.rbarbosa@gmail.com> em 02 mar. 2021.

DE PONTIEU, B. *et al.* The Interface Region Imaging Spectrograph (IRIS). **Solar Physics**, v. 289, n. 7, p. 2733–2779, 2014.

DEL TORO INIESTA, J. C.; RUIZ COBO, B. Inversion of the radiative transfer equation for polarized light. **Living Reviews in Solar Physics**, v. 13, n. 1, p. 1–84, 2016.

DEL TORO INIESTA, J. C. **Introduction to spectropolarimetry**. Cambridge: Cambridge University Press, 2003.

DROUILLARD II, T. F. *et al.* Polarimetry using liquid crystal variable retarders. **Emerging Optoelectronic Applications**, v. 5363, p. 86–97, 2004.

FELLER, A. *et al.* Fast solar polarimeter : description and first results. In: NAGENDRA, K.N.; STENFLO, J. O.; ZHONGQUAN, Q.; SAMPOORNA, M. (Ed.). **Solar polarization, 7**. [S.l.]: ASP, 2014. (ASP Conference series, 489).

FOX, M. **Quantum optics**: an introduction. [S.l]: OUP Oxford, 2006.

GANDORFER, A. *et al.* The filter imager SuFI and the image stabilization and light distribution system ISLiD of the sunrise balloon-borne observatory: instrument description. **Solar Physics**, v. 268, n. 1, p. 35–55, 2010.

GOLDSTEIN, D. H. **Polarized light**. 2.ed. [S.l.]: CRC Press, 2011.

GÓMEZ, J. M. R. **Evolution of the electron density , temperature distribution in the solar corona during solar cycles 23 and 24**. 2017. 158 f. Thesis - INPE, São José dos Campos, 2017.

GONZALEZ, N. B. **Spectropolarimetry of sunspot penumbrae.** 2006. 123 f. Thesis (Master) - Georg-August-Universität, Göttingen,2006.

HARIHARAN, P. **Basics of interferometry**. 2.ed.Sydney: Elsevier, 2007.

HOFFMAN, A.; LOOSE, M.; SUNTHARALINGAM, V. CMOS detector technology. **Experimental Astronomy**, v. 19, n. 1/3, p. 111–134, 2005.

HOWELL, S. B. **Handbook of CCD astronomy**. 2.ed. Cambridge: Cambridge University Press, 2006.

ICHIMOTO, K. *et al.* Polarization calibration of the solar optical telescope onboard Hinode. In: SAKURAI, T. (Ed.). **The Hinode mission.** [S.l.]: Springer, 2008. p. 170-207.

IGLESIAS, F. A.; FELLER, A. Instrumentation for solar spectropolarimetry: state of the art and prospects. **Optical Engineering**, v. 58, n. 8, 2019.

IGLESIAS, F. A. **Development of a high-cadence, high-precision solar imaging polarimeter with application to the FSP prototype**. 2016. 148 f. Thesis (PhD) - Technische Universität Braunschweig, Braunschweig, 2016.

JANESICK, J. *et al.* **Fundamental performance differences between CMOS and CCD imagers**. San Diego: International Society for Optics and Photonics, 2007.

JANESICK, J. *et al.* **Fundamental performance differences between CMOS and CCD imagers**. San Diego: International Society for Optics and Photonics, 2009.

JANESICK, J. *et al.* **Fundamental performance differences between CMOS and CCD imagers**. San Diego: International Society for Optics and Photonics, 2010.

JANESICK, J. **Scientific charge-coupled devices**. Bellingham: SPIE Press, 2001.

JANESICK, J.; ANDREWS, J.; ELLIOTT, T. **Fundamental performance differences between CMOS and CCD imagers**. Orlando: International Society for Optics and Photonics, 2006.

KANO, R. *et al.* The hinode X-ray Telescope (XRT): camera design, performance and operations. **Solar Physics,** v. 249, n. 2, p. 263–279, 2008.

KELLER, C. U. Recent progress in imaging polarimetry. **Solar Physics**, v. 164, n. 1/2, p. 243–252, 1996.

KOSUGI, T. *et al.* The Hinode (Solar-B) mission: an overview. **Solar Physics**, v. 243, n. 1, p. 3–17, 2007.

KRIVOVA, N. A.; SOLANKI, S. K. Models of solar irradiance variations: current status. **Journal of Astrophysics and Astronomy**, v. 29, p. 151–158, 2008.

LABSPHERE. **Technical guide**: integrating sphere uniform light source applications. 2008. Disponível em: <http://www.labsphere.com/uploads/technical-guides/a-guide-to-integrating-sphere-uniform-light-Source-applications.pdf>.

LANDSTREET, J. D. Basics of spectropolarimetry. **Proceedings of the International Astronomical Union**, v.9, n.S307, p. 311–320, 2014.

LEMEN, J. R. *et al.* The Atmospheric Imaging Assembly (AIA) on the Solar Dynamics Observatory (SDO). **Solar Physics**, v. 275, n. 1/2, p. 17–40, 2012.

LITES, B. W. *et al.* The Hinode spectro-polarimeter. **Solar Physics**, v. 283, n. 2, p. 579–599, 2013.

MAGNAN, P. Detection of visible photons in CCD and CMOS: a comparative view. **Nuclear Instruments and Methods in Physics Research, Section A: Accelerators, Spectrometers, Detectors and Associated Equipment**, v. 504, n. 1/3, p. 199–212, 2003.

MARTÍNEZ PILLET, V. *et al.* The Imaging Magnetograph eXperiment (IMaX) for the sunrise balloon-borne solar observatory. **Solar Physics**, v. 268, n. 1, p. 57–102, 2010.

MCTIER, M. A. S.; KIPPING, D. M.; JOHNSTON, K. 8 in 10 Stars in the milky way bulge experience stellar encounters within 1000 AU in a gigayear. **Monthly Notices of the Royal Astronomical Society**, v. 8, p. 1–8, 2020.

MEADOWLARK OPTICS. **Liquid crystal variable retarders**. [S.l.]: Meadowlark Optics, *[*S.d.].

MESEGUER, J. J. P. **Design and optimization of a space camera with application to the PHI solar magnetograph**. 2013. 147 f. Thesis (Master) - Technical University Carolo-Wilhelmina zu Braunschweig, Braunschweig, 2013.

NORTON, A. A. *et al.* Spectral line selection for HMI: A comparison of Fe i 6173 Å and Ni i 6768 Å. **Solar Physics**, v. 239, n. 1/2, p. 69–91, 2006.

ODENWALD, S. **The day the sun brought darkness**. Disponível em: <https://www.nasa.gov/topics/earth/features/sun_darkness.html>. Acesso em: 11 fev. 2019.

PATTY, C. H. L. *et al.* Imaging linear and circular polarization features in leaves with complete for Mueller matrix polarimetry. **Biochimica et Biophysica Acta (BBA)-General Subjects**, v. 1862, n. 6, p. 1350–1363, 2018.

QIAN, B. *et al.* Generation of vector beams using a Wollaston prism and a spatial light modulator. **Optik**, v. 148, p. 312–318, 2017.

REINHOLD, T. *et al.* The Sun is less active than other solar-like stars. **Science**, v. 368, n. 6490, p. 518–521, 2020.

RODRIGUEZ, J. M. Polarización de la luz : conceptos básicos y aplicaciones en astrofísica. **Revista Brasileira de Ensino de Física**, v. 40, n. 4, p. 10, 2018.

SANTIAGO, J. M. B. **The fine structure of the sunspot penumbra**. 2004. 149 f. Thesis (Master) - Georg-August Universität, Göttingen, 2004.

SCHMIDT, W. *et al.* The GREGOR solar telescope on Tenerife. **ASP Conference Series**, v.463, p.365-377, 2012.

SCHOU, J. *et al.* The Helioseismic and magnetic imager instrument design and calibration. **Solar Physics**, v. 275, p. 1–22, 2012.

SCHRIJVER, C. J.; ZWAAN, C. **Solar and stellar magnetic activity**. Cambridge: Cambridge University Press, 2000.

SHEKHTMAN, L.; THOMPSON, J. **Sun**: in depth. NASA Science. Disponível em: <https://solarsystem.nasa.gov/solar-system/sun/in-depth/>. Acesso em: 8 dec. 2018.

SOLANKI, S. K. *et al.* The polarimetric and helioseismic imager on solar orbiter. **Astronomy and Astrophysics,** v.643, n.A11, 2019.

STEKEL, T. R. C. **Study of magnetic structures of an arch filament system in the solar photosphere and chromosphere**. 2019. 208 f. Thesis (Doctor in Space Geophysics) - Instituto Nacional de Pesquisas Epaciais, São José dos Campos, 2019.

STENFLO, J. O. **Solar magnetic fields**: polarized radiation diagnostics. Zurich: Kluwer Academic, 1994.

STIX, M. **The sun**: an introduction. 2. ed. Berlin: Springer, 2004.

SUEMATSU, Y. *et al.* The solar optical telescope of Solar-B (Hinode): the optical telescope assembly. **Solar Physics**, v. 249, p. 197–220, 2008.

TRIPPE, S. Polarization and polarimetry: a review. **Journal of the Korean Astronomical Society**, v. 47, n. 1, p. 15–39, 2014.

TSUNETA, S. *et al.* The solar optical telescope for the hinode mission: an overview. **Solar Physics**, v. 249, n. 2, p. 167–196, 2008.

VIEIRA, L. E. et al. **Brazilian experimental solar telescope** - Galileo Solar Space Telescope. 58 slides. São José dos CAmpos: Instituto Nacional de Pesquisas Espaciais, 2016. 58 slides

WACHTER, R. *et al.* Image quality of the Helioseismic and Magnetic Imager (HMI) Onboard the Solar Dynamics Observatory (SDO). **Solar Physics**, v. 275, n. 1–2, p. 261–284, 2012.

WOODS, T. N. *et al.* Extreme Ultraviolet Variability Experiment (EVE) on the Solar Dynamics Observatory (SDO): overview of science objectives, instrument design, data products, and model developments. **Solar Physics**, v. 275, n. 1/2, p. 115–143, 2012.

ZEEMAN, P. On the influence of magnetism on the nature of the light emitted by a substance. **The Astrophysical Journal**, v. 5, p. 332–347, 1897.

ANNEX A

Figure A.1 Relative spectral power as a function of the wavelength of the Philips Neon lamp.
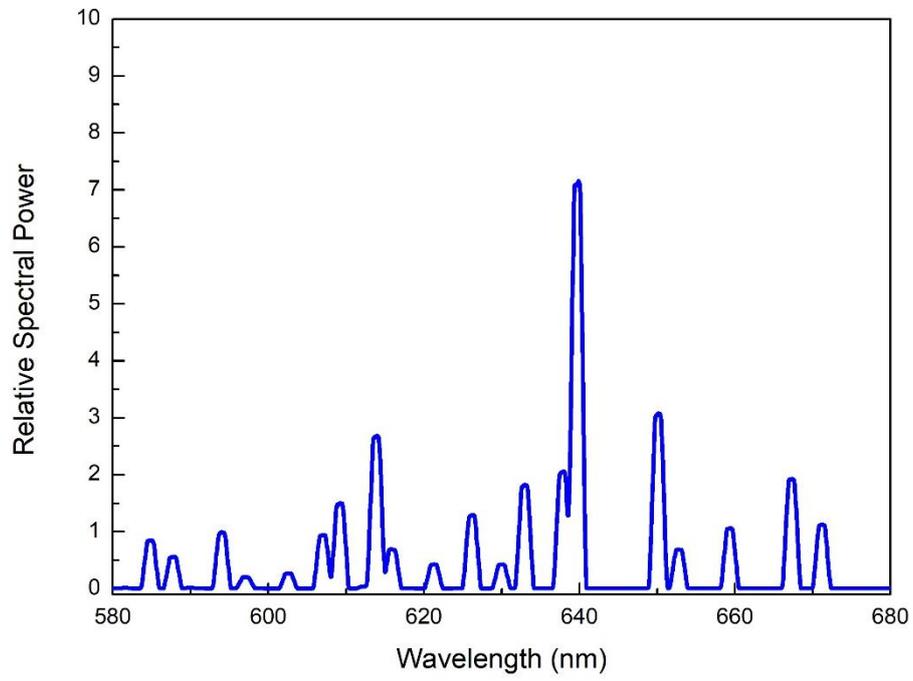
Source: Carlesso (2021).

ANNEX B

Figure B.1 Maximum normalized intensity for each state of polarization. Reference polarizer at 10°.
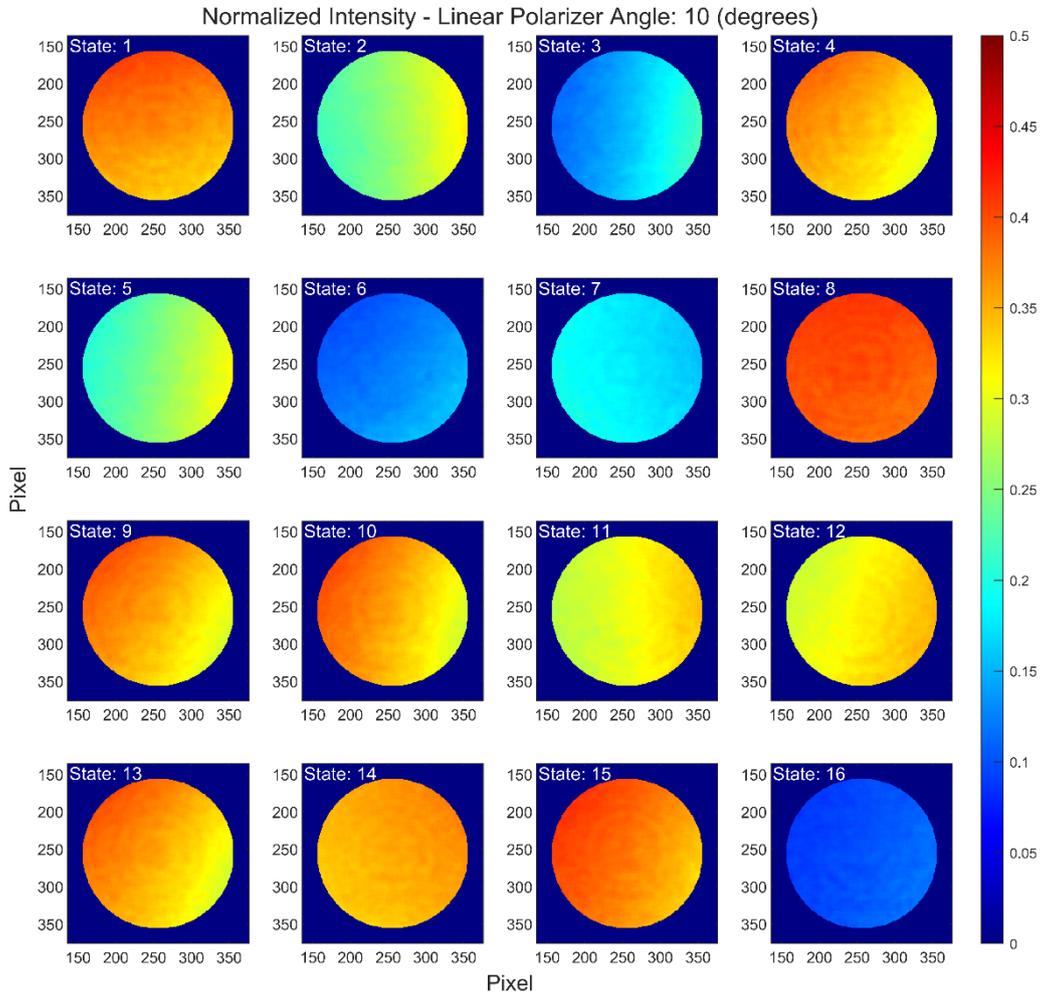
Source: Author.

Figure B.2 Maximum normalized intensity for each state of polarization. Reference polarizer at 20°.
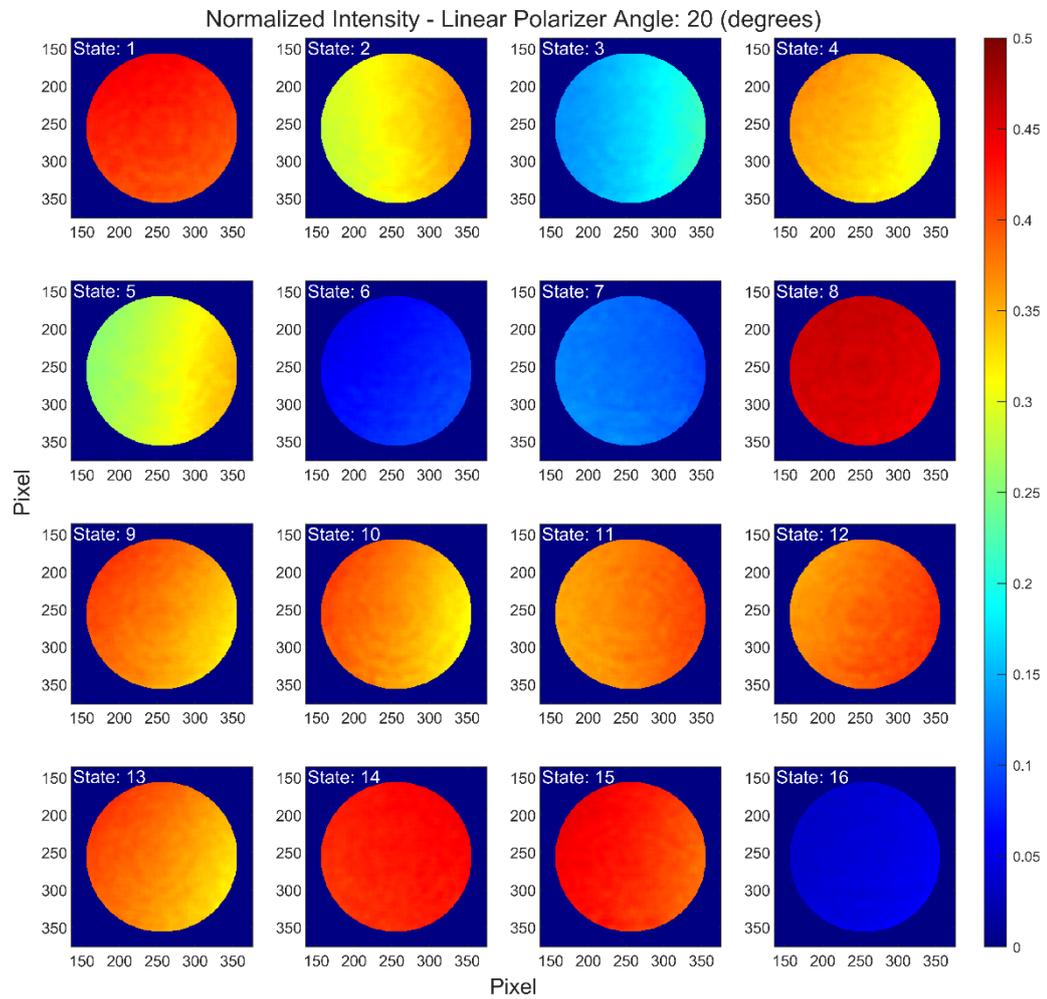
Source: Author.

Figure B.3 Maximum normalized intensity for each state of polarization. Reference polarizer at 30°.

Source: Author.

Figure B.4 Maximum normalized intensity for each state of polarization. Reference polarizer at 45°.
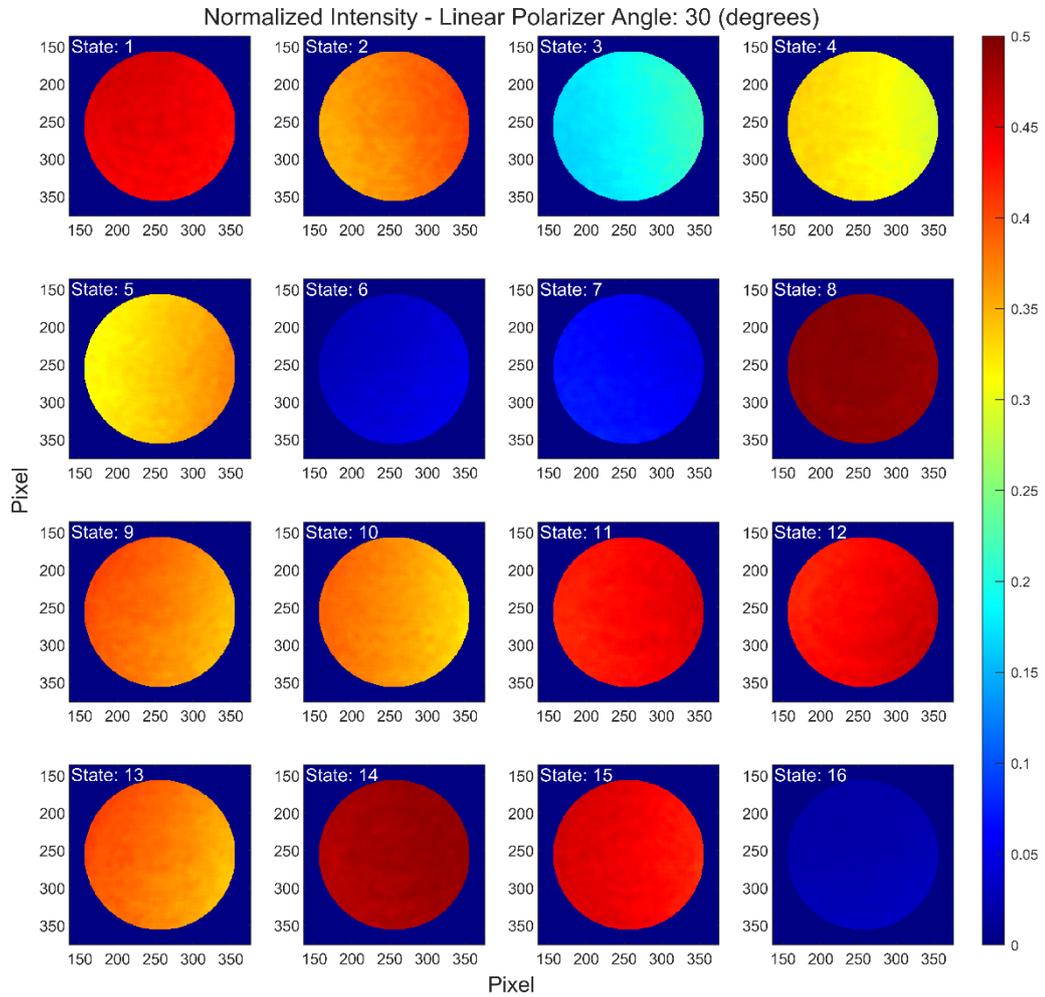
Source: Author.

Figure B.5 Maximum normalized intensity for each state of polarization. Reference polarizer at 90°.
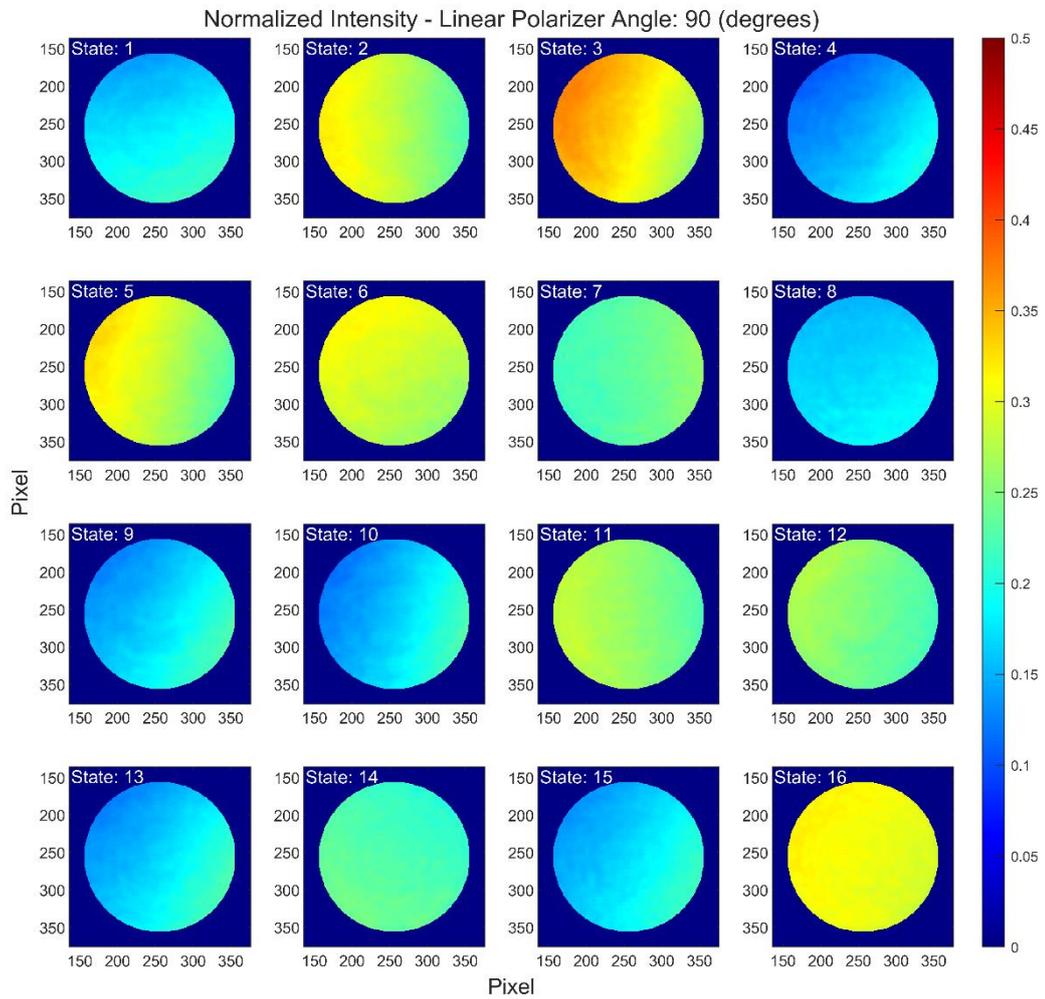
Source: Author.

Figure C.1 Mueller Matrix image for M1 State 02.

Mueller Matrix (M1[2]) - State:02
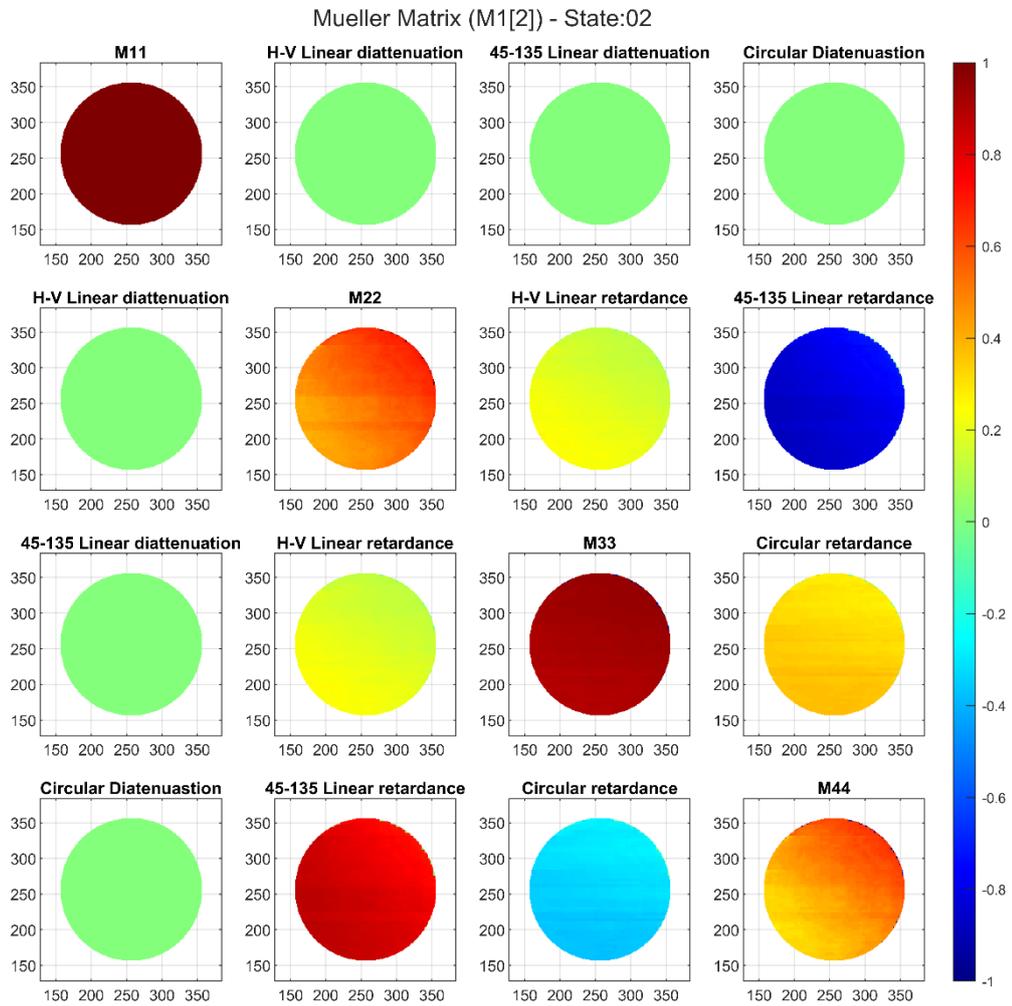
Source: Author.

Figure C.2 Mueller Matrix image for M1 State 03.
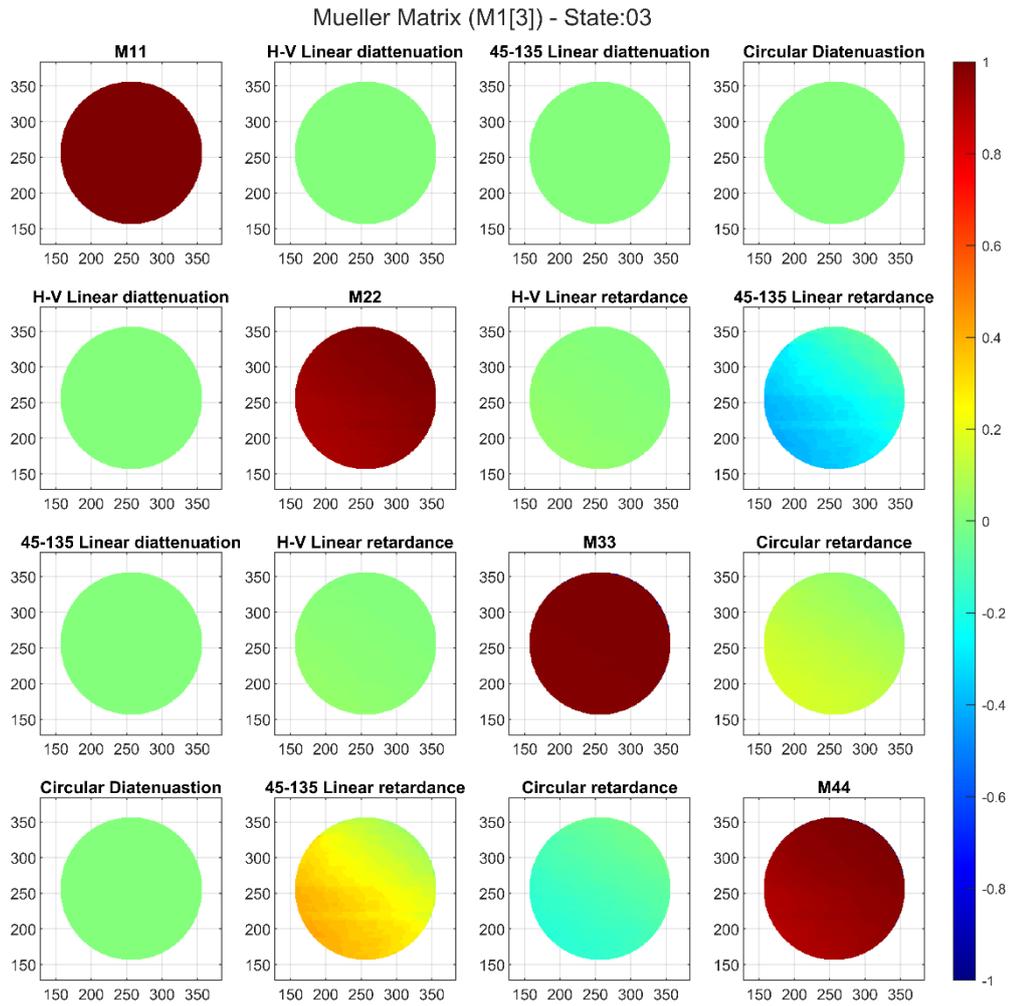
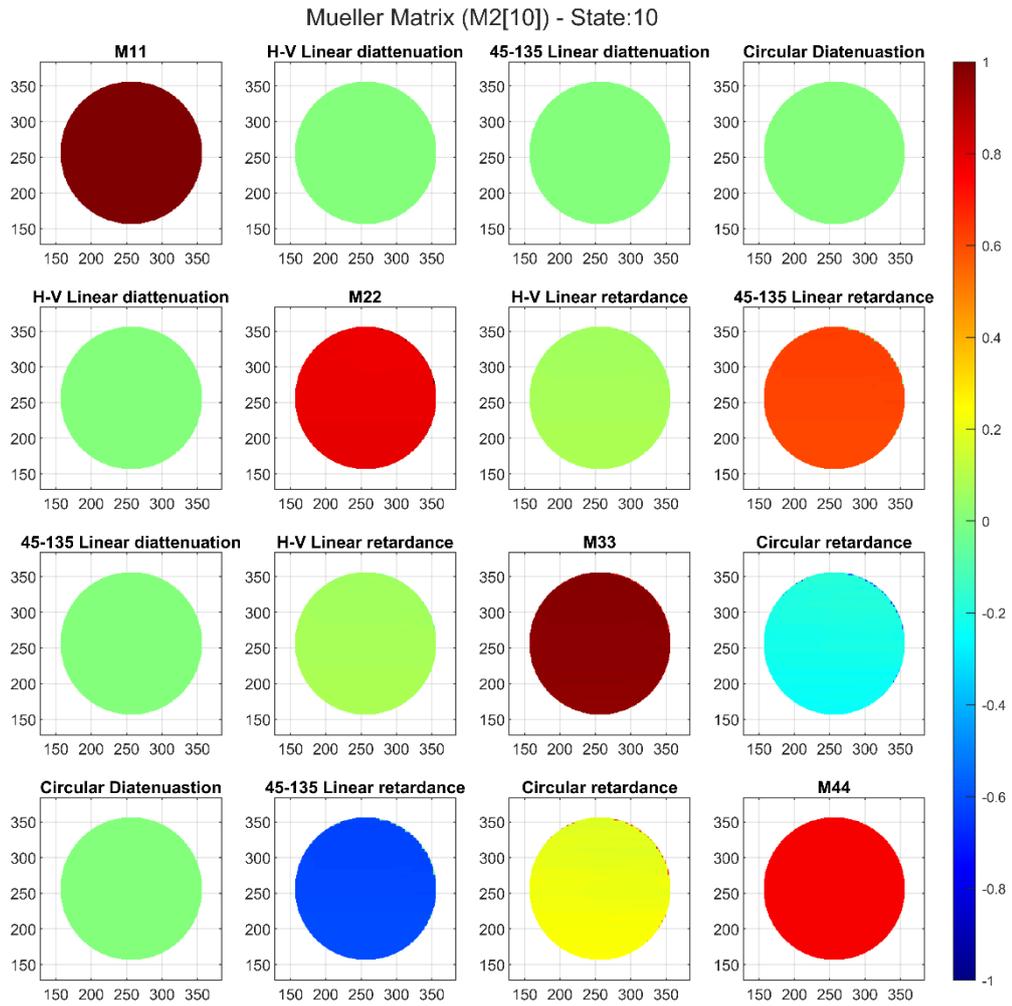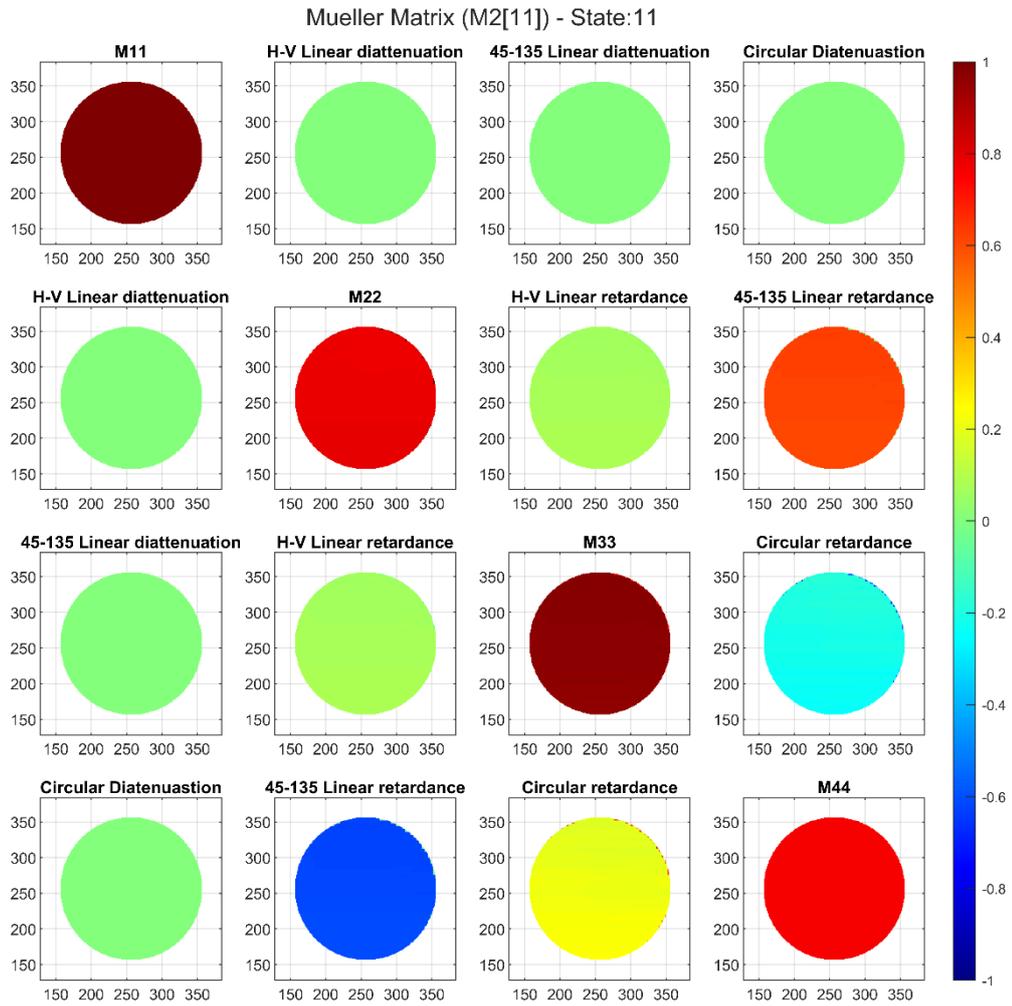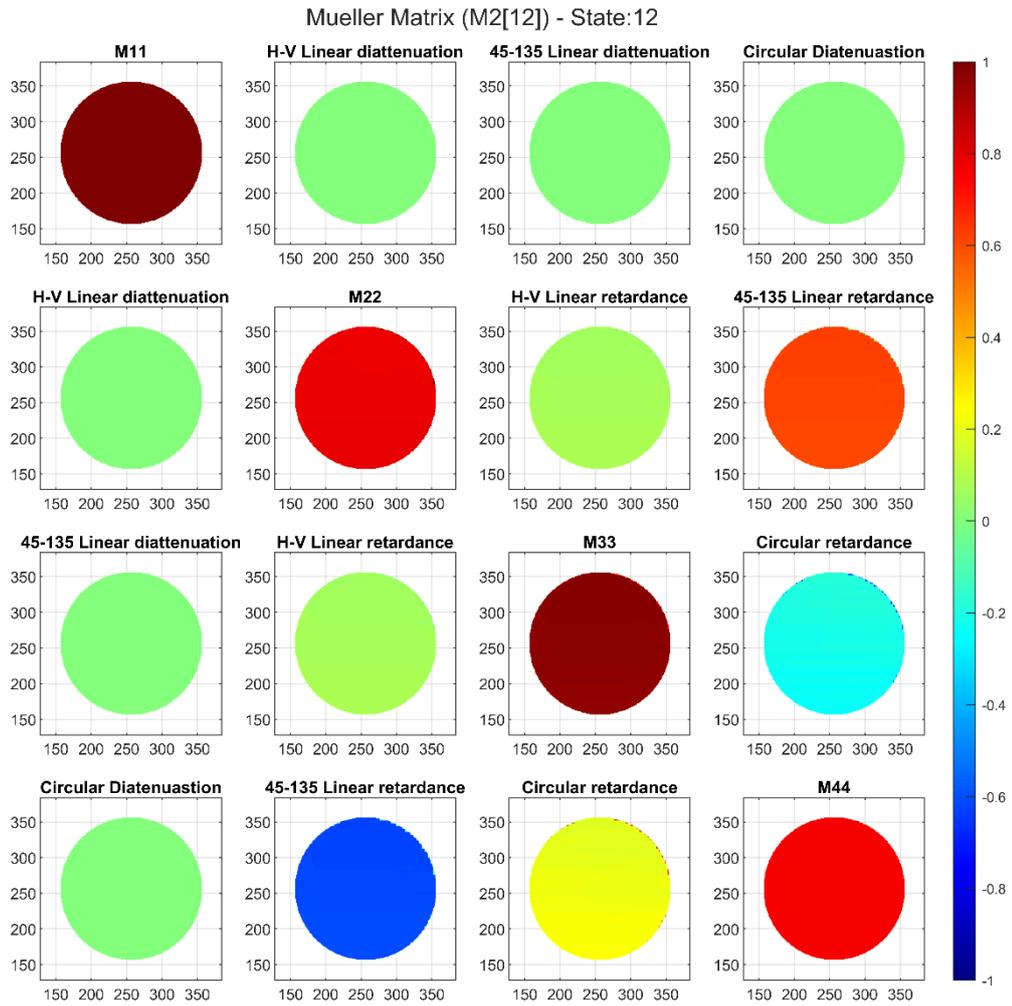Source: Author.
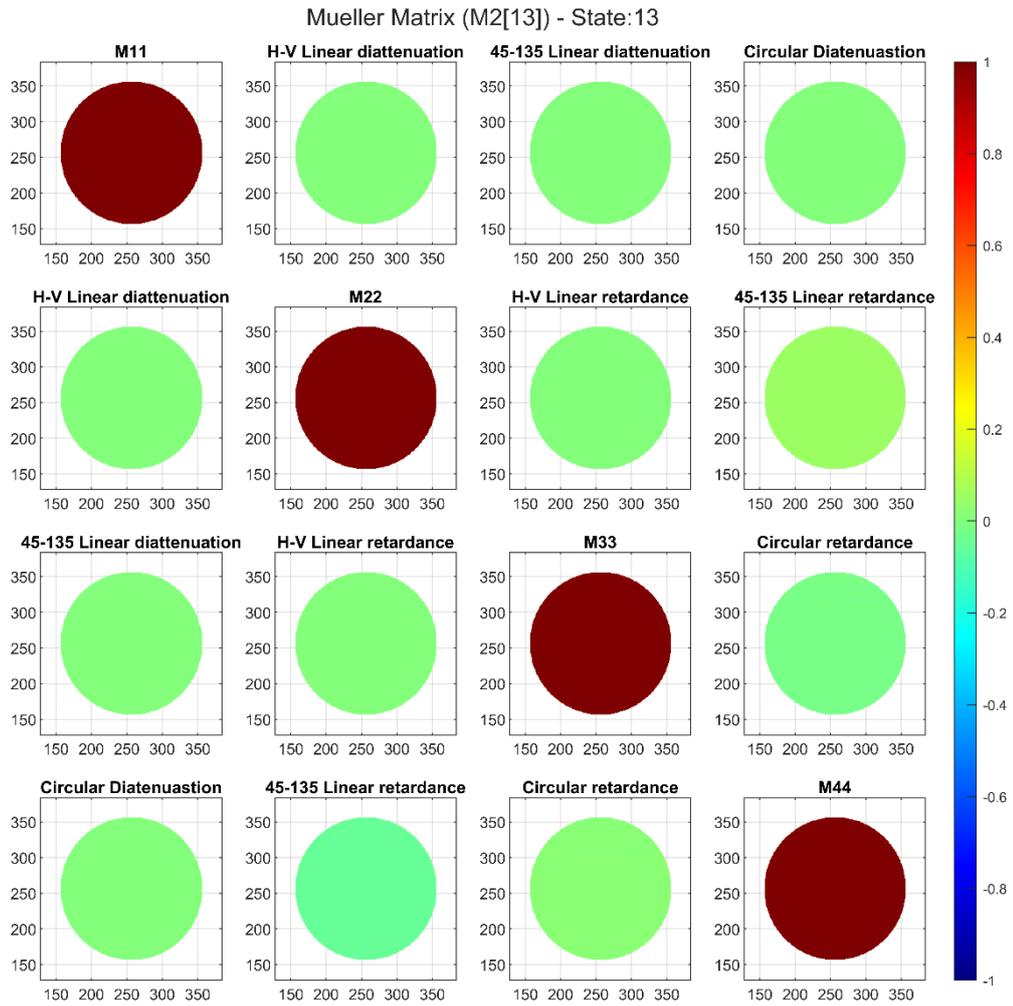
Figure C.3 Mueller Matrix image for M1 State 04.

Mueller Matrix (M1[4]) - State:04
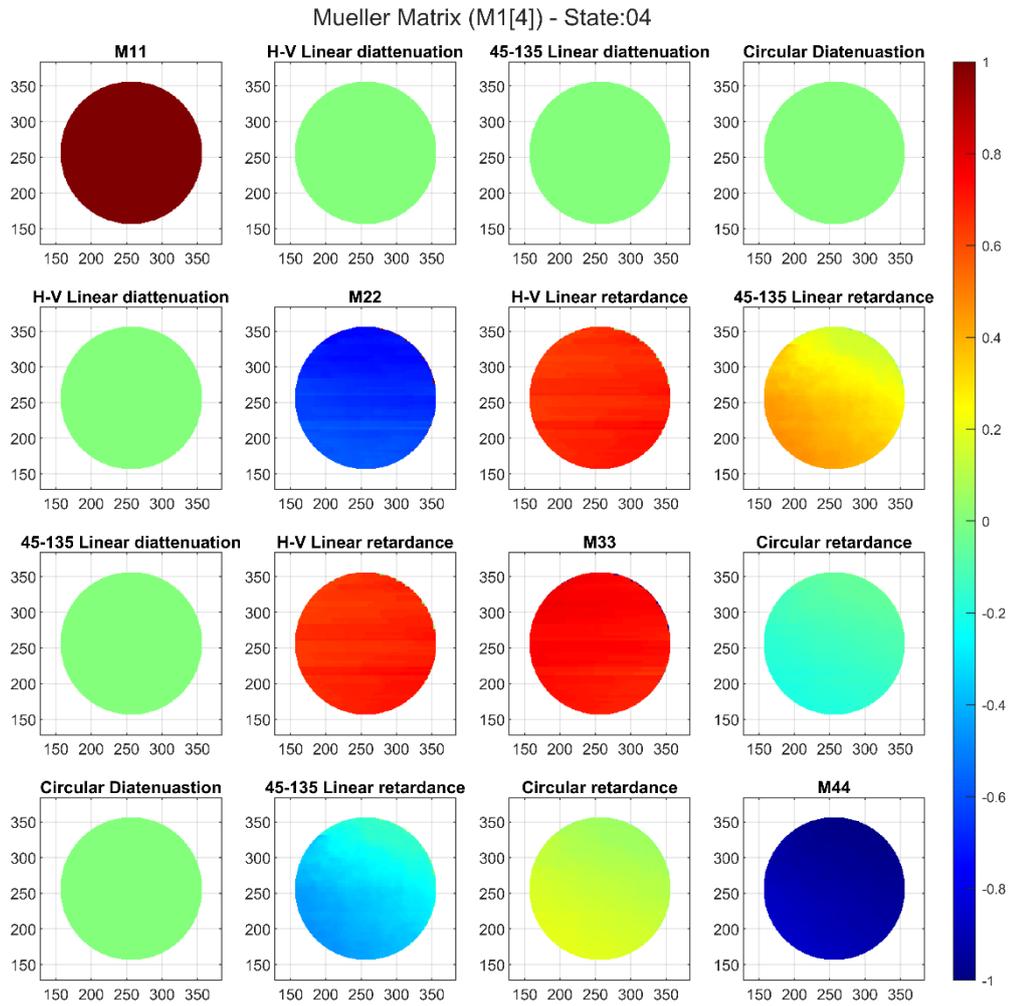
Source: Author.

Figure C.4 Mueller Matrix image for M1 State 05.

Mueller Matrix (M1[5]) - State:05
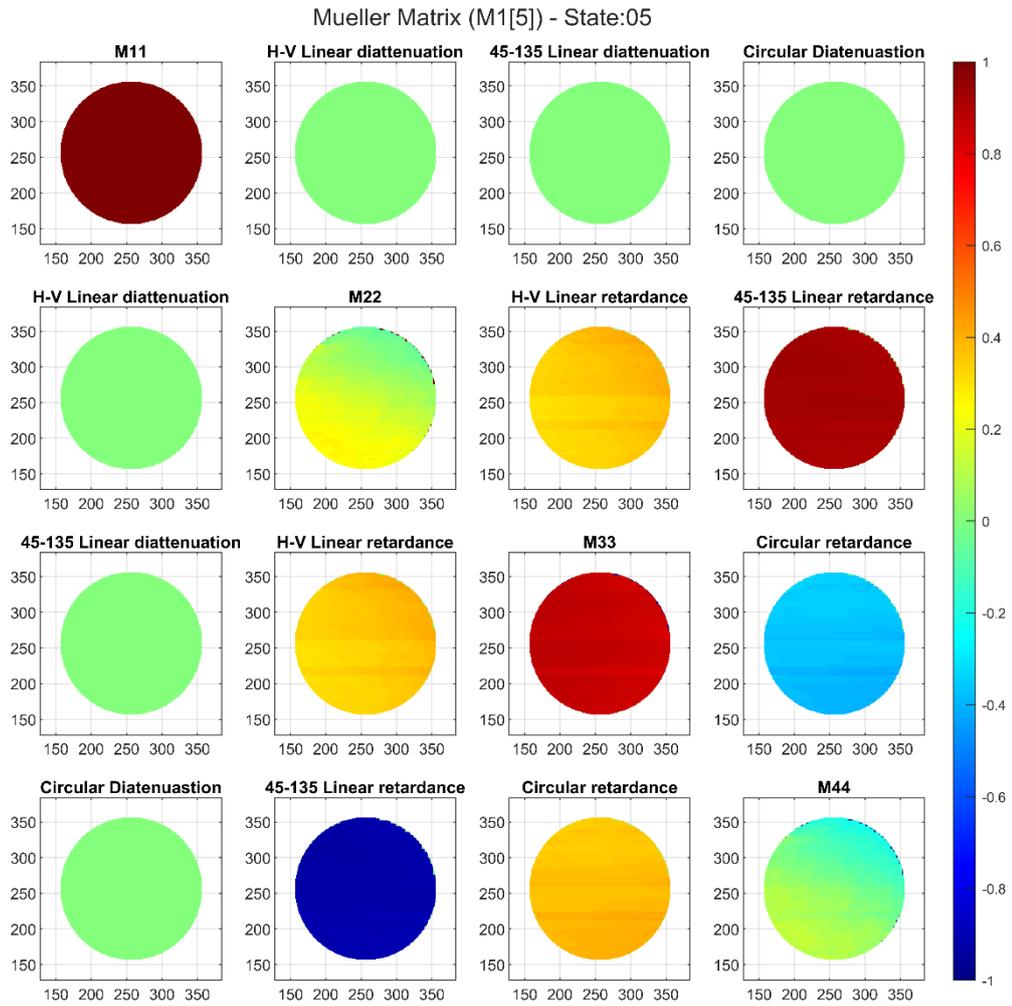
Source: Author.

Figure C.5 Mueller Matrix image for M1 State 06.

Mueller Matrix (M1[6]) - State:06
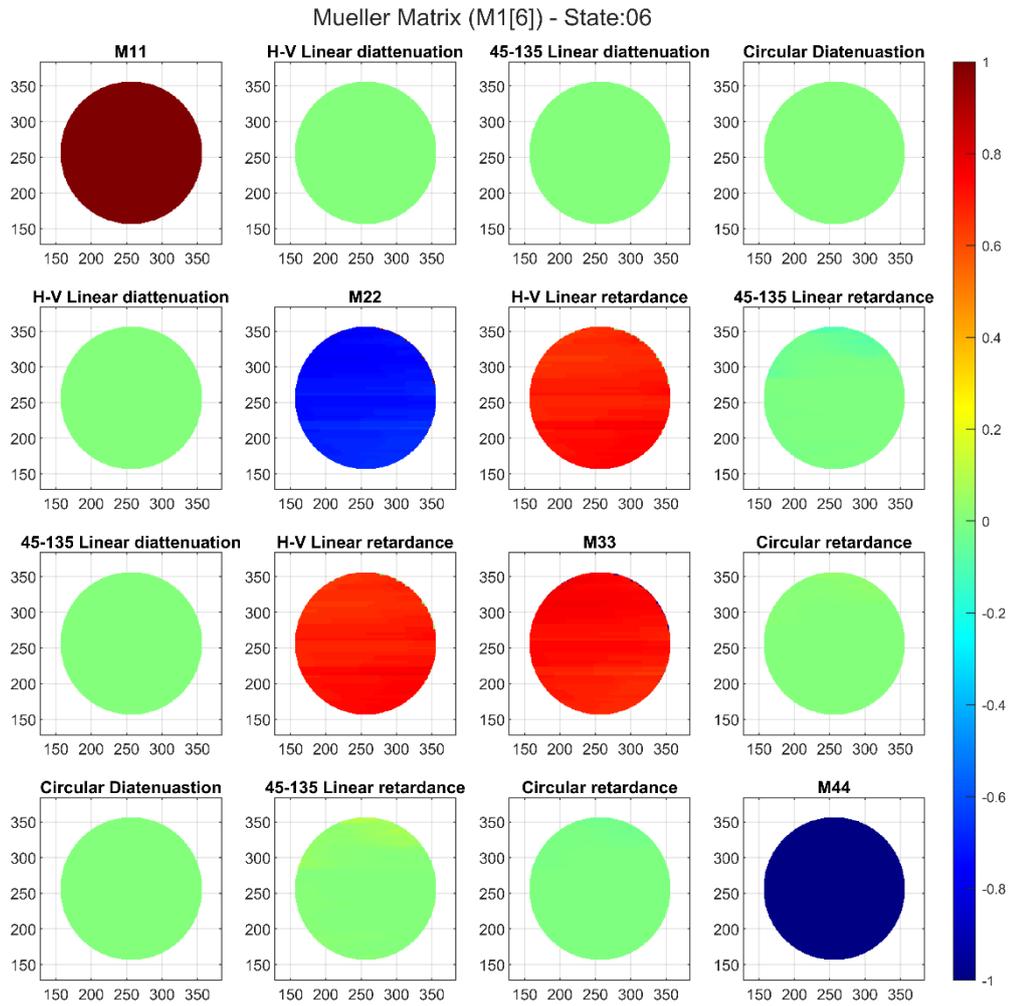
Source: Author.

Figure C.6 Mueller Matrix image for M1 State 07.

Mueller Matrix (M1[7]) - State:07
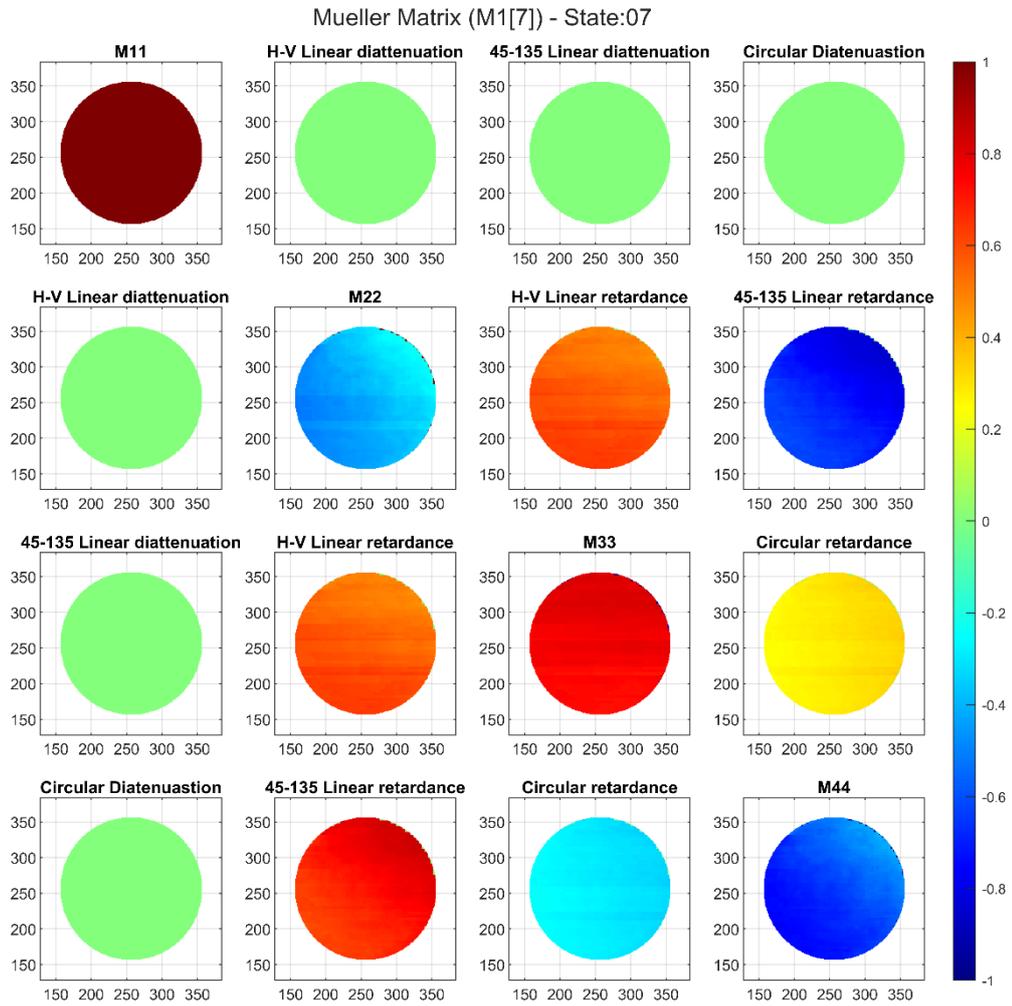
Source: Author.

Figure C.7 Mueller Matrix image for M1 State 08.
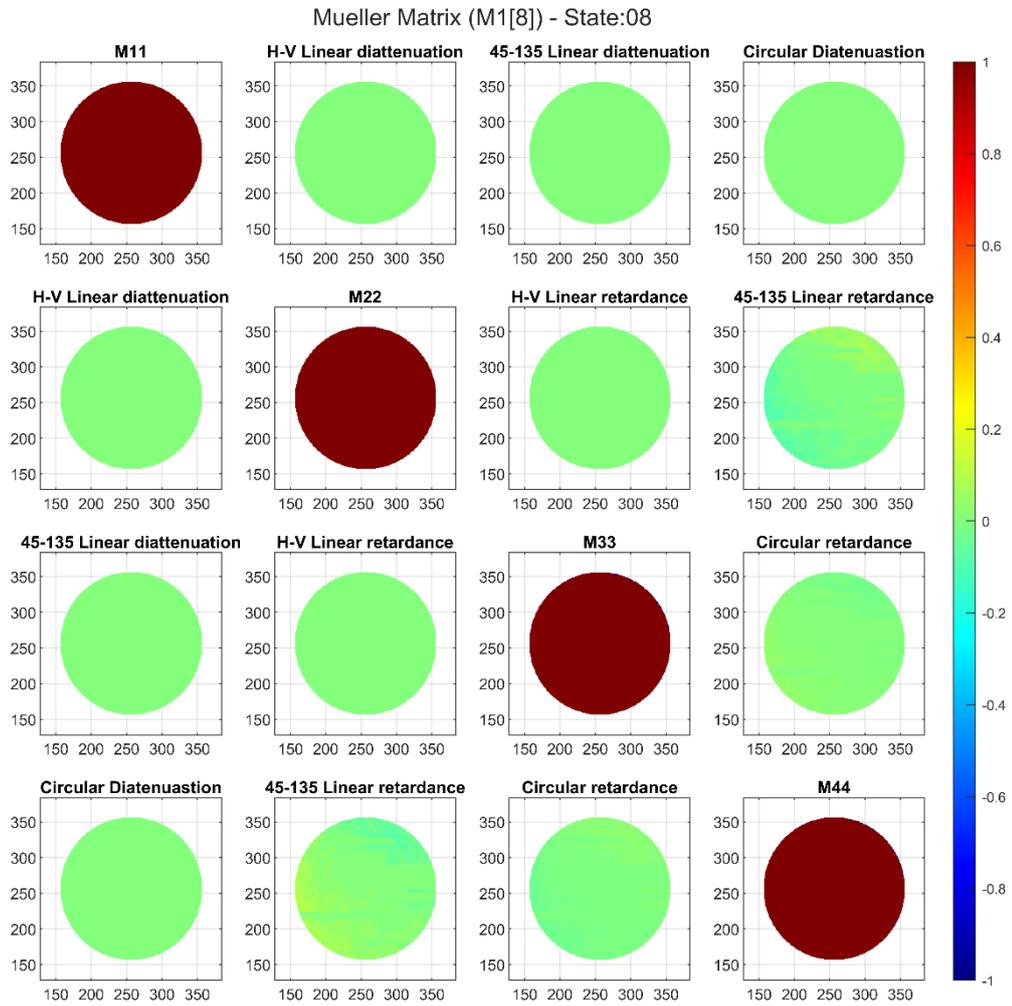
Source: Author.

Figure C.8 Mueller Matrix image for M1 State 09.

Mueller Matrix (M1[9]) - State:09
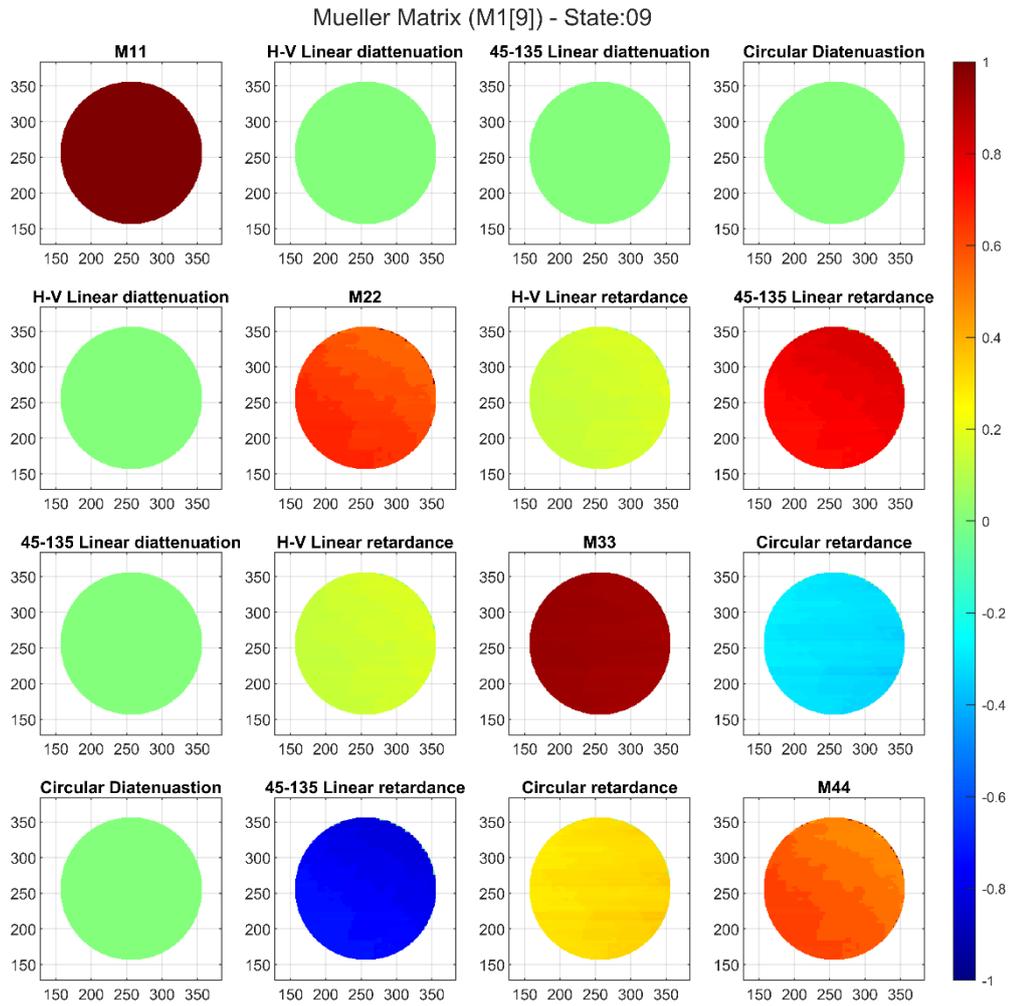
Source: Author.

Figure C.9 Mueller Matrix image for M1 State 10.
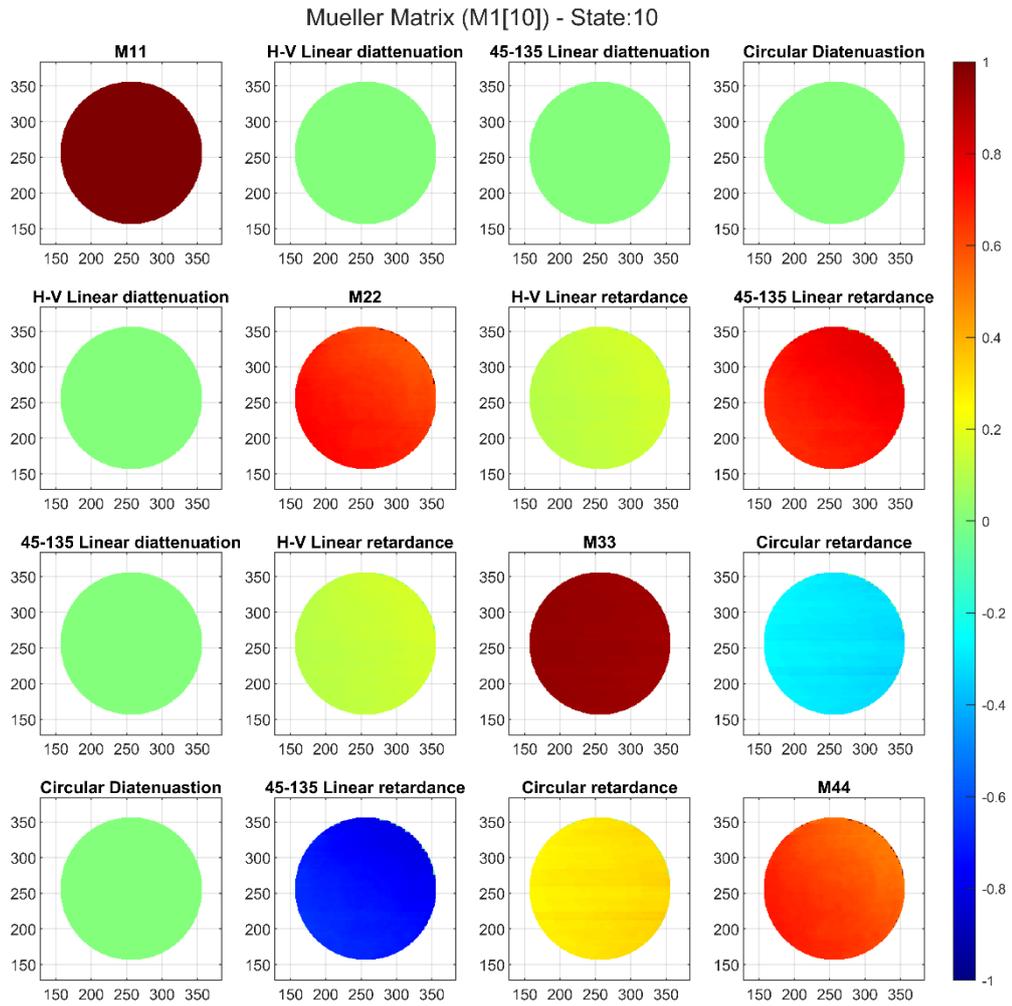
Source: Author.
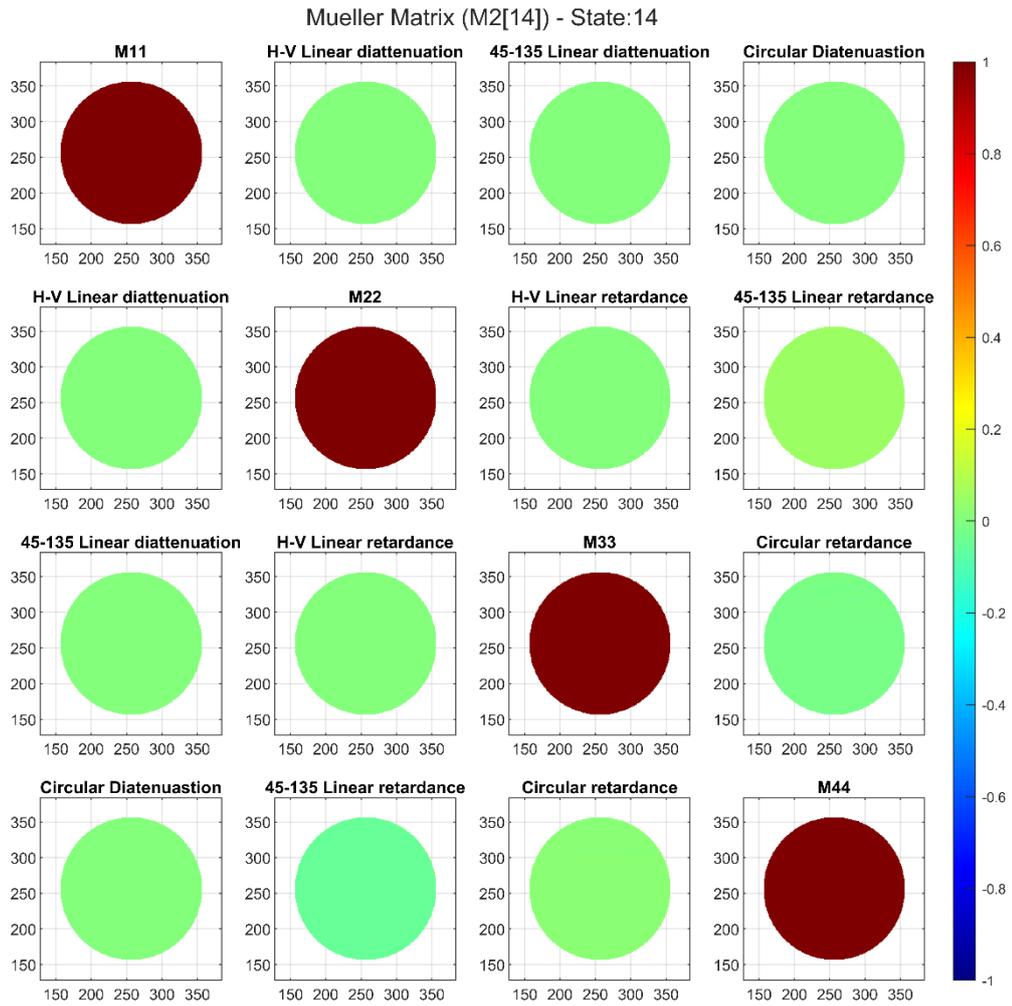
Figure C.10 Mueller Matrix image for M1 State 11.

Mueller Matrix (M1[11]) - State:11
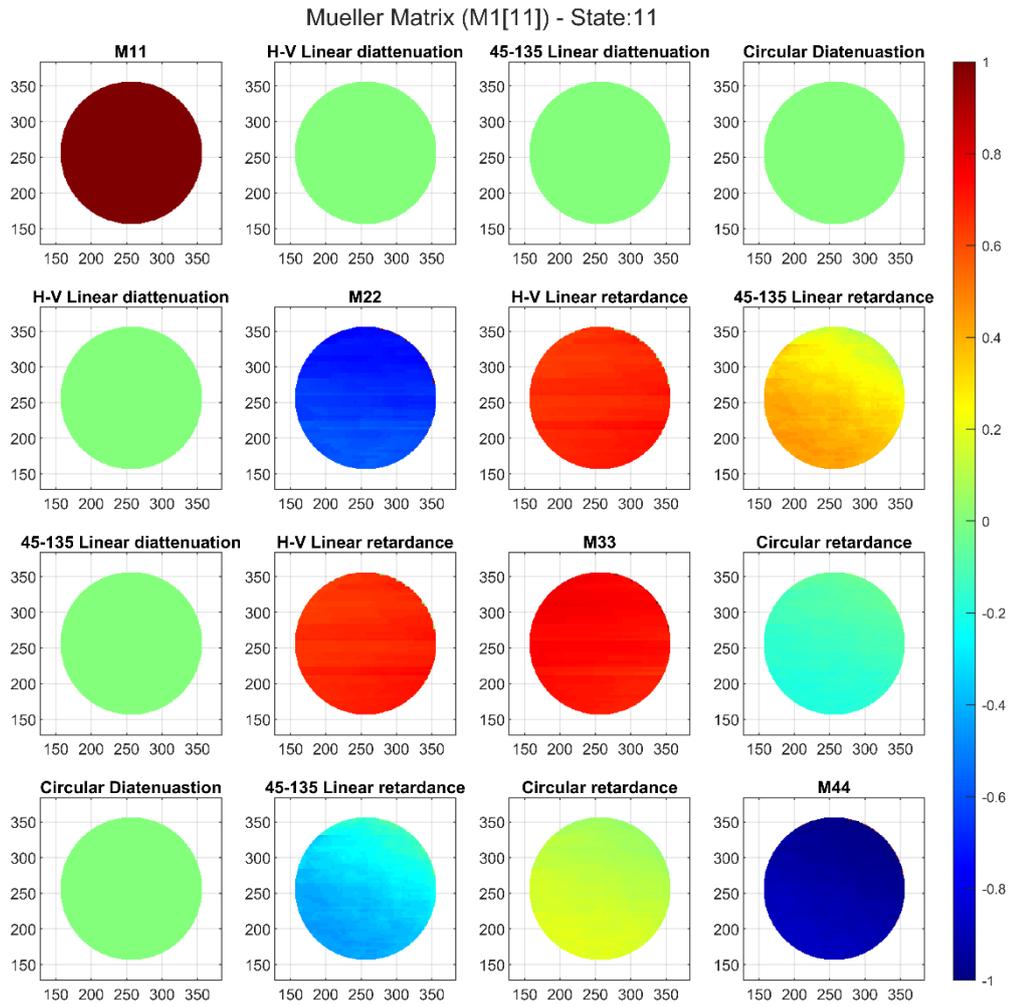
Source: Author.

Figure C.11 Mueller Matrix image for M1 State 12.
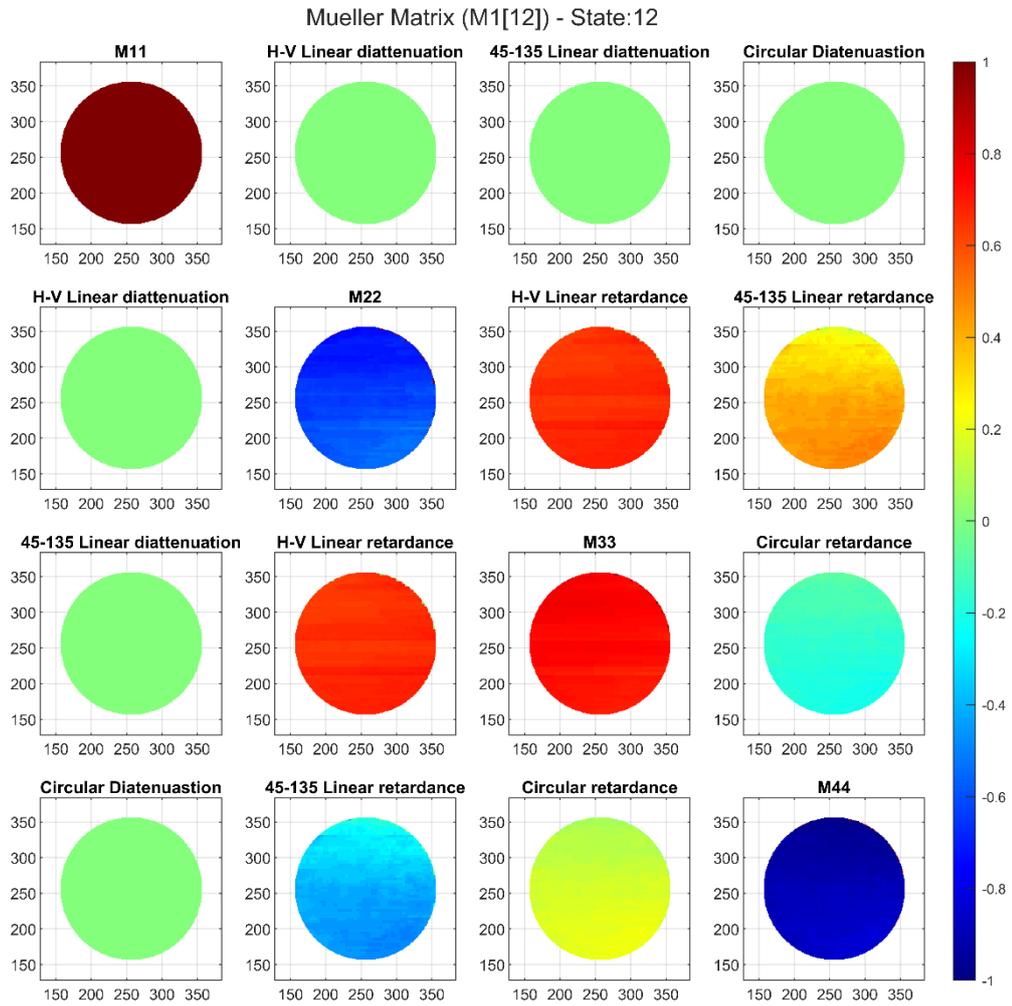
Source: Author.
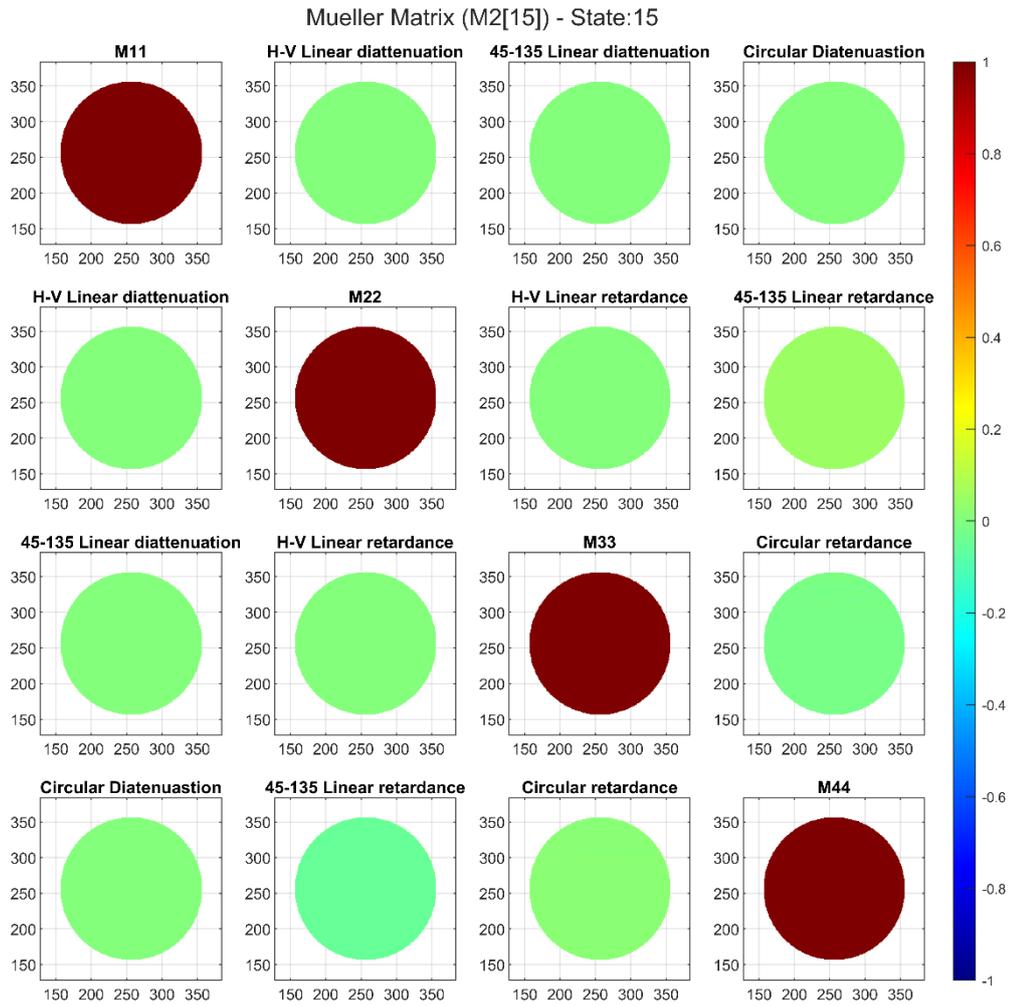
Figure C.12 Mueller Matrix image for M1 State 13.
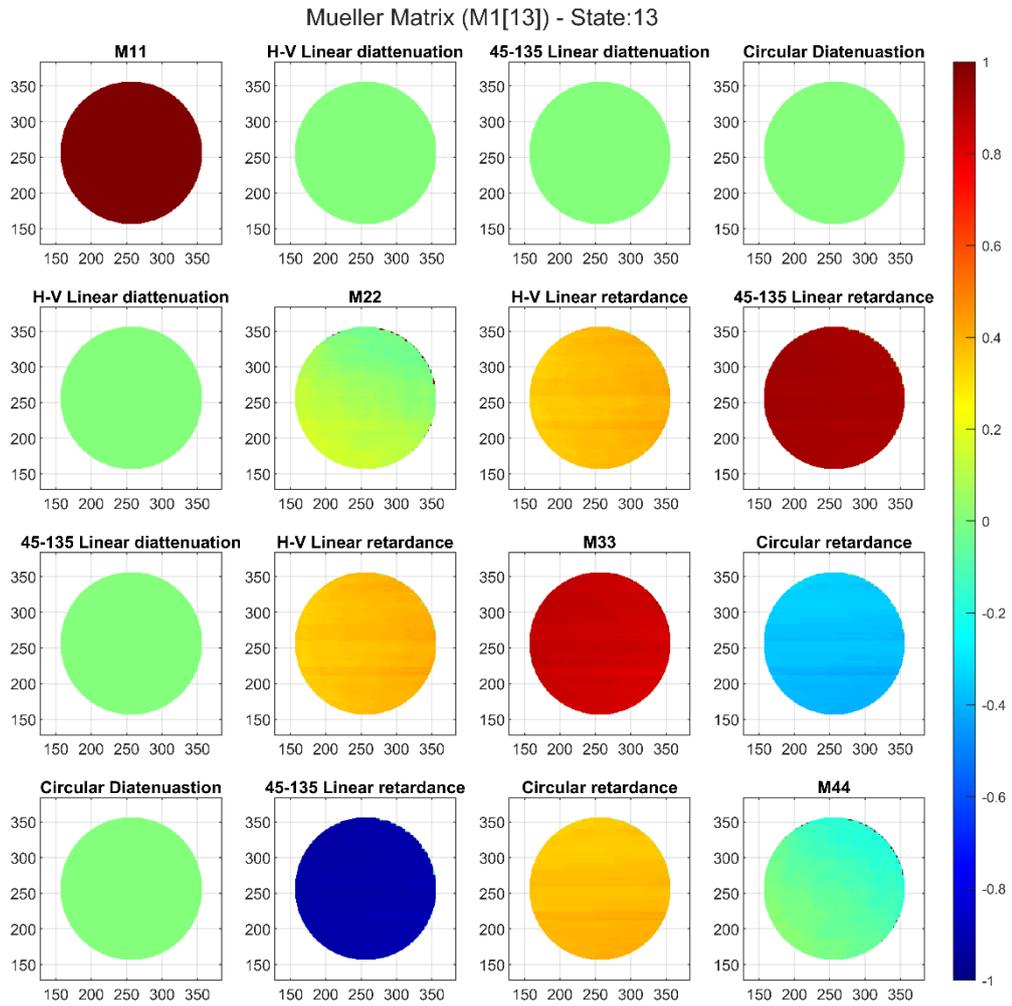
Source: Author.
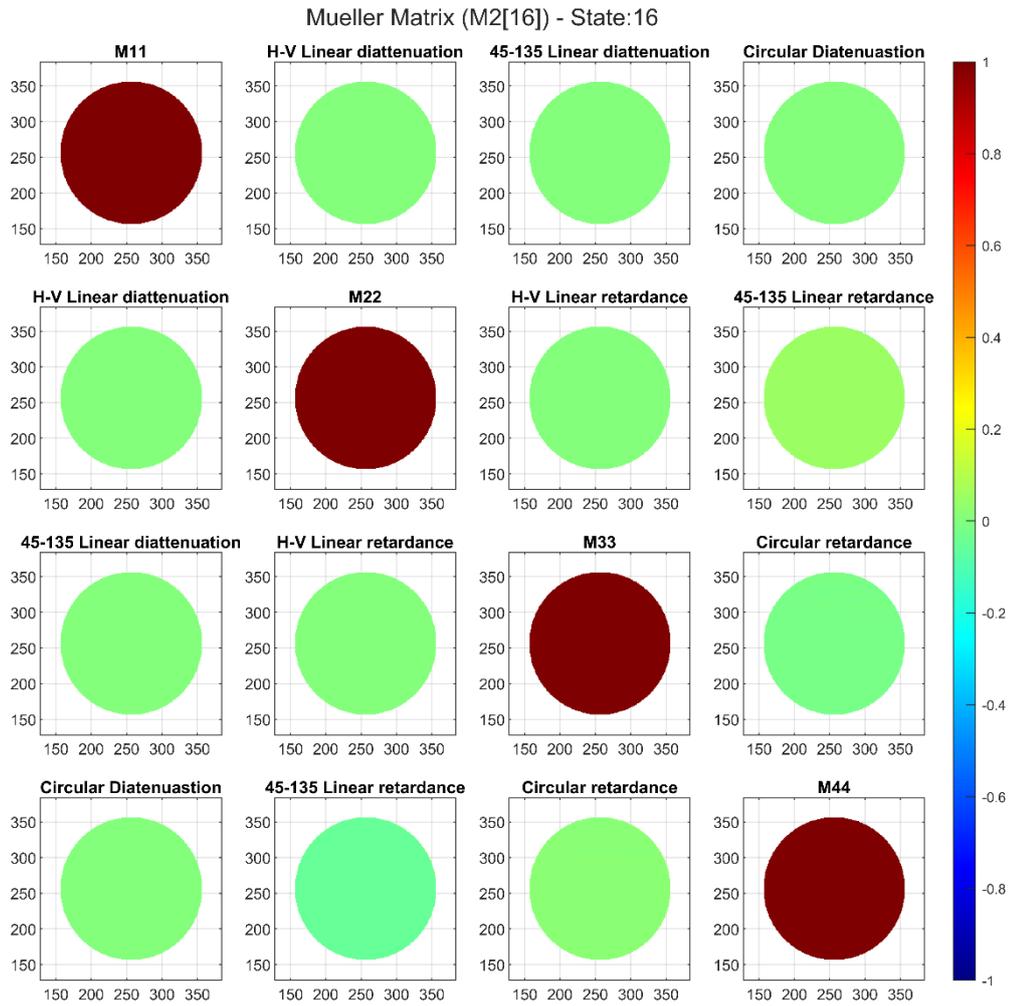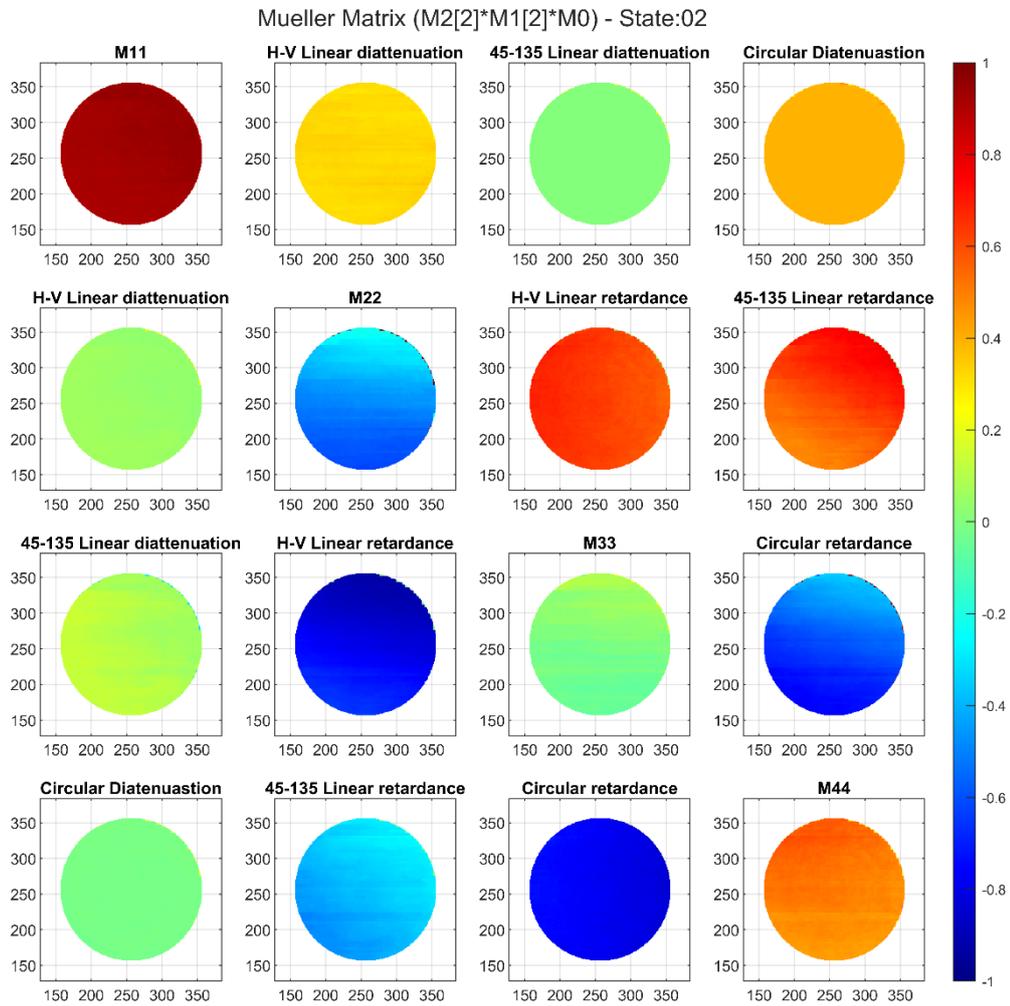
Figure C.13 Mueller Matrix image for M1 State 14.

Mueller Matrix (M1[14]) - State:14
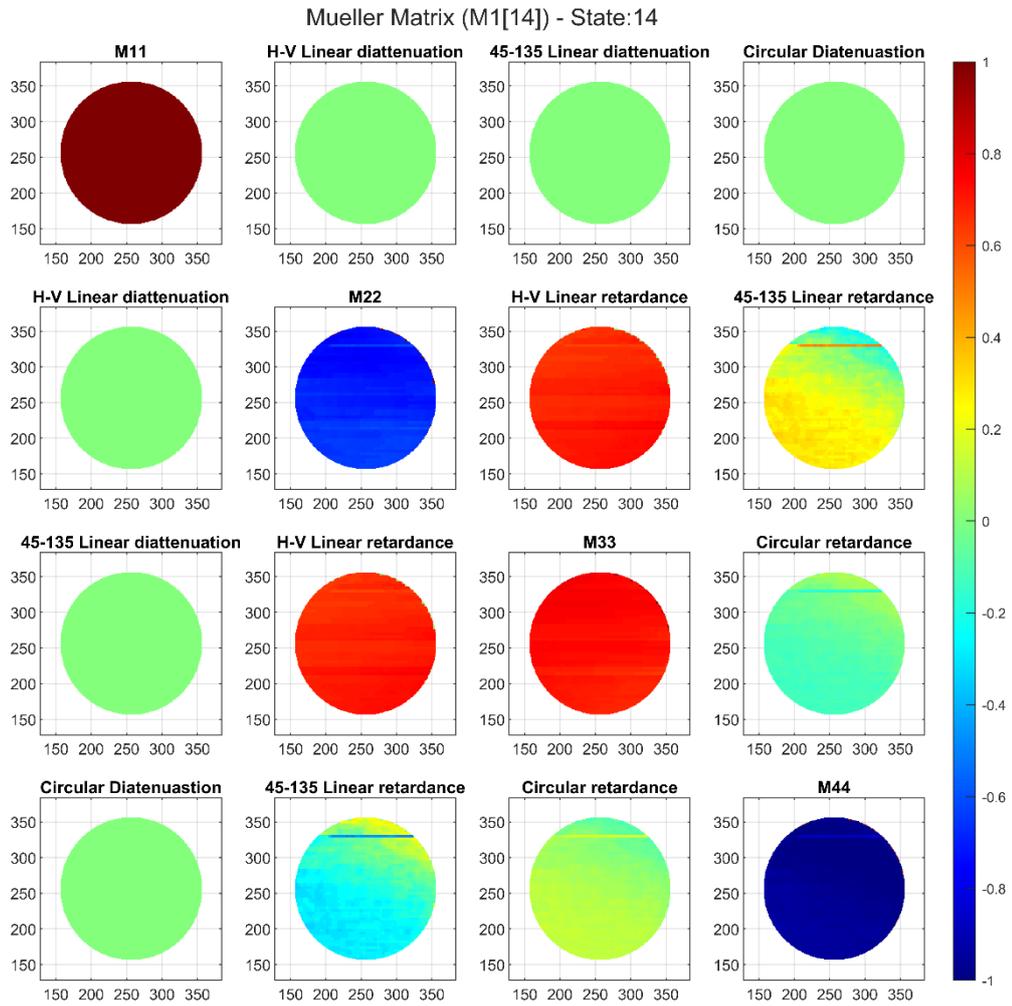
Source: Author.

Figure C.14 Mueller Matrix image for M1 State 15.
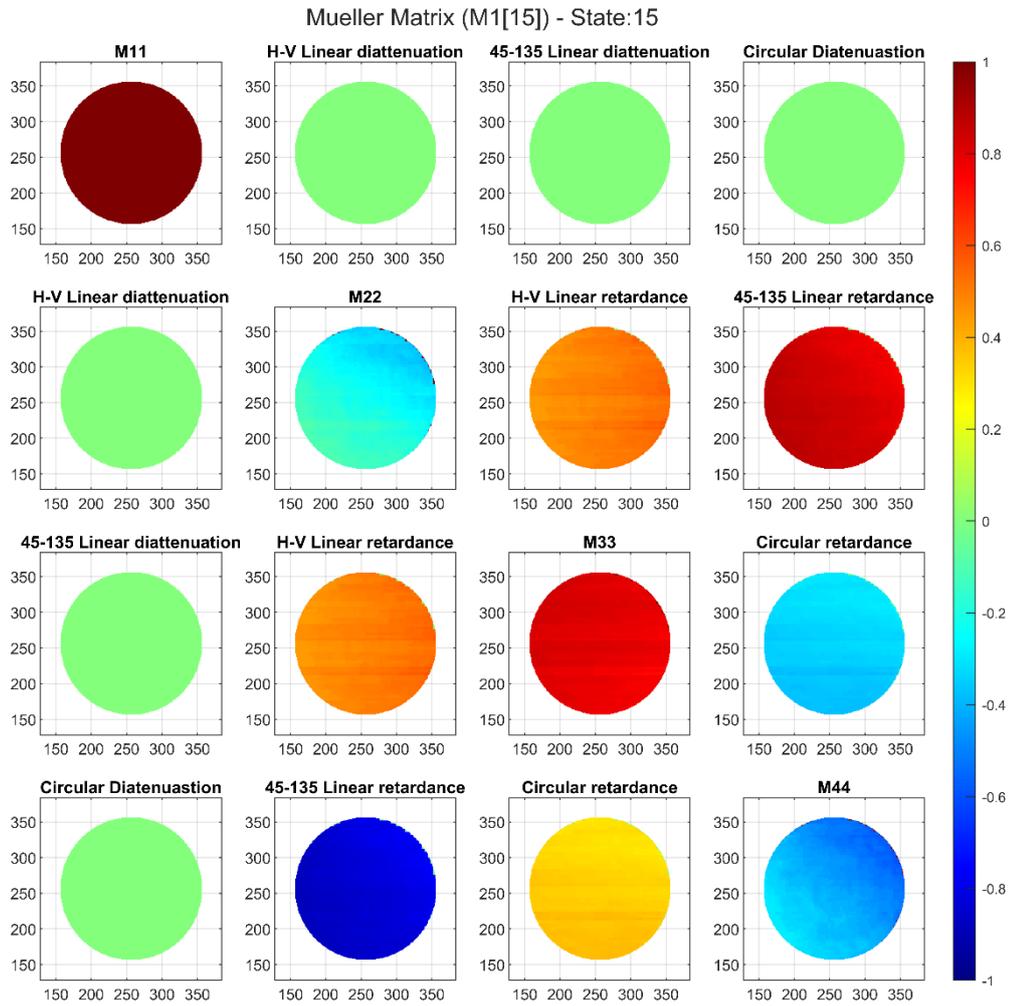
Source: Author.
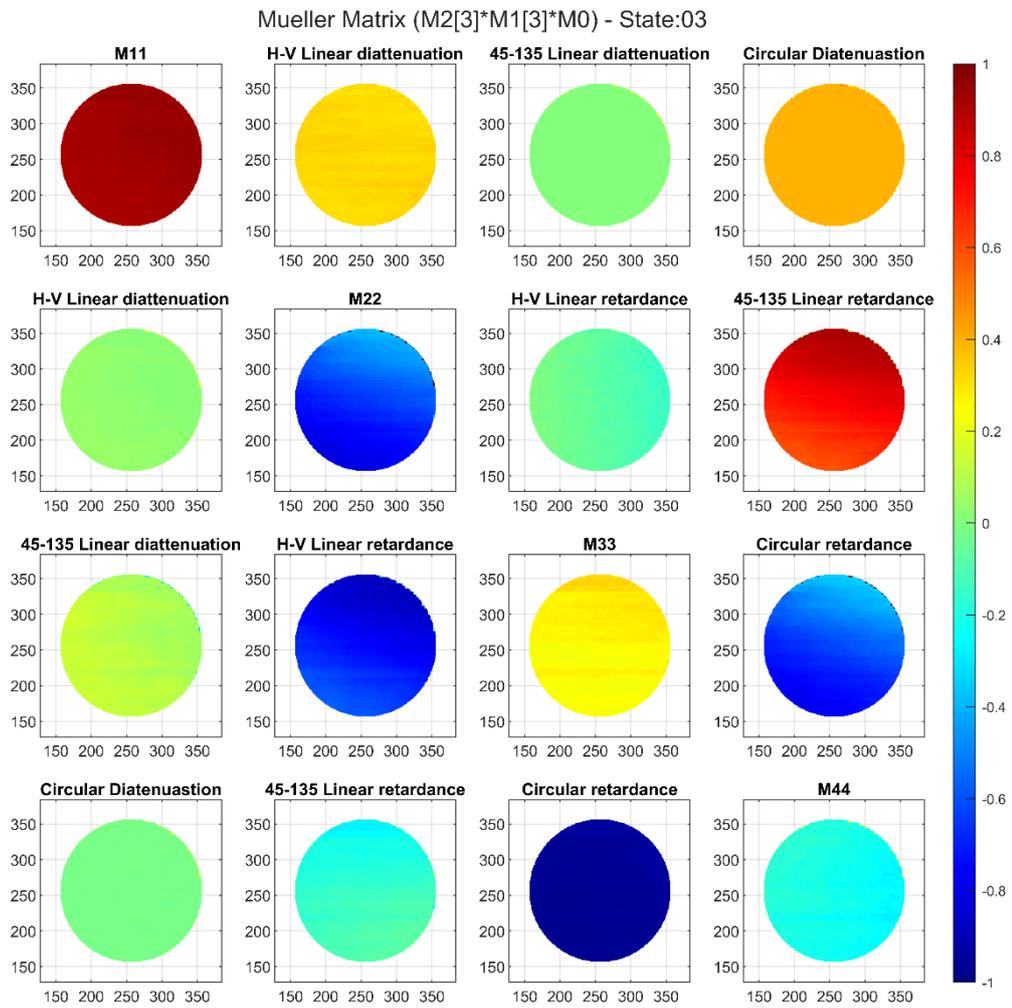
Figure C.15 Mueller Matrix image for M1 State 16.

Mueller Matrix (M1[16]) - State:16
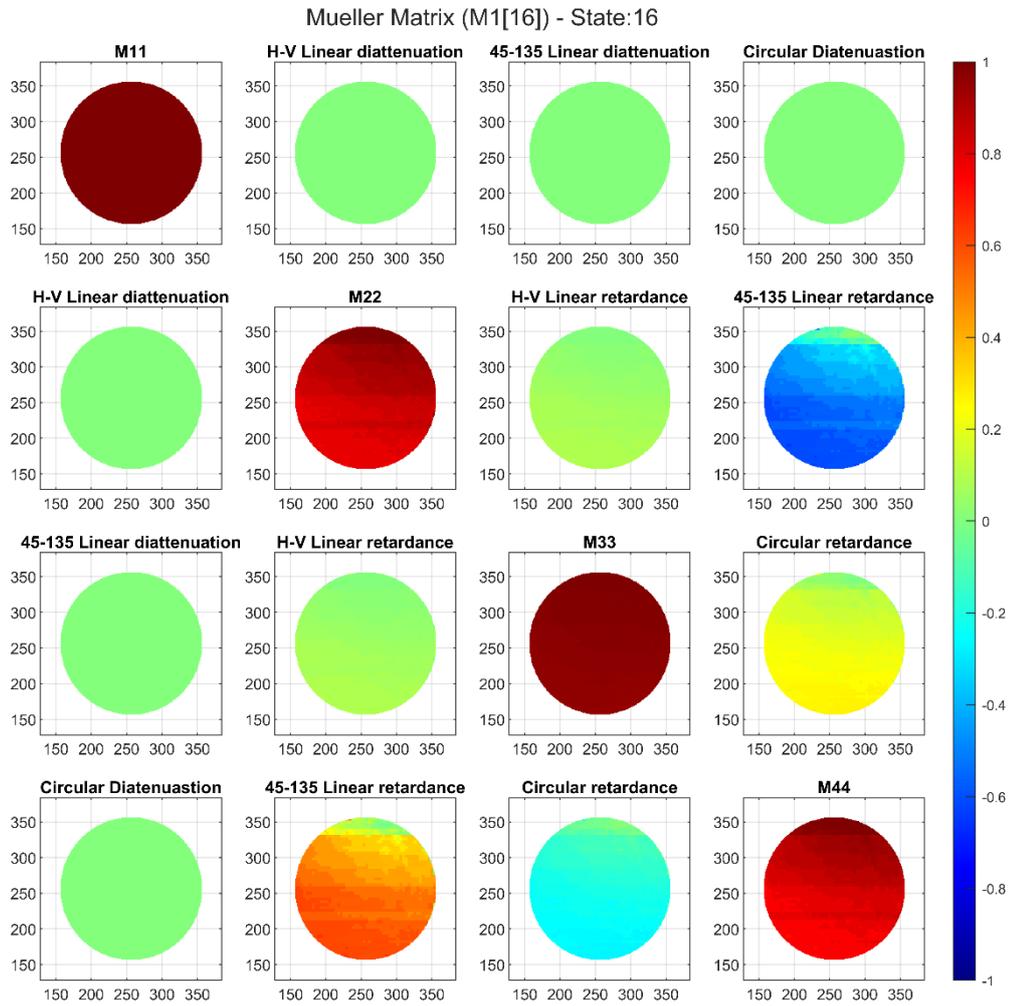
Source: Author.

ANNEX D

Figure D.1 Mueller Matrix image for M2 State 02.
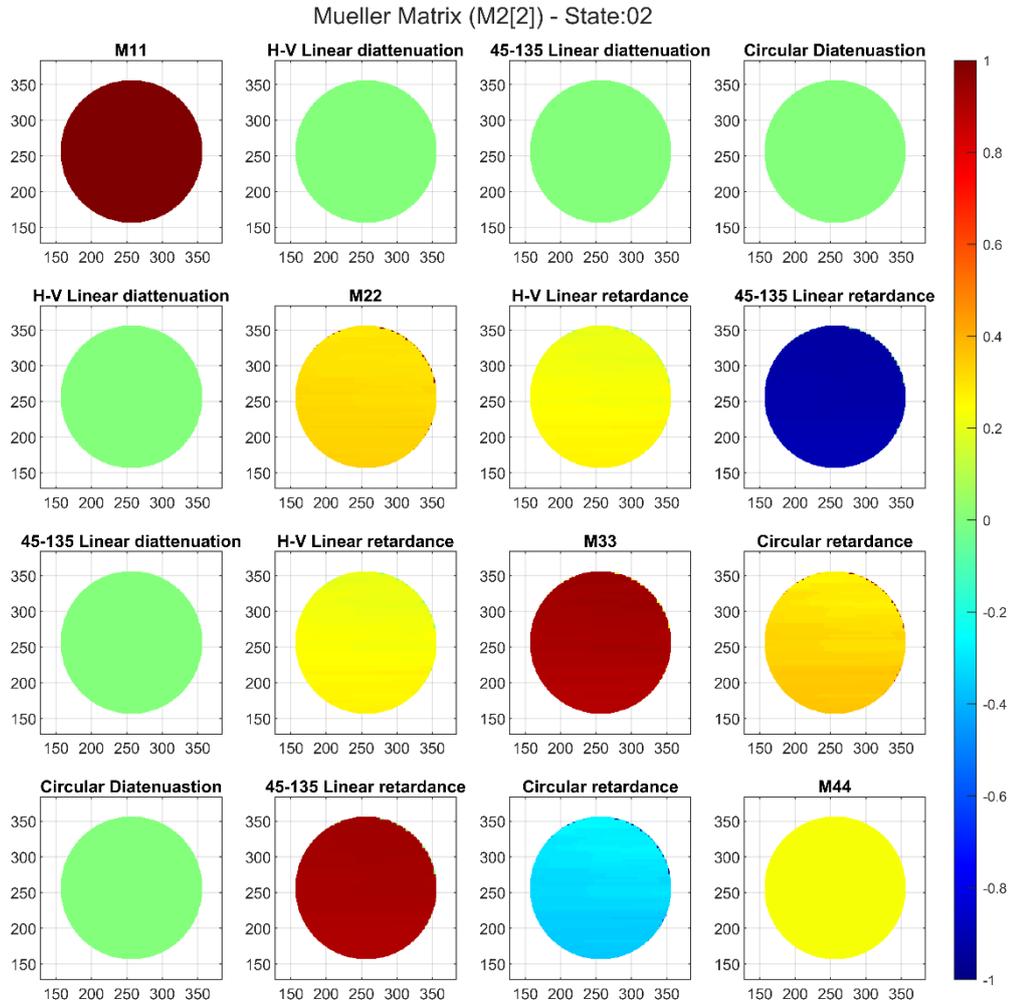
Source: Author.

Figure D.2 Mueller Matrix image for M2 State 03.

Mueller Matrix (M2[3]) - State:03
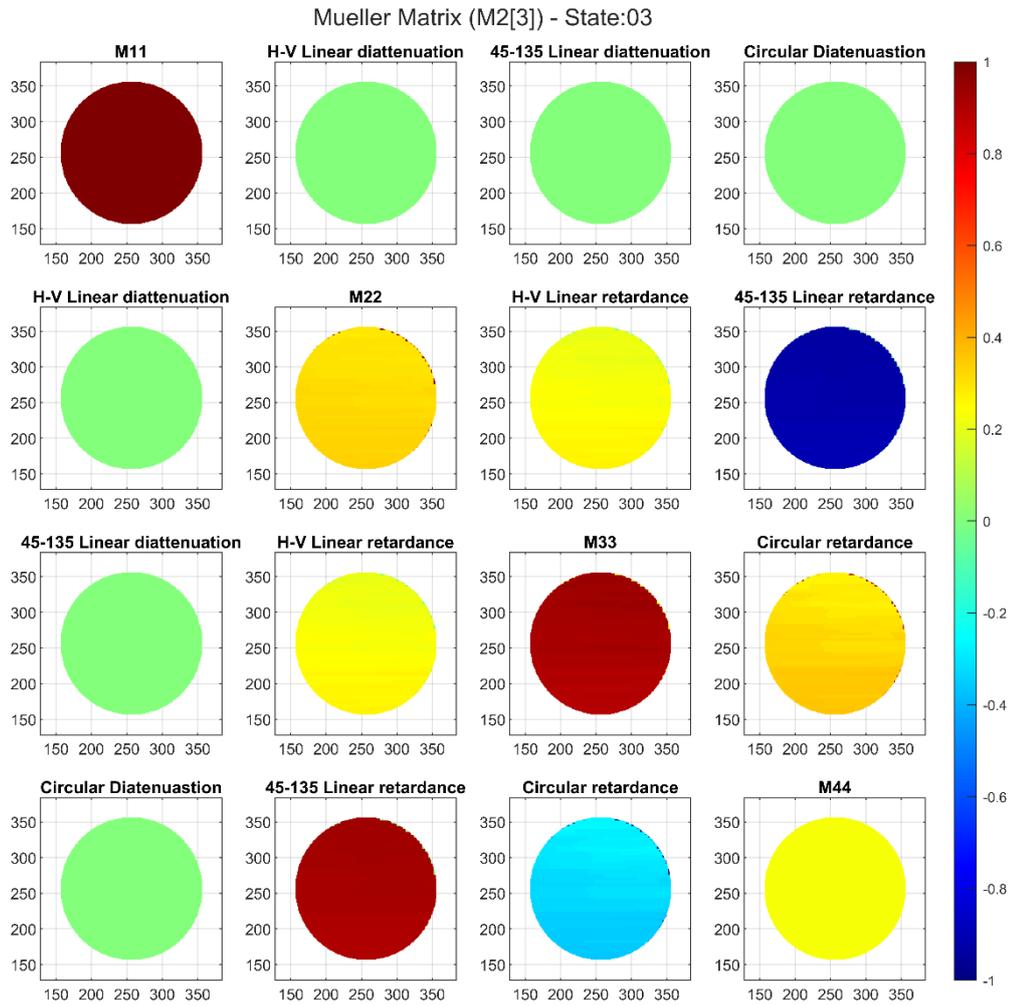
Source: Author.

Figure D.3 Mueller Matrix image for M2 State 04.

Mueller Matrix (M2[4]) - State:04
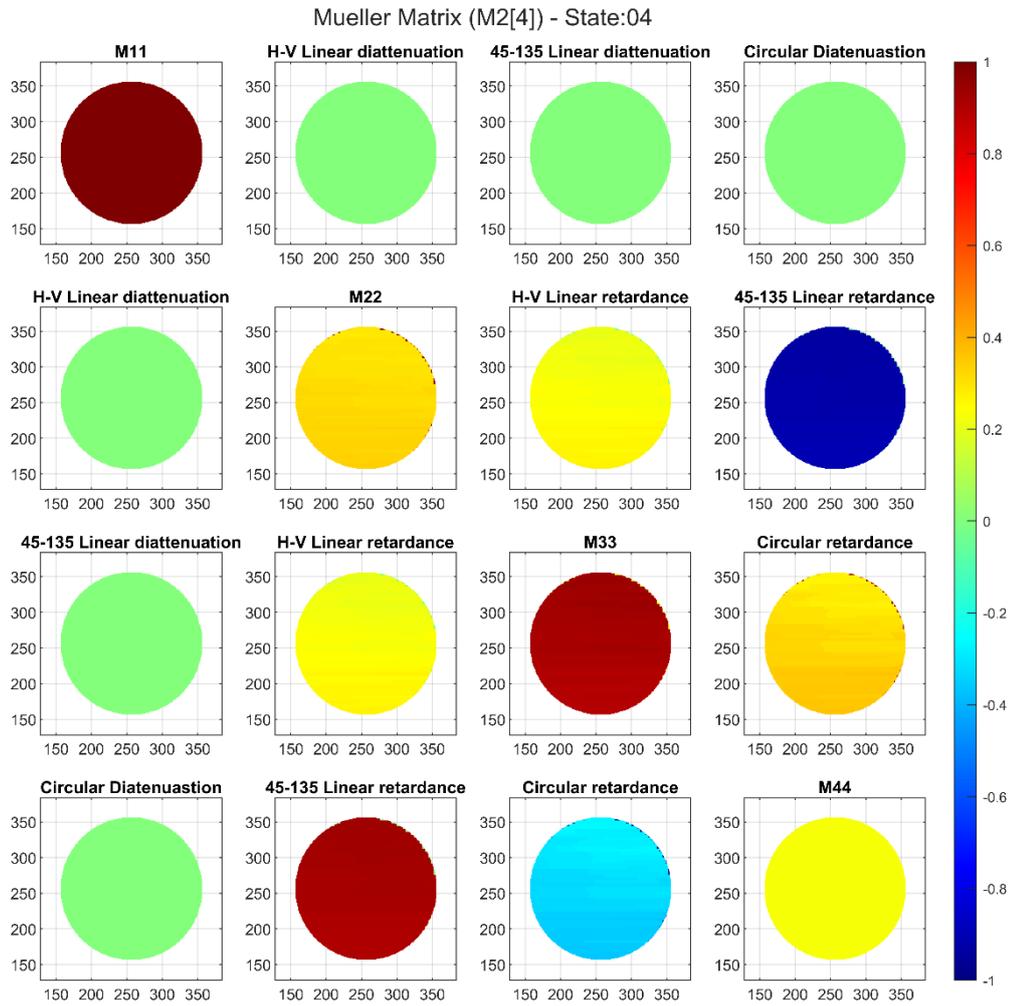
Source: Author.

Figure D.4 Mueller Matrix image for M2 State 05.

Mueller Matrix (M2[5]) - State:05
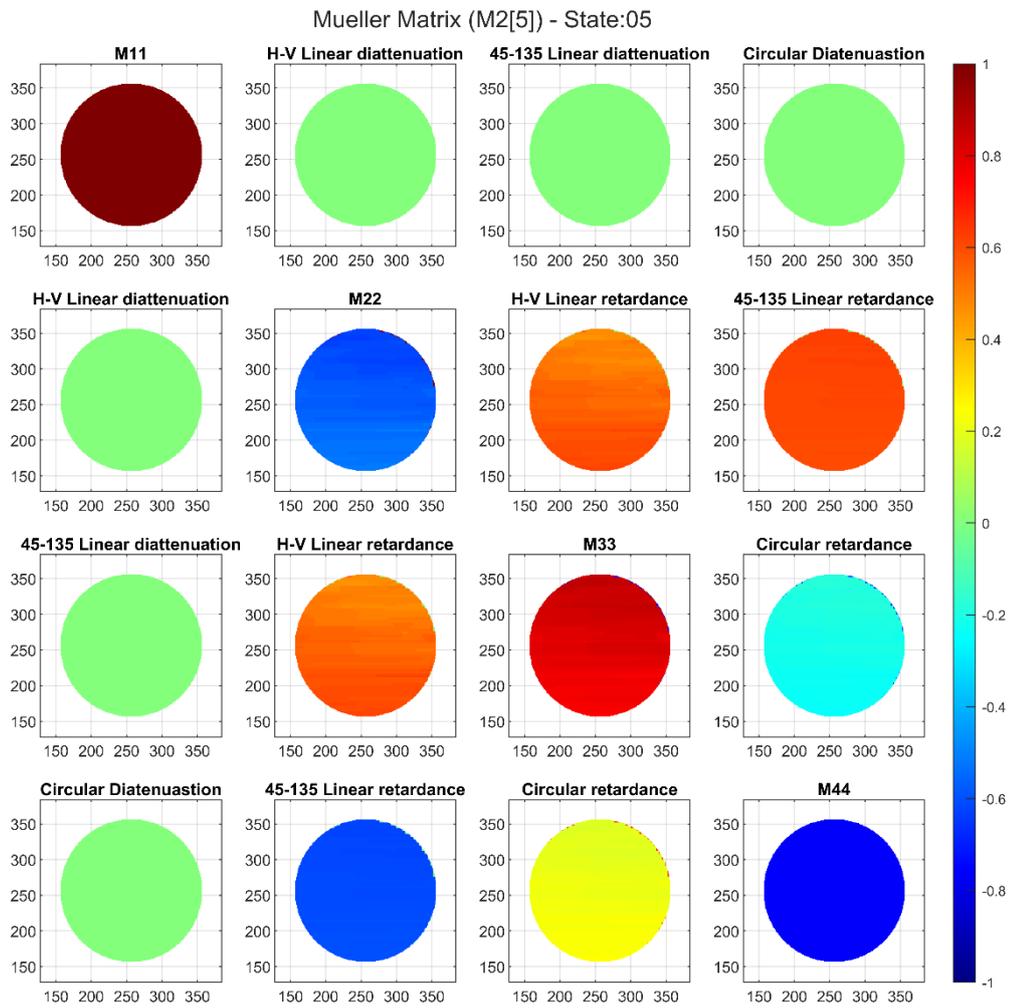
Source: Author.

Figure D.5 Mueller Matrix image for M2 State 06.

Mueller Matrix (M2[6]) - State:06
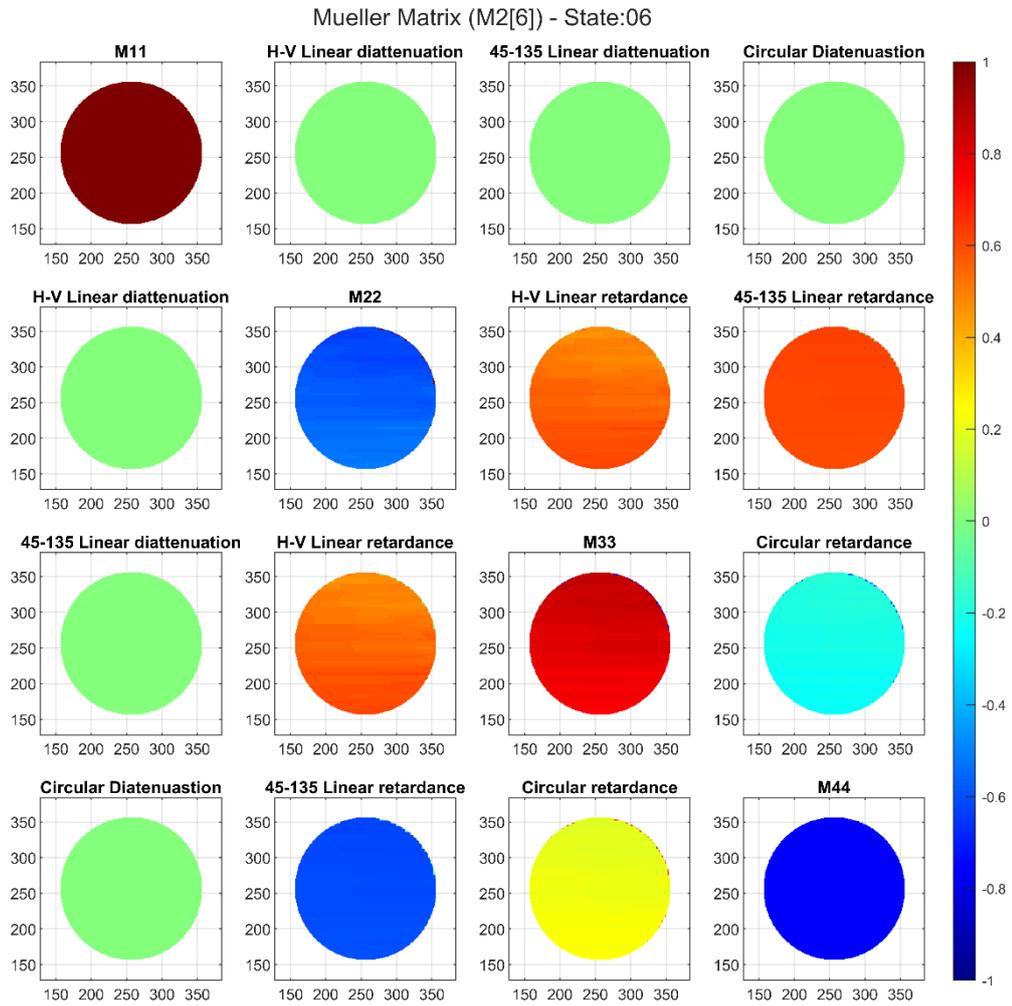
Source: Author.

Figure D.6 Mueller Matrix image for M2 State 07.
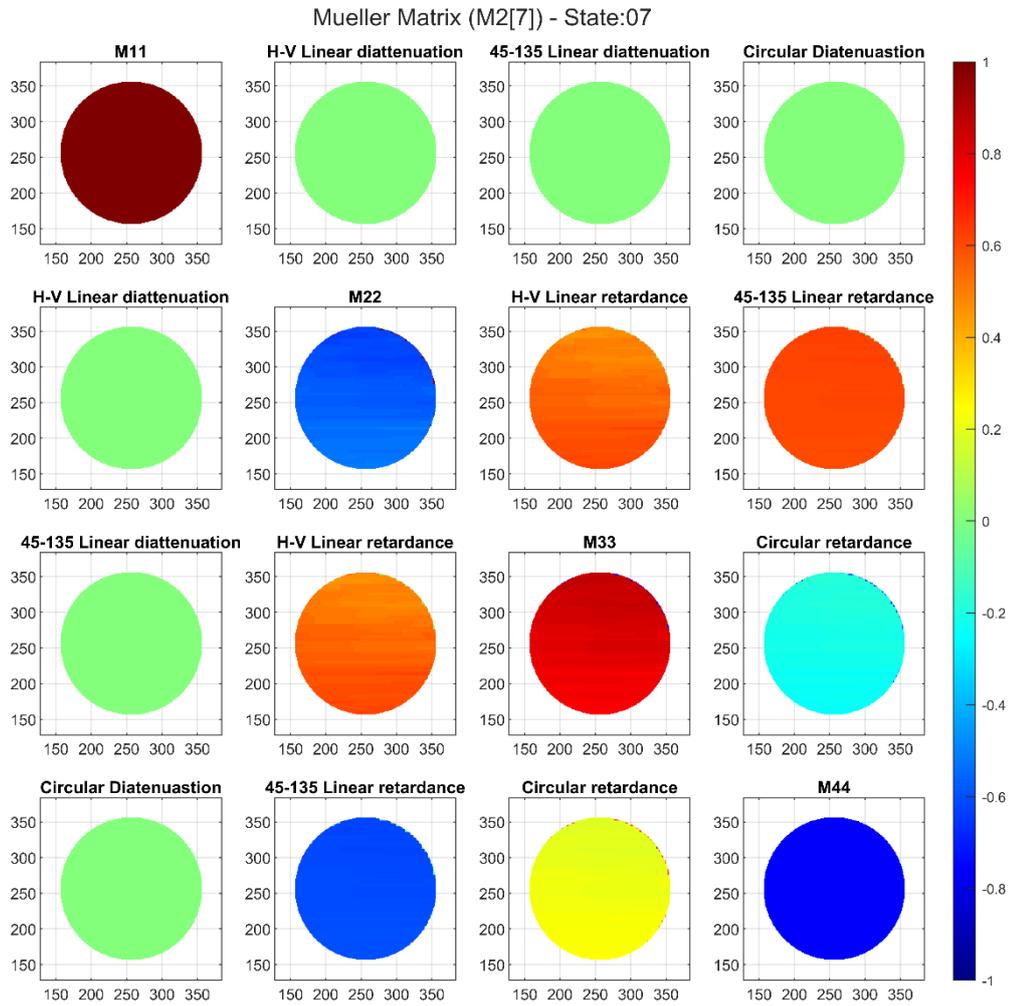
Source: Author.

Figure D.7 Mueller Matrix image for M2 State 08.

Mueller Matrix (M2[8]) - State:08
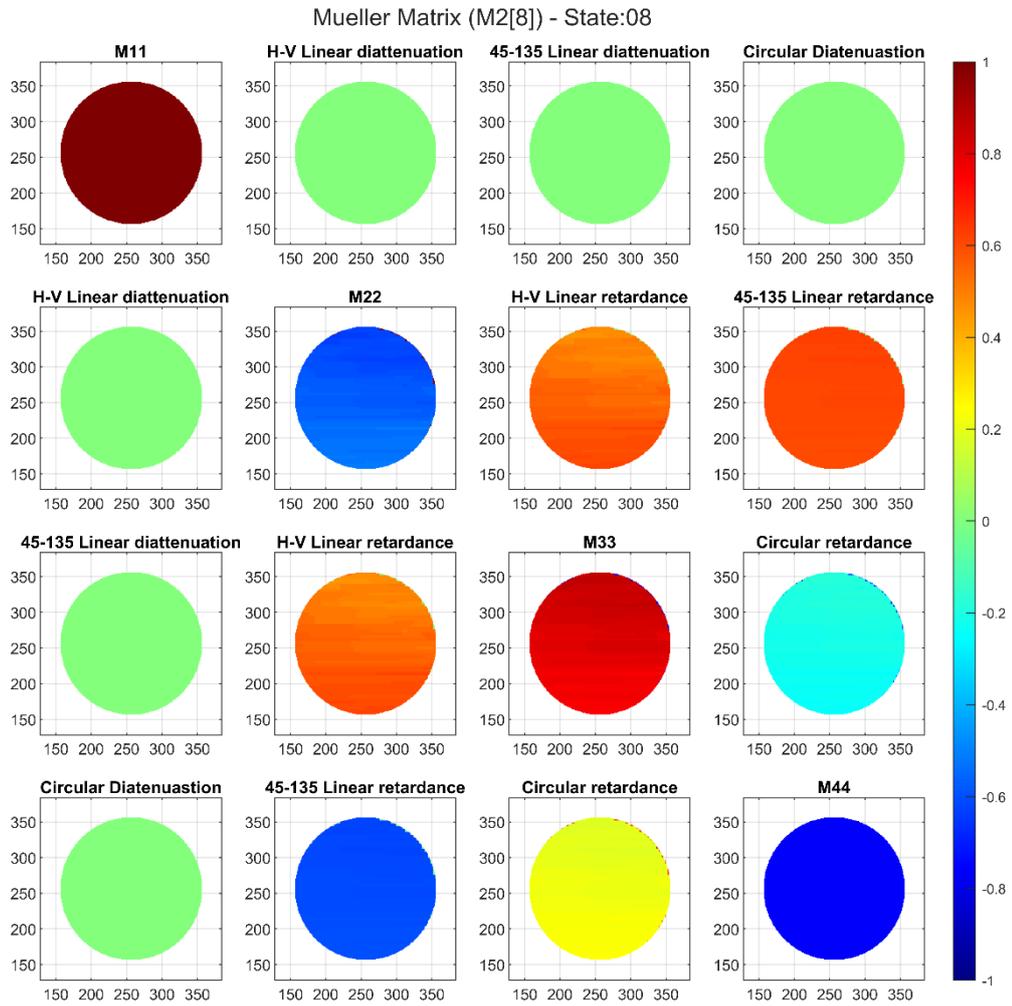
Source: Author.

Figure D.8 Mueller Matrix image for M2 State 09.
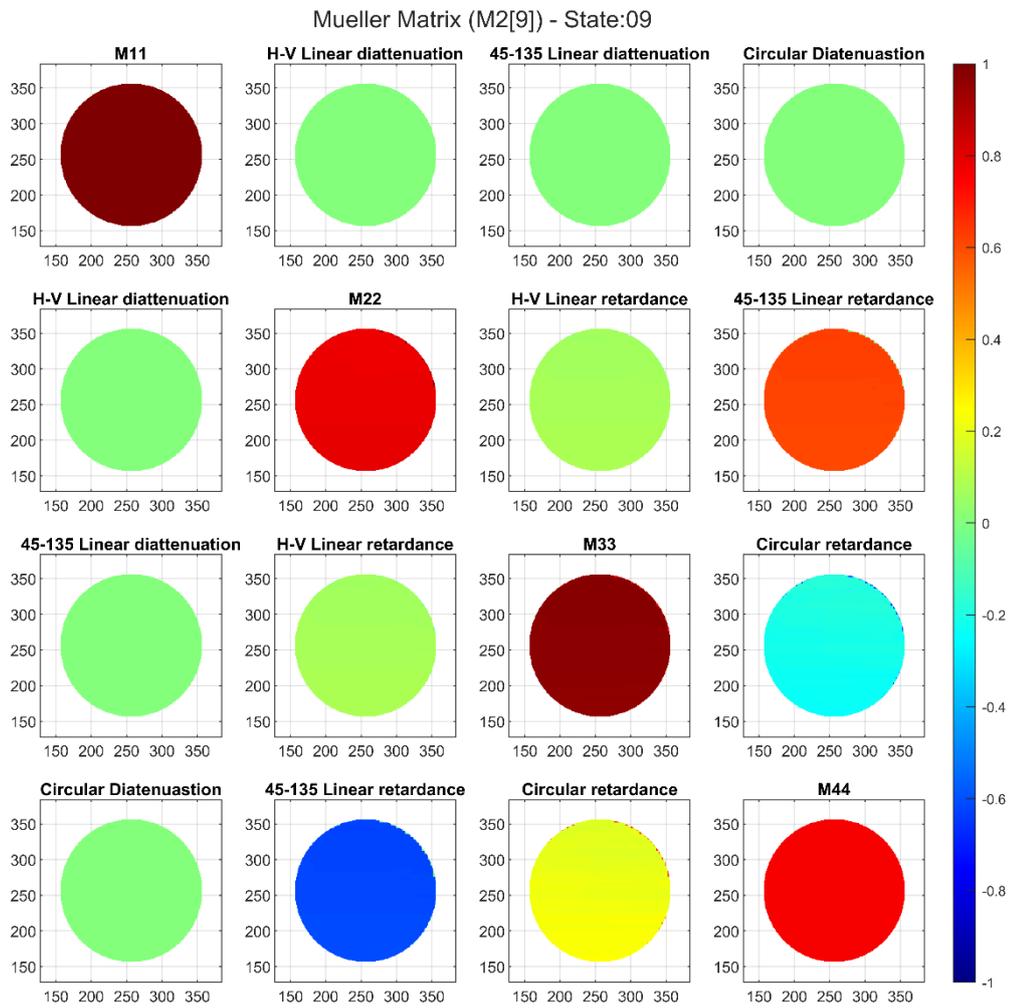
Source: Author.

Figure D.9 Mueller Matrix image for M2 State 10.

Source: Author.

Figure D.10 Mueller Matrix image for M2 State 11.

Source: Author.

Figure D.11 Mueller Matrix image for M2 State 12.

Mueller Matrix (M2[12]) - State:12

Source: Author.

Figure D.12 Mueller Matrix image for M2 State 13.

Source: Author.

Figure D.13 Mueller Matrix image for M2 State 14.

Mueller Matrix (M2[14]) - State:14

Source: Author.

Figure D.14 Mueller Matrix image for M2 State 15.

Source: Author.

Figure D.15 Mueller Matrix image for M2 State 16.

Mueller Matrix (M2[16]) - State:16

Source: Author.

ANNEX E
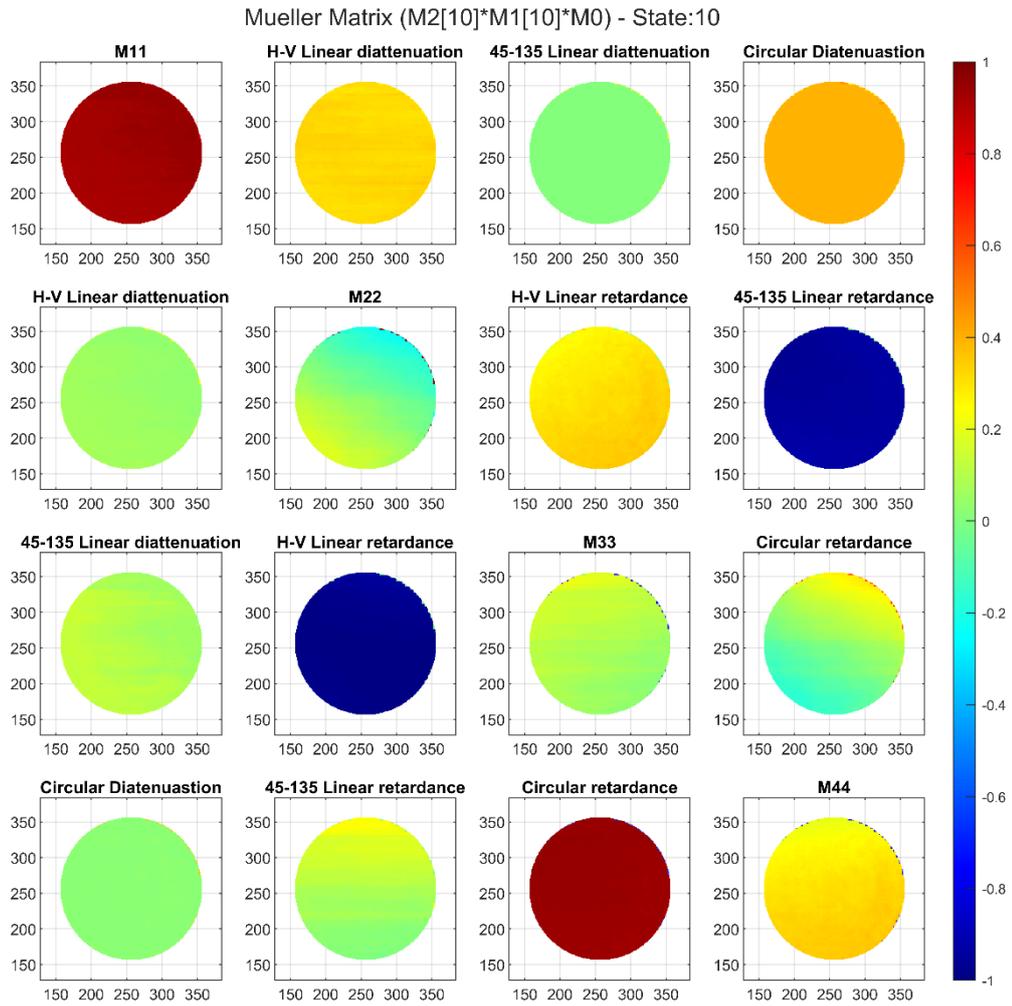
Figure E.1 Mueller Matrix image for M2 [2] X M1 [2] X M0.

Source: Author.
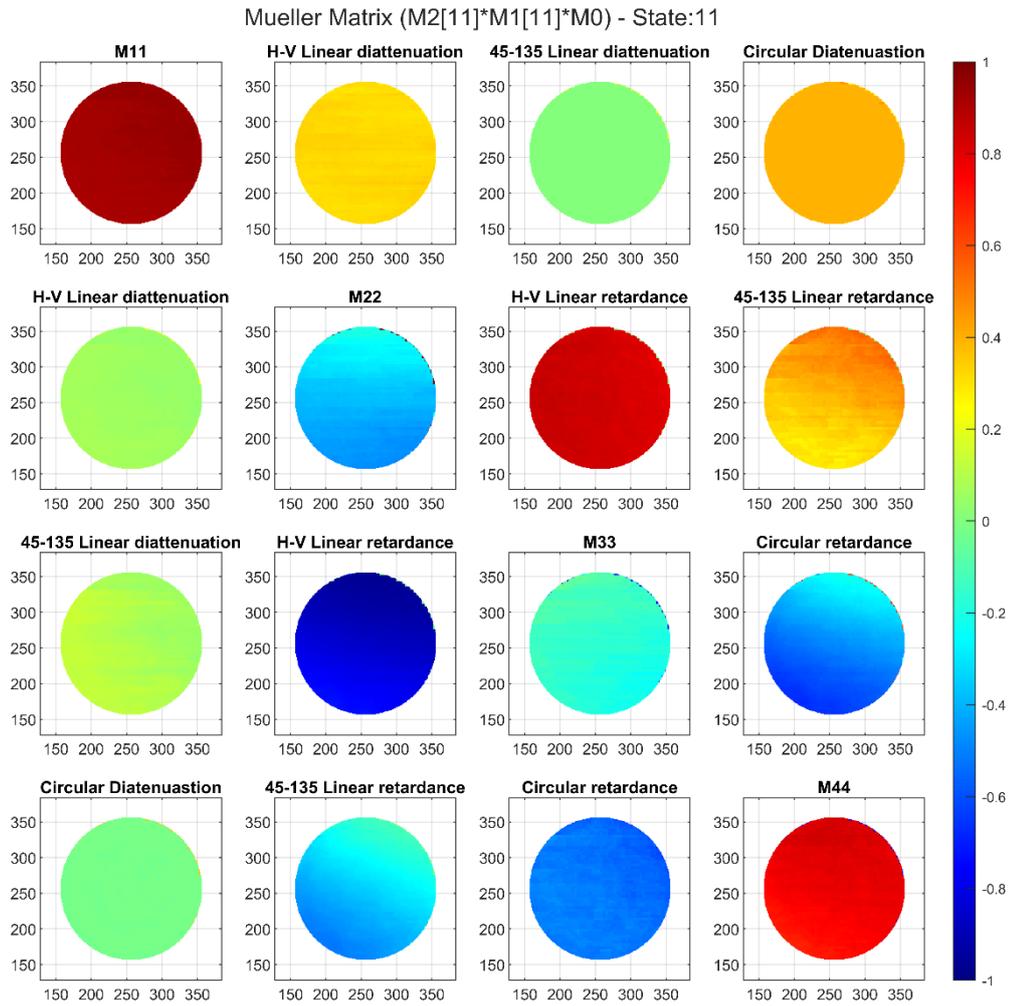
Figure E.2 Mueller Matrix image for M2 [3] X M1 [3] X M0.

Mueller Matrix (M2[3]*M1[3]*M0) - State:03

Source: Author.

Figure E.3 Mueller Matrix image for M2 [4] X M1 [4] X M0.

Mueller Matrix (M2[4]*M1[4]*M0) - State:04
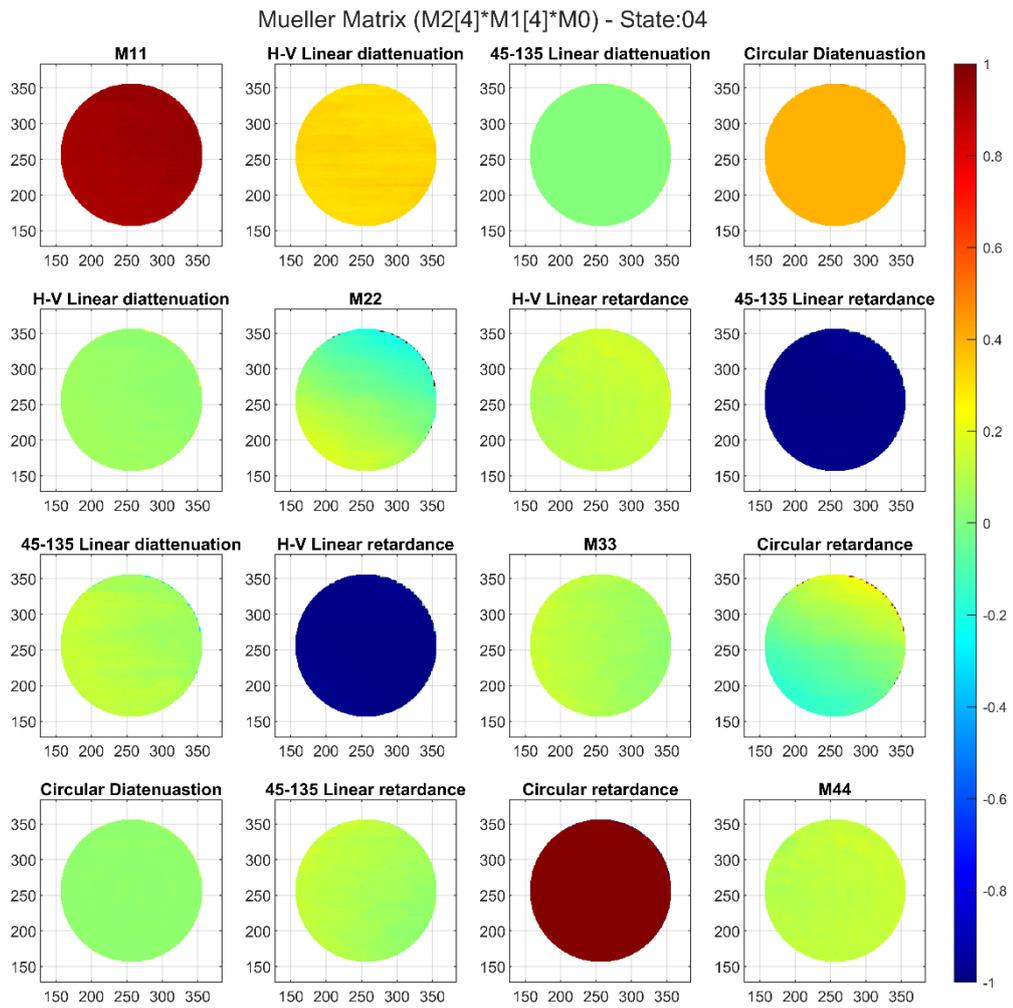
Source: Author.

Figure E.4 Mueller Matrix image for M2 [5] X M1 [5] X M0.

Mueller Matrix (M2[5]*M1[5]*M0) - State:05
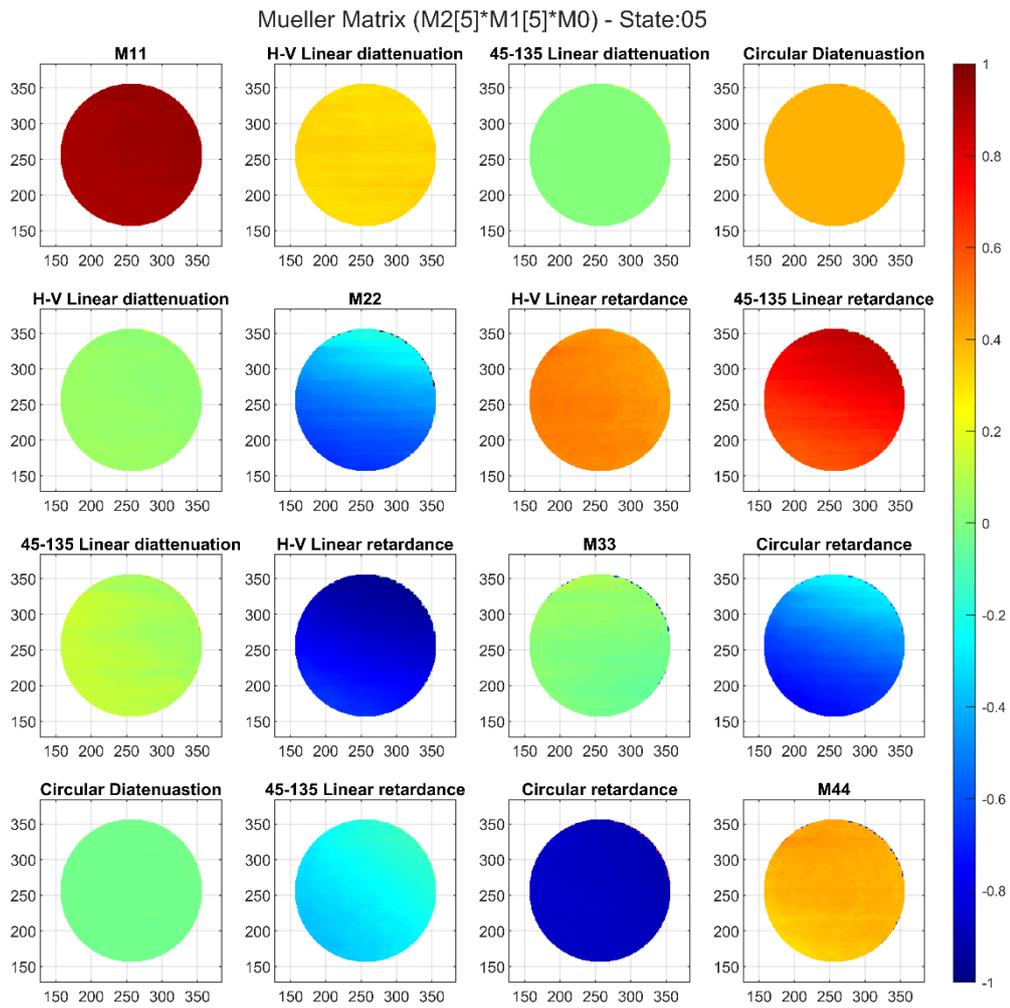
Source: Author.

Figure E.5 Mueller Matrix image for M2 [6] X M1 [6] X M0.
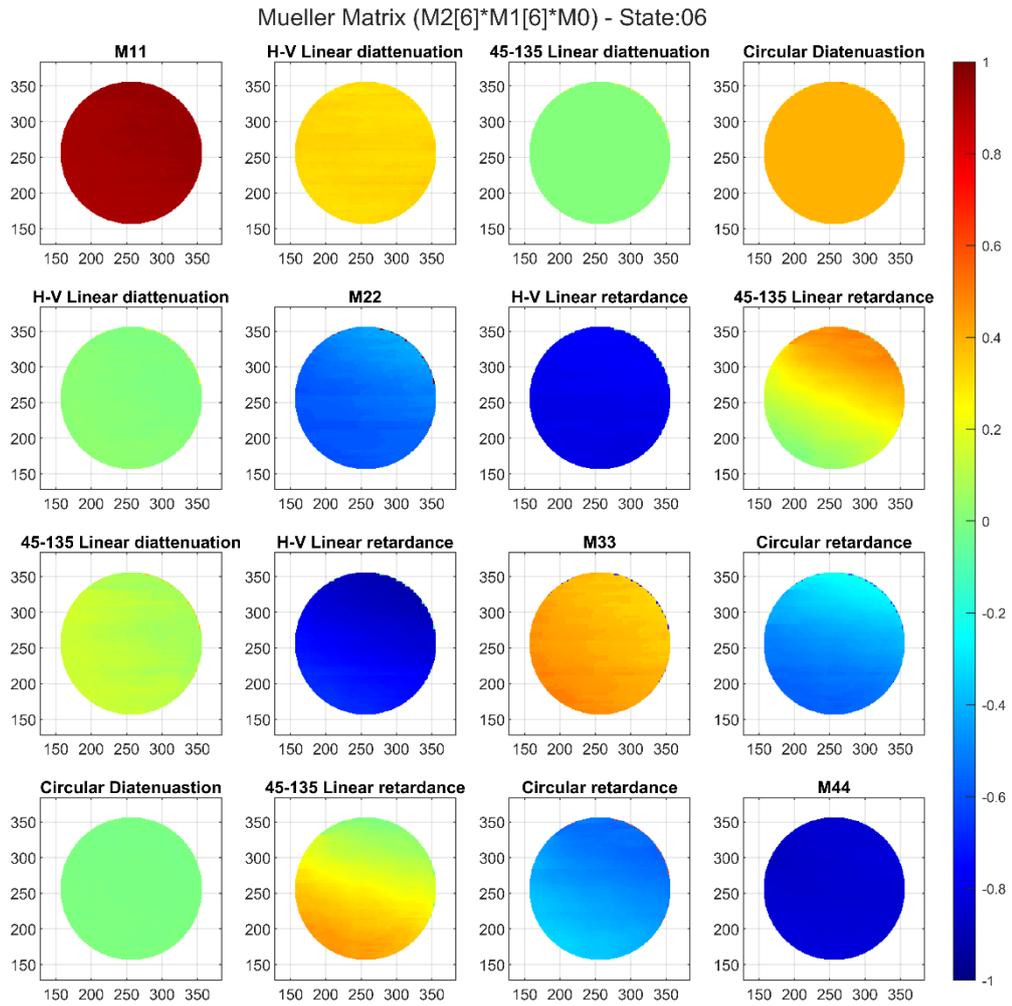
Source: Author.
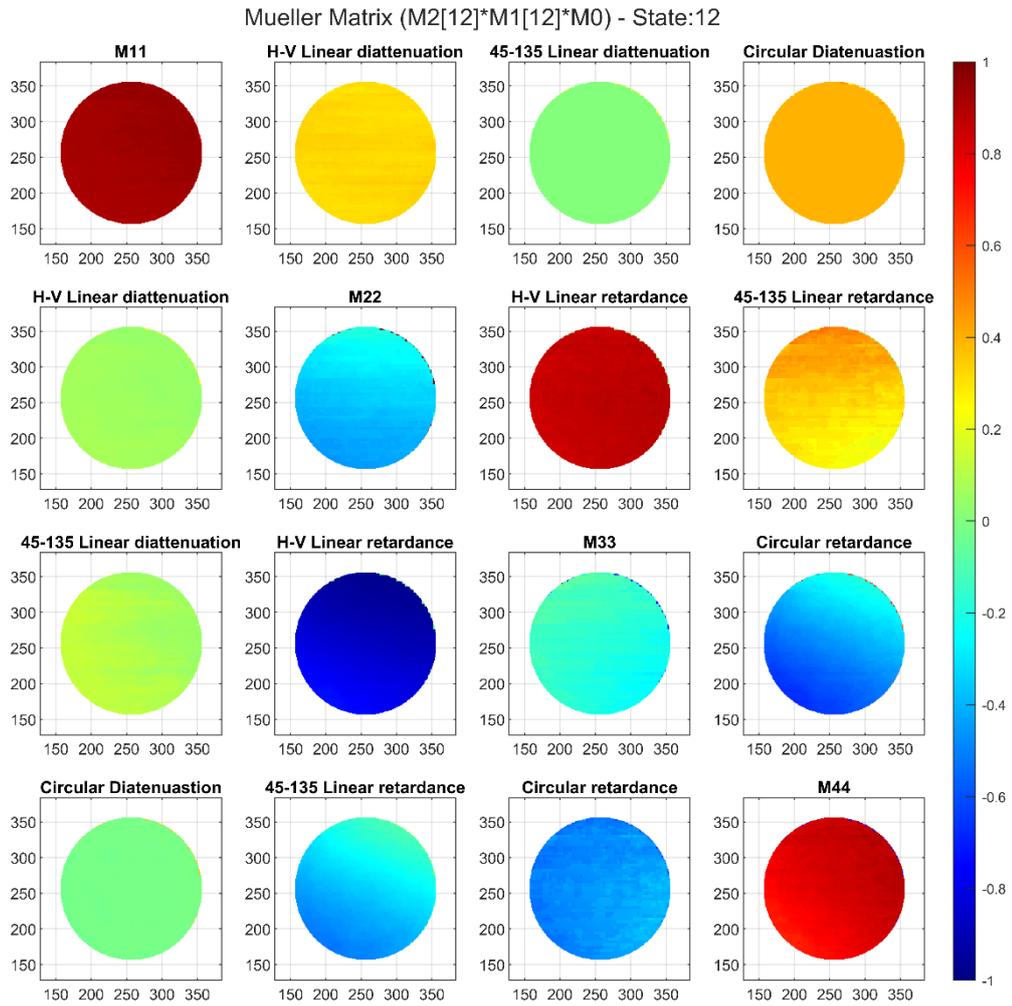
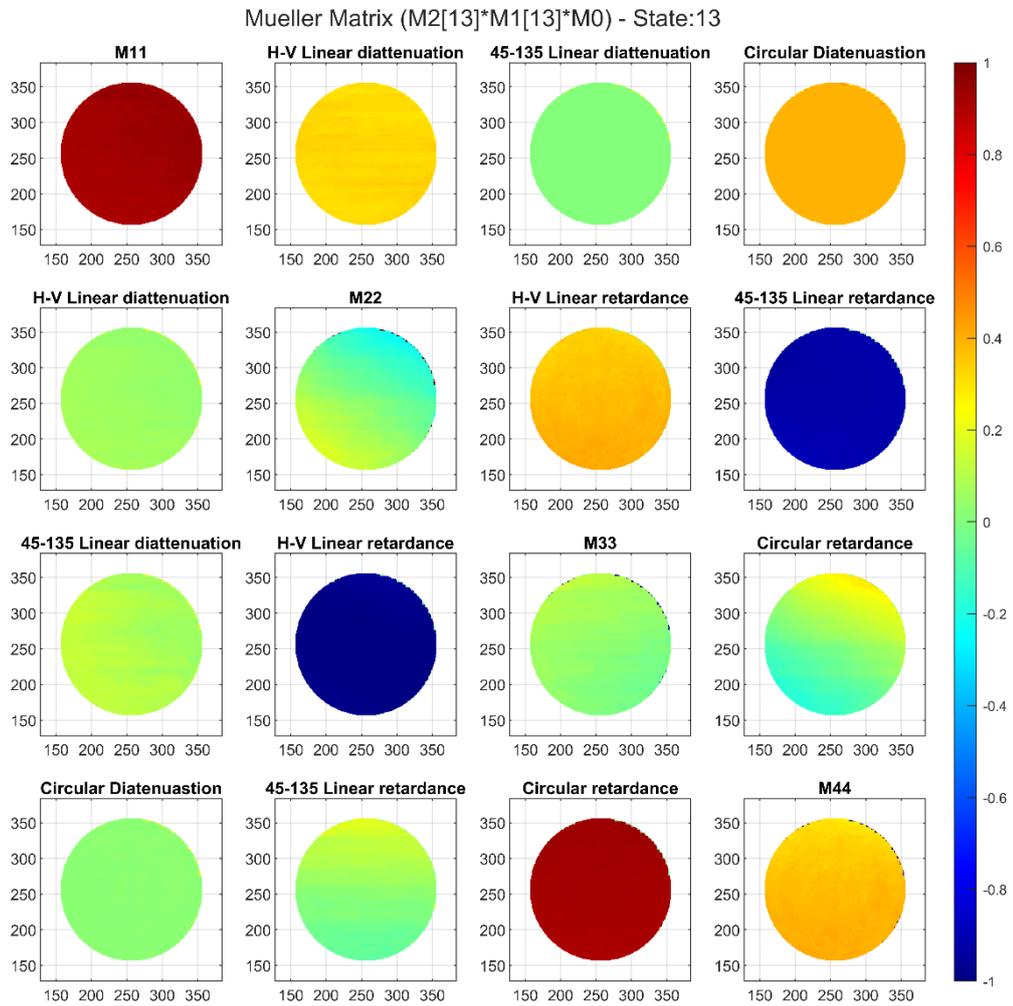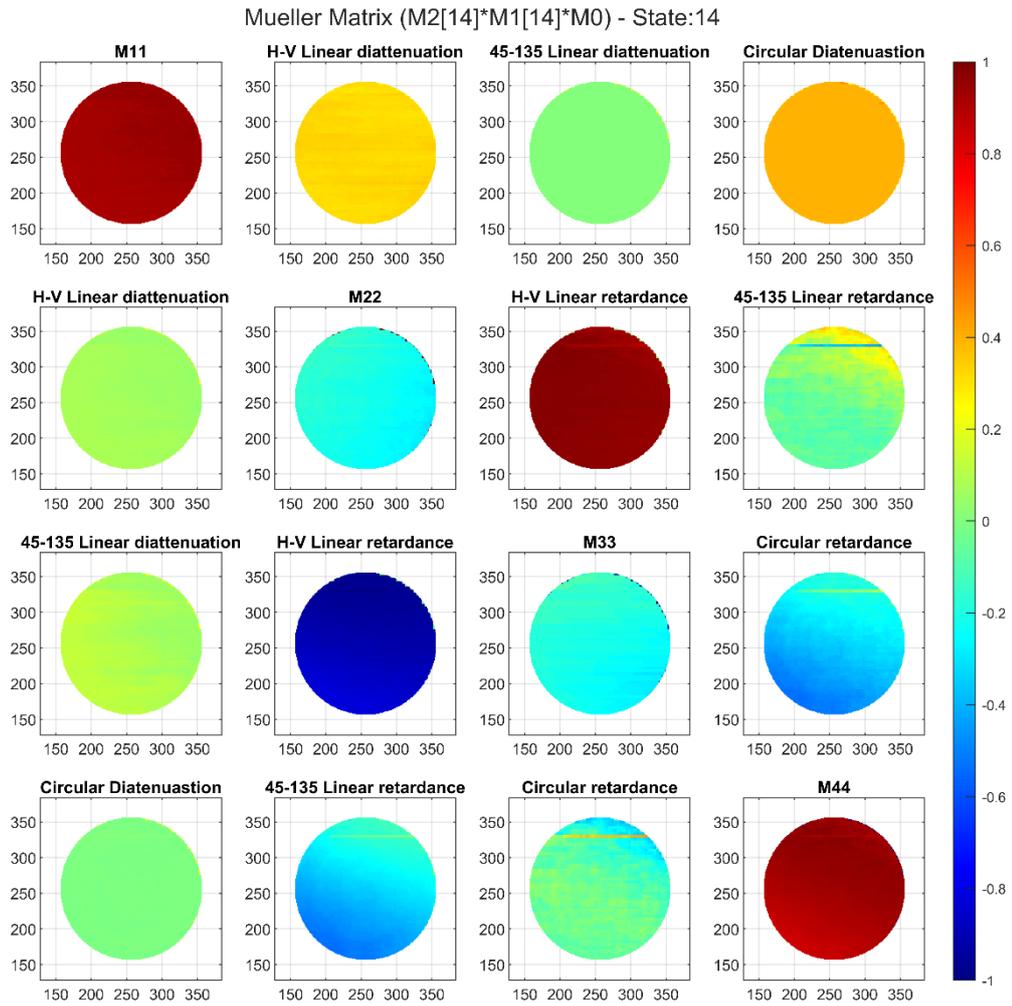Figure E.6 Mueller Matrix image for M2 [7] X M1 [7] X M0.

Mueller Matrix (M2[7]*M1[7]*M0) - State:07
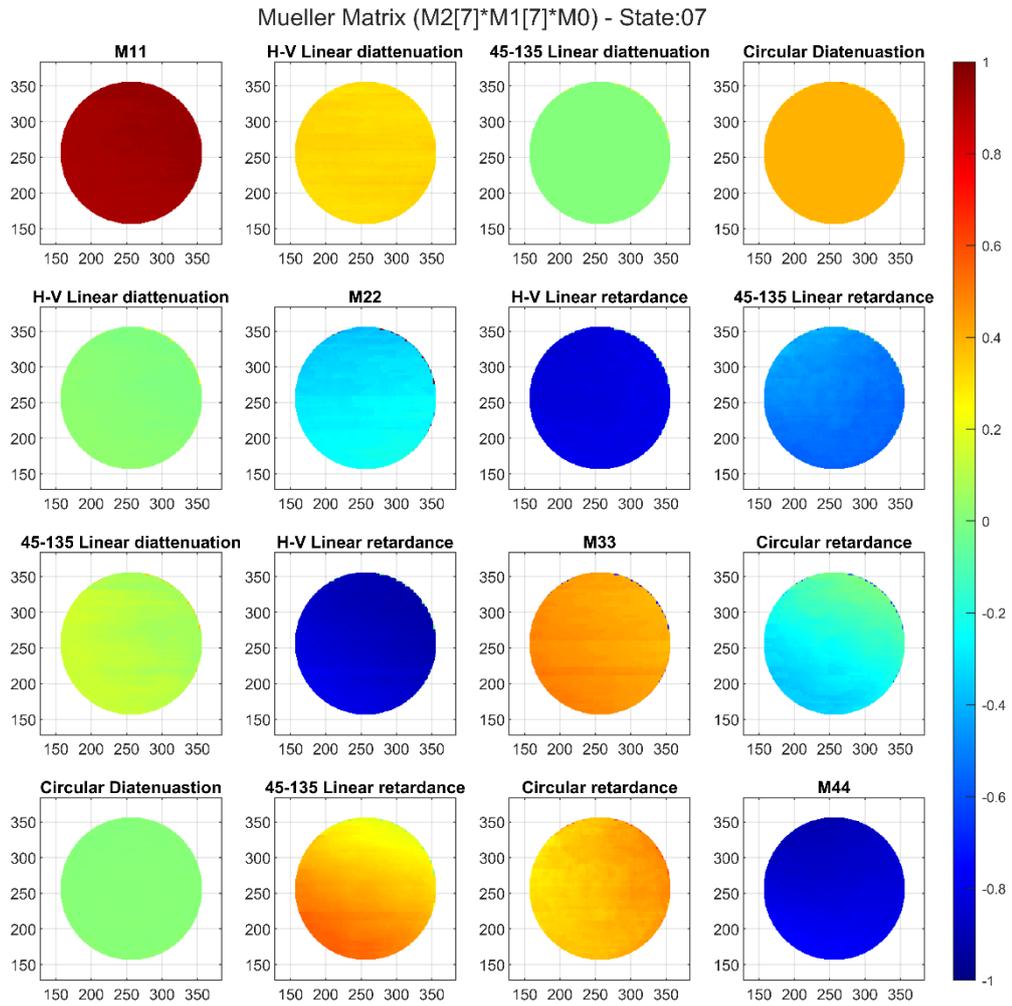
Source: Author.

Figure E.7 Mueller Matrix image for M2 [8] X M1 [8] X M0.

Mueller Matrix (M2[8]*M1[8]*M0) - State:08
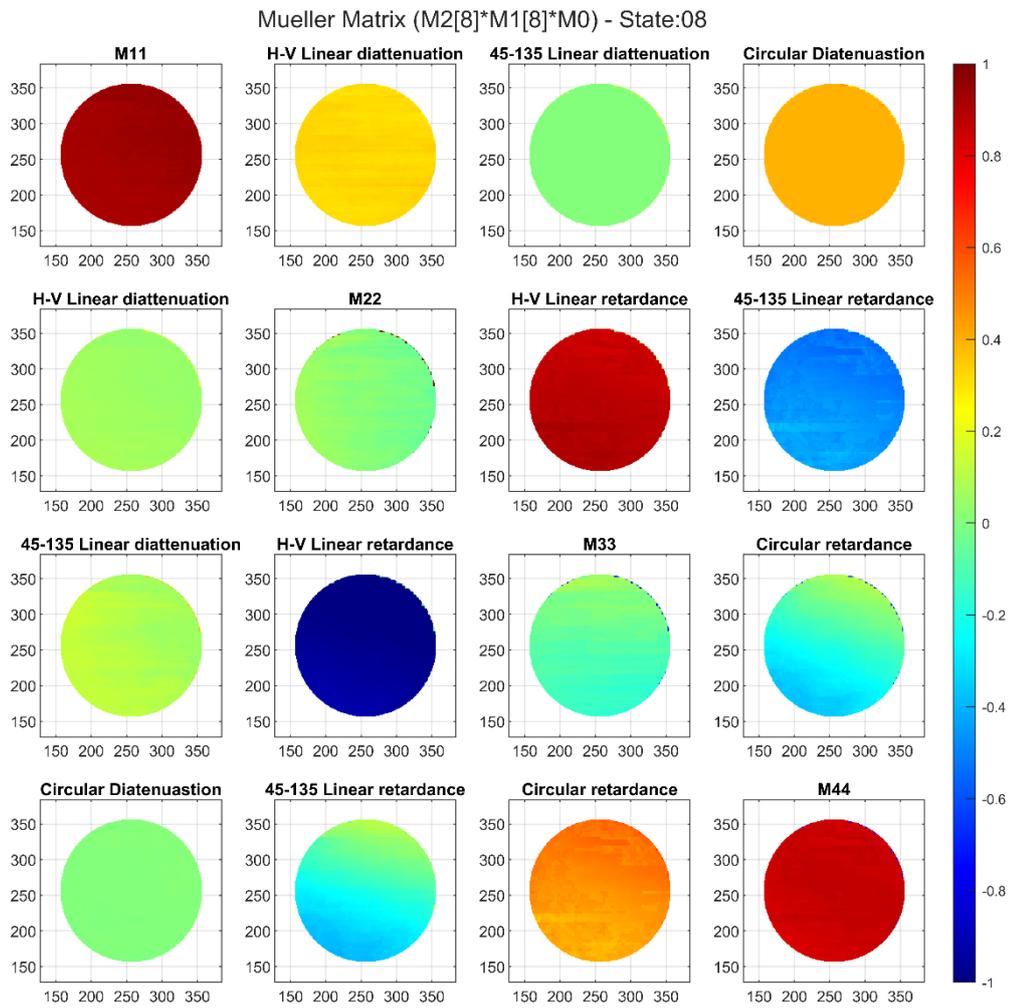
Source: Author.

Figure E.8 Mueller Matrix image for M2 [9] X M1 [9] X M0.
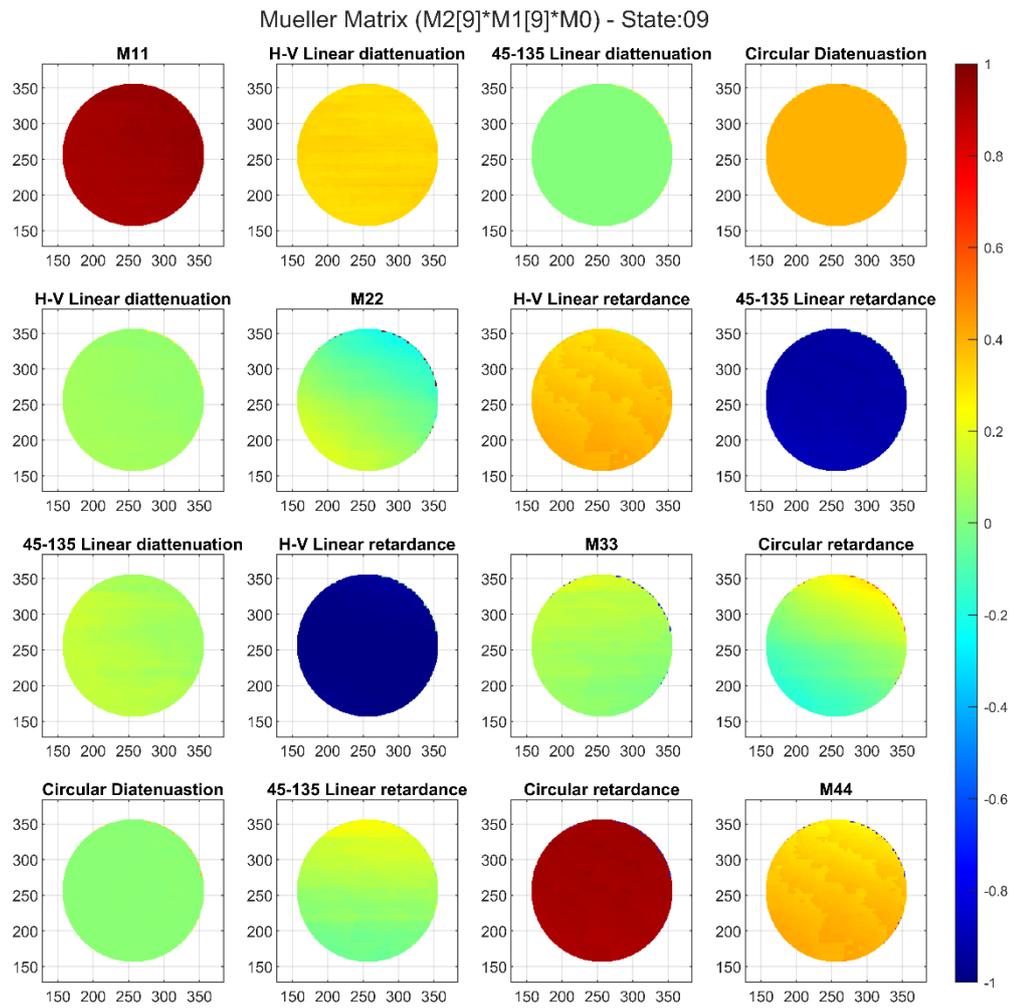
Source: Author.

Figure E.9 Mueller Matrix image for M2 [10] X M1 [10] X M0.

Source: Author.

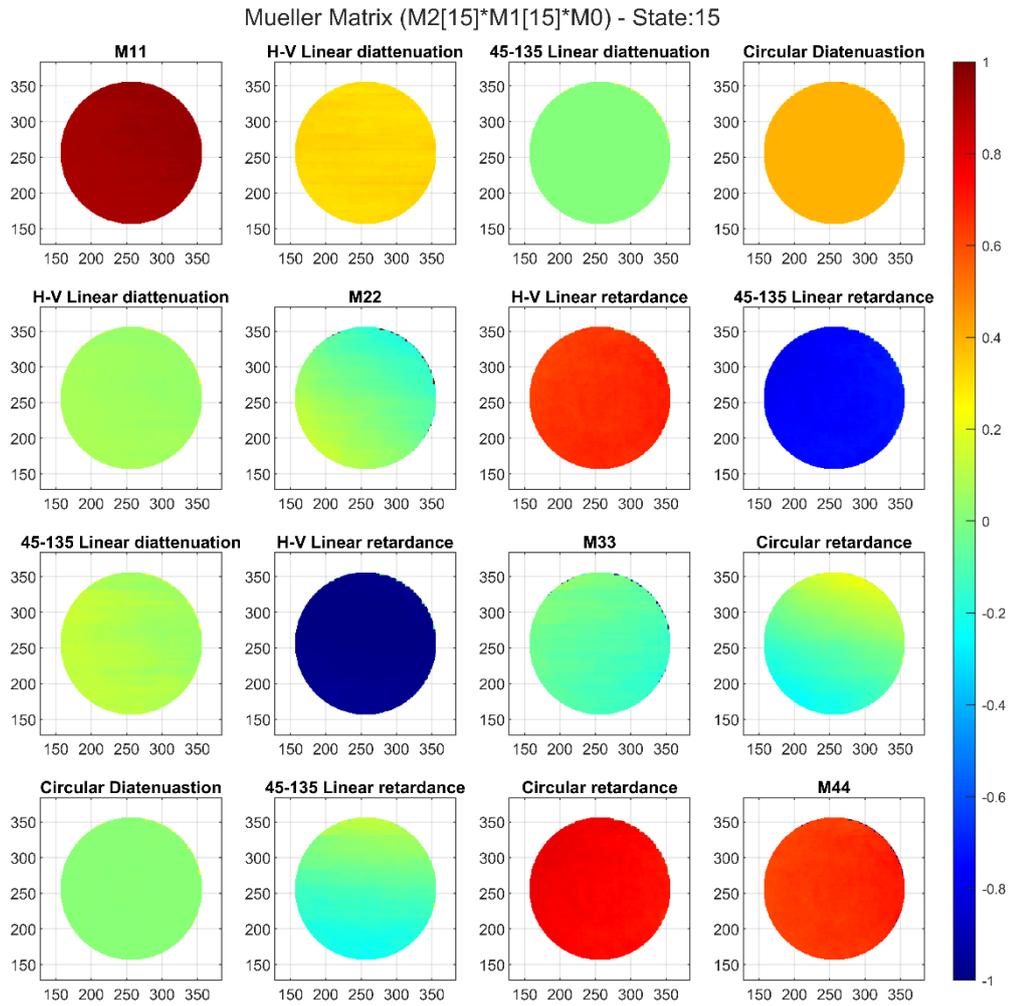Figure E.10 Mueller Matrix image for M2 [11] X M1 [11] X M0.

Mueller Matrix (M2[11]*M1[11]*M0) - State:11

Source: Author.

189

Figure E.11 Mueller Matrix image for M2 [12] X M1 [12] X M0.

Mueller Matrix (M2[12]*M1[12]*M0) - State:12

Source: Author.

Figure E.12 Mueller Matrix image for M2 [13] X M1 [13] X M0.

Source: Author.

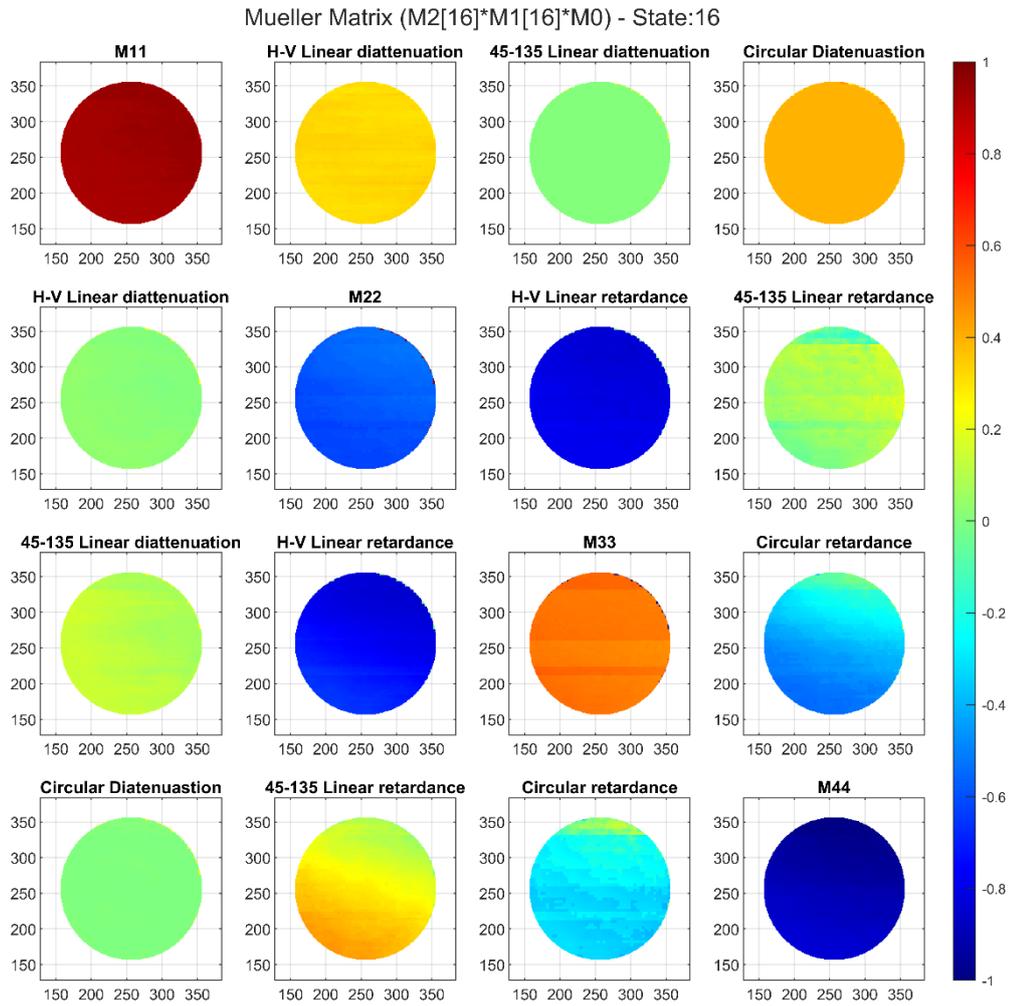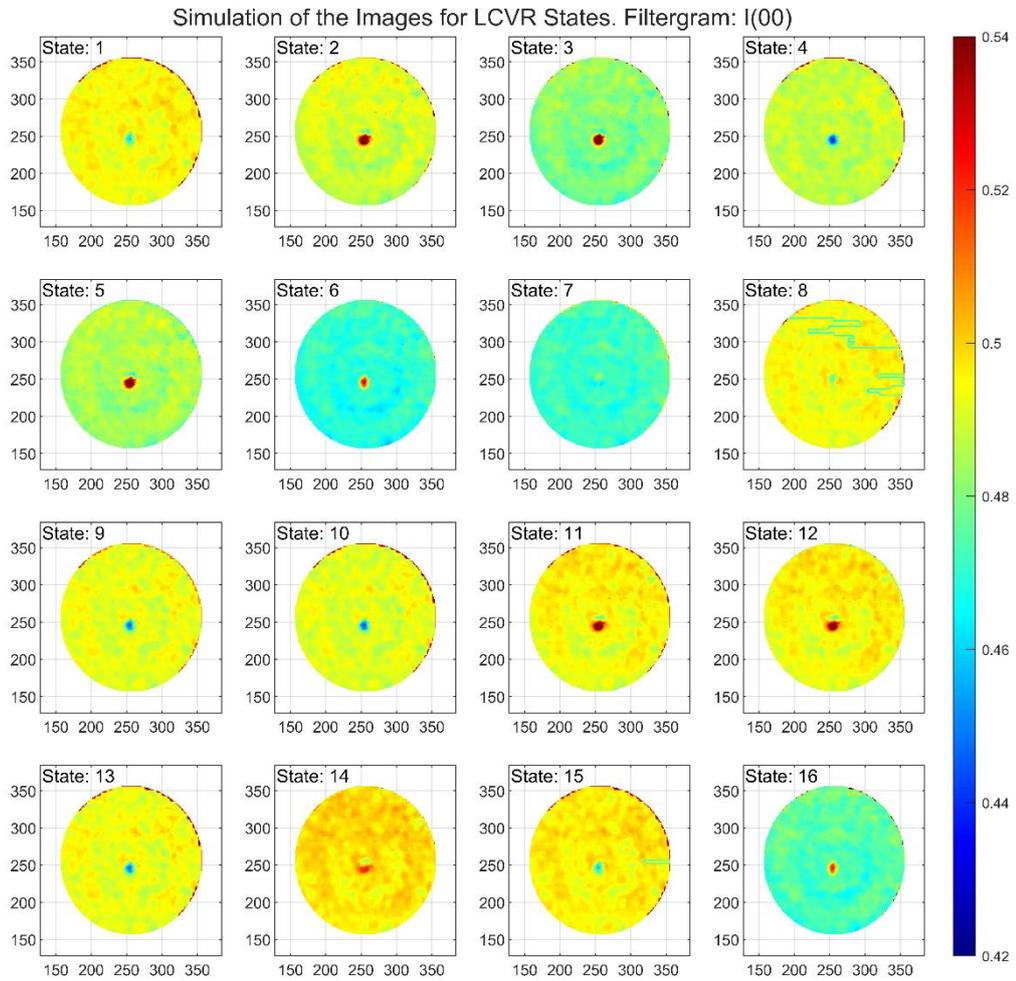Figure E.13 Mueller Matrix image for M2 [14] X M1 [14] X M0.

Mueller Matrix (M2[14]*M1[14]*M0) - State:14

Source: Author.

Figure E.14 Mueller Matrix image for M2 [15] X M1 [15] X M0.

Source: Author.

Figure E.15 Mueller Matrix image for M2 [16] X M1 [16] X M0.

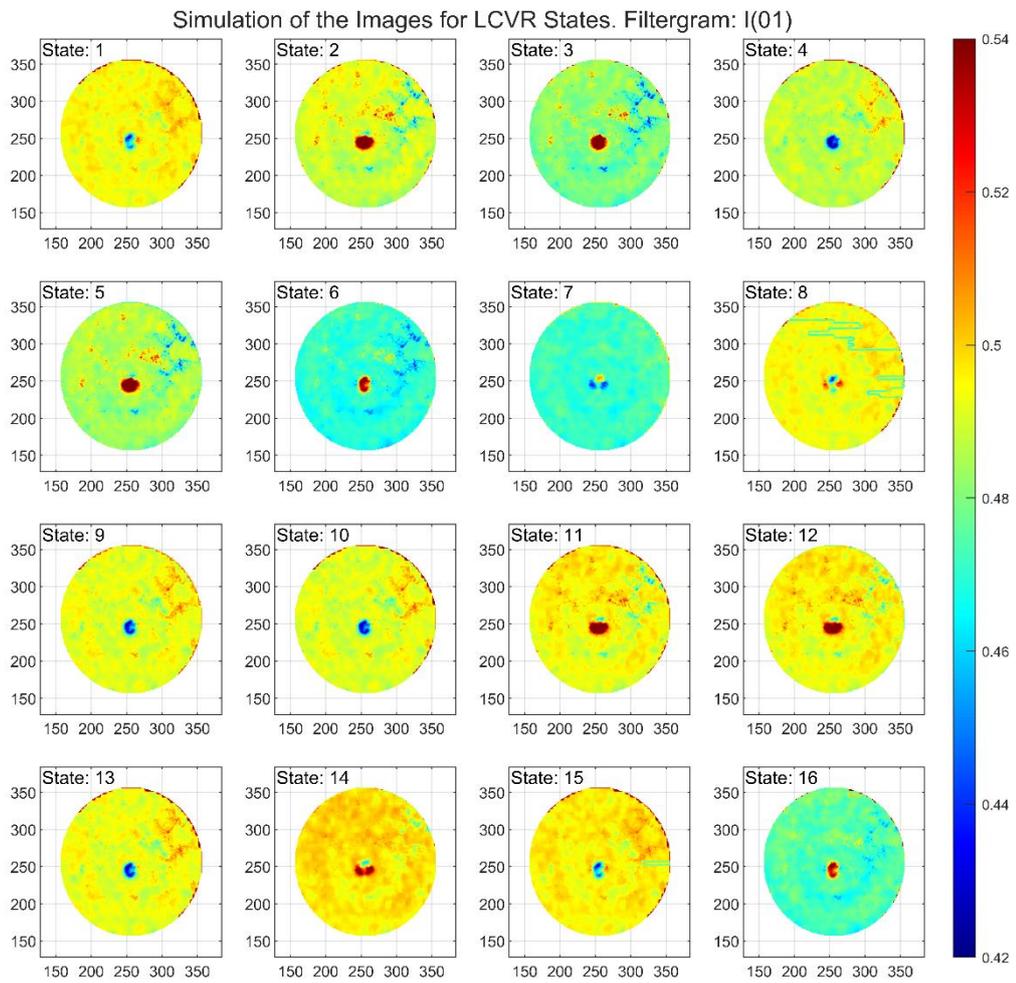Mueller Matrix (M2[16]*M1[16]*M0) - State:16

Source: Author.

ANNEX F

Figure F.1 Simulation for each PCPS's polarization state for HMI filter 00.

Source: Author.

Figure F.2 Simulation for each PCPS's polarization state for HMI filter 01.

Simulation of the Images for LCVR States. Filtergram: I(01)
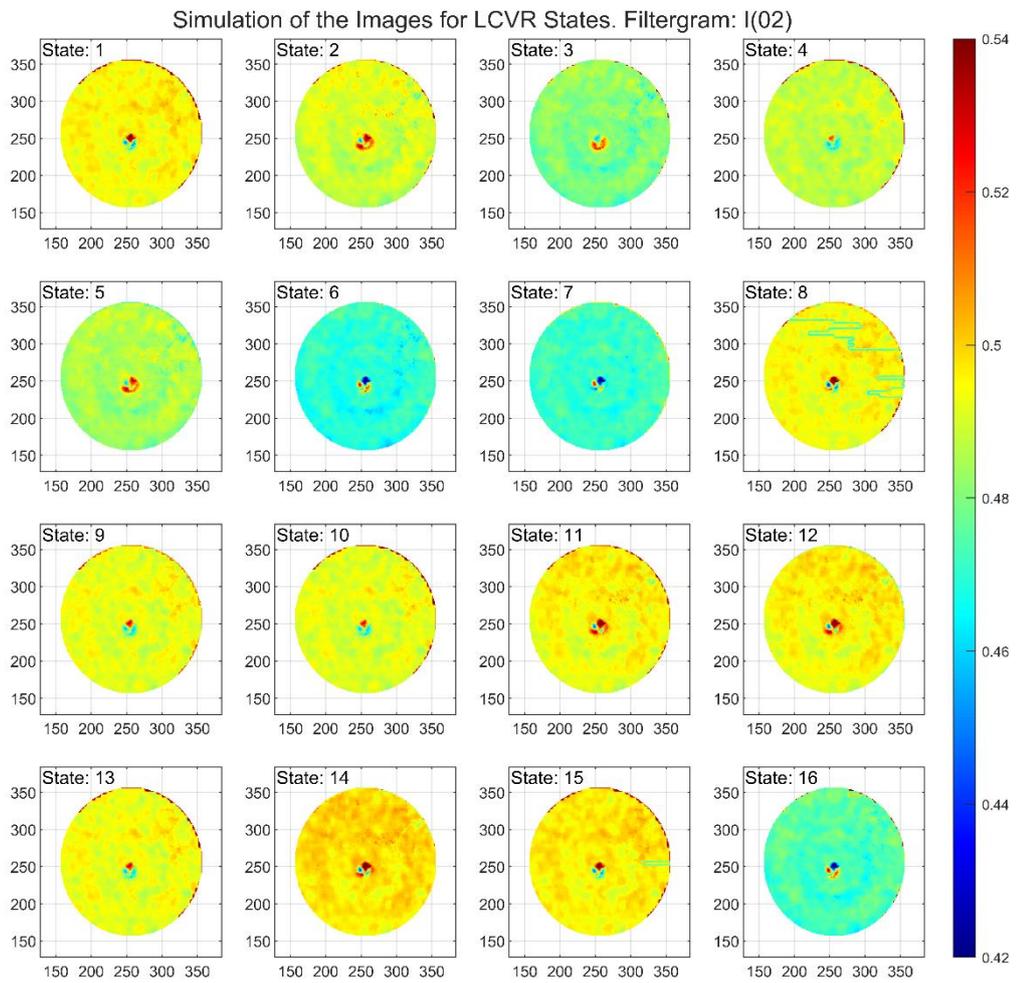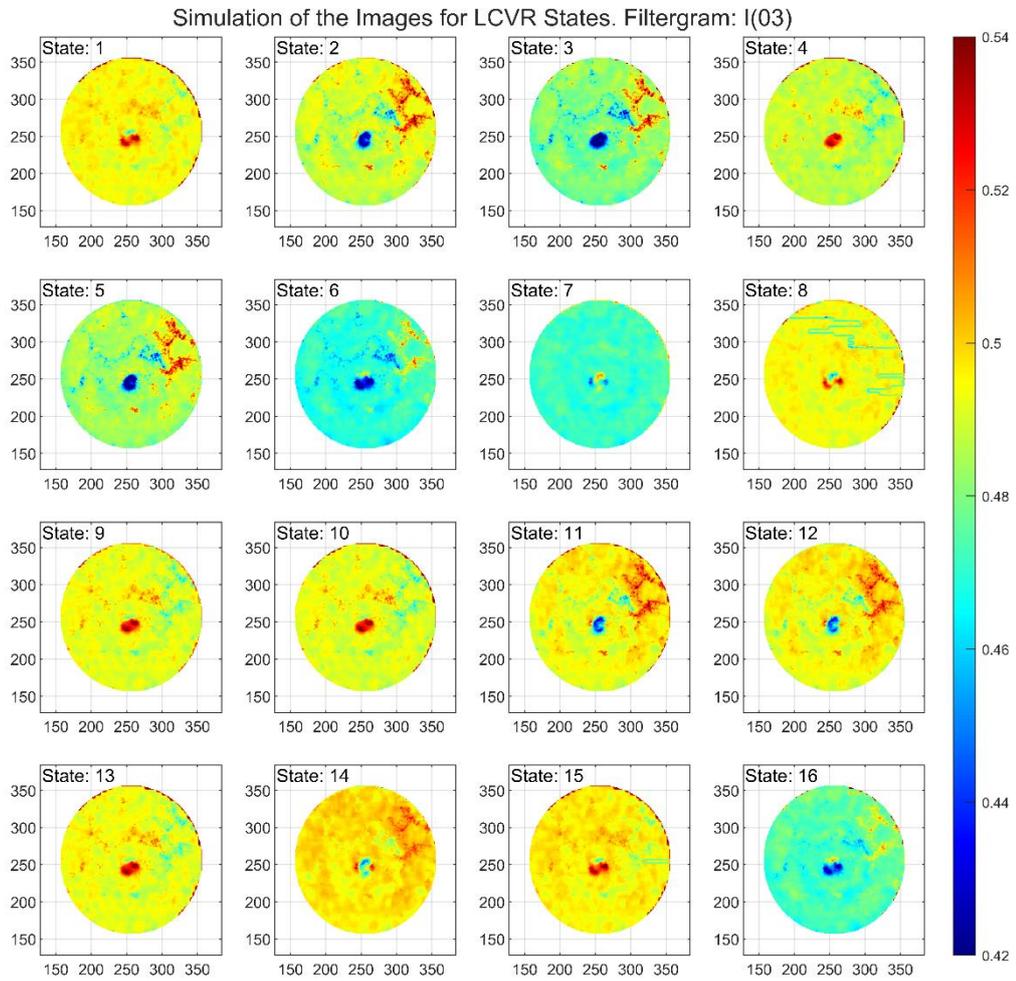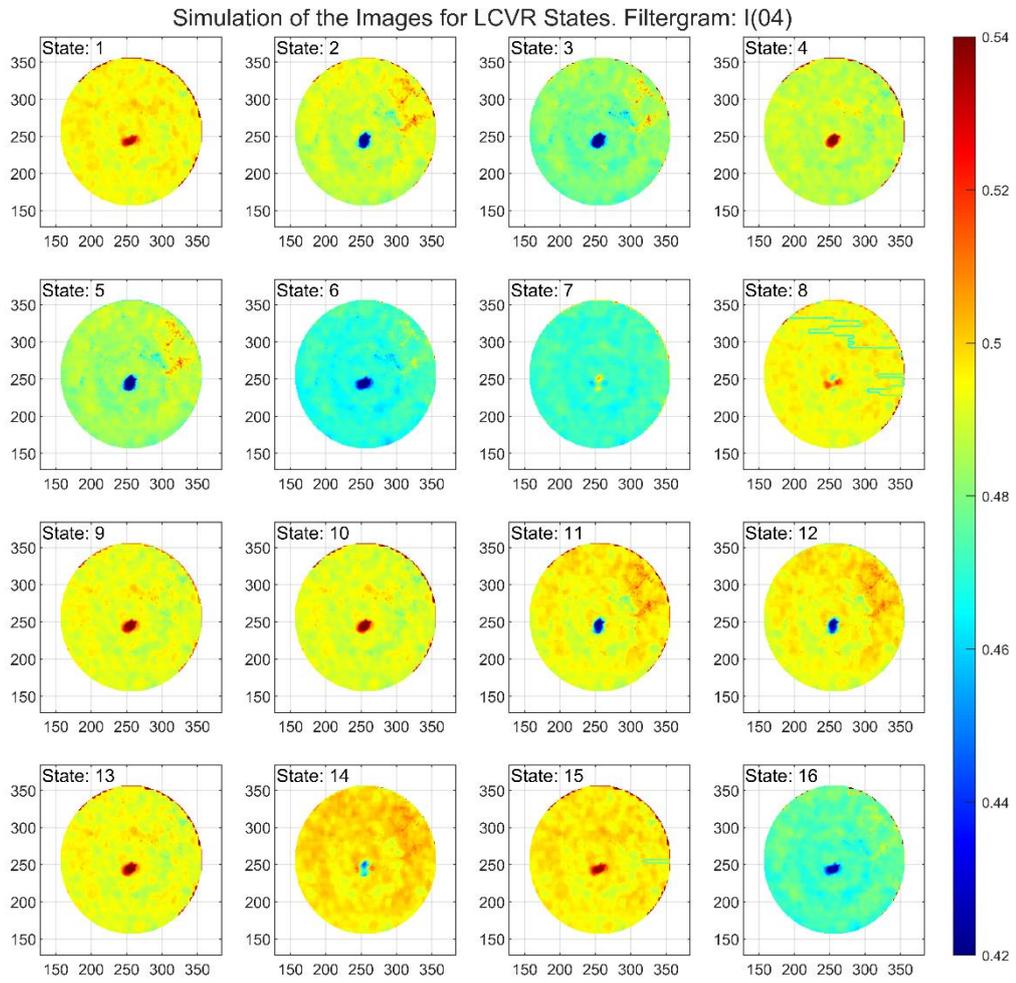
Source: Author.

Figure F.3 Simulation for each PCPS's polarization state for HMI filter 02.

Source: Author.

Figure F.4 Simulation for each PCPS's polarization state for HMI filter 03.

Simulation of the Images for LCVR States. Filtergram: I(03)

Source: Author.

Figure F.5 Simulation for each PCPS's polarization state for HMI filter 04.

Source: Author.